

SLAC-482
UC-414

STUDY OF DEEP INELASTIC SCATTERING
OF POLARIZED ELECTRONS OFF POLARIZED
DEUTERONS

Masao Kuriki

Stanford Linear Accelerator Center
Stanford University, Stanford, CA 94309

SLAC-REPORT-482
March 1996

Prepared for the Department of Energy
under contract number DE-AC03-76SF00515

Printed in the United States of America. Available from the National Technical Information Service, U.S. Department of Commerce, 5285 Port Royal, Springfield, Virginia 22161

*Ph.D. thesis

Acknowledgments

This study has been done as a collaborative work of over eighty physicists and graduate students at Stanford Linear Accelerator Center. First, I would like to thank all of the member of the collaboration and the staff of the SLAC for their excellent work.

I appreciate Professor Charles Prescott for all of his support during my staying at SLAC. Special thanks to Professor Charlie Young for his good advice and huge contribution to the analysis. The discussion with Professor Peter Bosted about the error analysis was very fruitful. I am grateful to Dr. Takashi Akagi for his help to everything what I did. Without his critical advice, this thesis would have been impossible. It was a wonderful experience for me working with the graduate students: Todd Averett, Johannes Bauer, Robin Erbacher, Jeff Fellbaum, Philippe Grenier, Tingjun Liu, Paul Raines, and Philippe Steiner. I am especially grateful to Johannes Bauer for his co-work on the operation and the analysis of the Hodoscope system, Robin Erbacher and Paul Raines for their contributions checking my english in this thesis.

I would like to express my deepest thanks to the staff of Tohoku University, especially Proffesor Haruo Yuta giving me the wonderful chance to participate this experimet. The ciritical discussion with Proffesor Koya Abe was very helpful and inspired me.

This thesis was made possible by the supporting and confidence of my family. I appreciate my father and mother for their encouragement both physically and spiritually.

This thesis is dedicated to my best friend, Akihiro Ohnogi died in 1995

Abstract

This thesis describes a 29GeV electron - nucleon scattering experiment carried out at Stanford Linear Accelerator Center (SLAC). Highly polarized electrons are scattered off a polarized ND_3 target. Scattered electrons are detected by two spectrometers located in End Station A (ESA) at angles of 4.5° and 7° with respect to the beam axis.

We have measured the spin structure function g_1 of deuteron over the range of $0.029 < x < 0.8$ and $1.0 < Q^2 < 12.0(\text{GeV}/c)^2$ giving the integral of g_1^d over the range $0 < x < 1$ to be $0.0396 \pm 0.0035 \pm 0.0039$ at average $Q^2 = 3.0(\text{GeV}/c)^2$.

This integral indicates a discrepancy of more than three standard deviations from the prediction of the Ellis-Jaffe sum rule, $\int_0^1 g_1^d dx = 0.068 \pm 0.005$ at $Q^2 = 3.0(\text{GeV}/c)^2$ while our result of g_1^d is in good agreement with SMC results. Combined with g_1 of the proton, the measurement of the integral of $\int_0^1 (g_1^p - g_1^n) dx = 0.1586 \pm 0.0103 \pm 0.0162$, was consistent with the prediction by the Bjorken sum rule, $\int_0^1 (g_1^p - g_1^n) dx = 0.169 \pm 0.008$. We also obtained the strong coupling constant at $Q^2 = 3.0(\text{GeV}/c)^2$ to be $0.417_{-0.110}^{+0.086}$, using the power correction for the sum rule up to third order of α_s . This result is in agreement with the strong coupling constant $\alpha_s(Q^2 = 3.0(\text{GeV}/c)^2)$ obtained from various experiments.

Using our deuteron results and the axial vector couplings of hyperon decays, the total quark polarization along the nucleon spin is found to be $0.286 \pm .055$, implying that quarks carry only 30% of the nucleon spin. The strange sea quark polarization is also determined to be $-0.101 \pm .023$. These measurements are in agreement with other experiments and provide the world most precise measurement of these quark polarization.

Contents

1	Introduction	12
2	Theory of the deep inelastic scattering	18
2.1	Spin-averaged cross section	20
2.2	Spin-dependent cross section	22
2.3	Cross section asymmetry	24
2.4	Virtual photon cross section	25
2.5	g_1 of deuteron	28
2.6	Sum rules	30
2.6.1	Bjorken sum rule	30
2.6.2	Ellis-Jaffe sum rule	33
3	Experimental setup	36
3.1	Polarized electron	36
3.1.1	Unstrained GaAs	38
3.1.2	Strained GaAs	39
3.2	Beam line	42
3.3	Møller system	46
3.4	Polarized target	50
3.5	Spectrometers	57
3.5.1	Čerenkov counter	61
3.5.2	Hodoscope	64

3.5.3	Shower counter	72
3.5.4	Trigger counter	78
3.5.5	Trigger electronics	82
3.6	Data acquisition and data handling	86
4	Analysis	90
4.1	Event selection	90
4.1.1	Beam analysis	90
4.1.2	Shower cluster finding	97
4.1.3	Track finding	99
4.1.4	Electron identification	103
4.2	The cross section asymmetry	116
4.2.1	The dead time correction	118
4.2.2	beam polarization	121
4.2.3	Target polarization	122
4.2.4	Dilution factor	124
4.2.5	Nitrogen correction	126
4.2.6	Positron subtraction	127
4.2.7	Radiative correction	131
4.2.8	Results	135
4.2.9	Study for the systematic effects on the asymmetry	137
5	Results	141
5.1	g_1 at a common Q^2	141
5.2	Deuteron spin structure function	148
5.3	Proton spin structure function	150
5.4	Neutron spin structure function and $g_1^p(x) - g_1^n(x)$	152
5.5	systematic error	154
5.5.1	Beam polarization	154

5.5.2	Target polarization	156
5.5.3	Dilution factor	157
5.5.4	Radiative correction	157
5.5.5	Total cross section	158
5.5.6	D-state probability	160
5.5.7	Nitrogen correction	160
5.6	Integrals of $g_1(x)$	162
5.6.1	integral in data region	162
5.6.2	Low x extrapolation	163
5.6.3	High x extrapolation	168
5.7	Test of the sum rules	170
5.7.1	Ellis-Jaffe sum rule for deuteron	171
5.7.2	Ellis-Jaffe sum rule for neutron	176
5.7.3	Bjorken sum rule	178
5.8	Quark polarization	183
6	Conclusion and a look into the future	185
A	The E143 Collaboration	197
B	Spin-dependent cross section	199
B.1	Lepton tensor	199
B.2	Hadron tensor	200
B.3	Tensor contraction and the cross section	202
C	Kauer and Carlitz model	205
D	Derivation of nitrogen correction	208

List of Tables

3.1	Čerenkov efficiency from ADC spectra	64
3.2	Hodoscope dimensions on 4.5° spectrometer.	66
3.3	Hodoscope dimensions 7° spectrometer	66
3.4	U-hodoscope dimensions	67
3.5	Time resolution of the hodoscopes	71
3.6	E/P for electron track	77
3.7	Data summary	87
4.1	Time resolution for hodoscope in the tracking	100
4.2	Track classification	100
4.3	Tracking efficiency	103
4.4	Efficiency for electron ID and pion contamination of the requirement for the Čerenkov counters	106
4.5	Efficiency for electron ID and pion contamination of the requirement for the E/P ratio	108
4.6	Efficiency for electron ID and pion contamination for neural network . . .	114
4.7	Probability matrix for the dead time correction	119
5.1	$A_1(x)$ for both spectrometers	144
5.2	$g_1(x)/F_1(x)$	146
5.3	$g_1(x)$ for deuteron	151
5.4	g_1 integral for the data region	163

5.5	The results of the low-x extrapolation of g_1	167
5.6	Fitting with $g_1(x)$ at high x region	168
5.7	The integral of $g_1(x)$ in the region of $0.8 < x < 1.0$	171
5.8	The integral of g_1, Γ at $Q^2 = 3.0(\text{GeV}/c)^2$	172
5.9	The integral of g_1, Γ at $Q^2 = 10.0(\text{GeV}/c)^2$	172

List of Figures

1.1	Γ^p from EMC	14
1.2	Aerial view of SLAC	16
2.1	Feynman diagram of the e-N scattering	19
2.2	Polarized cross sections	22
2.3	SU(3) baryon octet	33
3.1	Polarized electron source	37
3.2	Energy level of the unstrained GaAs	38
3.3	Layer of the strained GaAs	39
3.4	The lattice structure of the strained GaAs	40
3.5	Energy level of the strained GaAs	41
3.6	Electron polarization as a function of the photon wave-length	42
3.7	Beam acceleration and transportation	44
3.8	ESA beam line	44
3.9	Beam rastering	45
3.10	Foil array output	45
3.11	Chicane magnets	46
3.12	Møller polarimeter schematic view	48
3.13	Møller spectrum	49
3.14	Momentum spectrum of electrons from the Møller scattering	49
3.15	Energy level for e-P system	52

3.16 Schematic view of E143 polarized target	55
3.17 NMR signal of thermal equilibrium	56
3.18 Schematic view of the spectrometer system	57
3.19 Momentum acceptance of 4.5° spectrometer	58
3.20 Momentum acceptance of 7° spectrometer	58
3.21 Ray trace of in the 4.5° spectrometer	59
3.22 Ray trace of in the 7° spectrometer	59
3.23 Momentum resolution	60
3.24 Čerenkov counter schematic view	62
3.25 Finger overlap	65
3.26 Hodoscope system layout	65
3.27 High voltage splitter	68
3.28 Hodoscope timing sp4	69
3.29 Hodoscope timing sp7	70
3.30 Plane inefficiency for run 1334 in 4.5° spectrometer	73
3.31 Plane inefficiency for run 1334 in 7° spectrometer	73
3.32 The schematic view of the shower counter	74
3.33 Read out of the shower counter	74
3.34 Classification for the shower block (cluster)	76
3.35 Schematic view of the front trigger counter	78
3.36 Schematic view of the rear trigger counter	79
3.37 Cosmic ray test	80
3.38 Time spectrum of the front trigger counter with respect to the counter A	80
3.39 Time difference between counter A and counter B.	81
3.40 Time difference between counter B and the front trigger counter	81
3.41 Time difference between counter A and the rear trigger counter.	82
3.42 Time difference between counter B and the rear trigger counter.	82
3.43 E143 trigger logic	83
3.44 Logic of the main trigger	84

3.45	Logic of pion-or	85
3.46	Logic of the main-or trigger	86
3.47	DAQ system	88
4.1	Spectrum of the Good spill monitor	91
4.2	Spectrum of Bad spill monitor	93
4.3	Spectrum of Toroid 2 current monitor	93
4.4	Spectrum of the beam spot size	94
4.5	The distance of the beam position from the target center	95
4.6	Logic of PRNG	96
4.7	Evolution of Cellular automata	98
4.8	Track extrapolated position on target	101
4.9	Track extrapolated position at the target	101
4.10	Track-cluster matching (sp4)	101
4.11	Track-cluster matching (sp7)	101
4.12	C1 ADC spectrum (sp4)	104
4.13	C2 ADC spectrum (sp4)	104
4.14	C1 ADC spectrum (sp7)	105
4.15	C2 ADC spectrum (sp7)	105
4.16	E/P ratio on 4.5° spectrometer	107
4.17	E/P ratio on 7° spectrometer	107
4.18	Total energy deposited in the nine blocks	109
4.19	The energy ratio of the central block	109
4.20	Energy deposited in 16 blocks beyond the nine blocks	110
4.21	Number of blocks in a cluster	110
4.22	Illustration for the neural network.	111
4.23	Spectrum of the neural network response (sp4)	113
4.24	Spectrum of the neural network response (sp7)	113
4.25	Data profile on $x - Q^2$ plane	115

4.26	Data profile on $x - Q^2$ plane	115
4.27	Dead time correction (sp4)	120
4.28	Dead time correction (sp7)	120
4.29	The left-right asymmetry for the dead time correction (sp4)	120
4.30	The left-right asymmetry for the dead time correction (sp7)	120
4.31	The results of ESA Møller polarimeter	121
4.32	Target polarization	122
4.33	The beam heating correction	123
4.34	Dilution factor (sp4)	126
4.35	Dilution factor (sp7)	126
4.36	Dilution factor due to the positron contamination for A_{\parallel} (sp4)	129
4.37	Dilution factor due to the positron contamination for A_{\parallel} (sp7)	129
4.38	[Dilution factor due to the positron contamination for A_{\perp} (sp4)	129
4.39	[Dilution factor due to the positron contamination for A_{\perp} (sp7)	129
4.40	The asymmetric correction due to the positron contamination for A_{\parallel} (sp4)	130
4.41	The asymmetric correction due to the positron contamination for A_{\parallel} (sp7)	130
4.42	The asymmetric correction due to the positron contamination for A_{\perp} (sp4)	130
4.43	The asymmetric correction due to the positron contamination for A_{\perp} (sp7)	130
4.44	Feynman diagrams for the radiative correction	132
4.45	Radiative correction for A_{\parallel} (sp4)	133
4.46	Radiative correction for A_{\perp} (sp4)	133
4.47	Radiative correction for A_{\parallel} (sp7)	134
4.48	Radiative correction for A_{\perp} (sp7)	134
4.49	Radiative correction for the statistical error of A_{\parallel} (sp4)	135
4.50	Radiative correction for the statistical error of A_{\parallel} (sp7)	135
4.51	A_{\parallel} (sp4)	136
4.52	A_{\perp} (sp4)	136
4.53	A_{\parallel} (sp7)	136
4.54	A_{\perp} (sp7)	136

4.55	The χ^2 distribution of the difference of the A_{\parallel} taken with different target polarization direction in 4.5° spectrometer.	137
4.56	The χ^2 distribution of the difference of the A_{\perp} taken with different target polarization direction in 4.5° spectrometer.	137
4.57	The χ^2 distribution of the difference of the A_{\parallel} taken with different target polarization direction in 7° spectrometer.	138
4.58	The χ^2 distribution of the difference of the A_{\perp} taken with different target polarization direction in 7° spectrometer.	138
4.59	The χ^2 distribution of the difference of the A_{\parallel} taken with different magnetic field direction in 4.5° spectrometer.	139
4.60	The χ^2 distribution of the difference of the A_{\perp} taken with different magnetic field direction in 4.5° spectrometer.	139
4.61	The χ^2 distribution of the difference of the A_{\parallel} taken with different direction of the magnetic field in 7° spectrometer.	140
4.62	The χ^2 distribution of the difference of the A_{\perp} taken with different direction of the magnetic field in 7° spectrometer.	140
5.1	$A_1(x)$	142
5.2	The difference between $A_1(x)$ from both spectrometers	142
5.3	g_1/F_1	143
5.4	The difference of between g_1/F_1 from both spectrometers	143
5.5	The $g_1(x)/F_1(x)$ for deuteron	147
5.6	$A_1(x)$ for deuteron	147
5.7	$F_2(x, Q^2 = 3.0)$ by NMC parameterization	148
5.8	$R(x, Q^2 = 3.0)$	148
5.9	$g_1^d(x)$	149
5.10	$g_1(x)$ for proton	150
5.11	The neutron $g_1(x)$	153
5.12	$g_1^p(x) - g_1^n(x)$	153

5.13	Systematic error of $xg_1^d(x)$ due to the beam polarization	155
5.14	Systematic error of $xg_1^d(x)$ due to the target polarization	155
5.15	The systematic error of $xg_1^d(x)$ due to the dilution factor	158
5.16	The systematic error of $xg_1^d(x)$ due to the radiative correction	158
5.17	$F_2(x, Q^2)$ from NMC experiment	161
5.18	Systematic error of $xg_1^d(x)$ due to the F_1/D'	161
5.19	$F_2(x)$ from NMC and the reduced χ^2 of the Regge fit	164
5.20	Low x extrapolation of g_1 of deuteron	165
5.21	Low x extrapolation of g_1 of neutron	166
5.22	Low x extrapolation of $g_1^p - g_1^n$	166
5.23	High x extrapolation of the $g_1(x)$ for deuteron	169
5.24	High x extrapolation of the g_1 for neutron	169
5.25	High x extrapolation of $g_1^p(x) - g_1^n(x)$	170
5.26	$xg_1(x)$ for deuteron at $Q^2 = 10(\text{GeV}/c)^2$	174
5.27	Γ^d results with the prediction of the Ellis-Jaffe sum rule	175
5.28	$g_1(x)$ for neutron at $Q^2 = 2.0(\text{GeV}/c)^2$	176
5.29	Γ^n results with the prediction of the Ellis-Jaffe sum rule	177
5.30	$xg_1^p - xg_1^n$ at $Q^2 = 10(\text{GeV}/c)^2$	179
5.31	$\Gamma^p - \Gamma^n$ results with the prediction of the Bjorken sum rule	181
5.32	The strong coupling constant as a function of Q^2	182
5.33	Quark polarization	184
6.1	Feynman diagram of Photo-gluon fusion	188
C.1	Kauer Carlitz model for $A_1(x)$	207
D.1	Proton polarization	210
D.2	^{15}N polarization	210

Chapter 1

Introduction

The electron-nucleon scattering has played an important role in advancing our understanding of the nucleon structure. In Quantum electrodynamics (QED), the electron is treated exactly as a point like particle which does not have any structure, whereas the nucleon is treated as a substance which have a complex structure. In electron-nucleon scattering, virtual photons are exchanged between the electron and the substructure of the nucleon. Therefore, this makes us to investigate the nucleon structure by using the photon probe.

In the 1950's, the elastic and quasi-elastic electron-nucleon scattering experiments[1] indicated that the nucleon has a finite size of order 10^{-13} cm. Several experiments in the middle of 1960's[2] established that the cross section fell with increasing momentum transfer, suggesting a composite nucleon model. In 1969, results from deep inelastic scattering of electrons off a hydrogen target at SLAC[3] showed that the cross section is larger than expected by the composite model, and that the cross section has only a weak dependence on momentum transfer(Q^2). This behavior, refer to Bjorken scaling, is interpreted to imply that the nucleon is composed of point-like charged particles. These point like particles were named as partons by Feynman in 1967. The precise measurement of the nucleon structure[4] showed that the charged partons carry only a half of the nucleon momentum, and that neutral partons which carry the other half of the nucleon momentum

exist in the nucleon. These charged and neutral partons are later identified as quarks and gluons which are described by Quantum Chromodynamics(QCD). Now, we believe that the nucleon is composed of valence quarks, sea quarks, and gluons. There are three valence quarks in the nucleon which determine net quantum numbers such as charge and baryon number. Sea quarks are created in pair by gluon which have no net quantum number. Gluons mediate the color force which composes these partons together.

As nucleon spin is $1/2$, it had been assumed that only the valence quarks are responsible for the nucleon spin analogous to the baryon number or nucleon charge, and that sea quarks and gluons were not polarized in the nucleon. In such a naive picture, the SU(6) model of baryons describes well the magnetic moments of the baryons [5].

Bjorken derived a sum rule for the combination of the structure functions of the proton and neutron using current algebra and an assumption of iso-spin symmetry[6]. This sum rule predicts that the integral of the difference of spin structure functions of the proton and the neutron over Bjorken x from zero to one is equal to a sixth of the axial vector coupling strength in neutron beta decay, $\int_0^1 [g_1^p(x) - g_1^n(x)] dx = \frac{1}{6} g_A / g_V$. Because this sum rule can be derived also using QCD calculations, it is thought of as a fundamental sum rule. Bjorken himself said 'If the sum rule is violated, QCD is wrong.'[7]. This sum rule is usually called the Bjorken sum rule.

Ellis and Jaffe derived another sum rule predicting the spin structure functions of the proton and neutron[8] separately, $\int_0^1 g_1^{p(n)}(x) dx = \pm \frac{1}{12}(F + D) + \frac{5}{36}(3F - D)$ where the sign is plus for proton, minus for neutron and F and D are the hyperon decay constants. They assumed the SU(3) flavor symmetry and unpolarized sea quarks. The sum rule obviously depends on the nucleon model, so that it is thought to be less fundamental than the Bjorken sum rule. This sum rule is referred to the Ellis-Jaffe sum rule.

Even though these sum rules were established in the early 70s, we had to wait for the experimental proof until 1976 when deep inelastic scattering of polarized electrons and polarized nucleons was possible along with the development of polarized electron beam and polarized nucleon. The experiment was carried out by the SLAC-Yale collaboration [9], where a large asymmetry was observed as predicted by the quark-parton model. Their

results[10] were consistent with the Ellis-Jaffe sum rule for the spin structure function of proton within their large experimental error.

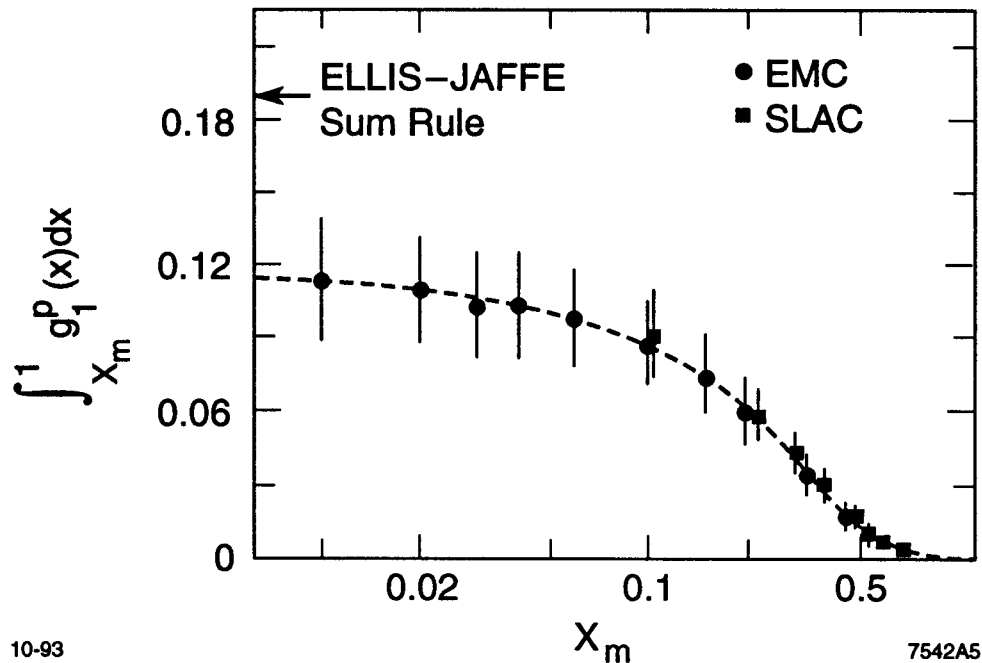


Figure 1.1: The integral of the spin-dependent structure function $g_1(x)$ for the proton with EMC and SLAC data. The horizontal axis shows Bjorken x in logarithm scale. The vertical axis is the integral of the $g_1(x)$ down to the x value. The arrow on the vertical axis shows the Ellis-Jaffe sum rule for the proton. The smooth extrapolation toward $x=0$ indicates that the extrapolated value is different from the prediction.

In 1988, EMC(European Muon Collaboration) at CERN published the results from high precision measurements of the scattering of polarized muons off polarized protons in butanol[11], indicating that the spin structure function of the proton was in disagreement with the Ellis-Jaffe sum rule as shown in Figure 1.1. They concluded that the quark carries only a small fraction of the proton spin and the strange sea quark has a significant fraction of opposite polarization with respect to the proton spin. This new and surprising results were called as 'the spin crisis' and denied the naive idea that only valence quarks carry the nucleon spin, and sea quarks and gluons are not polarized.

The E142 Collaboration at SLAC published the results from the first measurement

of the neutron spin structure function using ${}^3\text{He}$ target [12]. Their results were consistent with the Ellis-Jaffe sum rule at $Q^2 = 2.0(\text{GeV}/c)^2$ within one standard deviation ¹ and with the Bjorken sum rule obtained using the QCD correction to third order in α_s within one standard deviation. However, their measurements denoted that the quark carried only about a half of the nucleon spin.

These measurements suggested that our understanding of the nucleon spin is far from the whole picture. We need not only to do more theoretical work, but also more experiments. Where is the other part of the nucleon spin? Why do quarks carry only a small fraction of whole nucleon spin although the SU(6) model is successful for predicting the magnetic moment of baryons. We have to find answers for these questions.

This 'Spin Crisis' has led several experiments to measure the nucleon spin structure functions to find the answer, and to reach further understanding of the nucleon spin; the Spin Muon Collaboration (SMC) at CERN [15],[16], HERMES at DESY[17] and E143 at SLAC [18],[19].

The E143 is an international collaboration consisting of about 90 physicists and graduate students from 17 institutes. The purpose of E143 was to investigate the spin structure functions of both the proton and the deuteron. The experiment was implemented using the highly polarized electron beam accelerated by the Linac and the solid ammonia target located in End Station A (ESA). Figure 1.2 shows the aerial view of the SLAC. The long structure stretched from up to down is the 3 km long Linac. The building at the end of the Linac is ESA. The experiment was carried out in ESA with the high statistics. This high statistical measurement was able to test the Ellis-Jaffe and Bjorken sum rules with a higher accuracy than the EMC and E142 measurements. It gave more understanding of how the nucleon spin is carried by quarks. The variation of the beam energy also provided the information of Q^2 dependence of the spin structure functions.

This thesis describes E143 investigating the electron scattering off deuterons in ND_3

¹A reanalysis by D. M. Kawall and J. A. Dunne is giving the integral of the g_1 for neutron to be $-.036 \pm .009$ which is two standard deviations away from the prediction by Ellis-Jaffe [13] [14].

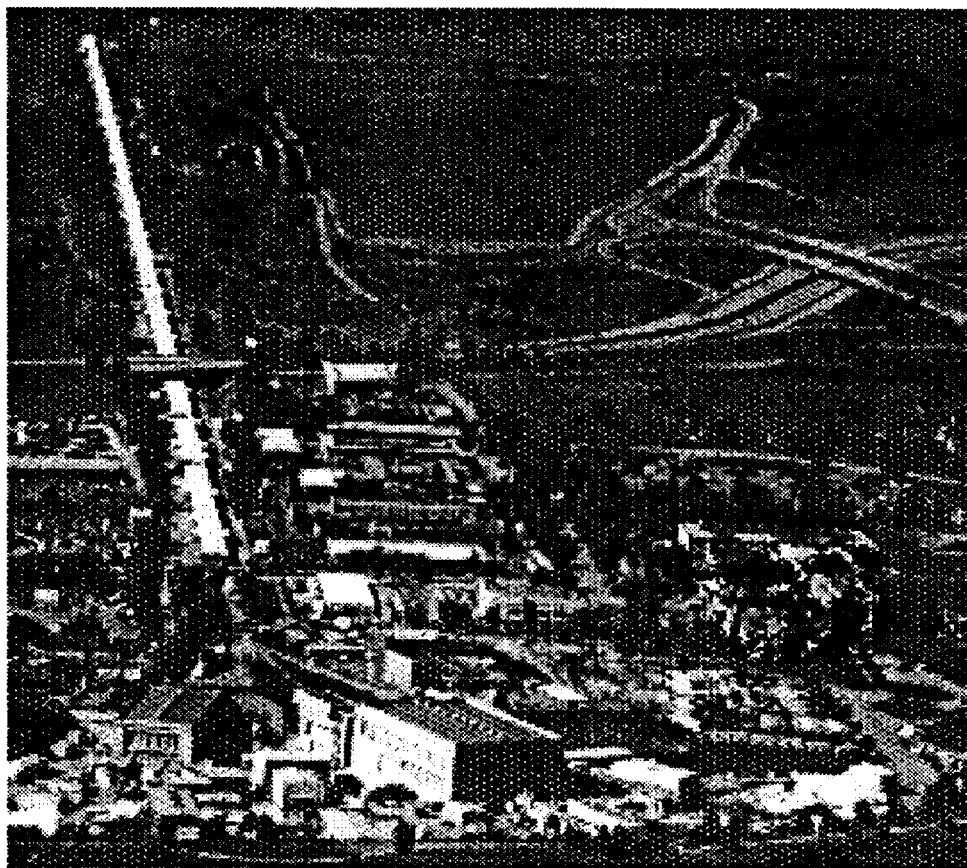


Figure 1.2: Aerial view of the Stanford Linear Acceleration Center. The long structure stretched from up to down is 3 km long Linear accelerator (Linac). The building at the end of the Linac is End Station A where the experiment was carried out.

at 29 GeV and presents the results from this experiment. This measurement determined the spin structure function g_1 of deuteron with high accuracy. The covered x range is $0.029 < x_{Bj} < 0.8$ at an average $Q^2 = 3.0(\text{GeV}/c)^2$.

In Chapter 2, the formulae of deep inelastic electron-nucleon scattering are derived. The principle of spin structure function measurement and the Ellis-Jaffe and Bjorken sum rules are explained. The experimental setup and devices are described in Chapter 3. In Chapter 4, the analysis procedures to reconstruct electron tracks and to calculate the cross section asymmetry including various corrections will be explained. In Chapter 5, the measured data and the results of the structure function and the integral are given including the estimation of systematic errors. Finally, a conclusion and a look into the future are given in Chapter 6.

Chapter 2

Theory of the deep inelastic scattering

Electron-nucleon scattering at large momentum transfer range occurs mainly through the exchange of a photon in electromagnetic interactions. Figure 2.1 shows the Feynman diagram of electron-nucleon scattering, where k and k' are the four momenta, s and s' are the polarization vectors of the electrons in the initial and final states, θ is the angle of the scattered electron with respect to the electron direction of the initial state, q is the four momentum transfer defined by $q = k - k'$, p is the four momentum of the nucleon, and λ is the polarization vector of the nucleon. The gray circle at the photon nucleon vertex involves complex interactions due to the substructure of the nucleon and hadronization process. The substructure of the nucleon is parameterized later using several assumptions. Lines from the circle indicate particles coming out from fragmentation of the initial nucleon.

The momenta of the particles involved in this process are expressed as

$$k_\mu = (E, \vec{k}), \quad (2.1)$$

$$p_\mu = (M, \vec{0}), \quad (2.2)$$

$$k'_\mu = (E', \vec{k}'), \quad (2.3)$$

where E and \vec{k} are the energy and the momentum for the electron of the initial state, E' and \vec{k}' are the energy and the momentum for the electron of the final state, and M is the nucleon mass.

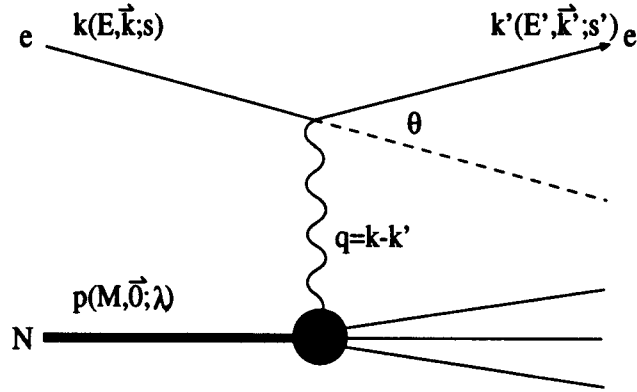


Figure 2.1: Feynman diagram of electron-nucleon deep inelastic scattering

We also define several kinematical variables for our convenience neglecting electron mass,

$$\begin{aligned}
 Q^2 = -q^2 &= 2(k \cdot k') = 2EE'(1 - \cos \theta) \\
 &= 4EE' \sin^2(\theta/2) \\
 &= 2MxyE,
 \end{aligned} \tag{2.4}$$

$$\nu = E - E', \tag{2.5}$$

$$x = \frac{Q^2}{2p \cdot q} = \frac{Q^2}{2M\nu}, \tag{2.6}$$

$$y = \frac{\nu}{E} = \frac{p \cdot q}{p \cdot k}. \tag{2.7}$$

The variable x is called 'Bjorken x ' and sometimes denoted as x_B .

In the following sections, the cross sections for the unpolarized and polarized processes, ie. the spin-averaged and spin-dependent cross sections for the deep-inelastic e-N scattering will be described. The spin structure function, g_1 is expressed using the spin-averaged and spin-dependent cross sections. After that, the sum rules giving predictions for the integrated value of g_1 will be explained.

2.1 Spin-averaged cross section

The spin-averaged cross section is that of electron scattering off nucleons averaged over the electron and nucleon spin of the initial and final states. Using the assumptions as discussed in Appendix B.2, the differential cross section in laboratory system is expressed as given in Equation (B.23) by

$$\frac{d^2\sigma}{dE'd\Omega} = \frac{e^4}{16\pi^2 Q^2 \tan^2(\theta/2)} \frac{E}{E'} \left[W_2(\nu, Q^2) + 2 \tan^2(\theta/2) W_1(\nu, Q^2) \right], \quad (2.8)$$

where $W_1(\nu, Q^2)$ and $W_2(\nu, Q^2)$ are the nucleon structure functions of two independent kinematical variables, ν and Q^2 . If we impose the Bjorken scaling of the structure functions in the limit of $(\nu, Q^2 \rightarrow \infty)$, the structure functions can be written as a function of a single variable, x , by

$$F_1(x) = \lim_{\nu, Q^2 \rightarrow \infty} M W_1(\nu, Q^2) \quad (2.9)$$

$$F_2(x) = \lim_{\nu, Q^2 \rightarrow \infty} \nu W_2(\nu, Q^2) \quad (2.10)$$

The scaling means that the structure function depends only x which is proportional to the ratio of the Q^2 to the ν , and is independent of Q^2 or ν as demonstrated by many experiments. This scaling denotes that the deep inelastic scattering of electron and nucleon is interpreted as the incoherent sum of the elastic scattering of electrons and charged partons (quark) in nucleons and x is interpreted as the momentum fraction which the scattered quark has in the nucleon. This experimental fact is an evidence that the quarks compose the nucleon. Scaling is now explained by the asymptotic freedom in QCD: the strong coupling constant depends on the momentum transfer Q^2 and it decreases with increasing momentum transfer. The quark acts like a free particle in the large Q^2 region due to the small strong coupling constant.

As mentioned in Chapter 1, a nucleon is composed of three valence quarks, sea quarks, and gluons in the Parton Model picture. Because the gluon does not contribute to the electromagnetic interaction, the structure functions, $F_1(x)$ and $F_2(x)$ are expressed as the incoherent sum of the quark distribution functions, $q_i(\uparrow(\downarrow), x)$ and $\bar{q}_i(\uparrow(\downarrow), x)$ for

the quarks and anti-quarks by

$$F_1(x) = \frac{1}{2} \sum_i e_i^2 [q_i(\uparrow, x) + \bar{q}_i(\uparrow, x) + q_i(\downarrow, x) + \bar{q}_i(\downarrow, x)] \quad (2.11)$$

$$F_2(x) = \frac{1}{2} \sum_i x e_i^2 [q_i(\uparrow, x) + \bar{q}_i(\uparrow, x) + q_i(\downarrow, x) + \bar{q}_i(\downarrow, x)], \quad (2.12)$$

where the sum is taken over all quark flavors and the arrow denotes the quark helicity with respect to the nucleon spin. The largest contribution to these functions comes from the light three quarks and those from the heavy flavors, c, b, and t are suppressed due to the heavy masses of c, b, and t quarks.

The spin-averaged cross section is rewritten using these new functions by

$$\frac{d^2\sigma}{dE'd\Omega} = \frac{e^4}{16\pi^2 Q^2 \tan^2(\theta/2)} \frac{E}{E'} \left[\frac{1}{\nu} F_2(x) + \frac{2}{M} \tan^2(\theta/2) F_1(x) \right]. \quad (2.13)$$

The spin-averaged cross section can be expressed using the $F_1(x)$ and $R(x)$ which is the cross section ratio for the longitudinally and transversely polarized virtual photons. Using the $R(x)$ defined by Equation (2.47), the relation between $F_1(x)$ and $F_2(x)$ is given by

$$F_2 = F_1 \frac{2x(1+R)}{1+\gamma^2}, \quad (2.14)$$

where γ is

$$\gamma^2 = \frac{4M^2 x^2}{Q^2} = \frac{Q^2}{\nu^2}. \quad (2.15)$$

Substituting the Equation (2.14) into the Equation (2.13), the unpolarized cross section is expressed using the F_1 and R as,

$$\frac{d^2\sigma}{dE'd\Omega} = \frac{e^4}{16\pi^2 Q^2} \frac{E}{E'} \frac{4(E+E')}{\nu M} \frac{F_1(x)}{D'}, \quad (2.16)$$

where D' is given by

$$D' = \frac{(1-\epsilon)(2-y)}{y(1+\epsilon R)}, \quad (2.17)$$

with

$$\epsilon = \frac{1}{1 + 2(1 + \frac{\nu^2}{Q^2}) \tan^2(\theta/2)}. \quad (2.18)$$

2.2 Spin-dependent cross section

In the polarized electrons scattering off polarized nucleons, the cross section depends on the helicities of both particles of the initial state. We define the four cross sections of the polarized process for the different directions of the electrons and nucleons in the initial state as shown in Figure 2.2. The nucleon is polarized longitudinally or transversely to the electron beam axis. The electron is polarized along the beam axis, parallel or anti-parallel. The combinations of these two electron and nucleon spin states compose the four cross sections. The two cross sections for the longitudinally polarized nucleon are called as the parallel configurations and those for the transversely polarized nucleon are called as the perpendicular configurations.

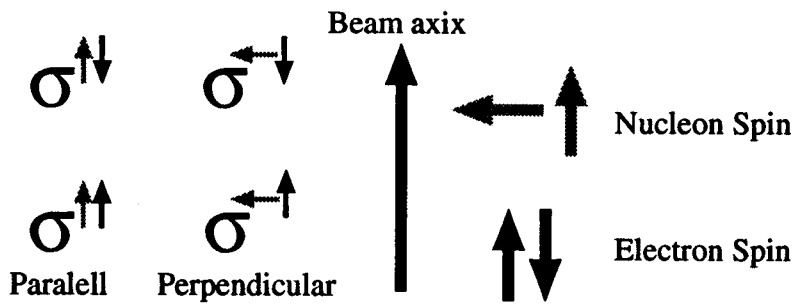


Figure 2.2: Definitions of the cross sections for the four combinations of the electron and nucleon spin. The gray and black arrows indicate the direction of the spin for nucleons and electrons respectively, where the electron beam direction is from bottom to top. The nucleon is polarized longitudinally or transversely with respect to the beam axis. The electron is polarized parallel or anti-parallel to the beam axis. We call these cross sections as the longitudinal or transverse configurations according to the direction of the nucleon spin. The cross sections are indicated by σ with two arrows for superscripts. The two arrows show the spin direction of nucleons and electrons respectively.

To extract the spin dependent part of the cross sections for the parallel and perpendicular configuration, we give the following cross section differences of the two different

orientations of the electron spin as derived in Equations (B.24) and (B.26),

$$\frac{d^2(\sigma^{\uparrow\downarrow} - \sigma^{\uparrow\uparrow})}{dE'd\Omega} = \frac{e^4}{16\pi^2 Q^2} \frac{E'}{E} 4 \left[MG_1(\nu, Q^2)(E + E' \cos \theta) - Q^2 G_2(\nu, Q^2) \right], \quad (2.19)$$

$$\frac{d^2(\sigma^{\leftarrow\downarrow} - \sigma^{\leftarrow\uparrow})}{dE'd\Omega} = \frac{e^4}{16\pi^2 Q^2} \frac{E'}{E} 4E'H \sin \theta \left[MG_1(\nu, Q^2) + 2EG_2(\nu, Q^2) \right], \quad (2.20)$$

where $G_1(\nu, Q^2)$ and $G_2(\nu, Q^2)$ are the spin structure functions and H is the sign of the inner product of the nucleon spin vector and the momentum of the scattered electron in the perpendicular configuration.

While $W_1(\nu, Q^2)$ and $W_2(\nu, Q^2)$ represent the spin-averaged structures of nucleons, $G_1(\nu, Q^2)$ and $G_2(\nu, Q^2)$ are the spin-dependent structure functions of the nucleon. We expect to see a scaling of the spin structure functions in analogy to the spin-averaged structure functions:

$$g_1(x) = \lim_{\nu, Q^2 \rightarrow \infty} M^2 \nu G_1(\nu, Q^2), \quad (2.21)$$

$$g_2(x) = \lim_{\nu, Q^2 \rightarrow \infty} M \nu^2 G_2(\nu, Q^2), \quad (2.22)$$

where $g_1(x)$ and $g_2(x)$ are the spin structure functions in the scaling limit. The cross section differences are expressed in terms of the scaled spin structure functions, $g_1(x)$ and $g_2(x)$ by,

$$\frac{d^2(\sigma^{\uparrow\downarrow} - \sigma^{\uparrow\uparrow})}{dE'd\Omega} = \frac{e^4}{16\pi^2 Q^2} \frac{E'}{E} 4 \left[\frac{g_1(x)}{M\nu} (E + E' \cos \theta) - \frac{Q^2}{M\nu^2} g_2(x) \right], \quad (2.23)$$

$$\frac{d^2(\sigma^{\leftarrow\downarrow} - \sigma^{\leftarrow\uparrow})}{dE'd\Omega} = \frac{e^4}{16\pi^2 Q^2} \frac{E'}{E} 4E'H \sin \theta \left[\frac{g_1(x)}{M\nu} + \frac{2E}{M\nu^2} g_2(x) \right], \quad (2.24)$$

Similar to $F_1(x)$ or $F_2(x)$, the spin structure function g_1 is expressed by the quark distributions as,

$$\begin{aligned} g_1(x) &= \frac{1}{2} \sum_i e_i^2 [q_i(\uparrow, x) + \bar{q}_i(\uparrow, x) - q_i(\downarrow, x) - \bar{q}_i(\downarrow, x)] \\ &= \frac{1}{2} \sum_i e_i^2 \Delta q_i(x), \end{aligned} \quad (2.25)$$

where i is the quark flavor and Δq_i is defined to be the helicity distribution of a quark flavor labeled i , $\Delta q_i(x) = [q_i(\uparrow, x) + \bar{q}_i(\uparrow, x)] - [q_i(\downarrow, x) + \bar{q}_i(\downarrow, x)]$.

On the other hand, the spin structure function g_2 has no explicit interpretation in the parton model. It relates the quark momentum transverse to the nucleon momentum. g_2 is expected to be small in contrast to the g_1 and sensitive to the higher twist effect in QCD[20].

2.3 Cross section asymmetry

In order to investigate the spin structure of nucleons, we measure the asymmetries of the cross sections for the different spin orientation of electrons instead of the cross section difference. Two cross section asymmetries for two different nucleon spin direction, parallel and perpendicular to the electron beam are defined by

$$A_{\parallel} = \frac{\sigma^{\uparrow\downarrow} - \sigma^{\uparrow\uparrow}}{\sigma^{\uparrow\downarrow} + \sigma^{\uparrow\uparrow}}, \quad (2.26)$$

$$A_{\perp} = \frac{\sigma^{\leftarrow\downarrow} - \sigma^{\leftarrow\uparrow}}{\sigma^{\leftarrow\downarrow} + \sigma^{\leftarrow\uparrow}}, \quad (2.27)$$

where the notation of the cross sections are the same as given in Figure 2.2. An advantage of using the cross section asymmetry over the cross section difference is that the target density, the spectrometer acceptance and, the detection efficiency are canceled in the asymmetry which reduces the systematic errors due to these factors.

Substituting Equations (2.16), (2.23) and, (2.24) into Equations (2.26) and (2.27), the cross section asymmetries are expressed in terms of the structure functions to be,

$$A_{\parallel} = \frac{1}{(E + E')} \frac{D'}{F_1(x)} \left[(E + E' \cos \theta) g_1(x) - \frac{Q^2}{\nu} g_2(x) \right], \quad (2.28)$$

$$A_{\perp} = \frac{E' H \sin \theta}{(E + E')} \frac{D'}{F_1(x)} \left[g_1(x) + \frac{2E}{\nu} g_2(x) \right]. \quad (2.29)$$

The spin structure functions $g_1(x)$ and $g_2(x)$ can be expressed in terms of the cross section asymmetries by

$$g_1(x) = \frac{F_1(x)}{D'} \left[A_{\parallel} + \tan \frac{\theta}{2} A_{\perp} \right], \quad (2.30)$$

$$g_2(x) = \frac{y F_1(x)}{2 \sin \theta D'} \left[\frac{E' \cos \theta + E}{E'} A_{\perp} - H \sin \theta A_{\parallel} \right]. \quad (2.31)$$

These formulae show that the spin structure functions for nucleons, $g_1(x)$ and $g_2(x)$ are derived from the measurements of the cross section asymmetry.

2.4 Virtual photon cross section

For studying the nucleon structure, the virtual photon-nucleon interaction provides more direct information for the spin dependent scattering than the electron-nucleon scattering process.

For the photon-nucleon scattering, only four cross sections are independent under the assumptions of angular momentum conservation, parity and time reversal invariances. These four cross sections are given with the following helicity configurations by,

$$\begin{aligned}\sigma_{\frac{3}{2}}^T &: (1, \frac{1}{2}; 1, \frac{1}{2}) \\ \sigma_{\frac{1}{2}}^T &: (1, -\frac{1}{2}; 1, -\frac{1}{2}) \\ \sigma^L &: (0, \frac{1}{2}; 0, \frac{1}{2}) \\ \sigma^{TL} &: (1, -\frac{1}{2}; 0, \frac{1}{2})\end{aligned}$$

where the first two numbers in the parenthesis denote the the helicities for the initial photon and nucleon, and the second two numbers for the final photon and nucleon respectively. These cross sections are expressed in terms of the nucleon structure functions by [21]

$$\sigma_{\frac{3}{2}}^T = \frac{4\pi^2\alpha}{MK} \left[F_1 + g_1 - \frac{2Mx}{\nu} g_2 \right], \quad (2.32)$$

$$\sigma_{\frac{1}{2}}^T = \frac{4\pi^2\alpha}{MK} \left[F_1 - g_1 + \frac{2Mx}{\nu} g_2 \right], \quad (2.33)$$

$$\sigma^L = \frac{4\pi^2\alpha}{K} \left[\frac{1}{\nu} \left(1 + \frac{\nu^2}{Q^2} \right) F_2 - \frac{1}{M} F_1 \right], \quad (2.34)$$

$$\sigma^{TL} = \frac{4\pi^2\alpha}{K} \frac{\sqrt{Q^2}}{M\nu} [g_1 + g_2], \quad (2.35)$$

where K is the flux of the virtual photons defined by $K = \nu - \frac{Q^2}{2M}$ [5].

Using these cross sections, we introduce the new asymmetries A_1 and A_2 for the virtual photon-nucleon scattering as follows,

$$A_1 = \frac{\sigma_{\frac{3}{2}}^T - \sigma_{\frac{1}{2}}^T}{\sigma_{\frac{3}{2}}^T + \sigma_{\frac{1}{2}}^T}, \quad (2.36)$$

$$A_2 = \frac{\sigma_{\frac{1}{2}}^{TL}}{\sigma_{\frac{3}{2}}^T + \sigma_{\frac{1}{2}}^T}. \quad (2.37)$$

This A_1 is similar to the A_{\parallel} in Equation (2.26), but polarized electrons are replaced by the polarized virtual photon. Using Equations (2.32), (2.33), and (2.35), A_1 and A_2 can be expressed in terms of the spin structure functions by

$$A_1(x) = \frac{1}{F_1}(g_1(x) - \gamma^2 g_2(x)), \quad (2.38)$$

$$A_2(x) = \frac{\gamma}{F_1}(g_1(x) + g_2(x)). \quad (2.39)$$

We notice that the factor γ^2 is very small (typically, less than 0.05) in our kinematical region. Therefore, $g_1(x)$ dominates the virtual photon asymmetry A_1 . If the term of the $\gamma^2 g_2(x)$ is neglected in Equation (2.38), $A_1(x)$ can be expressed in terms of the quark distributions by

$$A_1(x) = \frac{g_1(x)}{F_1(x)} = \frac{\sum_i e_i^2 [q_i(\uparrow, x) + \bar{q}_i(\uparrow, x) - q_i(\downarrow, x) - \bar{q}_i(\downarrow, x)]}{\sum_i e_i^2 [q_i(\uparrow, x) + \bar{q}_i(\uparrow, x) + q_i(\downarrow, x) + \bar{q}_i(\downarrow, x)]}, \quad (2.40)$$

where q_i is defined in Equation (2.12). In the naive SU(6) model, the $A_1(x)$ is given to be 5/9 for the proton and 0 for the neutron.

Via the virtual-photon cross section asymmetry $A_1(x)$, the cross section asymmetry A_{\parallel} can be expressed in terms of the parton distribution. From Equations (2.30), (2.31), (2.38) and (2.39), the cross section asymmetries A_{\parallel} and A_{\perp} are expressed in terms of the virtual photon cross section asymmetries, A_1 and A_2 by

$$A_{\parallel}(x) = D(A_1(x) + \eta A_2(x)) \quad (2.41)$$

$$A_{\perp}(x) = d(A_2(x) - \zeta A_1(x)) \quad (2.42)$$

where D , d , η , and ζ are the kinematical quantities defined by[22]

$$D = \frac{1 - \frac{E'\epsilon}{E}}{1 + \epsilon R}, \quad (2.43)$$

$$\eta = \frac{\epsilon\sqrt{Q^2}}{E - E'\epsilon}, \quad (2.44)$$

$$d = \epsilon\sqrt{\frac{2\epsilon}{1 + \epsilon}}, \quad (2.45)$$

$$\zeta = \frac{\eta(1 + \epsilon)}{2\epsilon}, \quad (2.46)$$

with ϵ defined in Equation (2.18) and $R(x)$ is the cross section ratio for longitudinal to transverse virtual photon defined by,

$$R = \frac{2\sigma^L}{\sigma_{\frac{3}{2}}^T + \sigma_{\frac{1}{2}}^T}. \quad (2.47)$$

Substituting Equations (2.32), (2.33), and (2.34) into Equation (2.47), the R is expressed in terms of the $F_1(x)$ and $F_2(x)$ by

$$R = \left(1 + \frac{\nu^2}{Q^2}\right) \frac{MF_2}{\nu F_1} - 1. \quad (2.48)$$

In Equation (2.41), the contribution from the second term in the right-hand side is small due to the small factor, η (typically 0.1) and the small quantity, $A_2(x)$ in contrast to $A_1(x)$. Therefore A_{\parallel} is nearly proportional to A_1 which is expressed in terms of the parton distributions. The D in Equation (2.41) is the proportional coefficient between $A_1(x)$ and $A_{\parallel}(x)$ and is called as the depolarization factor. It is a pure QED factor indicating the depolarization effect of the process of the emitting the virtual photon. Using the depolarization factor, the $A_{\parallel}(x)$ is expressed in terms of the parton distributions by

$$A_{\parallel}(x) \simeq D \frac{\sum_i e_i^2 [q_i(\uparrow, x) + \bar{q}_i(\uparrow, x) - q_i(\downarrow, x) - \bar{q}_i(\downarrow, x)]}{\sum_i e_i^2 [q_i(\uparrow, x) + \bar{q}_i(\uparrow, x) + q_i(\downarrow, x) + \bar{q}_i(\downarrow, x)]}, \quad (2.49)$$

where the depolarization factor decreases with the increasing x as $D \sim 0.78$ at $x = 0.03$ and $D \sim 0.23$ at $x = 0.8$. Therefore, the investigation for the A_{\parallel} is equivalent that for the helicity distribution of the quarks in the nucleon with an analyzing power of the factor D .

2.5 g_1 of deuteron

The deuteron is a system consisting of a proton and a neutron. The spin structure function for deuteron, then, can be expressed in terms of those functions for proton and neutron.

The deuteron is a spin 1 and parity even particle composed of two spin 1/2 nucleons. Thus, the deuteron is a mixture of S ($L=0$) and D ($L=2$) states. These S and D states are expressed using the Clebsh-Gordon coefficients by

$$|J = 1, J_z = 1 \rangle_S = |L = 0, L_z = 0 \rangle |S = 1, S_z = 1 \rangle \quad (2.50)$$

$$\begin{aligned} |J = 1, J_z = 1 \rangle_D &= \sqrt{\frac{3}{5}} |L = 2, L_z = 2 \rangle |S = 1, S_z = -1 \rangle \\ &\quad - \sqrt{\frac{3}{10}} |L = 2, L_z = 1 \rangle |S = 1, S_z = 0 \rangle \\ &\quad + \sqrt{\frac{1}{10}} |L = 2, L_z = 0 \rangle |S = 1, S_z = 1 \rangle, \end{aligned} \quad (2.51)$$

where J and J_z are the magnitude and the Z-component of the total angular momentum, $L(S)$, $L_z(S_z)$ are the magnitude and the Z-component of the orbital angular momentum (spin).

A probability that a nucleon spin is anti-parallel to the deuteron spin in the D-state is calculated to be

$$\frac{3}{5} + \frac{3}{10} \cdot 0.5 = \frac{3}{4}, \quad (2.52)$$

where 0.5 comes from that one of two nucleons has a spin anti-parallel to the deuteron spin in the $S_z = 0$ state. If the polarized deuterons contain the D-state with a fraction w_D , the deuteron cross section, $\sigma_d^{\uparrow\uparrow}$, is expressed in terms of nucleon cross sections, $\sigma_N^{\uparrow\uparrow}$ and $\sigma_N^{\downarrow\uparrow}$ by

$$\sigma_d^{\uparrow\uparrow} = \left(1 - \frac{3}{4}w_D\right) \sigma_N^{\uparrow\uparrow} + \frac{3}{4}w_D \sigma_N^{\downarrow\uparrow}, \quad (2.53)$$

where the first arrow is the nucleon spin and the second arrow is the helicity of electron. The nucleon cross section is the sum of those for the proton and neutron, $\sigma_N = \sigma_p + \sigma_n$.

Similarly, $\sigma_d^{\uparrow\downarrow}$ can be written by,

$$\sigma_d^{\uparrow\downarrow} = \left(1 - \frac{3}{4}w_D\right) \sigma_N^{\uparrow\downarrow} + \frac{3}{4}w_D\sigma_N^{\downarrow\downarrow}, \quad (2.54)$$

Taking into account the D-state probability, the cross section asymmetry of the deuteron is described as follows

$$A_{\parallel}^d = \frac{\sigma_d^{\uparrow\downarrow} - \sigma_d^{\uparrow\uparrow}}{\sigma_d^{\uparrow\downarrow} + \sigma_d^{\uparrow\uparrow}} = \left(1 - \frac{3}{2}w_D\right) \frac{\sigma_N^{\uparrow\downarrow} - \sigma_N^{\uparrow\uparrow}}{\sigma_N^{\uparrow\downarrow} + \sigma_N^{\uparrow\uparrow}}, \quad (2.55)$$

where we assume the parity invariance on the cross sections, ie. $\sigma_N^{\uparrow\uparrow} = \sigma_N^{\downarrow\downarrow}$, $\sigma_N^{\downarrow\uparrow} = \sigma_N^{\uparrow\downarrow}$, and $\sigma_N^{\uparrow\downarrow} = \sigma_N^{\downarrow\uparrow}$.

Equation (2.55) shows that the asymmetry of the deuteron is smaller than the spin-aligned proton and neutron system by a factor of $(1 - \frac{3}{2}w_D)$. The A_{\parallel}^d for deuteron is expressed in terms of the $A_{\parallel}^{p,n}$ for proton and neutron with conventions of $\sigma_d = 2F_1^d$, $\sigma_p = F_1^p$, $\sigma_n = F_1^{n1}$ by

$$A_{\parallel}^d = \left(1 - \frac{3}{2}w_D\right) \left(A_{\parallel}^p \frac{F_1^p}{2F_1^d} + A_{\parallel}^n \frac{F_1^n}{2F_1^d} \right), \quad (2.56)$$

Similarly, the transverse asymmetry, A_{\perp} , is expressed by

$$A_{\perp}^d = \left(1 - \frac{3}{2}w_D\right) \left(A_{\perp}^p \frac{F_1^p}{2F_1^d} + A_{\perp}^n \frac{F_1^n}{2F_1^d} \right), \quad (2.57)$$

Using these equations, the spin structure function g_1^d for deuteron is expressed in terms of those for proton and neutron, g_1^p and g_1^n by

$$2g_1^d = \left(1 - \frac{3}{2}w_D\right) (g_1^p + g_1^n). \quad (2.58)$$

Under the assumption that the D-state probability w_D is independent of x , we can integrate Equation (2.58) and obtain the relation between the integrals of deuteron, proton, and neutron,

$$2\Gamma_1^d = \left(1 - \frac{3}{2}w_D\right) (\Gamma_1^p + \Gamma_1^n), \quad (2.59)$$

where Γ_1^i is given by

$$\Gamma_1^i = \int_0^1 dx g_1^i(x), \quad (2.60)$$

where i stands for deuteron, proton, and neutron denoted by d, p, and n.

¹The factor for the F_1^N giving the cross section is identical for proton, neutron, and deuteron. Then, the factor is canceled in the formula of the asymmetry.

2.6 Sum rules

The Bjorken and Ellis-Jaffe sum rules will be explained in this section. These sum rules give predictions on integrals of the spin structure function $g_1(x)$ over x range from 0 to 1. The confirmation of these sum rules is the most important purpose in this experiment because we can examine the spin structure of the nucleon and the dynamics of the quarks with these sum rules.

2.6.1 Bjorken sum rule

The Bjorken sum rule is originally derived by Bjorken base on current algebra assuming Iso spin symmetry on proton and neutron quark distribution function[6], giving that the integral of the difference of spin structure functions g_1 of proton and neutron is equal to one sixth of the neutron beta decay axial coupling. Now, this sum rule is derived by QCD calculation [23] and is also called as the QCD sum rule.

The original derivation of the sum rule is based on current algebra stated from the ratio of the axial vector coupling constant to the vector coupling constant of neutron beta decay which is expressed in terms of the quark distributions by [24]

$$\begin{aligned} \left(\frac{g_A}{g_V}\right)_n &= \frac{1}{2} [u^p(\uparrow) - u^p(\downarrow)] - \frac{1}{2} [d^p(\uparrow) - d^p(\downarrow)] \\ &\quad - \left\{ \frac{1}{2} [u^n(\uparrow) - u^n(\downarrow)] - \frac{1}{2} [d^n(\uparrow) - d^n(\downarrow)] \right\}, \end{aligned} \quad (2.61)$$

where the $u^{p(n)}$ and $d^{p(n)}$ are the distribution functions of u and d quark including both of quark and anti-quark of proton (neutron) with the Z-component of the spin to the nucleon spin indicated by the arrows. Under the iso-spin symmetry, $u^p \equiv d^n$ and $d^p \equiv u^n$, and the ratio is given by

$$\begin{aligned} \left(\frac{g_A}{g_V}\right)_n &= [u^p(\uparrow) - u^p(\downarrow)] - [d^p(\uparrow) - d^p(\downarrow)] \\ &= \Delta u - \Delta d, \end{aligned} \quad (2.62)$$

where Δq_i is defined to be $q_i^p(\uparrow) - q_i^p(\downarrow)$ which is explained to the expectation value of the helicity of the quark flavor i in the proton.

Assuming that u, d, and s quark exist in the nucleon, $g_1(x)$ in (2.25) derived from Parton model can be written by

$$\begin{aligned} 2g_1(x) &= \sum_i e_i^2 [q_i(\uparrow) - q_i(\downarrow)] \\ &= \frac{4}{9}\Delta u(x) + \frac{1}{9}\Delta d(x) + \frac{1}{9}\Delta s(x), \end{aligned} \quad (2.63)$$

where e_i is the charge of the quark i in the unit of electron charge. $g_1^p(x)$ and $g_1^n(x)$ are expressed with the iso-spin symmetry by,

$$2g_1^p(x) = \frac{4}{9}\Delta u^p(x) + \frac{1}{9}\Delta d^p(x) + \frac{1}{9}\Delta s^p(x), \quad (2.64)$$

$$2g_1^n(x) = \frac{1}{9}\Delta u^p(x) + \frac{4}{9}\Delta d^p(x) + \frac{1}{9}\Delta s^p(x), \quad (2.65)$$

where the quark distribution functions correspond to that in proton. If we subtract g_1^n from g_1^p , we can obtain the difference without the strange quark:

$$g_1^p(x) - g_1^n(x) = \frac{1}{6} [\Delta u(x) - \Delta d(x)]. \quad (2.66)$$

These $\Delta u(x)$ and $\Delta d(x)$ are the helicity distribution of the u and d quarks with the momentum fraction x . The integral of these helicity distribution over x gives the expectation value of the helicity in the proton to be,

$$\frac{\int_0^1 \Delta q(x) dx}{\int_0^1 dx} = \Delta q \quad (q = u, d). \quad (2.67)$$

Therefore, the integral of the Equation (2.66) over x is given to be

$$\Gamma_1^p - \Gamma_1^n = \frac{1}{6} [\Delta u - \Delta d]. \quad (2.68)$$

Inserting Equation (2.62) into Equation (2.68), we obtain the Bjorken sum rule;

$$\Gamma_1^p - \Gamma_1^n = \frac{1}{6} \frac{g_A}{g_V}. \quad (2.69)$$

The only assumption used to derive the Bjorken sum rule is iso-spin symmetry which is a fundamental principle in particle physics. Therefore, this sum rule was thought to be fundamental. However, we can not compare this prediction with the measured results

directly because this sum rule is valid only in the scaling limit, ie. $Q^2 = \infty$. Although the scaling of the structure function is a good approximation, the structure function has Q^2 dependence as observed as the scaling violation due to the QCD effect. To make precise comparison of measurements with the Bjorken sum rule, the prediction of the Bjorken sum rule has to be corrected to the value at an actual kinematical region of the measurements.

The QCD correction is calculated to third order of the strong coupling constant α_s [25] to be

$$\int_0^1 dx [g_1^p(x) - g_1^n(x)] \equiv \Gamma^p - \Gamma^n = \frac{1}{6} \frac{g_A}{g_V} \left[1 - \frac{\alpha_s}{\pi} - 3.58 \left(\frac{\alpha_s}{\pi} \right)^2 - 20.22 \left(\frac{\alpha_s}{\pi} \right)^3 \right]. \quad (2.70)$$

The predicted value at $Q^2 = 3.0(\text{GeV}/c)^2$ with $\alpha_s = 0.360 \pm .050$ [26]² and $g_A/g_V = 1.2573 \pm 0.0028$ [26] is,

$$\Gamma^p - \Gamma^n = 0.169 \pm .008, \quad (2.71)$$

where the error was estimated from the ambiguities of the strong coupling constant and the neutron axial vector coupling.

From Equation (2.70), the ratio of the $\Gamma^p - \Gamma^n$ obtained from experiments to the prediction from the Bjorken sum rule in the scaling limit is expressed in terms of the strong coupling constant,

$$\frac{\Gamma^p - \Gamma^n}{\frac{1}{6} \frac{g_A}{g_V}} = 1 - \frac{\alpha_s}{\pi} - 3.58 \left(\frac{\alpha_s}{\pi} \right)^2 - 20.22 \left(\frac{\alpha_s}{\pi} \right)^3. \quad (2.72)$$

The measurement for the $\Gamma^p - \Gamma^n$, then, determines the strong coupling constant at the measured Q^2 .

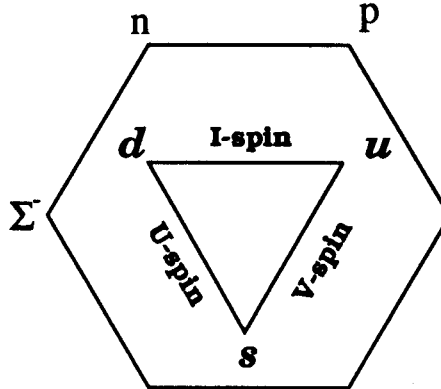


Figure 2.3: SU(3) baryon octet: proton, neutron and Σ^- are involved by an octet of spin 1/2 baryons as shown in the figure. The each particle is plotted by the iso-spin and the hyper charge, $B + S$. The baryons in the octet are assumed to be symmetry under transformations exchanging doublets of iso-spin, V-spin, and U-spin. This symmetry suggest that the baryons are composed by three kinds of the quarks, u, d, and s which are symmetry under the exchange of each two flavor of the three quarks.

2.6.2 Ellis-Jaffe sum rule

The Ellis-Jaffe sum rule give a prediction for the spin structure function for each nucleon separately, while the Bjorken sum rule predicts the difference of proton and neutron. The assumptions of SU(3) flavor symmetry and the unpolarized strange quark in the nucleon are used to extract the Ellis-Jaffe sum rule and depend on the nucleon model. Therefore, this sum rule is thought as a less fundamental sum rule than the Bjorken sum rule.

Similar to the case for the Bjorken sum rule, we need two axial vector couplings of β decay which are involved in the spin 1/2 baryon octet as shown in Figure 2.3. The ratio of the axial vector coupling constant to the vector coupling constant of Σ^- beta decay is expressed in terms of the quark distributions in neutron under the V-spin symmetry by

²We used the strong coupling constant at τ mass for the running coupling constant, because the $m_\tau^2 = 3.16(\text{GeV}/c)^2$ is very close to $3.0(\text{GeV}/c)^2$. Although the combined result of the strong coupling constants from the τ decay rates was calculated to be $\alpha_s(m_\tau^2) = 0.360 \pm 0.041$ by the Particle Data Group (PDG), the theoretical uncertainty may be underestimated. Therefore, I assigned the uncertainty of the strong coupling constant to be 0.05 which was larger than the calculated value.

[24]

$$\begin{aligned} \left(\frac{g_A}{g_V}\right)_{\Sigma^-} &= -[u^n(\uparrow) - u^n(\downarrow)] + [s^n(\uparrow) - s^n(\downarrow)] \\ &= -\Delta u^n + \Delta s^n \end{aligned} \quad (2.73)$$

Using iso-spin symmetry, $\Delta u^n = \Delta d^p$ and $\Delta s^n = \Delta s^p$, the axial vector coupling of the Σ^- beta decay is, then, written in terms of quark distributions in proton by,

$$\left(\frac{g_A}{g_V}\right)_{\Sigma^-} = \Delta d - \Delta s. \quad (2.74)$$

This equation gives a formula on quark helicity distributions in proton other than Equation(2.62).

Using g_1^p and g_1^n given in Equations (2.64) and (2.65) together with Equation(2.62) and (2.74), the integrals of g_1 are given by

$$\Gamma_1^{p(n)} = \pm \frac{1}{12} \left(\frac{g_A}{g_V}\right)_n + \frac{5}{36} \left[\left(\frac{g_A}{g_V}\right)_n + 2 \left(\frac{g_A}{g_V}\right)_{\Sigma^-} \right] + \frac{1}{3} \Delta s, \quad (2.75)$$

where + for proton and - for neutron. If we assume the contribution from the strange quark is zero, i.e. strange quark is not polarized in nucleon, the g_1 integrals are expressed by these well measured axial vector couplings. These relations are known as Ellis-Jaffe sum rule.

As mentioned in the previous section, the QCD correction is very important to compare the predictions with a measurement. The QCD correction for the Ellis-Jaffe sum rule up to third order of α_s [27] is calculated to be

$$\begin{aligned} \Gamma_1^{p(n)}(Q^2) &= \left[1 - \frac{\alpha_s}{\pi} - 3.5833 \left(\frac{\alpha_s}{\pi}\right)^2 - 20.2153 \left(\frac{\alpha_s}{\pi}\right)^3 \right] \left(\pm \frac{1}{12} a_3 + \frac{1}{36} a_8 \right) \\ &+ \left[1 - 0.333 \frac{\alpha_s}{\pi} - 0.5495 \left(\frac{\alpha_s}{\pi}\right)^2 - O(\alpha_s)^3 \right] \frac{1}{9} a_0, \end{aligned} \quad (2.76)$$

with conventions of $a_3 = \Delta u - \Delta d$, $a_8 = \Delta u + \Delta d - 2\Delta s$, and $a_0 = \Delta u + \Delta d + \Delta s$.

Under the assumption of SU(3) flavor symmetry, any axial vector couplings between the spin 1/2 baryons are expressed by two constants F and D. Neutron beta decay is equal to $F + D$ and Σ^- beta decay is $F - D$. These constants were determined to be

$F + D = 1.2573 \pm 0.0028$ and $F/D = 0.58 \pm 0.02$ [26]. The a_3 and a_8 are expressed using F and D to be

$$a_3 = F + D \quad (2.77)$$

$$a_8 = 3F - D. \quad (2.78)$$

Note that a_0 is equal to a_8 providing the strange quark is not polarized. Then, the $\Gamma_1^{p(n)}$ is given in terms of the F and D by,

$$\begin{aligned} \int_0^1 dx g_1^{p(n)}(x, Q^2) = & \left[1 - \frac{\alpha_s}{\pi} - 3.5833 \left(\frac{\alpha_s}{\pi} \right)^2 - 20.2153 \left(\frac{\alpha_s}{\pi} \right)^3 \right] \left(\pm \frac{1}{12}(F + D) + \frac{1}{36}(3F - D) \right) \\ & + \left[1 - 0.333 \frac{\alpha_s}{\pi} - 0.5495 \left(\frac{\alpha_s}{\pi} \right)^2 - O(\alpha_s)^3 \right] \frac{1}{9}(3F - D). \end{aligned} \quad (2.79)$$

The predictions for nucleons are calculated with $\alpha_s = 0.36 \pm 0.05$ at $Q^2 = 3.0(\text{GeV}/c)^2$ to be,

$$\Gamma^p = 0.160 \pm .008, \quad (2.80)$$

$$\Gamma^d = 0.068 \pm .005, \quad (2.81)$$

$$\Gamma^n = -0.009 \pm .006, \quad (2.82)$$

where the D-state correction for the deuteron is included to that for deuteron with $w_D = 0.06 \pm 0.01$ [28].

Without the assumption for the unpolarized strange quark in the nucleon, a_0 may not be equal to a_8 . Generally, including QCD correction, the measured Γ_1 determines the a_0 . From Equation(2.79), a_0 is expressed by

$$a_0 = \left[9\Gamma_1^{p(n)} - \left(\pm \frac{3}{4}(F + D) + \frac{1}{4}(3F - D) \right) \left(1 - \frac{\alpha_s}{\pi} \dots \right) \right] \left(1 - 0.333 \frac{\alpha_s}{\pi} \dots \right)^{-1}. \quad (2.83)$$

Once a_0 is calculated from the measured Γ_1 , quark polarizations are expressed in terms of a_0 , F , and D by

$$\Delta u = \frac{1}{3}(a_0 + 3F + D) \quad (2.84)$$

$$\Delta d = \frac{1}{3}(a_0 - 2D) \quad (2.85)$$

$$\Delta s = \frac{1}{3}(a_0 - 3F + D) \quad (2.86)$$

$$\Delta u + \Delta d + \Delta s = a_0. \quad (2.87)$$

Chapter 3

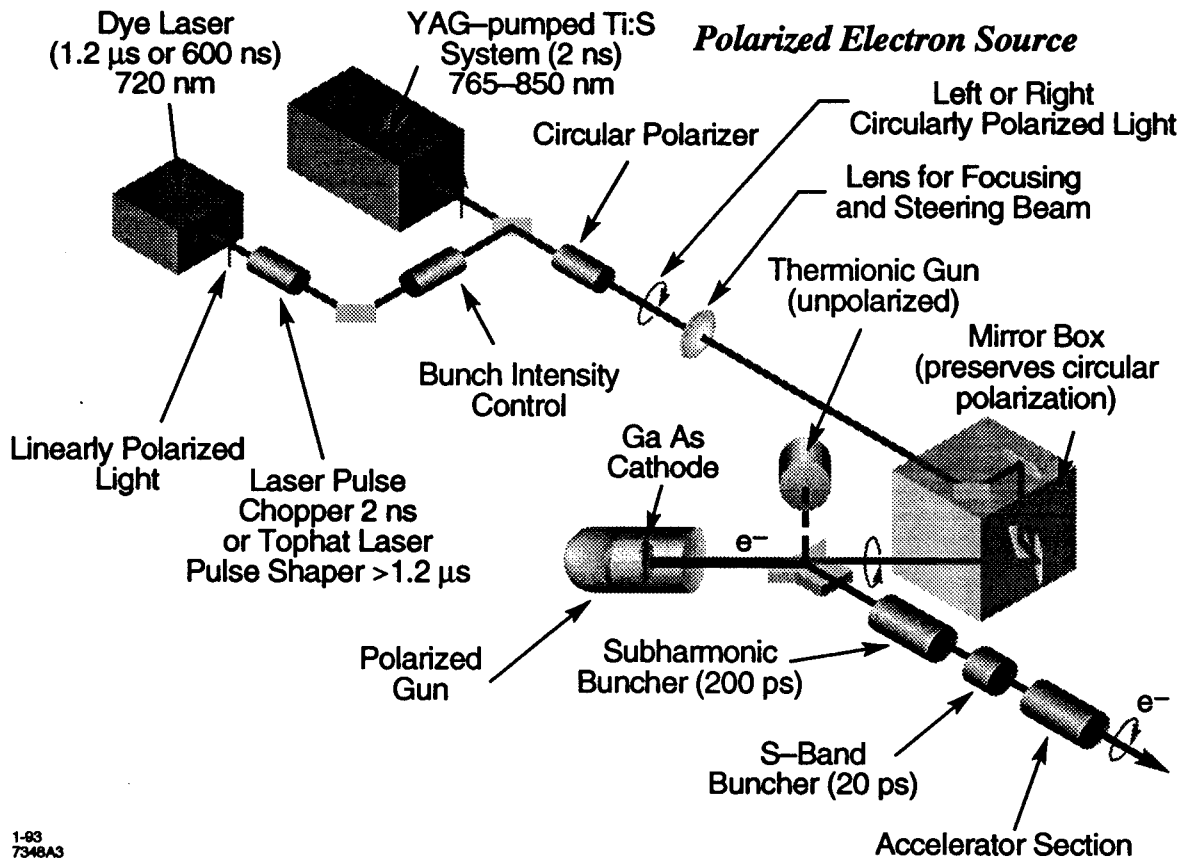
Experimental setup

In this chapter, the experimental setup will be explained which includes the polarized electron source, beam acceleration and transport, the Møller polarimeter, the polarized target, and the spectrometer system.

3.1 Polarized electron

The polarized electrons were produced by injecting circularly polarized photons onto the GaAs photo-cathode. Figure 3.1 shows the schematic view of the Polarized Electron Source (PES). The circularly polarized photons with wave length of 865 nm were produced by the Ti:Sapphire laser and excited the electrons into the conduction band. The excited electrons were polarized in the direction determined by the photon helicity which was changed randomly to reduce systematics. Subsequently, the left- and right-handed electrons in the conduction band are extracted by high voltage applied for the cathode and transported into the accelerator.

The photo-cathodes for the polarized electron gun based on GaAs crystals has been developed at SLAC. Recently, they established a new technology to improve the electron polarization using strained GaAs[29]. First, we will explain the principle of obtaining polarized electrons with the unstrained GaAs crystal, then, the mechanism to improve the electron polarization with the strained GaAs crystal.



1-83
7348A3

Figure 3.1: Polarized electron source: Dye Laser is replaced by Flash-lamped Ti:Sapphire laser system for E143 operation. Circularly polarized photons made by the laser are introduced into GaAs electron cathode and excited electrons in the bounding state into the conduction band. A static electric field and a bending magnet carry the emitted electrons into the Linear Accelerator.

3.1.1 Unstrained GaAs

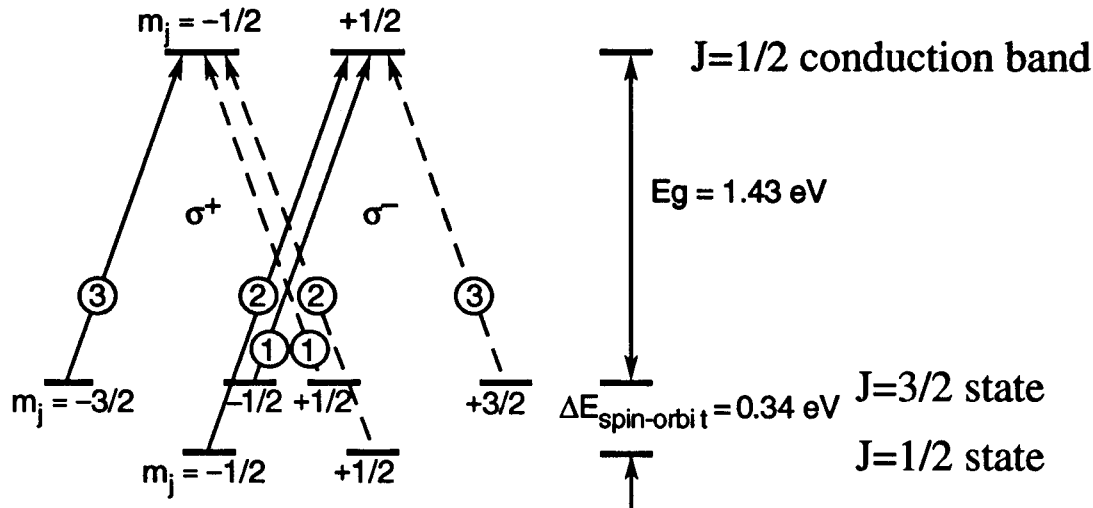


Figure 3.2: Energy level of the unstrained GaAs: the unstrained GaAs has bound states which have angular momentum $J = 3/2$ and $1/2$. These states are degenerate by the Z-component of the angular momentum. The transition by right-handed and left-handed photons are shown by the solid and dashed lines. The relative probability for these transitions determined by Clebsh-Gordon coefficients are shown in circles.

Figure 3.2 shows the band structure of the unstrained GaAs crystal. There are bound states with the magnitude of the angular momenta, $J = 3/2$ and $J = 1/2$ in GaAs which are degenerate with the Z-component of the angular momenta, $m_j = \pm 1/2, \pm 3/2$ as shown in the figure. The solid or dashed lines indicate the allowed transitions by the right- or left-handed photons respectively.

The transition probabilities into the conduction band at the energy level of 1.43 eV above the $J = 3/2$ states are proportional to the corresponding Clebsh-Gordon coefficients of $3/2 \otimes 1$ or $1/2 \otimes 1$. The numbers in the circle are the relative transition probabilities calculated from the coefficients.

The transition probability is also influenced by the transition energy. The transition from the $J = 1/2$ states is suppressed by using a laser with the wave length corresponding to 1.43 eV.

Providing the transition from the $J = 1/2$ states is negligible, the transition from the $m_j = \pm 3/2$ states has a probability three times larger than that for $m_j = \pm 1/2$ states as shown in Figure 3.2. If the incident photon is polarized in left- (right-) handed, the electrons with $+1(-1)$ helicity are produced three times more than those with $-1(+1)$ helicity. Therefore, the helicity of the electrons in the conduction band are determined by the photon helicity and the theoretical limit of the polarization is 50% for the unstrained GaAs. In practice, we need to optimize the laser photon energy to obtain the high electron current because the quantum efficiency of the transition from the $J = 3/2$ states decreases as the photon energy close to 1.43 eV.

3.1.2 Strained GaAs

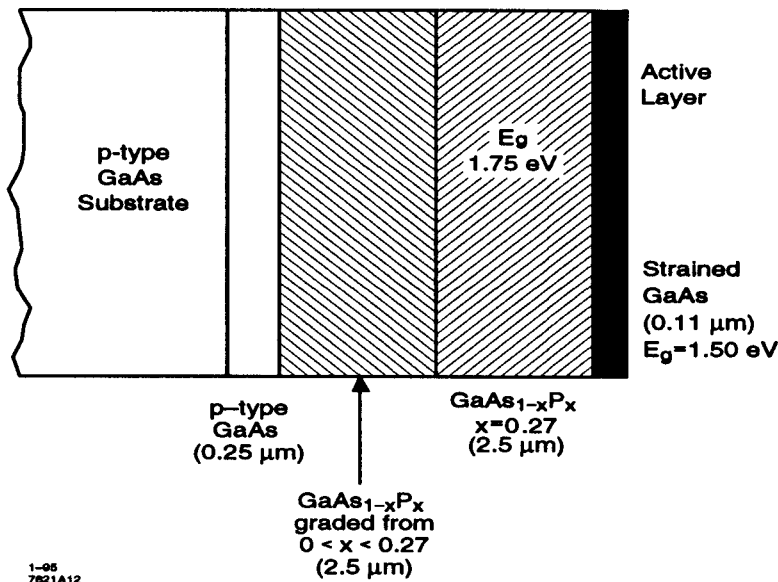


Figure 3.3: The strained GaAs was grown on the GaAsP substrate. The GaAsP substrate has 27% of the phosphorus contamination. This GaAsP was grown on the GaAs substrate via the graded GaAsP crystal as a buffer area. The phosphorus fraction in the buffer GaAsP substrate is increasing from 0 to 27% to accommodate the lattice mismatch.

As mentioned, the electron polarization is limited up to 50% for the unstrained GaAs crystal as the photo-cathode. To improve the electron beam polarization, a new photo-cathode for the electron gun was developed at SLAC by using a strained GaAs crystal. The strained GaAs is obtained as a thin layer of the GaAs crystal growing on GaAsP substrate as shown in Figure 3.3.

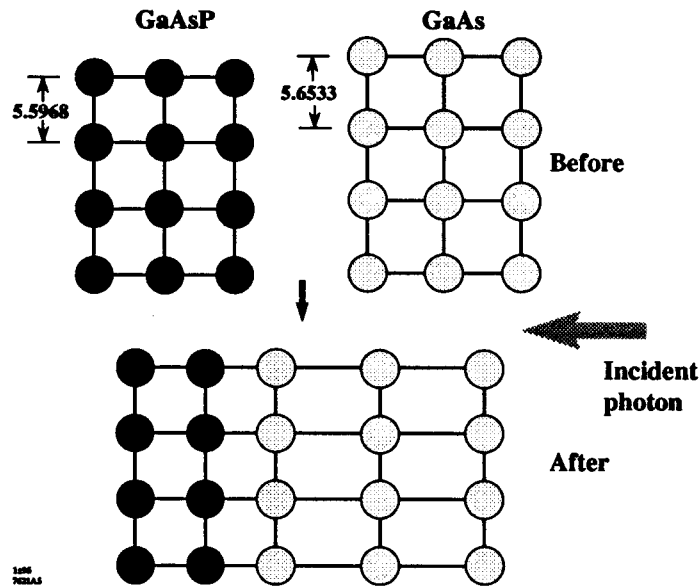


Figure 3.4: Schematic view of the strain for the GaAs crystal: The GaAs has a cubic structure with the lattice spacing of 5.65\AA . The strained GaAs is obtained by developing the GaAs crystal on GaAsP crystal which has the lattice mismatch by 1%. This mismatch on the lattice strains the GaAs crystal and the spacing of the lattice is changed as shown in the figure. The lattice is stretched in the direction perpendicular to the strained surface which we define to be the strained axis.

The GaAsP crystal has a smaller lattice size than the size of the GaAs and the mismatch strains the GaAs crystal. The schematic view of the strained GaAs crystal is shown in Figure 3.4. The unstrained GaAs crystal has a cubic structure with Ga and As nuclei placed one by one with the lattice spacing of 5.65\AA . The strained GaAs has the rectangle structure due to the lattice mismatch as shown in the figure. If the laser photon incidents to the strained GaAs in the direction shown in the figure, along the strained

axis, the $J = 3/2$ degenerate levels are split into states with a energy gap of 0.05 eV [30] according to m_j .

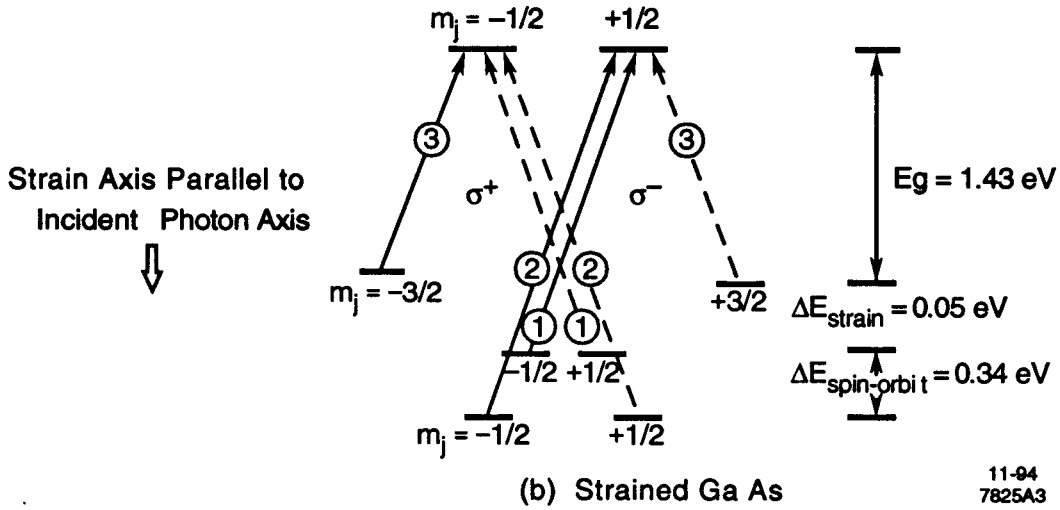


Figure 3.5: Energy level of the strained GaAs: the degeneration in $J = 3/2$ states come untied due to the strain. The states are split by the energy gap of 0.05 eV. This energy gap suppresses the transition from $m_j = \pm 1/2$ and improves the electron polarization.

The Figure 3.5 shows the energy levels of the strained GaAs crystal. Because of the energy gap of 0.05 eV in the strained GaAs, the transition to the conduction band from the states of $m_j = \pm 1/2$ is suppressed compared with that from the states of $m_j = \pm 3/2$. Thus, the polarization of the electrons in the conduction band is increased up to 100% if the photon energy is close to the transition energy, 1.43 eV. Figure 3.6 shows the electron polarization as a function of the wavelength of the laser indicating that the polarization using the strained GaAs cathode exceeded 50% and reached almost to 90%. The strained GaAs with the thickness of $0.1 \mu\text{m}$ was used in the experiment.

The photon energy optimization decreases the quantum efficiency of the main transition, resulting the decrease of the electron current. Fortunately, we needed only a low intensity beam of typically 3.0×10^9 electrons/pulse in contrast to that for SLD operation and the PES was able to maintain a high electron polarization between 85% and 87% during the experiment.

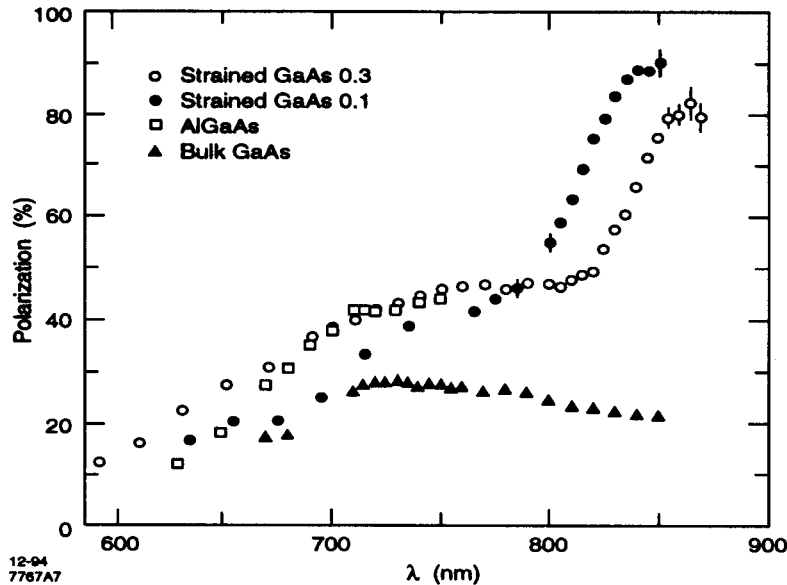


Figure 3.6: Electron polarization as a function of the photon wave length. The results by various electron cathodes are shown. The open and solid circles show the results by the strain GaAs with the thickness of 0.3 and 0.1 μm respectively.

The PES was operated at 120Hz. Because the AC line has 60 Hz frequency, every odd or even spill is created at the same phase of the AC line. To suppress the systematic effect on the electron beam due to the phase of the AC line, the electron helicity was changed spill by spill randomly by Pseudo Random Number Generator which generated 33 bits random sequence one by one and will be mentioned in Chapter 4 in detail.

The electron beam spill width was typically 2.2 μs . The current of the electron beam was a order of 10^9 electrons/spill.

3.2 Beam line

Figure 3.7 illustrates the beam acceleration and transportation into End Station A. The polarized electrons were injected into the 2-mile Linear Accelerator (Linac) and accelerated up to 29 GeV. The Linac retained the electron's longitudinal polarization during the acceleration. No depolarization effect was observed due to the acceleration and the

transportation of the electron beam into ESA[31].

The electron was bent at the end of Linac by a magnet at an angle θ_b of 428 mrad into the ESA beam line. In this bending process, the electron spin was rotated due to its anomalous magnetic moment. The angle of the direction of the electron spin from that of the electron momentum, $\Delta\phi$ is given by

$$\Delta\phi = \frac{0.136\pi(g-2)E}{2mc^2}, \quad (3.1)$$

where g is the gyro magnetic ratio of the electron, E is the beam energy, m is the mass of the electron. To retain the longitudinal electron polarization after the process, this $\Delta\phi$ has to be equal to $N\pi$ where N is an integer. This condition was satisfied by adjusting the beam energy to be[32],

$$E = 3.24 \cdot N. \quad (3.2)$$

The beam energy was decided to be 29.11GeV which was the highest energy satisfying the condition to keep the electron polarization.

Two Møller polarimeters located at the end of the Linac and in the ESA measured the beam polarization. These measurements for the beam polarization before and after the bending allowed us to calibrate the beam energy independently with the precision of 0.05% by using the relation of the polarization and the beam energy.

Two toroidal current monitors were placed on the beam line to measure the beam current. These monitors produced a signal proportional to the electron current passed through the toroidal coils. These devices were calibrated carefully with respect to the signal from a Digital to Analog Converter, DAC[33]. For some historical reason, these current monitors were called as Toroid2 and Toroid3. Toroid2 and Toroid3 were located at 9.1 meters upstream and 5.6 meters downstream of the target respectively. The systematic error was calculated to be less than 1.0% from the spreads of the reading of these monitors at the same DAC voltage [33].

Figure 3.9 shows the beam position on the target which was changed for each spill. This rastering reduced a depolarization effect caused by radiation damage and heat up of the target. Two pair of Helmholtz coils located at about 70 meters upstream of the

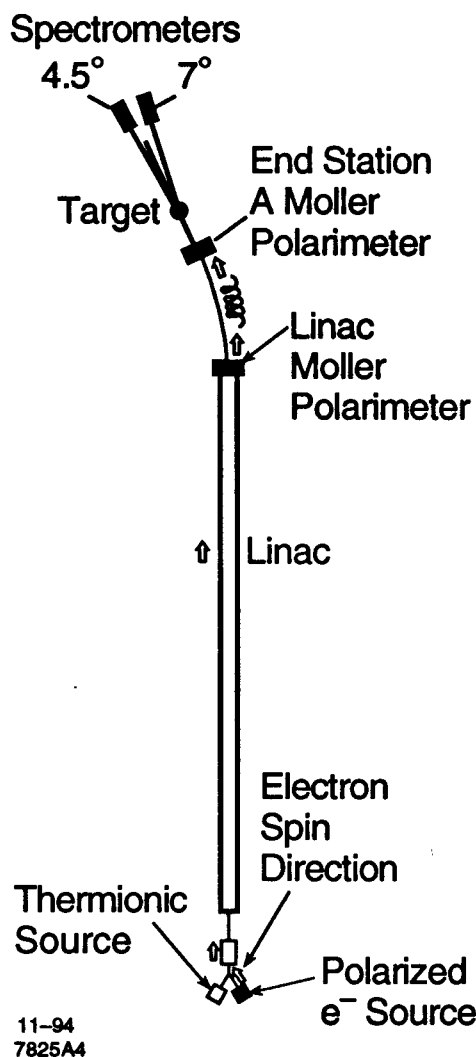


Figure 3.7: The polarized electrons produced by the PES were injected into the Linac and accelerated up to 29 GeV. The electrons were bent at the end of Linac and introduced into ESA. The electron spin was rotated in the bending magnet as shown in this figure and the beam energy was set to maximize (retain) the longitudinal polarization. The ESA Møller polarimeter was located at the entrance of ESA. Two independent spectrometers were placed in ESA to detect the scattered electron from the target. A part of SLD operation has been removed from the original figure.

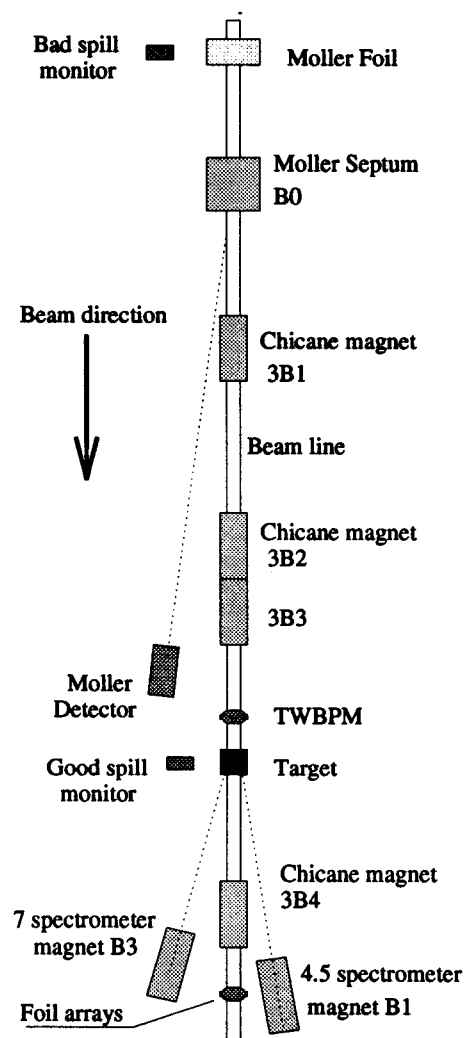


Figure 3.8: Schematic view of apparatus location in ESA: the electron beam passed through ESA from up to bottom in this figure. The Møller foil was at the entrance of ESA and was placed on the beam line only when we calibrated the electron polarization with the Møller system. Four chicane magnets were turned on only when we investigated A_{\perp} to correct the deviation of the electron beam due to the transverse magnetic field of the target. The spectrometer magnets B1 and B3 mark the beginning of the spectrometer systems.

target were used to steer the beam position for the rastering. The coils had a rounded rectangular shape, about 1.5m by 0.5m. They were controlled by Linac Main Control Center (MCC).

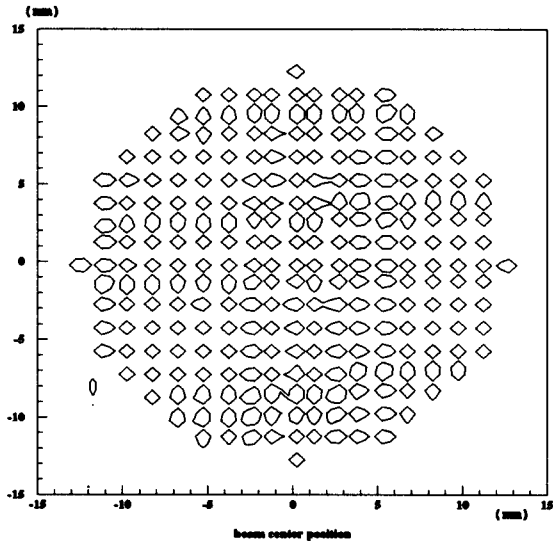


Figure 3.9: Beam rastering: the center of beam spill is plotted with respect to the target center. The center of beam spills are obtained by the foil arrays.

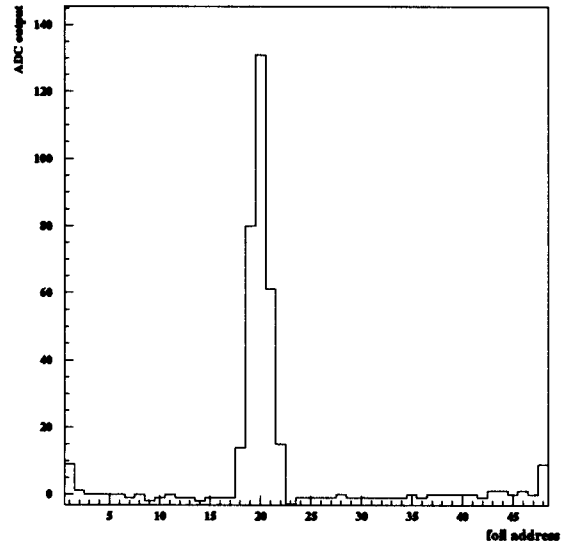


Figure 3.10: Output of a foil array: Horizontal axis corresponds to the address of the foil. Vertical axis shows the corrected ADC output.

We monitored the actual beam position with a set of two dimensional foil arrays which was located at 11 meters downstream of the target. Each foil array was consisted of 48 foil strips placed at 1 mm interval and an anode plane behind the foil array. Both of the foil and the anode plane made from the $25 \mu\text{m}$ thickness aluminum. The electron beam hitting the foils induces electron current between the foil and the anode, of which signal is proportional to the beam current through the foil. Figure 3.10 shows the distribution of the ADC readout signal from the foils which gives us the beam current profile.

There were two spill monitors used to trace the beam quality; one is the bad-spill monitor which is a scintillation counter placed about a meter off the beam line near the entrance of ESA. The monitor measured electron beam scattered off from the center of beam line. When the beam is stable and passes cleanly through the beam line, the bad spill monitor gives no signal. The other is the good-spill monitor which is a scintillation

counter located under the target and detected the scattered particles from the target. Thus the signal from this monitor indicates that the beam is on target.

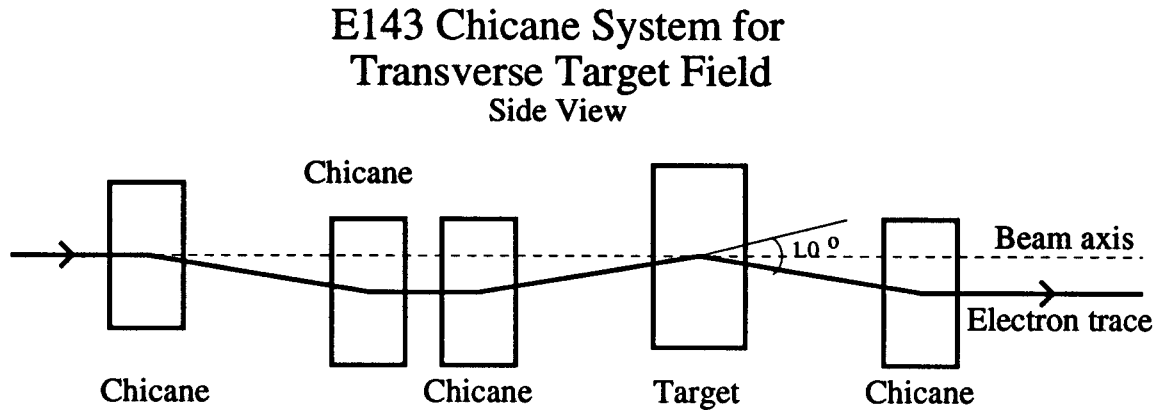


Figure 3.11: This is the schematic view of the chicane system. All chicane magnets induced magnetic fields perpendicular to the beam axis. The system corrected the electron spin to be parallel to the beam axis at the deuteron target. The unscattered electrons went to the beam dump unless hitting the beam pipe.

In order to study A_{\perp} , the target was rotated by 90° around the vertical axis mechanically. This also changes the strong target magnetic field perpendicular to the beam axis and bends the electron beam into a wrong direction off the beam dump. The magnetic field rotates the spin of electrons and produces a misaligned incident angle. To avoid these problems, a chicane system consisting of four chicane magnets was installed in the beam line as shown in Figure 3.11. All these magnetic fields were set perpendicular to the beam axis. Though the spin is rotated by these fields, the effects are canceled at the target and there is no depolarization effect. The beam level after the chicane system stayed lower than the nominal level, but parallel to the the beam line.

3.3 Møller system

The Møller system is the polarimeter to measure electron polarization by using the Møller scattering. The beam polarization in this experiment was calibrated by ESA Møller

system.

The cross section of Møller scattering is expressed in center of mass system by [34],

$$\frac{d\sigma}{d\Omega} = \frac{\alpha^2 (3 + \cos^2 \theta)^2}{s \sin^4 \theta} \left[1 - P_b P_f \frac{(7 + \cos^2 \theta) \sin^2 \theta}{(3 + \cos^2 \theta)^2} \right], \quad (3.3)$$

where θ is the scattering angle from the direction of the initial electron momentum, P_b and P_f are the beam and the target foil polarization. The cross section asymmetry for the different orientation of the electron helicity is expressed by

$$A = \frac{N^{\uparrow\downarrow} - N^{\uparrow\uparrow}}{N^{\uparrow\downarrow} + N^{\uparrow\uparrow}} = P_b P_f \frac{(7 + \cos^2 \theta) \sin^2 \theta}{(3 + \cos^2 \theta)^2}. \quad (3.4)$$

This asymmetry for the Møller scattering reaches to the maximum at the scattering angle of 90° . Using the target foil polarization, p_f obtained from the measurement for magnetization of the foil, we can determine the beam polarization, p_b from the measured asymmetry.

The Møller foil target was made of a ferro-magnetic material which contains 49% Fe, 49% Co, and 2% Va. The foil target was mounted at 20° off the beam axis and placed inside a 100 Gauss magnetizing field. Taking the gyro-magnetic ratio for the material to be $g_{eff} = 1.889 \pm 0.005$ [35], the electron polarization of the foil was given by

$$P_f = (0.94011 \pm 0.00280) \frac{M}{N\mu_B}, \quad (3.5)$$

where M is the foil magnetization, N is the number of electrons per unit volume, and μ_B is the Bohr magneton. To obtain the systematic error coming from the foil thickness, the target polarization for the six foils was measured and was found to be 0.0803 for the 20 μm foil and 0.0814 for the 30, 40, and 154 μm foils.

Figure 3.3 shows the schematic view of ESA Møller polarimeter. The target foil was located near the entrance of ESA. The scattered electron which passed through the window of the mask was bent by the magnet and its momentum was analyzed. The light gray area shows the detector acceptance for the scattered electrons. The scattered electron was detected by the single arm and double arm detectors. The single arm detector was consisted of eight silicon pad detectors. The double arm detector was assembled by

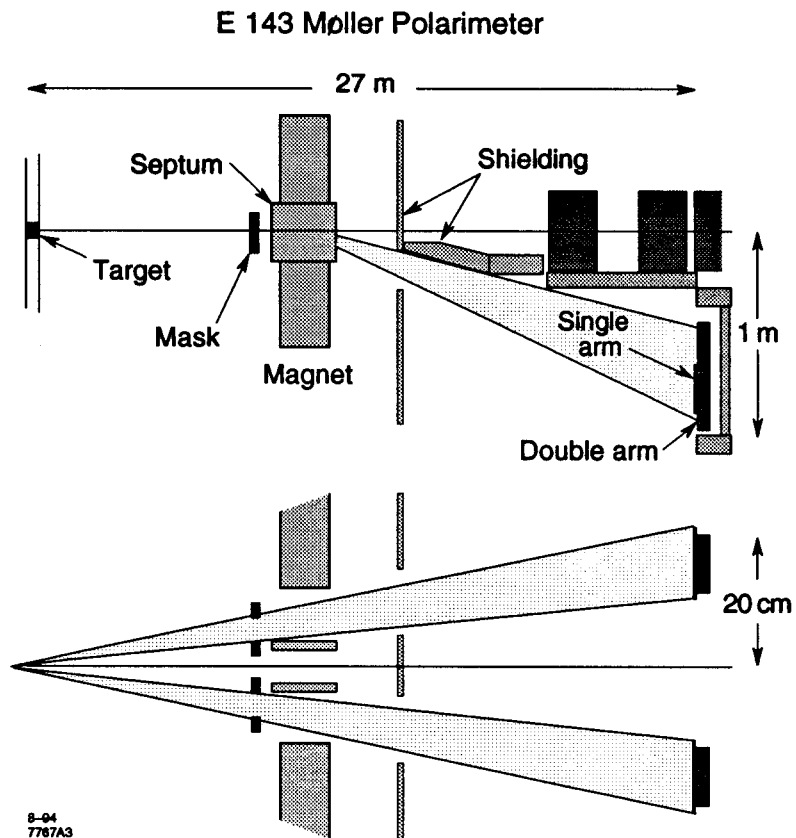


Figure 3.12: Møller polarimeter schematic view: The upper and lower parts show the horizontal and vertical views respectively. This figure is enhanced in the transverse direction with respect to the beam line. Polarized electrons come from the left side of the figure. Scattered electrons are bent by the magnet and detected by double arm and single arm detectors to analyze the momentum.

seven lead glass blocks of 4 · 4 inch mounted with a 2 inch photo-tube. The double arm detector was placed behind the single arm detector and two sets of these detectors were set above and below the horizontal plane respectively as shown in Figure 3.3. The double arm detector had a large acceptance covering the electron scattering angle between 70° and 110° in the center of mass frame. This acceptance was large enough to count both of the Møller electrons in time coincidence. One of the Møller electrons will be then detected in the upper array and the other in the lower array. Figure 3.13 shows the time difference between signals measured by the two detectors. This coincidence counting suppressed the back-ground rate and reduced the systematic error of the beam polarization measurements.

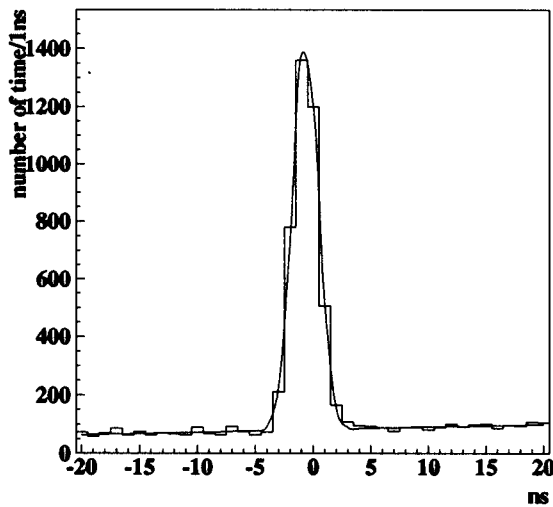


Figure 3.13: Time difference between signals from the two appropriate detectors in the upper and lower arrays of the double arm detectors. There is a sharp peak with 1.1 ns resolution on the low background.

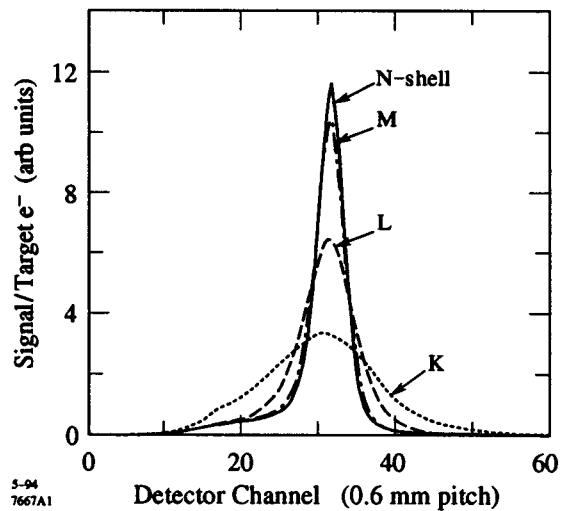


Figure 3.14: Horizontal axis shows the detector channel of the Silicon micro-strip detector corresponding to the momentum of the Møller electrons. Vertical axis is the number of times by a channel of the detector. The expected spectra by electrons on K, L, M, and N shell in atoms of the target foil are shown.

The recent study on the Møller scattering shows that the orbital momentum of electrons on the atomic shells influences the momentum spectrum of the scattered electron

[36]. Figure 3.14 shows the momentum distribution obtained from a Monte-Carlo simulation for the Linac Møller polarimeter. The spectra by electrons on K, L, M, and N shells of atoms in the target foil are shown in the figure. The momentum spectrum for electrons scattered with the electrons on K-shell is broader than others. Therefore, the fraction of Møller electrons from those shells in a certain momentum range is different from that in the whole momentum range. Because only electrons on the M-shell are polarized for the target material, the polarization of electrons in Møller target would change depending on the momentum acceptance of the detector. However, the double arm detector has a wide momentum acceptance to cover almost the whole momentum dependence range and the correction due to the K-shell effect was estimated to be less than 1% [34].

3.4 Polarized target

The polarized nucleon target is essential for the measurement of the spin structure of the nucleon. We used the frozen ammonia as the target material, in which three hydrogens bound to the nitrogen were replaced to deuterons for the deuteron measurement. There are two reasons why we choose ammonia as the target; one was that the deuterized ammonia, ND_3 , contains deuterons with a large fraction of about 30%, and the other is that the material has high radiation resistivity and stands against flux $4 - 8 \times 10^{15}$ particles/cm² before depolarizing to e^{-1} [37].

The target was frozen by a ⁴He evaporation type refrigerator at 1 K. Superconducting Helmholtz coils surrounding the target provided 5.1 Tesla magnetic field. The target was polarized by using the Dynamic Nuclear Polarization (DNP) method which uses microwaves to improve the nucleon polarization. In the following, this will be explained for the case of proton polarization.

We assume a simple system of electron and proton in a magnetic field neglecting the spin-spin interaction of these two particles. These particles have spin 1/2 and their spin states are degenerate without magnetic field. When magnetic field is applied, the

energy split of these states, ΔE and given by

$$\Delta E = \frac{\mu H}{2}, \quad (3.6)$$

where μ is the magnetic moment of the proton or the electron and H is strength of magnetic field. Using Boltzmann distribution of a form of $e^{\Delta E/k_B T}$ for the occupation number of the state, polarization of proton or electron in a magnetic field is given by

$$P = \frac{N \uparrow - N \downarrow}{N \uparrow + N \downarrow} = \frac{e^{\Delta E/2k_B T} - e^{-\Delta E/2k_B T}}{e^{\Delta E/2k_B T} + e^{-\Delta E/2k_B T}} = \tanh\left(\frac{\Delta E}{2k_B T}\right), \quad (3.7)$$

where k_B and T are the Boltzmann constant and the temperature, $N \uparrow$ and $N \downarrow$ are the number of protons or electrons with $+1/2$ and $-1/2$ spin along the magnetic field respectively. If we use 1 K° for temperature and 5 Tesla for magnetic field into Equation (3.7), we obtain the polarization of about 0.5% for proton and 100% for electron. We call this polarization due to the energy split as polarization at thermal equilibrium.

This proton polarization at the thermal equilibrium is not sufficient for the polarized proton target and we need introduce the DNP method. The basic idea of the DNP method is to utilize the high electron polarization to improve the proton polarization by using microwave.

Figure 3.15 shows the four energy states of four combinations of proton and electron spin in a magnetic field. The occupations for these four states at thermal equilibrium are shown in the column labeled as TE. w_1 , w_2 , w_3 , and w_4 indicate the transition between the two states as shown in the figure.

If the target was exposed to the microwave with the energy corresponding to the transition w_3 , the electrons and protons in the $|e : -1/2, p : -1/2 \rangle$ state are carried into the $|e : 1/2, p : 1/2 \rangle$ state. The electrons and protons in $|e : 1/2, p : 1/2 \rangle$ state falls into $|e : -1/2, p : -1/2 \rangle$ or $|e : -1/2, p : 1/2 \rangle$ states thermally. Because the transition w_4 is even slower than the transition w_3 or w_1 [20], the occupation fraction of the electrons and protons in the $|e : -1/2, p : 1/2 \rangle$ states increases and the occupation fractions of the electrons and protons in these states are settled as shown in the column of w_3 . As the result, the proton polarization is improved to be $\tanh(\Delta/2)$ corresponding to the electron polarization in thermal equilibrium, instead of $\tanh(\delta/2)$.

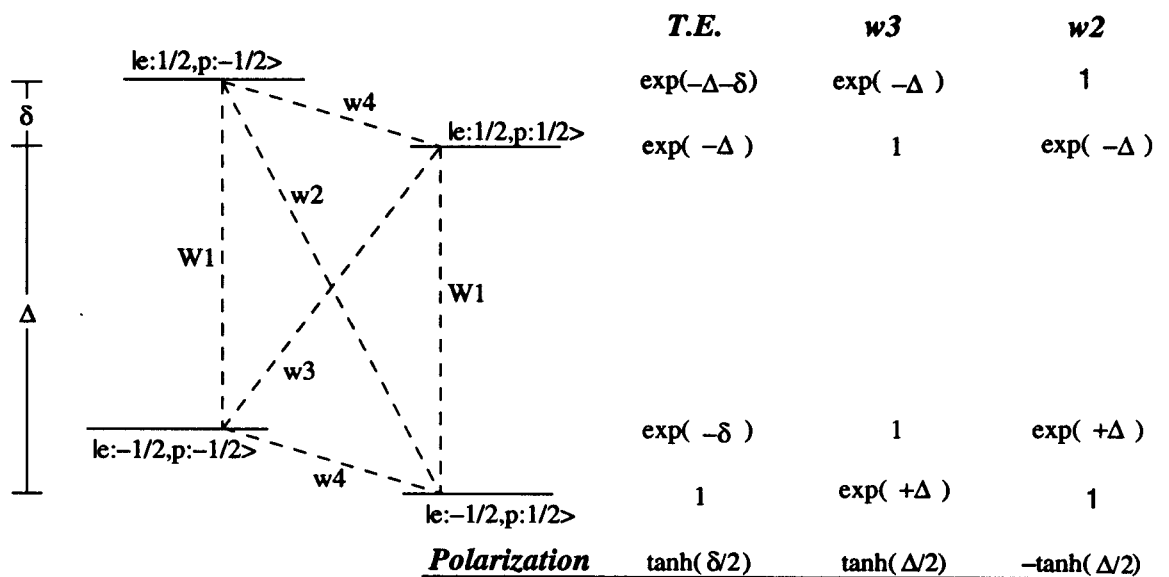


Figure 3.15: The energy states of electron-proton system in a magnetic field are shown. The indices of ket vector indicate electron and proton spin. The energy split due to the proton spin is expanded in the figure. The quantities in the right side indicate the relative occupation of the states in three cases. T.E. stands for thermal equilibrium according to the Boltzmann distribution. Saturation w_2 and w_3 indicate the occupations when we drive these transition with microwave cause relaxation between these two states. The lowest number gives proton polarization under these conditions.

If the target was irradiated by the microwave with the energy corresponding to the transition of w2, the occupation fraction of the particles in the $|e : -1/2, p : -1/2 \rangle$ state increases and the occupation fractions of the particles in these four states are settled as shown in the column of w2. The magnitude of the proton polarization is to be same as that for the case of w3, but the direction of the proton spin is opposite to that for the case of w3. The wave length inducing the transitions w2 and w3 are 140.127 ± 0.213 GHz where plus for w2 and minus for w3 [20].

The deuteron is a spin 1 particle and makes three energy splits in a magnetic field according to the spin states. The polarization of the deuteron, P_d is defined by,

$$P_d = \frac{N^{+1} - N^{-1}}{N^{+1} + N^0 + N^{-1}}, \quad (3.8)$$

where $N^{\pm 1,0}$ is the number of deuteron in the spin states indicated by the superscripts. If the magnitudes of the energy splits between $S_Z = \pm 1$ and $S_Z = 0$ are identical, a microwave with a certain frequency enhances the deuteron polarization as well as that for the proton.

Although the polarized deuteron is obtained with one frequency microwave, the improvement of the deuteron polarization using the 44 MHz frequency modulation of the microwave was discovered by SMC [38]. It is understood as that the two energy splits due to the deuteron spin are not identical. Letting the frequency of the microwave be ν_1 for the transition between the deuteron spin $S_Z = 1$ and $S_Z = 0$ and ν_2 for the transition between $S_Z = 0$ and $S_Z = -1$, the polarized deuteron is obtained with microwaves of the frequencies of $\nu_e - \nu_1$ and $\nu_e - \nu_2$ where ν_e is the frequency of the microwave required for the spin flip of electrons. The polarized deuteron in the opposite direction is obtained with microwaves of the frequencies of $\nu_e + \nu_1$ and $\nu_e + \nu_2$. In short, the deuteron polarization requires the microwaves with two different frequencies and the frequency modulation for a certain microwave provides these two frequencies.

We used the microwave frequencies of 136.48 GHz and 136.78 GHz frequency modulated by 44 MHz to implement the polarized deuteron in the positive and negative directions respectively. We found some improvement for the deuteron polarization by

3-5% with this frequency modulation.[20]

Figure 3.16 shows the E143 polarized target system. Liquid helium kept the ammonia target and the super conducting magnet at 1 K°. The magnet produced 5.1 Tesla magnetic field around the target cell to align the nucleon spin. The target insert had four cells which were filled by ND₃, NH₃, empty (nothing in it), and carbon or aluminum. We can select one of cells on the beam line by using a mechanical control. Each target cell had a dimension of $\phi 25 \cdot 30$ mm. The microwave was fed to the target cell through a pipe and horn from the top of the system. The power of the microwave was about 1 Watt at the target cell.

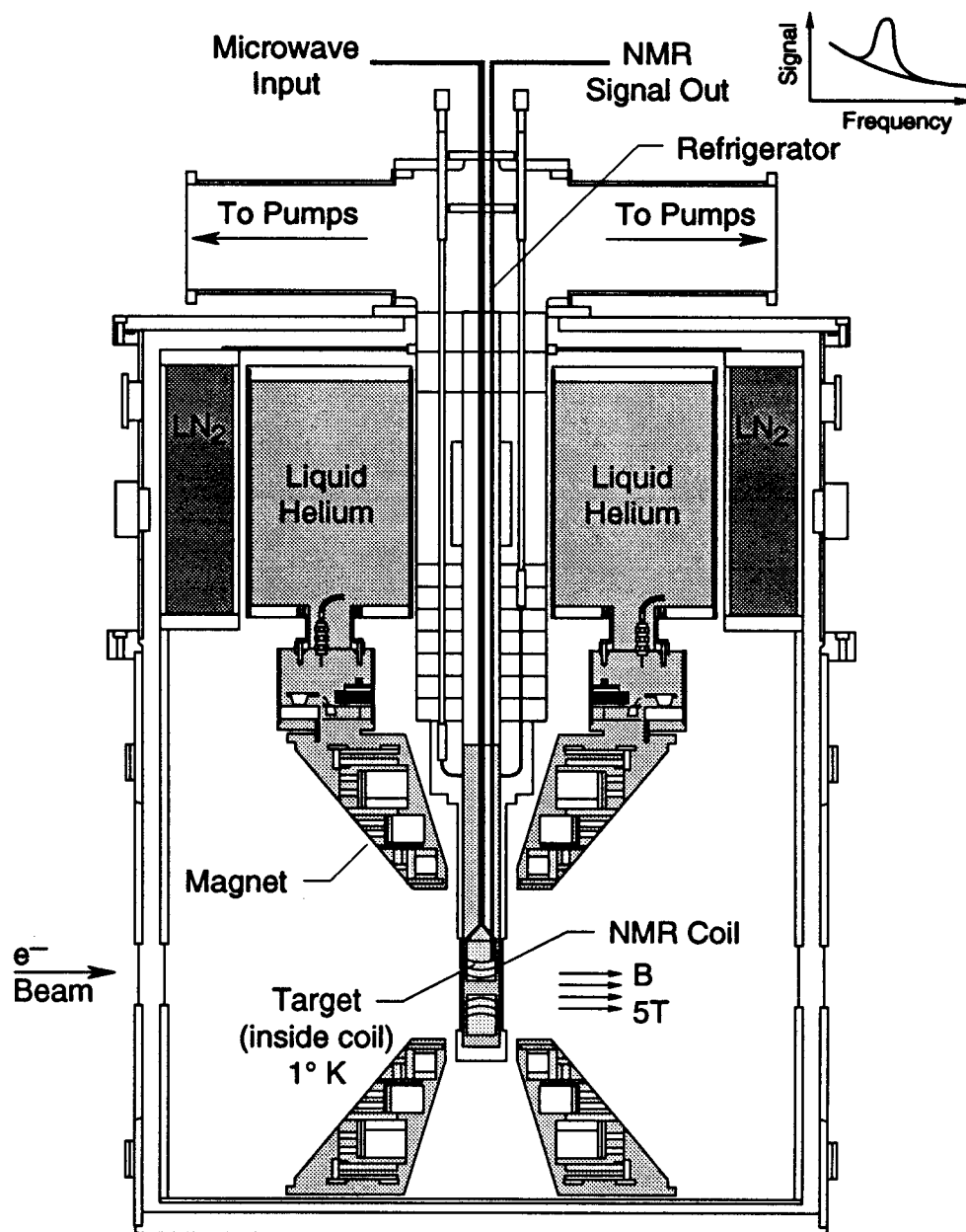
The target polarization was measured with Nuclear Magnetic Resonance (NMR). The NMR is induced by a oscillating magnetic field perpendicular to the static magnetic field, the super-conducting magnet in E143 target system. A small fraction of the nucleon in the material oscillates between the spin up and down states with a frequency of the oscillating magnetic field. This signal resonates at the frequency determined by the static magnetic field and the magnetic moment of the nucleus. This phenomenon is called as Nuclear Magnetic Resonance (NMR).

The NMR signal was measured by using the technique of the Q-meter. A coil made from Copper and Nickel was placed in each target cell perpendicular to the static magnetic field. When we induce the oscillating magnetic field by using this NMR coil, the inductance of the NMR coil is modified by the target material existing in the coil to be [39]

$$L(\omega) = L_0[1 + 4\pi\eta[\chi'(\omega) - i\chi''(\omega)]], \quad (3.9)$$

where ω is the frequency of the oscillation magnetic field, $L(\omega)$ is the inductance of the NMR coil at the given frequency, L_0 is the inductance of the coil in the vacuum, η is the filling factor of the material in the coil, $\chi'(\omega)$ and $\chi''(\omega)$ is the real and imaginary parts of the complex susceptibility of the material. The $\chi''(\omega)$ is related to the target polarization, p_t , by the relation of [39]

$$p_t = K \int_0^\infty \chi''(\omega) d\omega, \quad (3.10)$$



4-94

7656A1

Figure 3.16: The electron beam comes from the left side of the figure. The magnets induce the 5.1 Tesla magnetic field along the beam axis. We rotated the target system by 90° along the vertical axis in the investigation for the A_{\perp} .

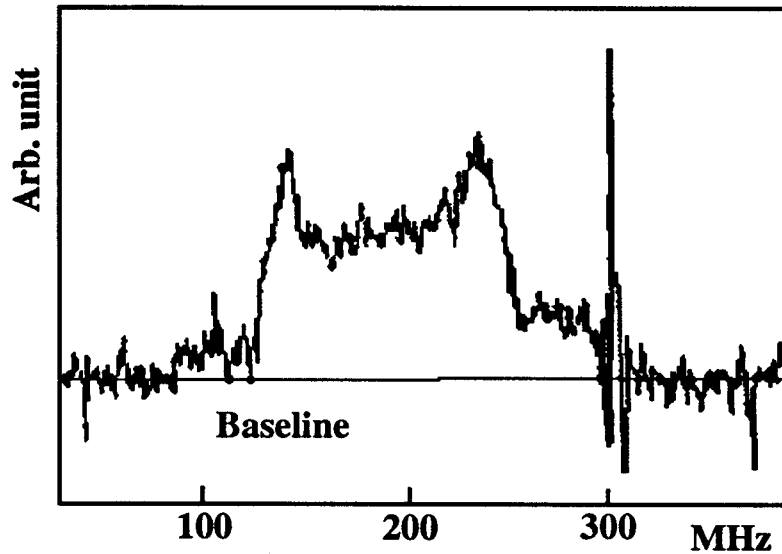


Figure 3.17: The NMR signal of the thermal equilibrium for ND_3 under 5.1 Tesla and 1 K measured by Q-meter circuit. It corresponds to about 0.068% polarization.

where K is a constant involving the nucleus property. The imaginary part of the inductance is the real part of the impedance of the coil. In the Q-meter, the circuit is driven by a constant current source and the variable capacitance is set to absorb the phase part of the impedance of the coil. Therefore, the voltage of the circuit of the Q-meter is proportional to the real part of the impedance of the coil and the variation of the χ'' with the frequency can be observed as the variation of the voltage of the coil. Figure 3.17 shows the NMR signal as a function of the frequency ω for thermal equilibrium of ND_3 target. This χ'' is zero for all frequencies except for a small band close to the resonant frequency as shown in Figure 3.17, thus the area of the NMR signal above the base line is proportional to the target polarization from the Relation (3.10). The target polarization in the experiment was calibrated by using this NMR signal of thermal equilibrium corresponding to 0.068%.

We used the enriched ^{15}N nucleus instead of the usual ^{14}N . While the ^{14}N nucleus has the magnetic moment equal to that for deuteron, the ^{15}N has the magnetic moment equal to that for proton and the NMR signal does not overlap to that for the deuteron. We were then able to measure both polarizations for the deuteron and the nitrogen nucleus in

the target and the effect of the nitrogen polarization was corrected properly as discussed in Section 4.2.5 and in Appendix D.

3.5 Spectrometers

Figure 3.18 shows a schematic view of the spectrometers. There were two independent spectrometers to detect electrons scattered off the ND_3 target. These spectrometers were located along an angle of 4.5° and 7° from the beam axis. We call these spectrometers the 4.5° and 7° spectrometers respectively. Both spectrometers had two bending dipole

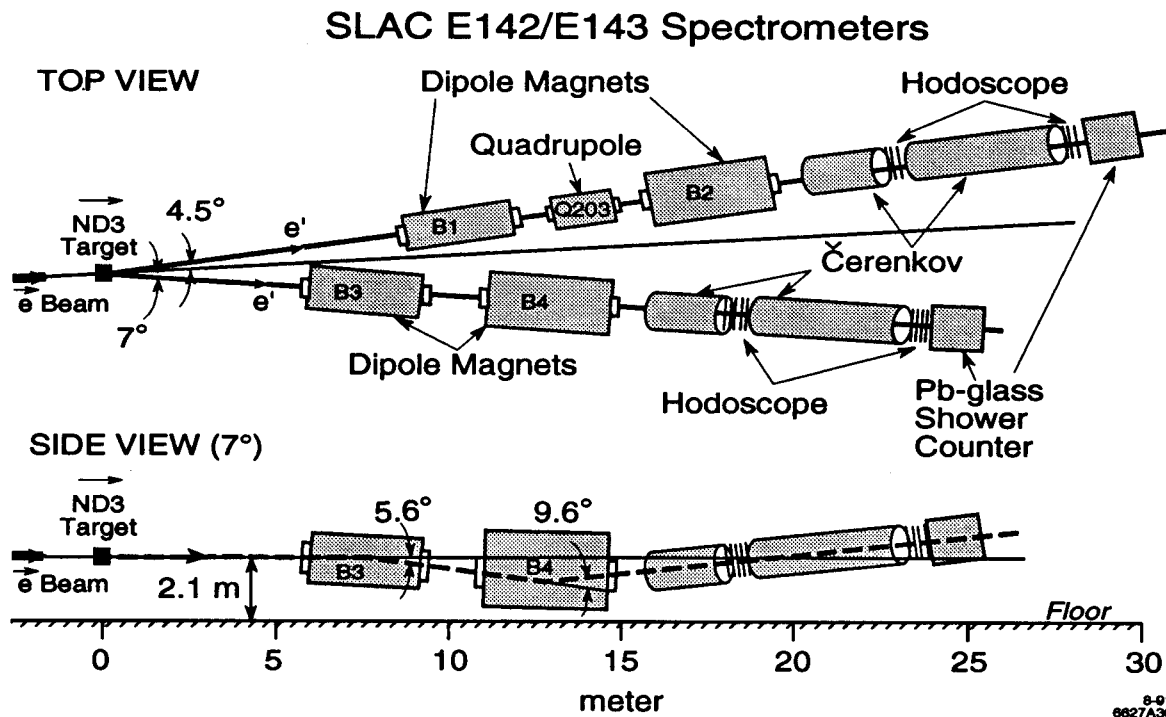


Figure 3.18: This figure shows horizontal and vertical views of the spectrometer layout. The scale shows the distance from the target in meter. The vertical view is the layout for the 7° spectrometer.

magnets. B1 and B3 have the length of 118 inch and B2 and B4 have the length of 136 inch. The central momenta for the spectrometers were set to 11.5 GeV/c and 12.5 GeV/c

for the 4.5° and 7° spectrometers. The two magnets in each spectrometer bent electrons in directions opposite to each other. This configuration has a larger momentum acceptance compared to the configuration bending in same direction [40]. Figures 3.19 and 3.20 show the momentum acceptance. The momentum acceptance of 4.5° and 7° spectrometers was from 6 and 7 GeV/c to beyond 20 GeV/c. respectively. The quadrupole magnet in the 4.5° spectrometer enhances the position dependence of electron momentum on the vertical axis and spreads electrons onto a larger detector area along the horizontal axis.

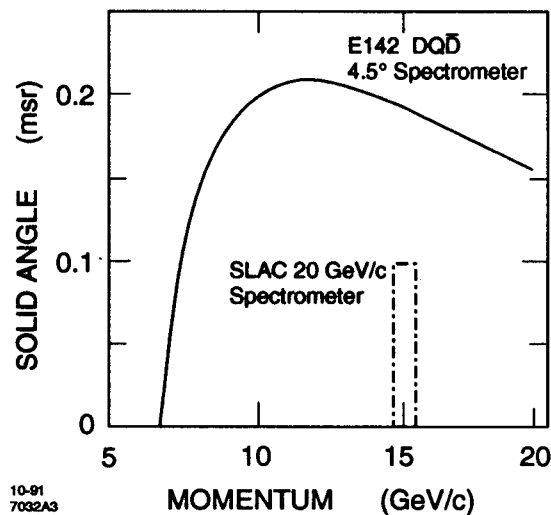


Figure 3.19: Momentum acceptance of the 4.5° spectrometer: the horizontal axis shows the momentum, the vertical axis shows the solid angle of the spectrometer acceptance. The solid line shows the solid angle of the acceptance of the E143 4.5° spectrometer. We indicate the acceptance of SLAC 20 GeV/c spectrometer by the half-dashed rectangle in contrast to the E143 spectrometer.

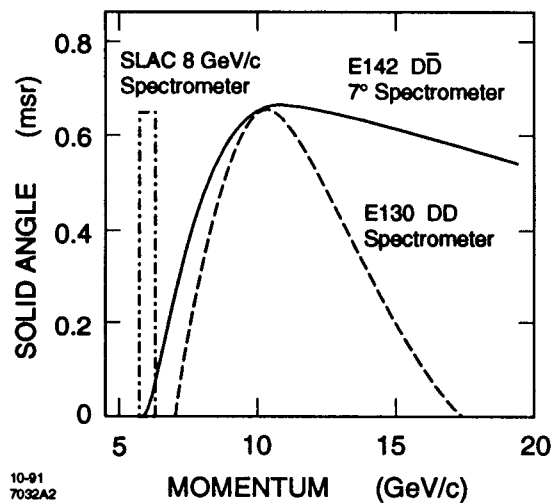


Figure 3.20: Momentum acceptance of the 7° spectrometer: the horizontal and vertical axes indicate the momentum and the solid angle of the spectrometer acceptance respectively. The solid line shows the solid angle of the acceptance of the E143 7° spectrometer. We indicate the acceptance of the E130 spectrometer and the SLAC 8 GeV/c spectrometer by the dashed line and the half-dashed rectangle respectively in contrast to the E143 spectrometer.

A large photon background from the bremsstrahlung, pion decays etc. were expected at the small scattering angles. The spectrometer suppressed the photon background

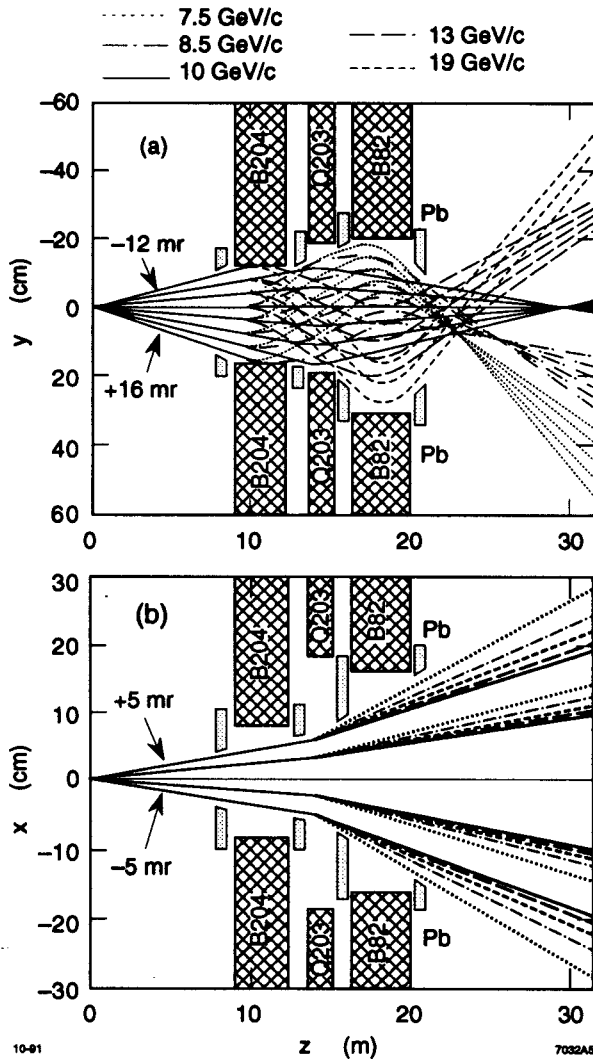


Figure 3.21: Electron trace on the 4.5° spectrometer: (a) is on the bending plane, and (b) is on the horizontal plane. The traces are drawn for various momenta from 7.5 GeV/c to 19 GeV/c. Note that the figure's geometry is distorted so that the trace of a 10 GeV/c electron at the center of the acceptance appears as a straight line.

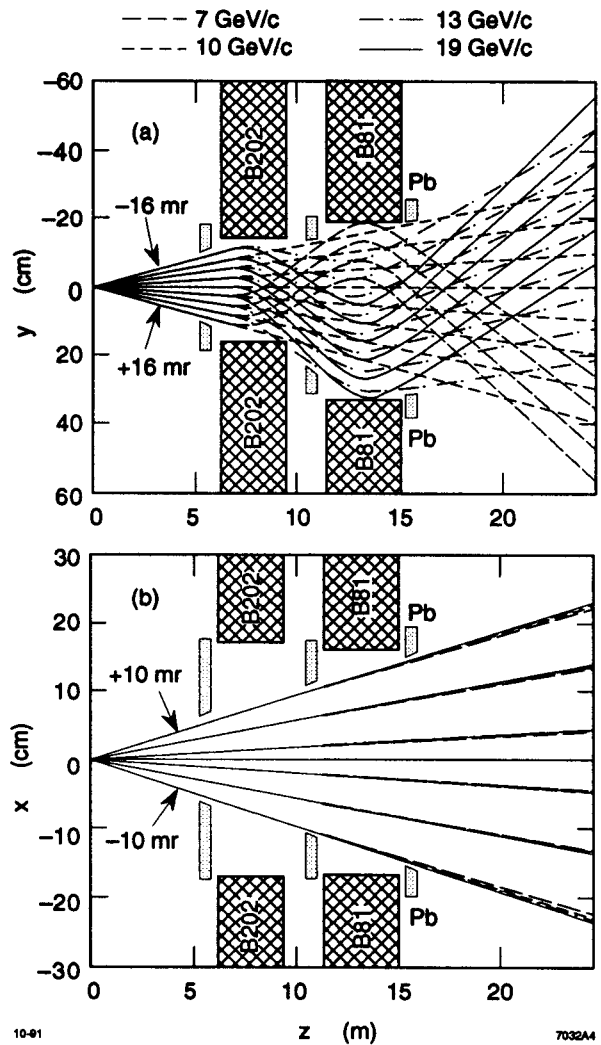


Figure 3.22: Electron trace in the 7° spectrometer: (a) is on the bending plane, and (b) is on the horizontal plane. The traces are drawn for various momenta from 7 GeV/c to 19 GeV/c. Note that the figure's geometry is distorted so that the trace of a 10 GeV/c electron at the center of the acceptance appears as a straight line.

with the two bounce system [40]. In this system, the magnets and the collimators were located such that the photon must hit those at least twice to reach the spectrometer acceptance.

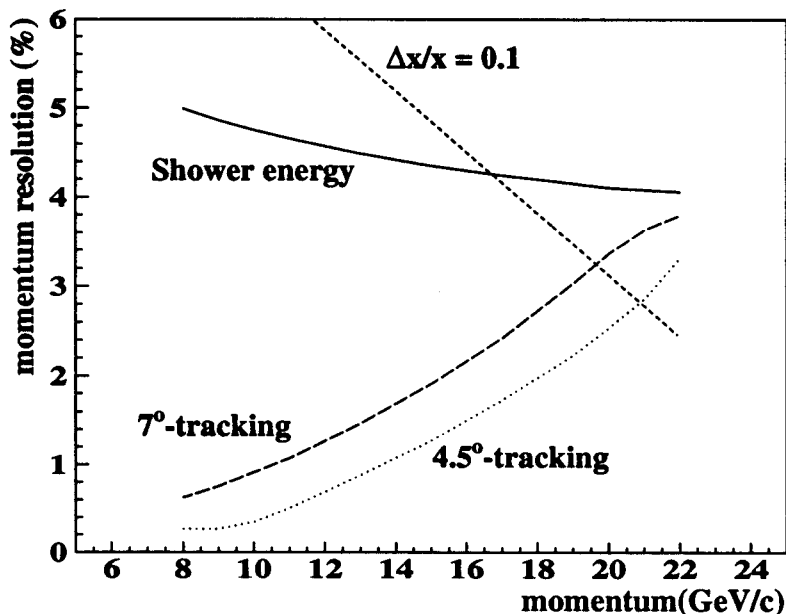


Figure 3.23: The dotted and dashed lines show the fractional momentum resolution for the 4.5° and 7° spectrometers respectively. The solid line shows the momentum resolution by the energy measurement with the lead glass shower counter. The small dashed line indicates the resolution corresponding to 10% error of Bjorken x .

Figures 3.21 and 3.22 show the ray-traces for the 4.5° and 7° spectrometers. Note that the figure's geometry is distorted so that the trace of a 10 GeV/c electron at the center of the acceptance appears as a straight line. In this configuration, we set the magnet layout to measure particle momenta from the trajectory gradients with largest possible acceptance. The momentum resolution of this configuration is worse than that for the same bending configuration, but it is acceptable for the experiment. Figure 3.23 shows the expected momentum resolution for each spectrometer and the momentum resolution coming from the requirement of $\Delta x/x$. The small dashed line in Figure 3.23 shows the momentum resolution to this requirement. The momentum resolutions of the 4.5° and 7°

spectrometers by the tracking shown by the dotted and dashes lines in this figure satisfied the requirement except in the high momentum region. It may be critical to the binning for the data in the high x region and will be studied in Section 5.6.3.

The several detectors were located after the bending magnets to detect electron tracks as shown in Figure 3.18. The detector systems are identical for both spectrometers composed of two threshold Čerenkov counters, seven hodoscope planes, a lead glass shower counter, and two scintillation trigger counters which will be explain in the following sections.

3.5.1 Čerenkov counter

Two threshold type Čerenkov counters were set in each spectrometer to identify electron tracks. Because electrons and pions give different momentum thresholds for emission of the Čerenkov light, we can identify the incident particle by measuring the Čerenkov light in the momentum region above the threshold. The signals obtained from the Čerenkov counter was used as one of the online trigger signals.

Čerenkov light is emitted when a charged particle passes through a medium faster than the light speed in the medium. The Čerenkov light is emitted in a cone of angle θ which is given by

$$\cos \theta = \frac{1}{n\beta}, \quad (3.11)$$

where, n is the refractive index of the medium, β is the relativistic β function. If $1/n\beta$ is larger than 1, the Čerenkov photon is not emitted. Defining that c' is the light speed in the medium and v is the speed of the particle, the Equation (3.11) is rewritten by

$$\cos \theta = \frac{c'}{v}, \quad (3.12)$$

From Equation (3.12), the Čerenkov light is often understood in the analogy of the shock wave emitted by the object moving with the ultrasonic speed.

Since the β of the high energy electron with a few GeV/c momentum is extremely close to 1.0, the high energy electron in a medium always emits the Čerenkov light to

the direction of angle, $\arccos(1/n)$, from the track. In order to implement the electron-pion separation, we have to choose a medium which gives $n\beta > 1.0$ for electrons and $n\beta < 1.0$ for pions in the experimental momentum region. If we want the separation up to 13 GeV/c of the momentum, the refractive index of the medium, n has to be less than 1.000058 because 13 GeV/c pion has $\beta = 0.9999424$. In such a medium, only the electron emits the Čerenkov light for the momentum lower than the threshold, 13 GeV/c.

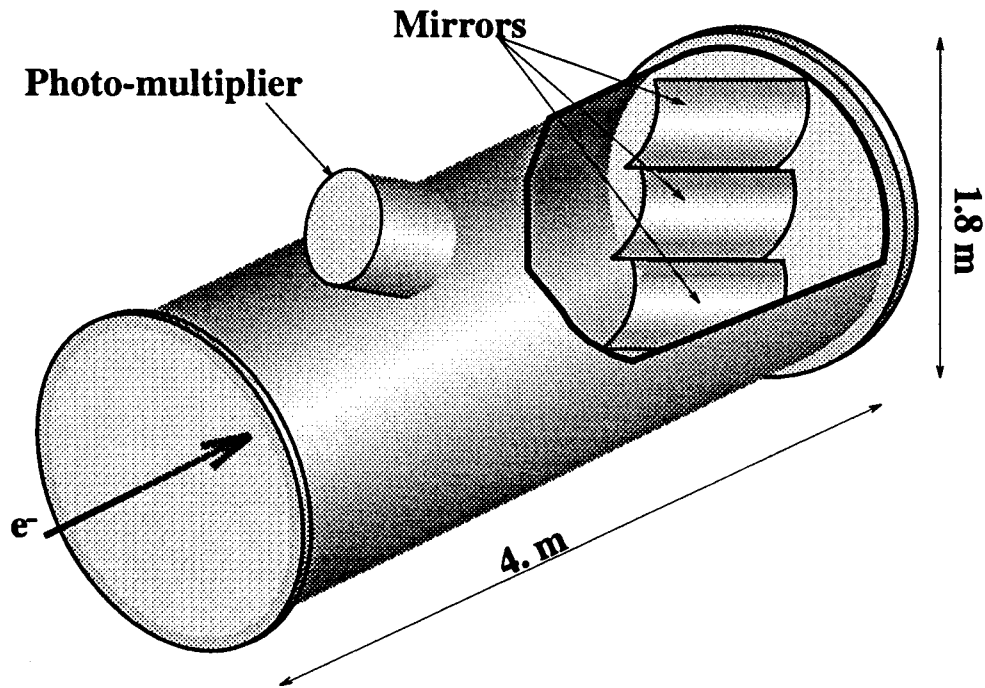


Figure 3.24: Schematic view of Čerenkov counter C2. The cylindrical tank was filled with depressured N_2 gas. Čerenkov photon emitted by the incident electron tracks were reflected by three mirrors and focused on the photo-tube.

The two Čerenkov counters are made of aluminum cylinders placed along the spectrometer axis. The dimensions of the cylinders are 400 cm in length by $\phi 160$ cm for the long counter (Čerenkov2, C2), 200 cm by $\phi 118$ cm for the short counter (Čerenkov1, C1). To minimize δ -ray production and multiple scattering, the aluminum window of 1 mm thickness was used.

We used N_2 gas as the medium. Since the N_2 gas produces scintillation light as

well as Čerenkov light for charged particles, pions below the Čerenkov threshold produce light. However, the N_2 gas has a good transparency at UV region, down to 150 nm wave length, and with use of the wave-length shifter, we improved the S/N ratio for Čerenkov light and the detection efficiency for electrons.

The Mirrors were placed at the end of the cylinder to collect Čerenkov photons to the photo-tubes. C2 had 3 mirrors which cover an area of 65 cm by 115 cm. C1 had 2 mirrors which cover areas of 40 cm by 51 cm and 38 cm by 51 cm for the 4.5° and 7° spectrometers respectively. All mirror surfaces were coated with aluminum and MgF_2 to optimize the mirror reflectivity. We obtained 90% of the reflectivity for 200 nm light. These mirrors were aligned properly by survey measurements using a solid state laser together with a simulation [41].

We used photo-tubes, Hamamatsu R1584-01 with UV glass window which have the large diameter and high quantum efficiency. The surfaces of the photo-tubes were coated with wave length shifter of 2430 nm thickness of para-terphenyl and overlaid with 25 nm thickness of MgF_2 to protect the wave length shifter against evaporation and aging.

The refractive index for a given gas pressure is given by using Lorenz-Lorentz relation [41],

$$\frac{n(\lambda)^2 - 1}{n(\lambda)^2 + 1} = K(\lambda)\rho, \quad (3.13)$$

where $n(\lambda)$ is the refractive index at wave length λ , ρ is the density of the gas, and K is a constant, $0.163cm^3/g$ for N_2 . The pion thresholds of the Čerenkov counters were set at 13 GeV for C2, and 9 GeV for C1. These pion thresholds correspond to N_2 pressures of 240 mmHg and 500 mmHg for the C2 and C1 respectively. Coincidence of these short and long Čerenkov counters selected electron tracks and rejected pion tracks cleanly because only a few % of pion emit scintillation light. The purity of the electron sample was estimated to be more than 99% from the study for the experimental data.

The number of photons by the Čerenkov emission is expected by the following formula [42],

$$N = 2\pi\alpha L \sin^2 \theta \int_{\lambda_1}^{\lambda_2} \frac{1}{\lambda^2} d\lambda, \quad (3.14)$$

where α is the fine structure constant, L is the length of the medium, θ is the Čerenkov angle, and λ_1 and λ_2 are the lower and upper limits for the sensitive region in the wave length. If we assume the sensitive region of the PMT between 150 nm and 550 nm in the wave length, the refractive index n is 1.000058, the length of the counter, L , is 4 m, the number of the Čerenkov photon is expected to be 106. Actually, the number is reduced due to the transparency of the N_2 gas, the mirror reflectivity, and quantum efficiency of the photo-tube, etc. Including these reduction factors, the number of the Čerenkov photon was estimated to be 8.2 ± 0.5 by a Monte-Carlo simulation [41].

Detection efficiency

The detection efficiencies of the Čerenkov counters were studied under an assumptions that the probability of detecting photo-electrons (Čerenkov ADC count) is Poisson distribution [41]. Table 3.1 shows the efficiencies defined to be the probability to produce one or more photons which was evaluated from the Čerenkov ADC spectrum. All of these

	4.5°.		7°.	
	C1	C2	C1	C2
Mean ADC	165.6 ± 56.6	127.1 ± 42.3	158.8 ± 54.2	137.2 ± 55.5
N_{pe}	8.6 ± 0.5	9.0 ± 0.5	8.6 ± 0.5	6.1 ± 0.5
Eff.	$99.98 \pm < 0.01$	$99.99 \pm < 0.01$	$99.98 \pm < 0.01$	$99.78 \pm < 0.11$

Table 3.1: Čerenkov counter efficiency from ADC spectra.

counters have high detection efficiencies of more than 99%. The numbers of Čerenkov photons N_{pe} were evaluated from the ADC spectra close to the value of 8.2 ± 0.5 obtained from the Monte-Carlo simulation.

3.5.2 Hodoscope

There were seven plane hodoscopes on each spectrometer. The purpose of hodoscope systems was to reconstruct charged particle tracks. A track is used to determine the

particle's momentum from the reverse matrix of the spectrometer magnet.

A hodoscope was assembled with finger scintillation counters which were placed parallel to each other so that hits on the finger of the hodoscope gave the information on the track position in the transverse direction with respect to the finger axis. Every finger overlapped its neighbor finger by $2/3$ of its width as shown in Figure 3.25. This configuration improved the effective spatial resolution of the hodoscope allowing a time coincidence measurement between fingers overlap.

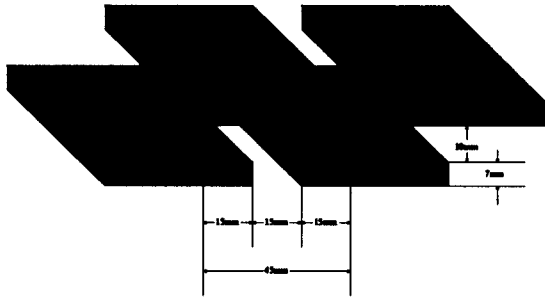


Figure 3.25: Finger overlap: The dimension is of H1U hodoscope.

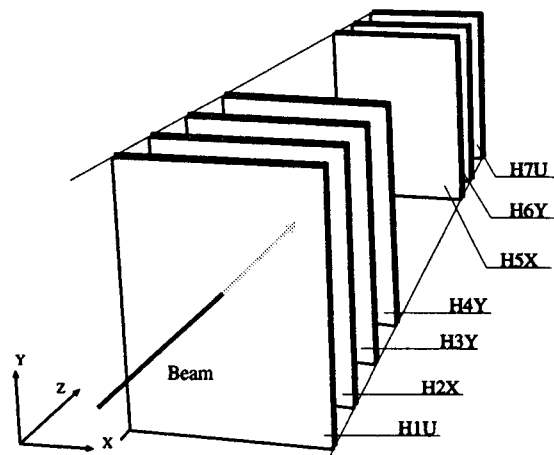


Figure 3.26: Hodoscopes schematic view: the first set was composed by four hodoscopes which determined position of tracks in u , x , y , y axes. The second set was composed by three planes which determined position in x , y , u axes. C2 counter was located between H4Y and H5X planes.

The seven hodoscopes were located along the spectrometer axis in order of H1U, H2X, H3Y, H4Y, H5X, H6Y, and H7U as shown in Figure 3.26, where X, Y, and U correspond to the x , y , and diagonal measurement of the track position respectively. The planes 1 through 4 were between Čerenkov 1 and Čerenkov 2, and planes 5 through 7 were between Čerenkov 2 and the shower counter.

Table 3.2 and 3.3 show the dimensions of the finger scintillators of the hodoscopes

in the 4.5° and 7° spectrometers. Table 3.4 lists the finger lengths for the U hodoscope. H2X, H3Y, H5X, and H6Y had a higher spatial resolution than others and therefore these hodoscopes dominated the momentum resolution of the spectrometer. H1U, H4Y, and H7U had a roll to improve the signal purity and reliability and to remove any accidental double hit. H2X, H3Y, H5X, and H6Y were built by Syracuse group originally for E142 which investigated deep inelastic scattering of the electron with gas ^3He target [23]. H4Y was built by SLAC, and H7U by French group for E142. H1U was built by TOHOKU group for E143.

Plane	width(mm)	length(mm)	thickness(mm)	number
H1U	45	Various	6.2	25
H2X	20	590	6.2	34
H3Y	30	430	6.2	31
H4Y	47.6	355.6	6.2	20
H5X	30	1070	6.2	27
H6Y	30	510	6.2	55
H7U	75	Various	10	21
Total finger number				213

Table 3.2: Hodoscope dimensions on 4.5° spectrometer.

Plane	width(mm)	length(mm)	thickness(mm)	number
H1U	45	Various	6.2	25
H2X	30	690	6.2	23
H3Y	30	430	6.2	36
H4Y	47.6	482.6	6.2	20
H5X	30	1070	6.2	27
H6Y	30	510	6.2	55
H7U	75	Various	10	21
Total finger number				207

Table 3.3: Hodoscope dimensions 7° spectrometer

H1U		H7U	
length(mm)	number	length(mm)	number
200	2	200	2
260	2	300	2
320	2	400	2
380	2	500	2
440	2	600	2
500	2	700	2
560	2	760	2
620	2	820	7
680	2		
720	1		
740	6		
Total	25	Total	21

Table 3.4: U-hodoscope dimensions

High voltage modules were located in the counting house located upstairs of ESA. We stretched more than 120 SHV coaxial cables from the counting house into ESA to supply high voltages for these photo-tubes. To reduce the number of the SHV cables from the counting house to ESA, we used high voltage splitters in the spectrometer. One long SHV cables provided high voltage for up to four photo-tubes. Figure 3.27 shows the circuit of the splitter; where the voltage was determined by a ratio of the variable resistance to the inner resistance of the photo-tube.

A photo-tube detected a signal from a single finger. Photo-tubes which were used for all hodoscopes except for the H1U plane are specified in Reference [23]. The photo-tubes for the H1U plane were H3167 by Hamamatsu. This photo-tube has a $\frac{3}{4}$ inch diameter, a length of 103 mm, a sensitive region of 300 - 650 nm in the wave length, a gain of 2.0×10^6 and a rise time of 1.8 ns at -1.5 kV. The upper limit for the high voltage is -1.9 kV. The scintillator used for the H1U plane is SCSN38 by Kuray which has a density of 1.05g/cm^3 and a refractive index of 1.59. The scintillation light wave length

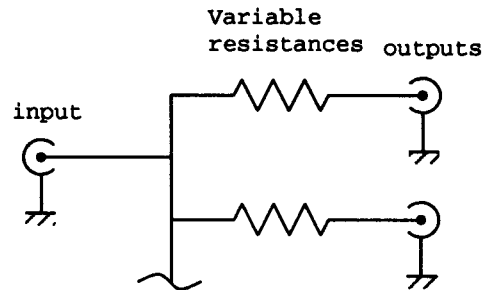


Figure 3.27: Hodoscope High voltage splitter. Only two of the four outputs are drawn.

distributes from 400 beyond 500 nm.

The output signals of the photo-tube was processed by a LeCroy 4413 discriminator mounted in two CAMAC crates in each spectrometer-hut. The threshold was -30 mV for H1U and -50 mV for the others. Output ECL signals with 20 ns width were sent to the counting house by twisted pair cables. Each signal went to a LeCroy 2277 TDC through a gate-card which ignored any signal when the input gate was closed. The gate was called as Hod-gate made by trigger logic which fired for passing charged particles. The LeCroy 2277 TDC recorded up to 16 signals for each channel. The resolution of the TDC is 1 ns and the TDC buffer is 16 bit for each signal. Therefore the dynamic range is $65\mu\text{s}$. Because the spill width was about $2.2\mu\text{s}$ in length, this dynamic range is enough to record the hodoscope hits for a spill.

timing calibration

The timing at each hodoscope was obtained by comparing the measuring timing with the expected timing of the reconstructed track passing through the hodoscope. Where the track reconstruction was performed by using information from the hodoscopes, the Čerenkov counters, and the shower counter. The procedure of the track reconstruction will be described in Section 4.1.3.

We first take time difference between the measured timing and the expected track

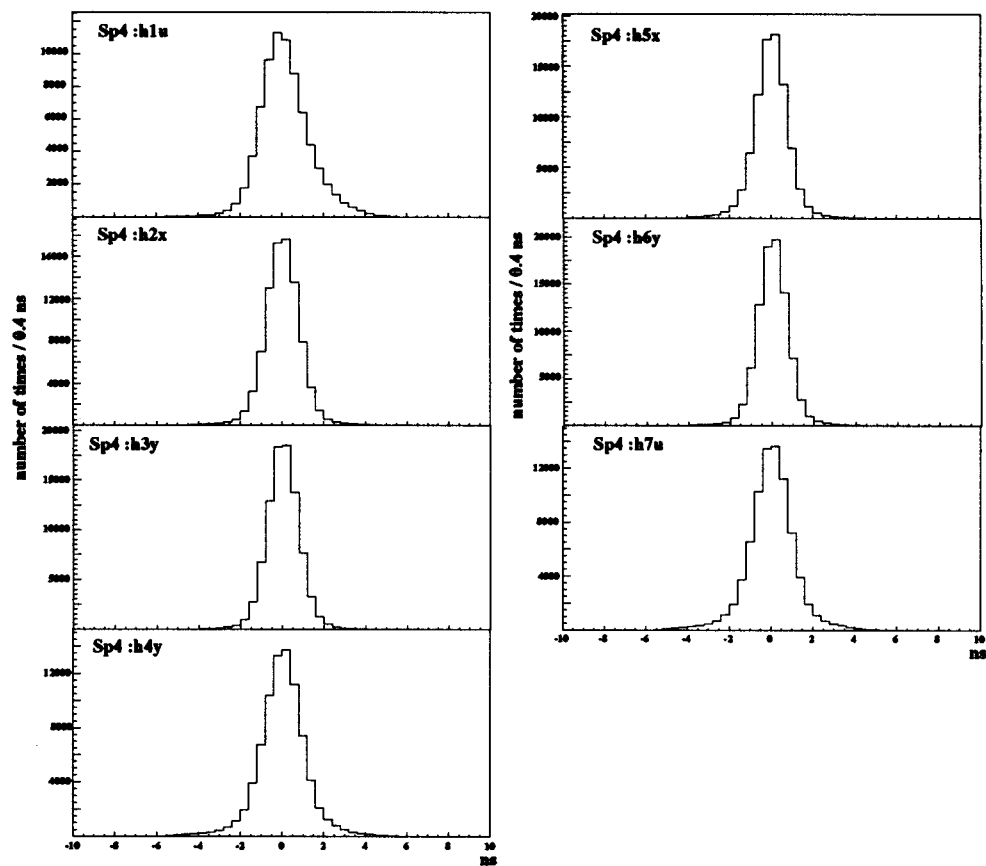


Figure 3.28: The spectra of Δt of the hodoscopes for the 4.5° spectrometer after the calibration. The time difference between the hodoscope hits and the reconstructed tracks are plotted. The results from fingers are accumulated together about a hodoscope plane.

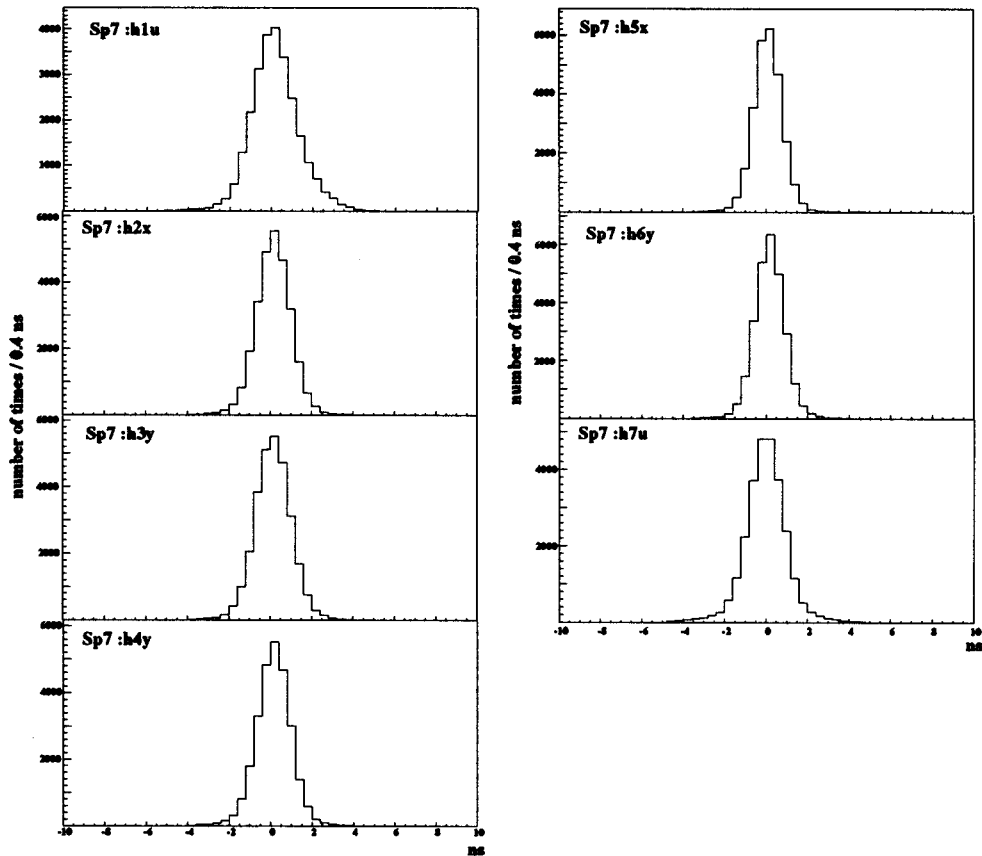


Figure 3.29: The spectra of the Δt for the 7° spectrometer after the calibration. The time difference between the hodoscope hits and the tracks are plotted. Results from fingers are accumulated together about a hodoscope plane.

timing at a given hodoscope as follows,

$$\Delta t = (t_m - t_d - t_p) - t_{rec} \quad (3.15)$$

where the t_m is the TDC count of the hodoscope fingers, the t_d is the propagation delay of scintillation light in the hodoscope finger, the t_p is the TDC pedestal including the time delay due to the electric line, and the t_{rec} is the timing of the reconstructed track passing the finger.

The propagation delay in the scintillator was calculated from the hit position and the propagation speed in the scintillator. The hit position on a finger was determined taking a time coincidence with another finger crossing to the finger. The propagation speed for each finger was calculated from E142 run as nearly equal to 15 cm/ns [23].

We tuned the Δt spectrum to center at 0 by adjusting the TDC pedestal t_p with iteration procedure. Figures 3.28 and 3.29 show the spectra of the Δt for the 4.5° and 7° spectrometers after several iterations. We plotted only the hits used for reconstruction of tracks. All hodoscopes were well calibrated resulting the sharp peaks at zero. Table 3.5 shows the time resolution of the hodoscopes evaluated from these plots. The time resolution of about 1 ns was obtained for all hodoscopes.

Plane	time resolution (ns) for 4.5° sp.	time resolution (ns) for 7° sp.
H1U	1.18	1.14
H2X	0.90	0.74
H3Y	0.72	0.93
H4Y	0.88	0.89
H5X	0.77	0.75
H6Y	0.69	0.77
H7U	1.05	1.04

Table 3.5: Time resolution of the hodoscopes

Hodoscope efficiency

We calculated the detection efficiency of the hodoscope defined by the probability to make hits for passing tracks.

The track was reconstructed by a fitting as described in Section 4.1.3. To improve the reliability for the track sample, we required,

1. Both Čerenkov counters have hits in the trigger,
2. Six planes of the seven hodoscopes have hits,
3. Spatial matching between the shower cluster and the track within 20 mm,
4. The track was reconstructed within 10 mm from the target center.

To ignore the effect of the finite spatial resolution of the tracking giving the improper finger address, we accepted the event when any finger within the width plus 50 mm from the track position has a hit.

Figure 3.30 and 3.31 show the inefficiency for the hodoscopes in the 4.5° and 7° spectrometers respectively for run 1334. Horizontal axis shows the hodoscope plane index from 1 to 7. Vertical axis shows the inefficiency of each plane in logarithm scale.

3.5.3 Shower counter

The shower counter was placed at the end of the spectrometer to measure energy of the electron. The shower counter is a multi-segment electro-magnetic calorimeter built with lead glasses. High energy electrons incident to the lead glass induce an electro-magnetic shower due to bremsstrahlung and pair creation and produce a large number of electrons, positrons, and gammas. These electrons and positrons lose their energy ionizing atoms and emitting Čerenkov light in the lead glass. The total amount of the Čerenkov light is proportional to the total path length of the electrons and positrons in the shower counter which is proportional to the initial energy of the electron [42], thus the shower counter

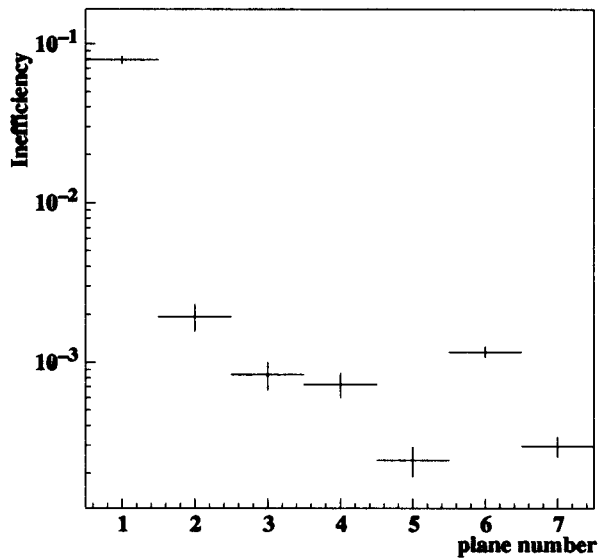


Figure 3.30: Plane inefficiency for run 1334 in 4.5° spectrometer

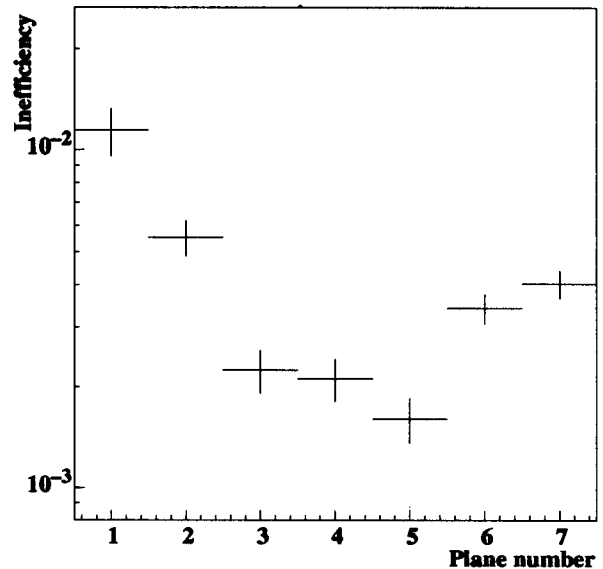


Figure 3.31: Plane inefficiency for run 1334 in 7° spectrometer

measures the energy of the electron by collecting the Čerenkov light in the lead glasses with photo-tubes.

The counter was built with 200 lead glass blocks of 62 · 62 · 750mm as shown in Figure 3.32. The radiation length of the lead glass is 3.7 cm. Because the 750 mm lead glass corresponds to 24 radiation length, electrons lose more than 99.9% of the energy in the lead glass.

The output from each photo-tube was divided into five lines as shown in Figure 3.33. These four lines went to ADC via 200 ns delay line. Each ADC channel was able to collect a datum once in a spill of 2.2 μ s because we read and initialized the ADC buffer after every spill. Thus, we were able to collect the data up to four times in a spill. Each four of the fifth line were summed and divided into two lines. One of them was sent to TDC via a discriminator to measure the timing of the signal. Another line was used to make the signal from the whole counter. This signal from the whole counter made one of online electron trigger signal as will be mentioned later.

There were three purposes for the shower counter; (1)providing online electron trigger signal, (2)measuring the electron energy, and (3)particle identification using a

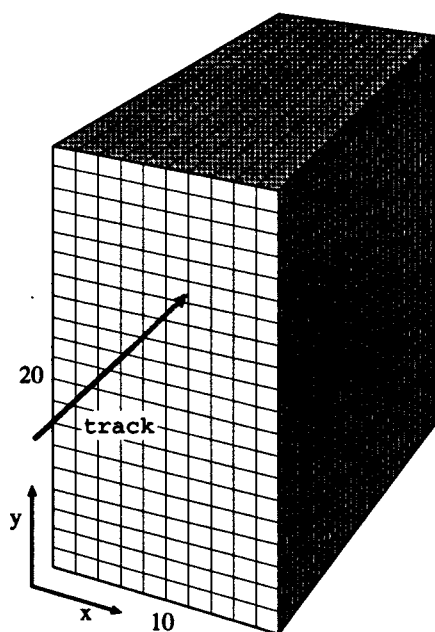


Figure 3.32: 200 of lead glass blocks were composed in fly-eye configuration. Photo-tubes which were mounted behind each lead glass detected the signal from the lead glass.

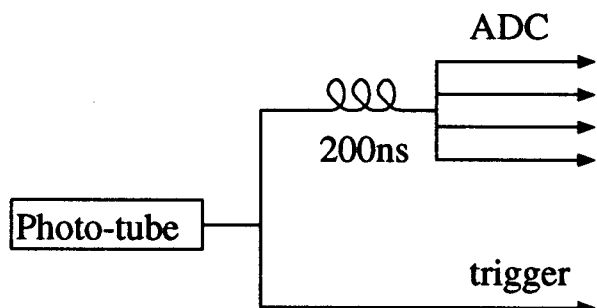


Figure 3.33: An output of each photo-tube was divided into five lines. One of them was used for online triggering and TDC. Other lines went to ADC for calorimetry via 200 ns delay line.

neural network algorithm. The calibration to calculate the electron energy deposit from the shower ADC is important for measuring the electron energy and will be described in the following section.

Shower counter calibration

As mentioned in the previous section, the light collected by photo-tubes is proportional to the energy deposited by electrons. In order to calculate the electron energy, we need to find the proportional constants between ADC counts and energy deposited by electrons. Energy deposit in each lead glass block can be calculated with the constant as follows,

$$E_i^j = F_i^j \times ADC_i^j \quad (i = 1, 200 : \quad j = 1, 4), \quad (3.16)$$

where E_i^j is the energy deposited on the i -th block of the j -th trigger in a spill, F_i^j is the proportional constant, and ADC_i^j is the ADC counts. There were 200 blocks, and 4 ADC channels for each block making a total of 800 constants for each shower counter.

The radiation length of the lead glass is enough so the electron loses all of its energy in it. Therefore, the energy deposited in the lead glass by an electron is equal to the tracking momentum giving $E/P=1$ which we use to obtain the calibration constants. Total energy deposited by an electron was found by clustering the blocks with energy deposit using Cellular Automata [43] which will be mentioned in Section 4.1.2.

The sample of clusters for doing the calibration required low pion contamination since pions produce a E/P of less than 1. Pions lose only a fraction of its energy in the lead glass. To reject any pion and junk cluster from the sample, we required the following conditions,

1. A track must be associated to the cluster within 10 ns in time and 50 mm in both x and y.
2. The energy deposited in the central block must be higher than 5 GeV.
3. The fraction of cluster energy deposited in the central block must be higher than 0.65.

4. Classified as an electron by the neural network.

Lead glass blocks are classified as shown in Figure 3.34. The first category is “non-edge block” which means not on the edge of lead glass array. The second is “edge-block” which has only three adjacent blocks. Last one is “corner block” which has only two adjacent blocks. Sometime we call a cluster whose center is on a non-edge (edge, corner) block as a non-edge (edge, corner) cluster. The calibration was done with different ways for these three classes of blocks.

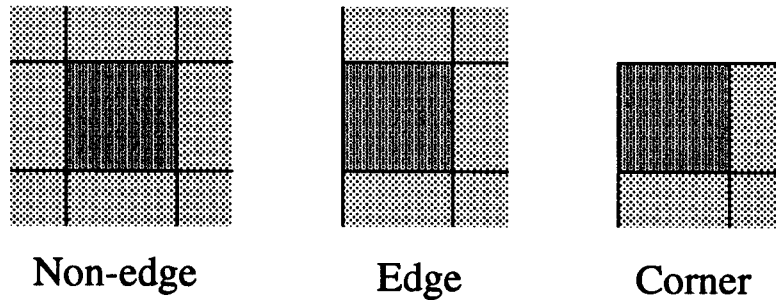


Figure 3.34: Classification for the shower block (cluster)

The electron energy is mostly deposited in the center block and spread over the surrounding eight blocks [44]. Hence, we required that the total energy deposited in these nine blocks gives $E/P = 1$ for the non-edge cluster. The constant for the block was corrected after every iteration by the averaged E/P as,

$$(F_i^j)' = \frac{F_i^j}{\langle E/P \rangle_i^j}, \quad (3.17)$$

where F_i^j is the constant for the i -th block and j -th ADC channel, $\langle E/P \rangle_i^j$ is an averaged E/P which was taken at this iteration, $(F_i^j)'$ is a new constant.

For the edge clusters, we can not require E/P to be 1 because a part of electron energy escapes out of the counter. However, the edge block and its adjacent five blocks are supposed to occupy a certain fraction of the energy deposit with respect to the total energy of electron. This fraction was estimated from the well calibrated non-edge block

data as 0.92 [44]. Hence, the constant for the edge block was calibrated by

$$(F_i^j)' = \frac{0.92F_i^j}{\langle E_{edge6}/P \rangle_i^j}, \quad (3.18)$$

where the $\langle E_{edge6}/P \rangle_i^j$ is defined similar to that for the non-edge cluster but the total energy deposited of the six blocks.

The edge block was calibrated also with a energy fraction to the total energy deposit when an electron passed through the adjacent block. It was estimated to be 6.5% [44] and we corrected the constant by

$$(F_i^j)' = \frac{0.065F_i^j}{\langle E_{edge}/P \rangle_i^j}. \quad (3.19)$$

In these two correction method for the edge block, we selected which gave a smaller correction than the other to prevent the divergence of the constant due to the statistical fluctuation.

The corner block was calibrated using a energy deposited in the corner block by an electron passing through the inside diagonal block. The ratio of the energy deposit to the electron momentum, E_{corner}/P was studied to be 2% [44]. We corrected the constant by

$$(F_i^j)' = \frac{0.02F_i^j}{\langle E_{corner}/P \rangle_i^j}. \quad (3.20)$$

Table 3.6 shows the results of the shower calibration. Each run corresponds to a typical run of a run block which was a bunch of runs classified due to some hardware changes.

run #	$\langle E/P \rangle 4.5^\circ$	$\langle E/P \rangle 7^\circ$
1560	$1.000 \pm .054$	$1.000 \pm .057$
2750	$1.000 \pm .054$	$1.001 \pm .059$
2926	$1.000 \pm .055$	$1.000 \pm .060$

Table 3.6: E/P after the calibration. The error is the standard deviation of the distribution of E/P.

3.5.4 Trigger counter

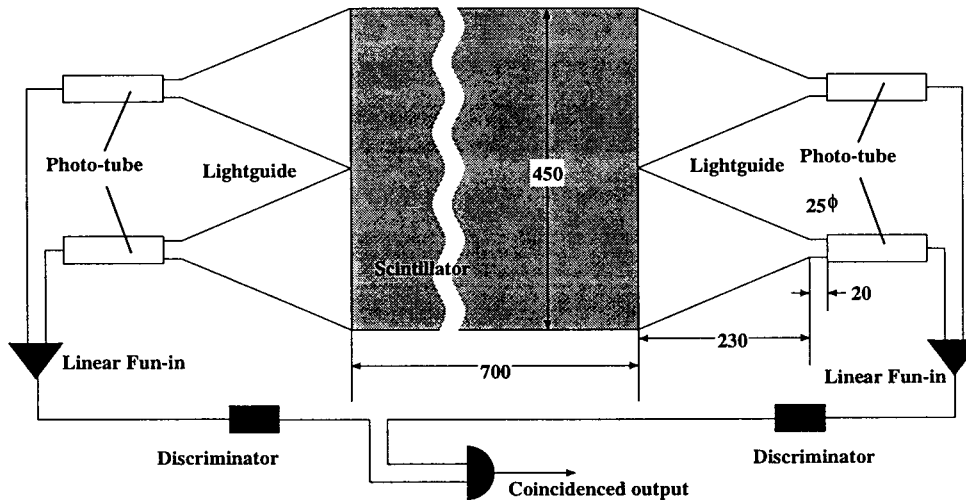


Figure 3.35: Front trigger counter: Fish-tale acrylic light guides introduced emitted photons into the photo-tubes. Two outputs on a side was combined linearly by a linear Fan-in. Then these signals are discriminated by 30 mV threshold. The coincidence of the outputs was sent to the trigger electronics. Outputs of the Fan-ins were also recorded by TDC independently.

E143 spectrometer had two scintillator trigger counters. The front trigger counter was set between Čerenkov counter 1 and Hodoscope H1U plane. The dimension of the counter was 700 · 450 · 6 mm as shown in Figure 3.35. The scintillator was made of Kuray SCSN38 with higher photon emission than for Bicron [45]. We used the photo-tube Hamamatsu H3690 which has a dimension of $\phi 1\frac{1}{8}$ inch \times 113 mm, a sensitive region of 300-650 nm in the wave length, a current gain of 5.3×10^6 and a rise time of 2.0 ns at -1.5 kV. The limit of the high voltage is -1.9 kV. Figure 3.35 shows the assembly of the photo-tube and the scintillator for the front trigger counter. These photo-tubes were connected through light-guides to the scintillator.

The rear trigger counter was placed between Čerenkov counter 2 and Hodoscope H5X plane. The scintillator was Kuray SCSN38 with the dimension of 1100 · 550 · 13 mm. Signals were read out by two photo-tubes through the twisted acrylic light guides

attached at each end of the scintillator. The photo-tubes were Hamamatsu H1161 of $\phi 60$ mm diameter with the sensitive wavelength from 300 to 650(nm). The current gain is 5.3×10^6 and the rise time is 2.6 ns at -2.0 kV.

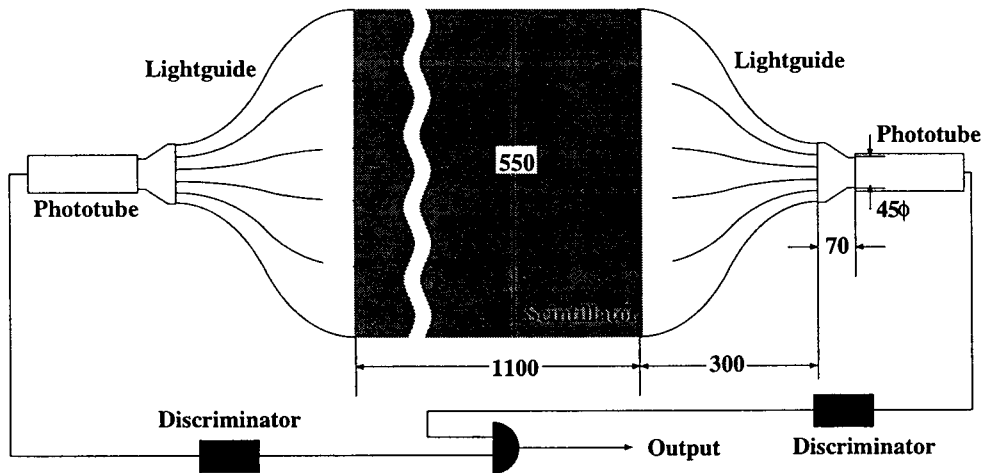


Figure 3.36: Rear trigger counter: The outputs from both sides were processed by a discriminator with 50 mV threshold. The coincidence of these signals was used as one of online trigger signal. Each outputs were recorded by TDC.

The coincidence of these front and rear scintillation trigger counters were used as an online trigger with a rate suppressed by a pre-scaler. The signal served as the hodoscope gate and the trigger for pions which will explained in Section 3.5.5.

Cosmic ray test

The time resolutions of the scintillation trigger counters were measured with the signal produced by cosmic-rays [46]. Figure 3.37 shows the location of the investigation. A coincidence of two scintillation counters, counter A and B, each having an area of $5 \cdot 5$ cm defined the timing and location of the passing of a cosmic-ray. The signals from the photo-tubes of both sides of the front trigger counter were processed by discriminators and a mean timer. The mean timer gives an averaged timing of two input signals by,

$$t_M = \frac{t_1 + t_2}{2} + t_{dl}, \quad (3.21)$$

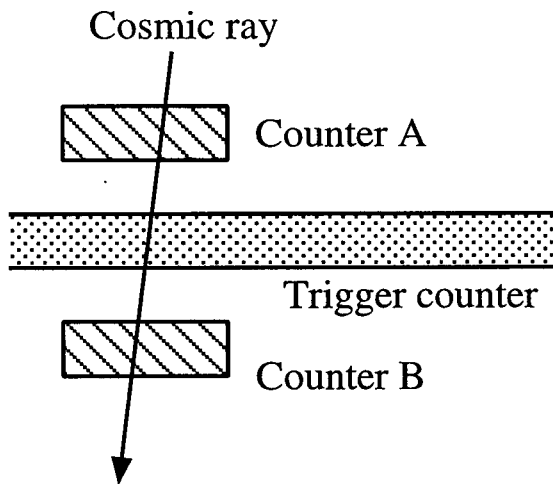


Figure 3.37: Setup of the time resolution measurement: Counter A and B are scintillation counters which have the dimension of $50 \cdot 50 \cdot 20\text{mm}$. The coincidence of these counters defined the passing of cosmic ray.

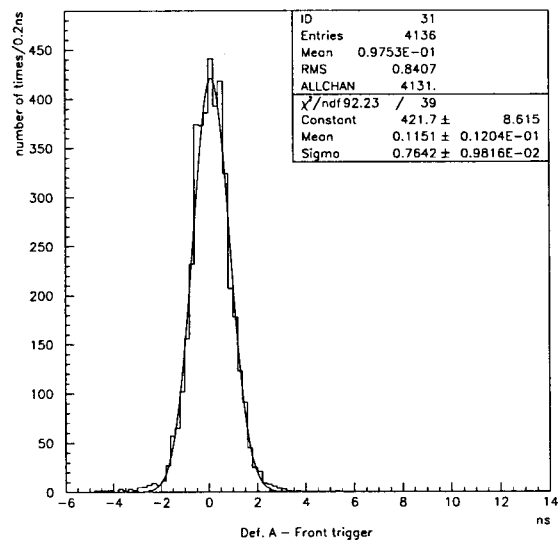


Figure 3.38: Time difference between counter A and the front trigger counter.

where t_M is the mean timer output, t_1 and t_2 are the timing of the inputs, and t_{dl} is the delay time of the circuit. We used the mean timer instead of the coincidence to compensate the timing shift due to the propagation of photons in the scintillator. The time differences of the three combinations among counter A, B, and the front trigger counter were recorded by TDC with 25 ps/channel. Dividing the area of the front trigger

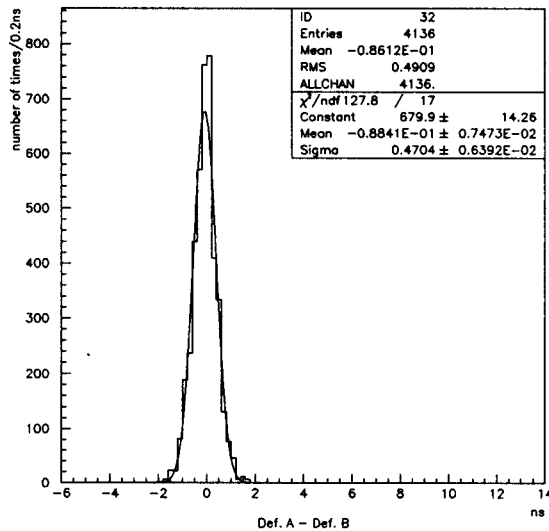


Figure 3.39: Time difference between counter A and counter B.

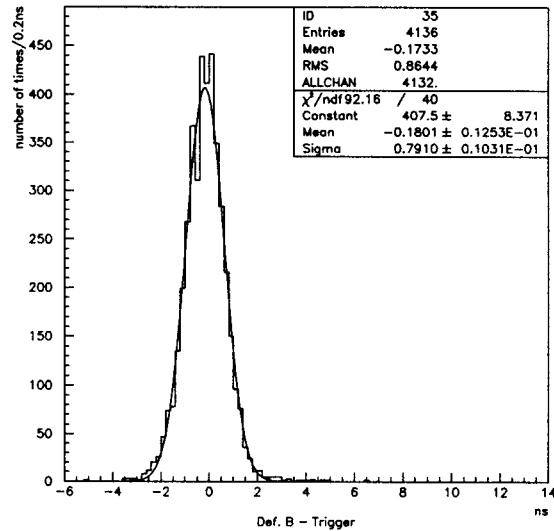


Figure 3.40: Time difference between counter B and the front trigger counter.

counter into three by three, we took the data at the divided nine points of the counter. Figure 3.38, 3.39, and 3.40 show the time differences. These histograms contain all of data which were taken at the nine points. The resolution of these distributions come from the intrinsic time resolutions of these individual counters. Thus, for example, the resolution in Figure 3.38, σ_d , can be written by

$$\sigma_d = \sqrt{\sigma_A^2 + \sigma_F^2}, \quad (3.22)$$

where σ_A and σ_F are the resolution of counter A and the front trigger counter respectively. Therefore, we calculated the intrinsic time resolutions for these three counters from these three distributions. The intrinsic time resolution of the front trigger counter was obtained to be 0.71 ns.

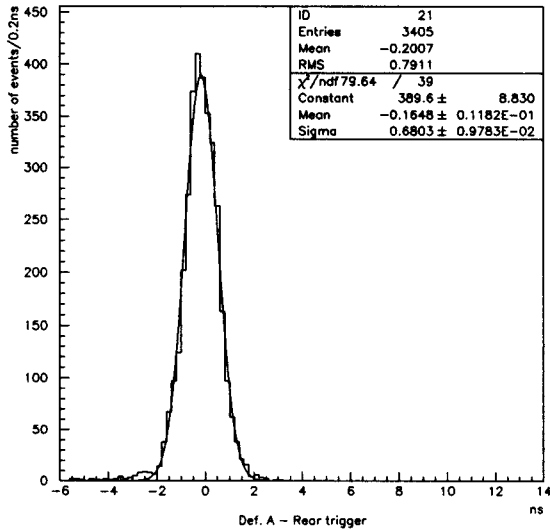


Figure 3.41: Time difference between counter A and the rear trigger counter

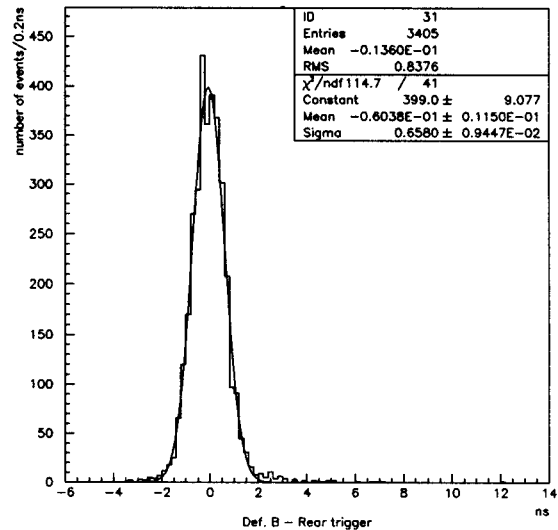


Figure 3.42: Time difference between counter B and the rear trigger counter.

Similarly, the resolution for the rear trigger counter was obtained from Figure 3.41 and 3.42 to be 0.56 ns.

3.5.5 Trigger electronics

E143 spectrometer system opened the gates for TDC and ADC whenever a trigger signal was generated. This trigger signal was generated independently in the 4.5° and 7° spectrometers. The number of the gate for the ADC and the hits for the TDC were limited up to four and sixteen, or less respectively in a spill. The number of electrons in a spill is typically one or less, on the contrary, the number of pions was higher than that for electrons. Thus, we imposed the following requirements for the trigger electronics for the efficient measurements of electrons and pions:

1. Open the ADC and TDC gate for all electrons,
2. Open the ADC and TDC gate in a fraction of times for pions to prevent the trigger burst by many pions.

Figure 3.43 shows the basic picture for the E143 trigger electronics. Basically, the passing

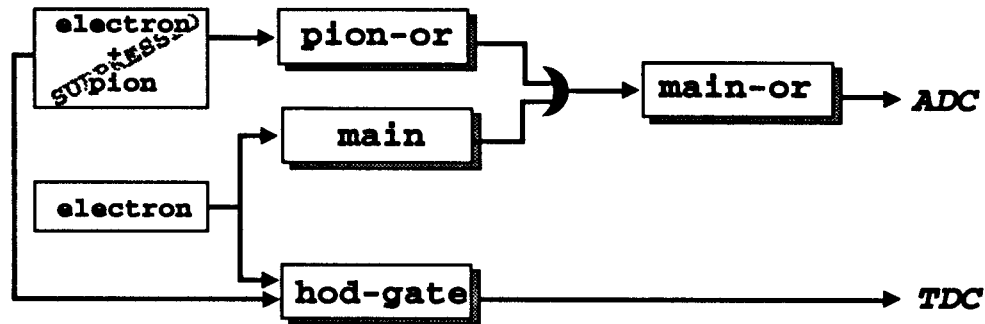


Figure 3.43: Basic idea of the E143 trigger logic: the main and pion-or triggers are generated when electrons and any charged particles pass through the spectrometer respectively. The “or” product of the main and pion-or triggers composes the main-or trigger which opens the ADC gate. The hod-gate trigger which opens the TDC gate is generated also when electrons and charged particles pass the spectrometer. The rate for the charged particles (not for electron) is suppressed by different factors for pion-or and hod-gate triggers.

of electrons and any charged particles are defined by the coincidence signal of the two Čerenkov counters and the two scintillator trigger counters respectively. The “or” product of the two coincidence signals composes the main-or trigger which opens the ADC gate and the hod-gate trigger which opens TDC gate. The difference of these trigger signals is the suppression factor for the coincidence signal for the scintillation trigger counters. This suppression is to prevent the trigger burst by many pions and the difference of the suppression factors is because of the acceptance of the number of signals of the ADC and TDC in a spill.

Figure 3.44 shows the logic of the main trigger and the other coincided signals in detail. S1 and S2 are the output signals from the front and rear trigger counters after processed through discriminators. HodSum is the logical sum of the output signals from all fingers of H2X hodoscope. The coincidence of S1, S2, and HSUM generated SciCoin. The rate of the signal was reduced by a pre-scaler with a factor N4 in order to prevent the trigger burst by many pion tracks. This pre-scale factor N4 was normally set to 4 for the 4.5° spectrometer and 1 for the 7° spectrometer.

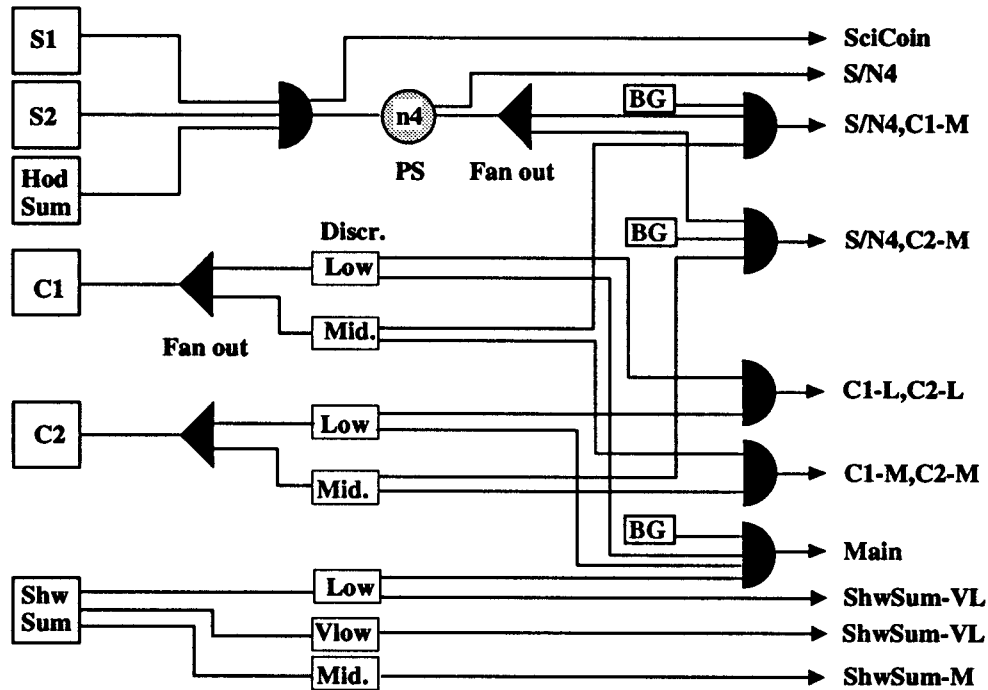


Figure 3.44: The logic of the main trigger and the other triggers are shown. S1 and S2 are signals from the front and rear trigger counters, HodSum is a sum of all outputs of the H2X hodoscope, C1 and C2 are outputs from the Čerenkov counters, ShwSum is a sum of outputs from the lead glass blocks, and BG is the beam gate opened whenever beam came into ESA. A black half circle is a coincidence and a gray circle is a pre-scaler to reduce the signal rate. The coincidence of the ShowSum, C1, C2, and BG composes the main trigger.

The Čerenkov counters are very important to identify electron tracks. The signals from these counters were processed through two discriminators with 30 mV and 50 mV thresholds. These signals were labeled as C1-L, C1-M for C1 and C2-L, C2-M for C2.

The shower counter provided four ADC and one trigger signal as shown in Figure 3.33. One of those outputs was used to make shower trigger signal. This trigger signal is the sum of signals from all 200 lead glasses and processed through discriminators with three threshold levels. The signals corresponding to these threshold level are denoted very low, low, and medium and labeled by ShwSum-VL, ShwSum-L, and ShwSum-M.

The main trigger was the coincidence of C1-L, C2-L, ShwSum-L, and beam gate which was open whenever beam came into ESA and sent from Linac Main Control Center (MCC). This main trigger provided information of the electron passing the counter for the online process. The rate of the main trigger was typically 1.5 for 4.5° spectrometer and 0.3 for 7° spectrometer per spill.

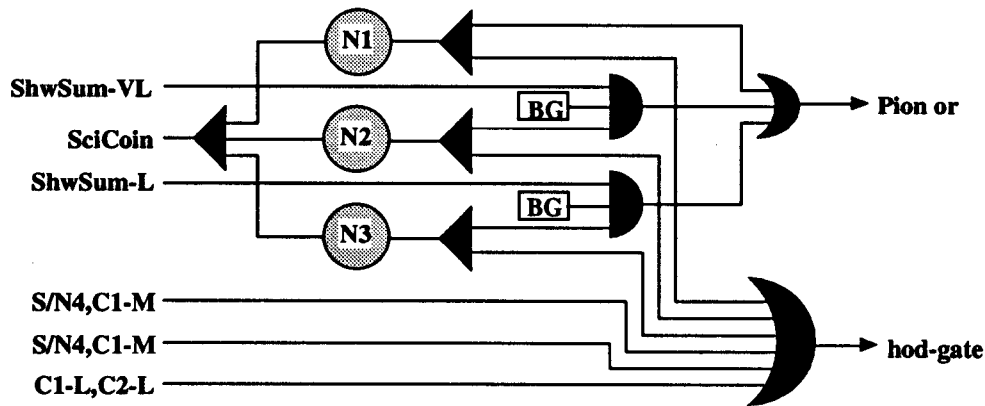


Figure 3.45: Logic of pion-or and hod-gate triggers is shown. The closed wedge-shape is the or logic. S/N4:C1-M, S/N4:C2-M, and C1-L:C2-L are given in Figure 3.44. The gray circles are the pre-scaler suppressing the signal rate.

Figure 3.45 shows the logic of the pion-or and the hod-gate triggers. The pion-or trigger was the trigger generated any charged particle including pion. These pre-scaler factors in the figure were set to 32 for 4.5° spectrometer and 8 for 7° spectrometer. Typically, the rate was 0.35/spill and 0.25/spill for 4.5° and 7° spectrometer respectively.

TDC recorded data for any hits of hodoscopes, shower counter, Čerenkov counters, and the other triggers when the hod-gate trigger was fired. Gate-card ignored ECL signals from the discriminator to TDC if the hod-gate was closed. The hod-gate was generated by or product of the SciCoin and the coincidence of the Čerenkov counters which is always enable to open the hod-gate for the electron.

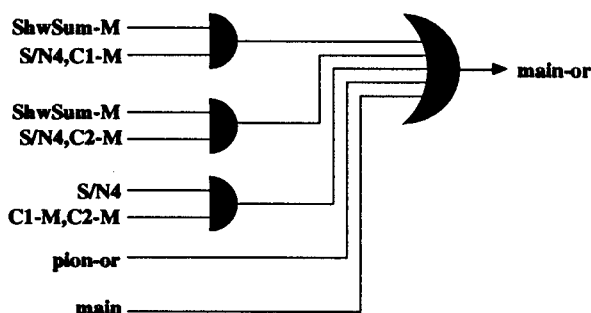


Figure 3.46: Logic of the main-or trigger which was generated by the main trigger which fired only for passing of electrons and the pion-or trigger which fired for the passing of charged particles. The main-or trigger opened the ADC gate for the shower counter and the Čerenkov counters.

Figure 3.46 shows the logic of the main-or trigger. The main-or trigger opened the ADC gate to record data for the energy deposit of the shower counter and spectra of the Čerenkov counters. The number of the main-or trigger was limited by the electronics of the shower counter up to four or less per spill by the electronics used for the shower counter. This trigger was primarily formed by the the main trigger and the pion-or trigger to record the electron data and the pion data reduced by pre-scaler.

3.6 Data acquisition and data handling

The experiment has been carried out from Nov. 1993 to Feb. 1994 at ESA of SLAC. The Linac was operated at 120 Hz with a $3.0 \cdot 10^9$ electron/spill current typically. Beam energy was switched 10, 16, and 29 GeV to study the Q^2 dependence of the structure functions. Table 3.7 lists the run summary.

Target field	Energy (GeV)	Target	Beam charge (electrons $\cdot 10^{15}$)	Electrons (triggers $\cdot 10^6$)
Longitudinal	29.13	NH ₃	130	39
		ND ₃	170	77
	16.20	NH ₃	37	11
		ND ₃	17	7.5
	9.8	NH ₃	19	6
		ND ₃	16	7
Transverse	29.13	NH ₃	56	17
		ND ₃	69	30
Either/none	all	C,Al,Empty	16	8
Total				$2 \cdot 10^8$

Table 3.7: E143 data summary: The longitudinal and transverse target fields mean the direction of the target polarization with respect to the beam axis. The transverse asymmetry A_{\perp} was measured only for 29 GeV beam.

The data were processed in the counting house of ESA. Figure 3.47 shows the online control and the data acquisition system which was based on CAMAC system controlled by VAX4000.300. Three DEC3000.400 computers analyzed and monitored online data on network. A VAX station 4000.60 was used as a tape server to store the data in 8mm data tapes which can save up to 2.5 Giga bytes of information. We used about 300 tapes for E143.

The data were processed with a E143 analysis program. It was a hybrid program compiled from C and Fortran source codes. C codes served as the main routine for process communication, graphical interface etc. The main part of the physics analysis was coded by Fortran.

We analyzed the data stored of the 8mm tapes with a basic event reconstruction process and stored the results in other 8mm tapes. The latter 8mm tapes were called DST which stands for Data Summary Tape. The date size was reduced by a factor 4 in the DST in contrast to the initial data. The physics calculation was done using the DST.

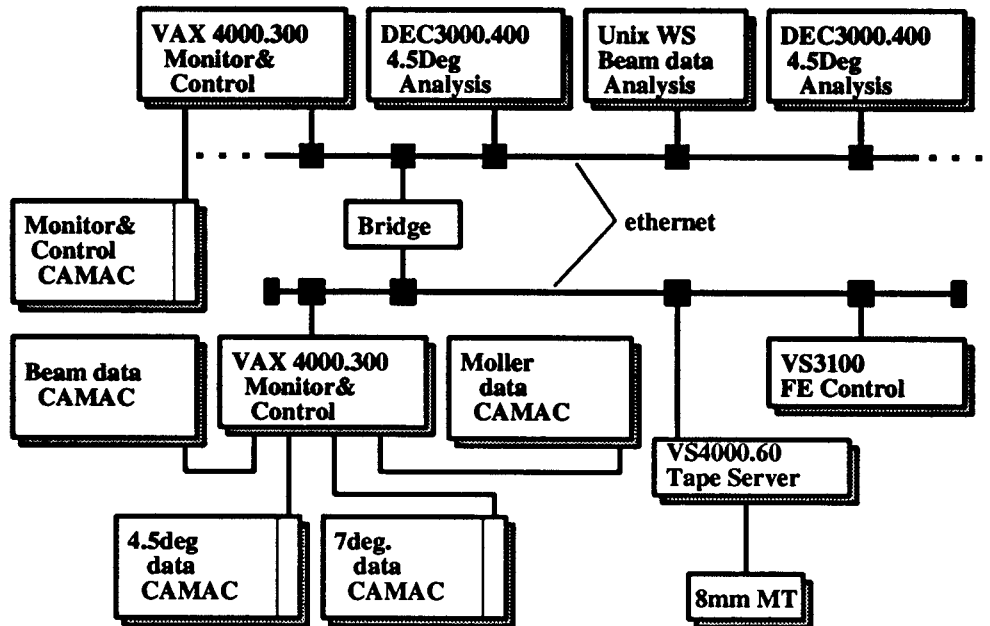


Figure 3.47: Data acquisition and control system

The DST contained the following information:

1. beam spill data
 - (a) Pulse height of good spill monitor
 - (b) Pulse height of bad spill monitor
 - (c) Output of Toroid current monitor
 - (d) Beam position and width
 - (e) Electron beam helicity
2. timing of trigger signals
3. Track data
 - (a) track momentum
 - (b) track direction and position

4. Čerenkov timing and pulse height

5. Shower cluster data

(a) Cluster centroid

(b) Cluster energy

(c) Neural network response

We made summary files from the DST. The summary file contained only the numbers of tracks binned in x and Q^2 according to different definitions. These definitions are summarized to be

1. Basic electron definition, energy = shower counter deposit,
2. Basic electron definition, energy = track momentum,
3. No tracking (defined only shower cluster and Čerenkov),
4. Basic pion definition(No main trigger, no Čerenkov hits, neural network indicates no electron), etc.

Chapter 4

Analysis

The purpose of this chapter is to describe the analysis to give the cross section asymmetries, A_{\parallel} and A_{\perp} from the data of deep-inelastic scattering of the 29 GeV electrons off the deuterized ammonia target. These asymmetries are used to calculate the spin structure functions g_1 as mentioned in Chapter 2.

The event reconstruction and the particle identification to select a good electron sample will be explained first. Then, the calculation of the asymmetries from the obtained electron sample will be explained including the corrections for the asymmetry.

4.1 Event selection

4.1.1 Beam analysis

We required to record data from the good beam spills by excluding the unstable beam spills in the analysis for the cross section asymmetry. The beam stability were examined with several devices; good spill monitor, bad spill monitor, toroid current monitor, and foil arrays, as given in the following sections.

1. The good spill monitor, a scintillation counter located under the deuteron target, measured scattered charged particles from the target. The signal from the monitor was read by a ADC module. We took data for the analysis only when the spill has

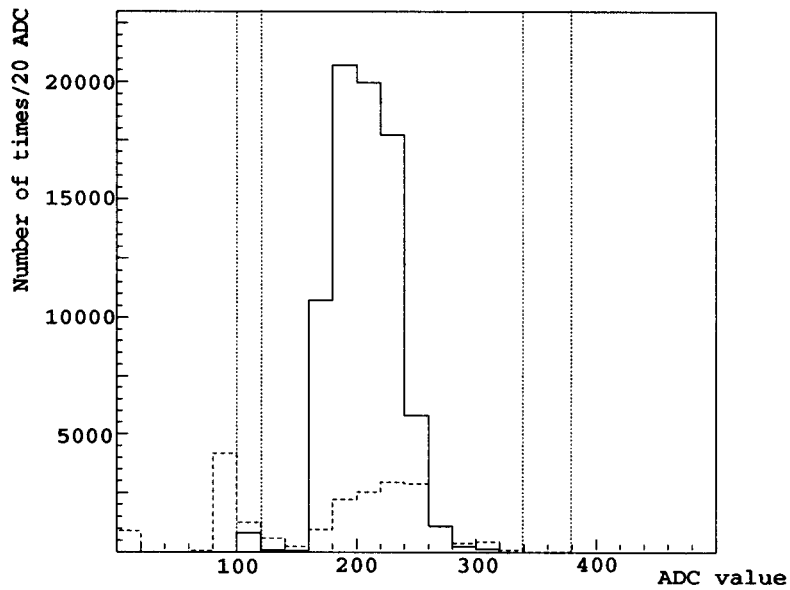


Figure 4.1: Spectrum of ADC value from the good-spill monitor on run 2876. The horizontal and vertical axes show the ADC count and the number of times per 20 ADC count respectively. The solid line shows the good-spill spectrum for the spills accepted by the other requirements. The dashed line shows the spectrum which was not accepted by other requirements. The dotted line shows upper and lower thresholds for the ADC value of the good-spill monitor.

the ADC value of the counter between the upper and lower limits determined by using the mean value of the ADC spectrum to be

$$\overline{ADC}_{gd} \cdot 0.5 < ADC_{gd} < \overline{ADC}_{gd} \cdot 1.75, \quad (4.1)$$

where ADC_{gd} is the ADC value from the good spill monitor, \overline{ADC}_{gd} is the averaged ADC value. In order to avoid the statistical fluctuation of the mean value, the first 236 spills of each run were excluded from the analysis and were only used to determine the mean value.

The lower limit excluded spills which did not hit the target and the upper limit excluded spills which hit high density materials around the target such that the magnet coil etc. Figure 4.1 shows an example of the spectrum of ADC value with the lower and upper limits indicated by the dotted lines.

2. The bad spill monitor was also a scintillation counter set at the entrance of the ESA 1 m from the beam line. This spill monitor gave no signal if the beam was stable. The limit for the ADC value of the bad spill monitor was determined by a dynamical method similar to that for the good spill monitor as,

$$ADC_{bd} < \min(\overline{ADC}_{bd} \cdot 3, 150.), \quad (4.2)$$

where ADC_{bd} is the ADC value from the bad spill monitor, \overline{ADC}_{bd} is the averaged ADC value. Figure 4.2 shows an example of the spectrum for the bad-spill monitor.

3. We used two toroidal current monitors to measure the beam current spill by spill. Figure 4.3 shows a spectrum of the toroid2 current monitor, where the x-axis is the beam current in the unit of 10^9 electrons/spill. We set the cut values for the current monitor as,

$$\max(\overline{I}_{tor2} - 0.75, 0.5) < I_{tor2} < \min(\overline{I}_{tor2} + 0.75, 5.0), \quad (4.3)$$

where I_{tor2} is the beam current measured by the toroid 2, \overline{I}_{tor2} is the average of the current. The lower threshold was set to avoid a run with low beam current.

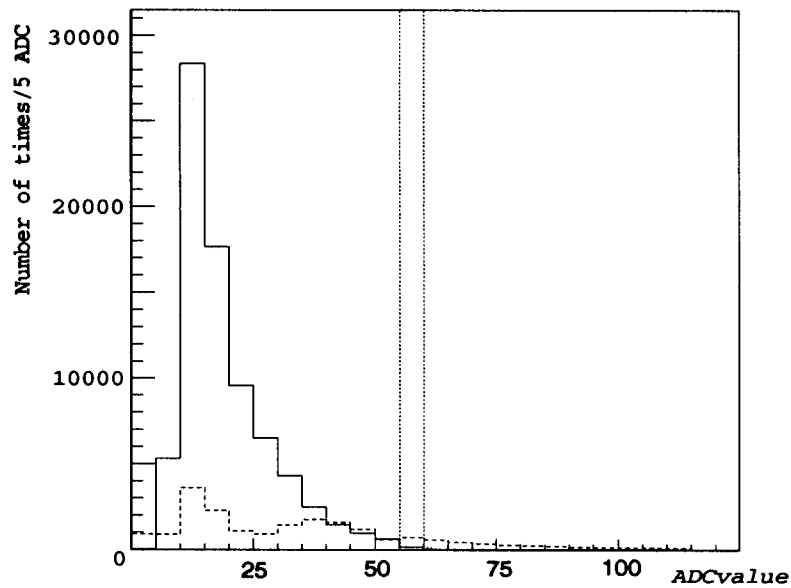


Figure 4.2: Spectrum of ADC value of the bad-spill monitor on run 2876 with the same convention as Figure 4.1.

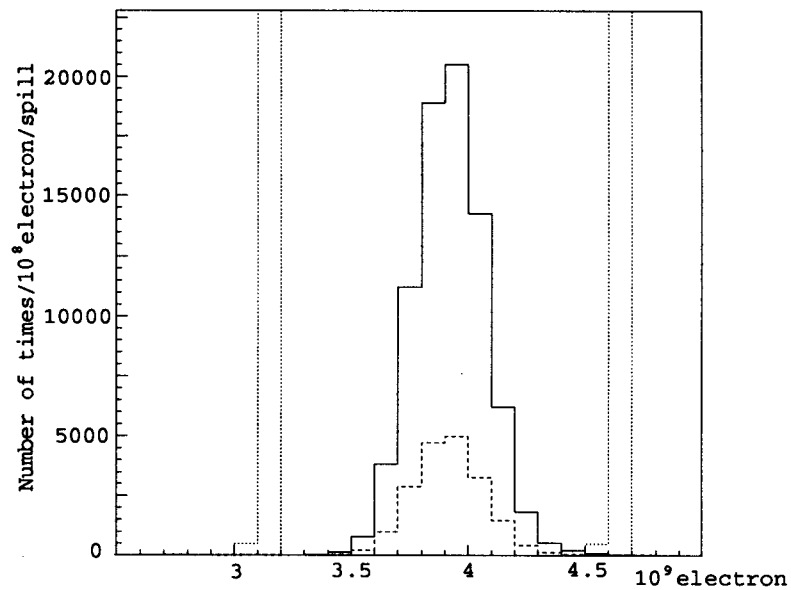


Figure 4.3: Spectrum of the beam current obtained from the toroid2 current monitor on run 2876 with the same convention as Figure 4.1.

4. Two foil arrays, each consisting of 48 foils, were set perpendicular to each other to measure the beam profile projected on x and y axes. Figure 4.4 shows the spectrum of the beam size obtained from the foil array spectra, where the beam size was defined to be $s_b = \sqrt{s_x^2 + s_y^2}$ with s_x and s_y which are the standard deviations of the beam profile in x and y-axes. The beam size s_b must satisfy the conditions,

$$\max(\bar{s}_b - 3\sigma_{s_b}, 0.5) < s_b < \min(\bar{s}_b + 3\sigma_{s_b}, 5.0), \quad (4.4)$$

where \bar{s}_b is the average of the beam size in mm, σ_{s_b} is the standard deviation of the spectrum of the beam size in mm.

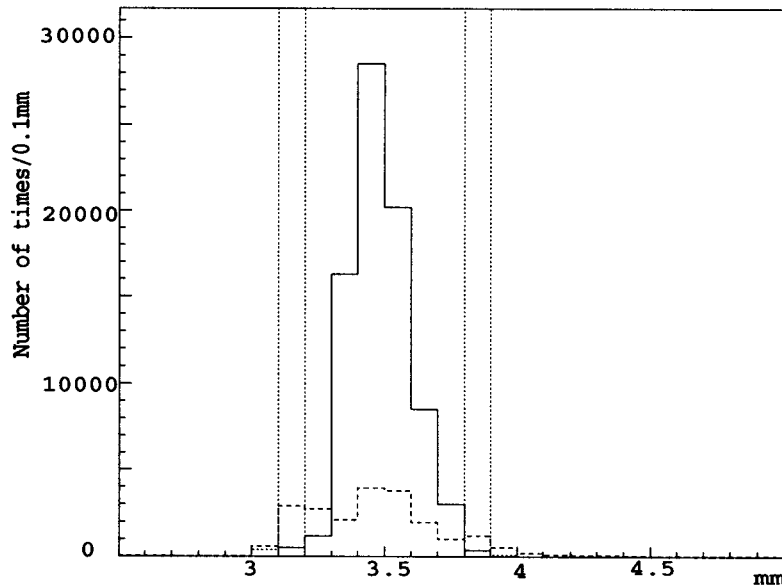


Figure 4.4: The spectrum of the beam spot size on run 2876 shows in mm with the same convention as Figure 4.1.

5. The beam position was changed spill by spill according to the rastering pattern as shown in Figure 3.9. We excluded the spills whose positions were off more than 12 mm from the center of the rastering pattern. The center of the raster pattern was determined by the averaged position of the beam spot dynamically.

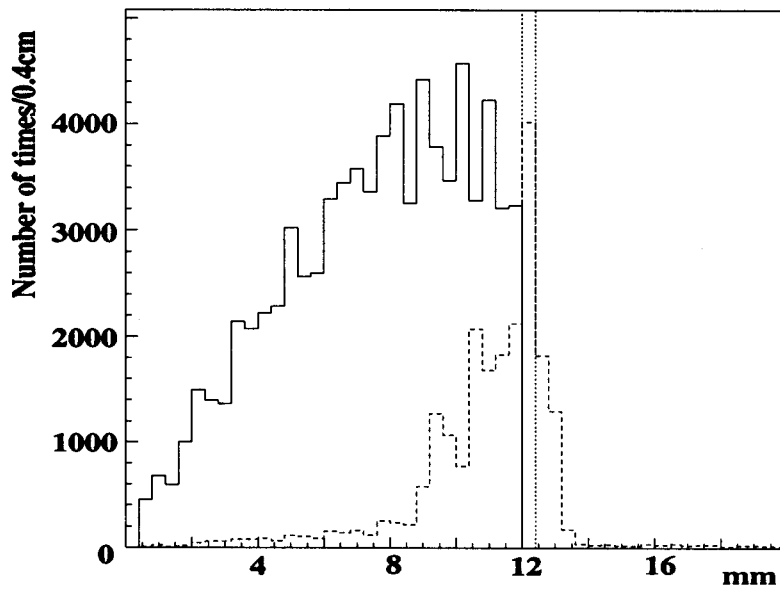


Figure 4.5: Horizontal axis shows the distance of the beam position from target center. The beam position was determined by foil arrays. The solid line shows the spectrum for the spills accepted by the other requirements. The dashed line shows the spectrum of the spills excluded by the other requirements. The dotted line shows the upper limit, 12 mm from the target center.

6. Figure 4.5 shows the spectrum of the distance of the beam positions from the target center for run 2876. Beam spills whose positions were deviated more than 12 mm from the center of the target were also excluded from the analysis. This requirement reduces the ambiguity of the energy correction for the scattered electron because the electron scattered at the outer part of the target pass through complex materials around the target.

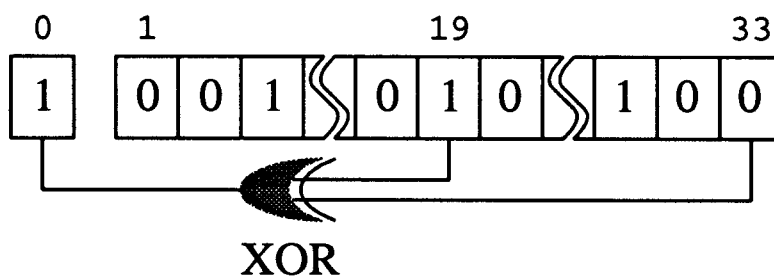


Figure 4.6: Pseudo random number generator, PRNG makes a 33 bit array pseudo-randomly. The previous 33 bits determine the next bit of the PRNG by the exclusive-or product of 19th and 33rd bits. This bit then decides the helicity of the beam spill. We assign 0 for left-handed spill and 1 for right-handed spill.

In addition, we checked the consistency of the beam helicity determination. The beam helicity was chosen by a Pseudo Random Number Generator (PRNG). Figure 4.6 shows the logic of the PRNG. The PRNG makes random numbers from an algorithm that uses as input the previous 33 bits in its sequence. Therefore, we can predict the following sequences generated by the PRNG, i.e. helicity of the next beam spill by knowing the initial 33 bit pattern. The information of the beam helicity actually used was read from the PES (Polarized Electron Source) and stored on tape. During the analysis, we examined the information from the PES comparing with the prediction by the PRNG. If the prediction was different from the PES information, the spill was excluded from the analysis. The next 32 spills were also excluded so that the prediction algorithm can be re-synchronized. Typically, less than 0.1% of the spills were excluded by this requirement.

4.1.2 Shower cluster finding

An electron incident on the lead glass shower counter deposits the energy on several lead glass blocks around the incident point. To reconstruct the energy of the electron from these energy deposits, we organized the hits on the blocks into clusters by using blocks having deposited energy of more than 50 MeV to reject the influence of fluctuation of the ADC pedestal. We adopted a cellular automata program which was a kind of Hopfield neural network [43] for the clustering.

The cellular automata program set a network which had 200 neurons corresponding to the lead glass blocks. Every neuron was connected to the nearest eight neurons in the real geometry by synapses which mediate information to each other. The state of the neuron was indicated by a real number. The initial states of the neurons were equal to the energy deposits on the lead glass blocks corresponding to these neurons. From the initial state, the network evolved according to the following two rules.

1. An evolution of a neuron was determined by the eight neurons surrounding it. If there is any neuron greater than the center neuron, the center neuron is set to be the greatest one among the eight neurons. If the center neuron is greater than any one of the eight neurons, the center neuron is not changed and labeled as the Virus.
2. The Virus is to be the center of the cluster. We had a special rule that a neuron seized once by a Virus is not involved by any other Virus.

These rules guaranteed the good separation if several particles are incident close to each other. Figure 4.7 shows such an example and indicate how the lead glass blocks are organized from the state 1 to state 3 through the evolution of the cellular automata. In this example, these blocks are clustered into two groups.

The total energy deposit of a cluster was calculated from the sum of the energy deposits of the blocks in the cluster. The centroid of the cluster, $x_{cluster}$ and $y_{cluster}$ was

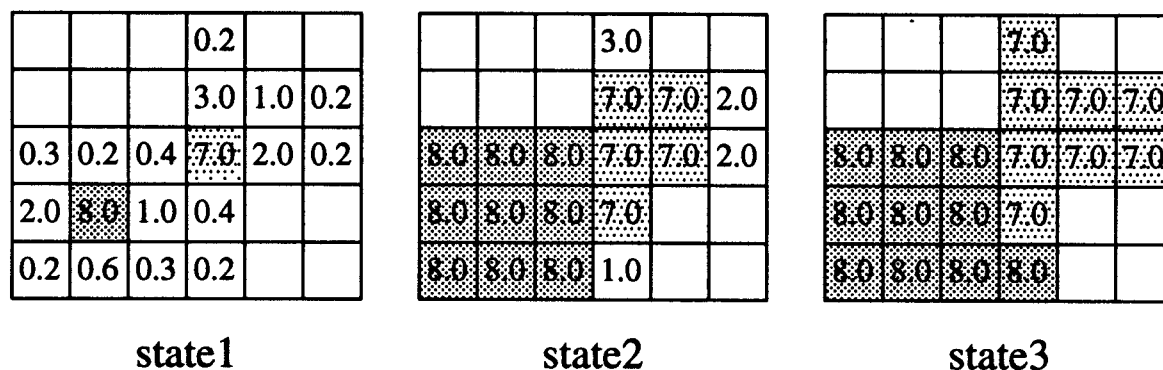


Figure 4.7: An evolution of cellular automata is shown in three steps. (a) The initial state. The states of the neurons are set to be equal to the energy deposit of the lead glass blocks. Neurons with no number mean that the energy deposit of the block is lower than the threshold, 50 MeV. Two cells filled by different gray colors are Viruses with the highest energy deposit in the surrounding blocks. (b) The next state. The neurons hatched by the light and dark gray colors are seized by these Viruses. (c) The final state. In this case, neurons are clustered into two groups. We notice that several cells seized by the 7.0 Virus were not seized by the 8.0 Virus in the evolution from (2) to (3) due to the second rules.

determined by,

$$x(y)_{cluster} = \frac{\sum_{i=1}^9 E_i x(y)_i}{\sum_{i=1}^9 E_i}, \quad (4.5)$$

where i stands for the associated blocks, E_i is the energy deposit of the i -th block, x_i and y_i are the x and y position of the center of the i -th block. From a study for the matching between the reconstructed track and the cluster centroid, the spatial resolution was obtained to be about 10 mm [47]. Figure 4.10 and 4.11 show the spectra of the distances in x and y of the centroid of the shower cluster from the position of the reconstructed track for the 4.5° and 7° spectrometers. We notice that this spatial resolution includes the resolutions from the shower cluster centroid and the tracking position.

4.1.3 Track finding

The tracking was performed by using information from the Čerenkov counters, the hodoscopes, and the shower counter. The information from these detectors were stored in a data format for the tracking routine. Every detector was virtually treated as a wire chamber in the tracking routine for convenience. The leading information contained in this data is

1. Three dimensional position specifying the wire location,
2. Vector parallel to the wire direction,
3. Spatial resolution of wires,
4. Timing of signals corrected by time of flight and propagation delay at the reference point (the surface of the shower counter),
5. Timing resolution.

In the case of hodoscopes, the line of the central axis of the finger is taken as the location and the vector of the wire. The spatial resolution was set to $1/\sqrt{12}$ of the finger width which was calculated from the square distribution. Table 4.1 shows the time resolution for each plane.

Because the Čerenkov counter covers all of the acceptance of the spectrometer, it was treated as a wire with a spatial resolution of 100 m. The time resolution of the counter was set to 1 ns.

A cluster of the shower cluster was interpreted as the hits of two wires along x and y axes whose intersection was at the center of the cluster. The position on the z coordinate was set to be zero at the surface of the shower counter. From a study for the matching in time between the shower cluster and the reconstructed track, the time resolution of the shower cluster was measured to be less than 1.0 ns [48]. Therefore, the spatial and time resolutions were set to 10 mm and 1.0 ns respectively.

Plane	4.5° spectrometer (ns)	7° spectrometer (ns)
1	1.4	1.3
2	1.1	1.1
3	1.1	1.1
4	1.4	1.0
5	1.1	0.9
6	1.1	1.0
7	1.4	1.2

Table 4.1: Time resolution for hodoscope fingers in ns: the time resolution for every finger in a hodoscope plane was assumed to be identical.

For the track reconstruction, we first search hits in the time window of 15 ns in which we have the most hits. These hits were fitted for the reconstruction of the first track. Any hit deviated from the fit in either time or space, was removed from the fitting. If the number of the remaining hits was greater than those in any track classification shown in Table 4.2, the track was accepted. The fitting procedure was repeated until all tracks was reconstructed.

Class	Čerenkov	Hodoscope	Shower
1	1	4	1
2	1	4	0
3	0	4	1
4	0	6	0

Table 4.2: Track classification according to the minimum number of hits on each detector.

Figures 4.8 and 4.9 show the distance between the extrapolated point on the target and the center of the target where the extrapolation back on the target was performed by using the reverse matrix of the spectrometer magnet. We required that a track was reconstructed within 10 mm from the center of the target to be included in the analysis.

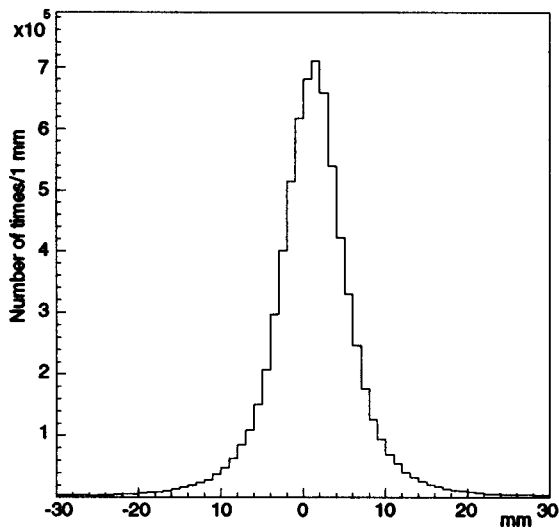


Figure 4.8: Track extrapolated position at target to the center of the target in the 4.5° spectrometer.

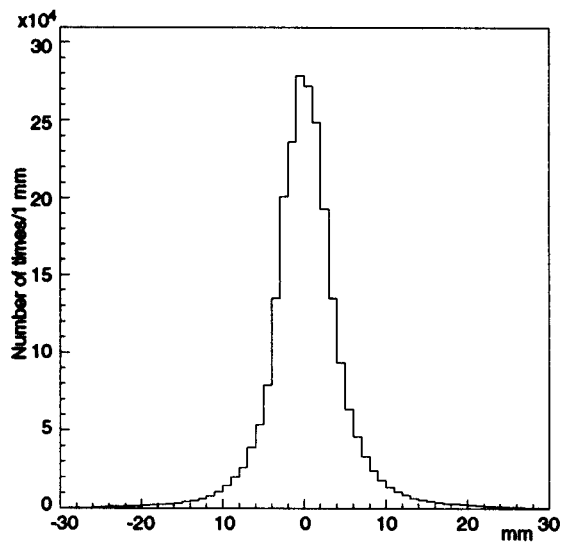


Figure 4.9: Track extrapolated position at the target to the center of the target in the 7° spectrometer.

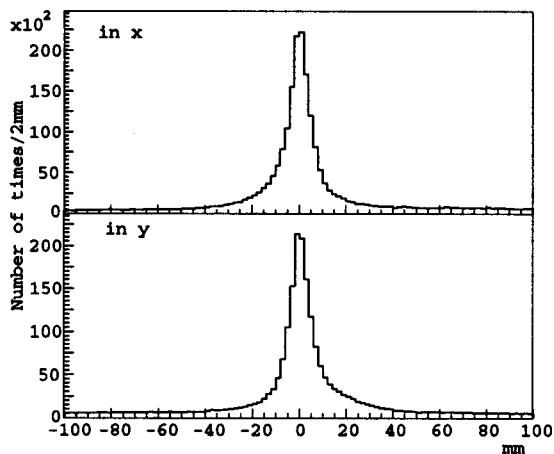


Figure 4.10: Matching of tracks and clusters for the 4.5° spectrometer: The upper figure shows the matching in x, and lower figure shows the matching in y.

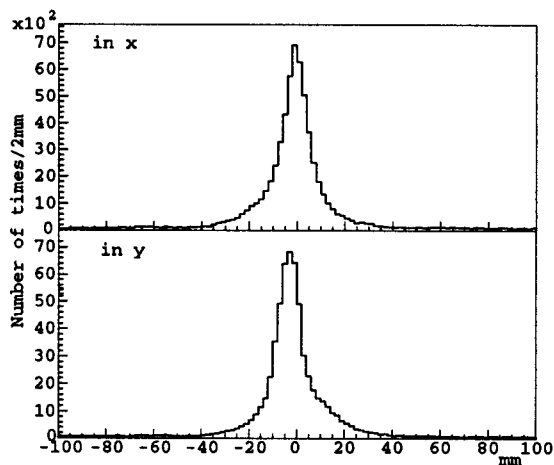


Figure 4.11: Matching of tracks and clusters for the 7° spectrometer: the upper figure shows the matching in x, and lower figure shows the matching in y.

Figure 4.10 and 4.11 show the difference in x and y between the extrapolated position of the tracks on the shower counter and the center of the the shower cluster. We required that tracks and clusters have to be within 40 mm in both x and y , and 10 ns in time.

Tracking efficiency

Tracking efficiency does not affect the cross section asymmetry providing it is identical for the beam spills of both electron helicities. Of course, it would be a serious problem if the efficiency is different for the beam helicity because it may give a false asymmetry.

We examined the tracking efficiency by using the shower cluster. The fraction when the reconstructed track was properly associating to a shower cluster was defined to be the tracking efficiency.

We first have to remove any cluster produced by noise or gamma from the cluster sample because these contamination improperly decrease the tracking efficiency in this definition. To improve the purity of the cluster sample, we required the following,

1. No edge cluster. The cluster on the edge is unreliable because a part of the energy may leak to the outside of the shower counter.
2. Cluster energy greater than 8 GeV. The junk cluster was expected to be distributed on such low energy region.
3. Both Čerenkov had a hit (low threshold)
4. Neural network response more than 0.9.

We adopted only electron clusters as the sample because we were able to require the Čerenkov hits and the neural network response and these requirements should purify the sample.

For the cluster sample, we examined matching with the tracks which was reconstructed by the regular tracking algorithm mentioned previously. We required that the

track is reconstructed within 40 mm in x and y, and 10 ns in time. These requirements were the same for those for the 'good track' in the usual analysis.

The tracking efficiencies were calculated separately for the beam helicity, +1 and -1 and the spectrometers. Table 4.3 shows the results for run 1334. The tracking efficiencies had no significant difference for the beam helicities and produced no false-asymmetry.

Spectrometer	4.5°	7°
helicity -1	93.5 ± 0.3	98.2 ± 0.5
helicity +1	93.4 ± 0.3	98.0 ± 0.5

Table 4.3: Tracking efficiency

4.1.4 Electron identification

It is important to reject any hadron track from the analysis to obtain the cross section asymmetry because the cross section is defined by the number of scattered electrons. In principle, we can separate electron and hadron(pion) tracks by using (1) the Čerenkov counter and (2) the E/P ratio.

Čerenkov ADC

Basically, the long and short Čerenkov counters generate no signal for pions with the momentum less than 9 GeV/c and 13 GeV/c respectively. We can then reject the low momentum pion using the requirement for coincidence of the two Čerenkov counters.

Figures 4.12 to 4.15 show the ADC spectra of the Čerenkov counters. We required that the track fired the coincidence signal of the Čerenkov counters and the shower counter(main trigger) and the Čerenkov ADC value to be more than 40 for the track to be electron.

The detection efficiencies for electrons and the pion contaminations were estimated for the Čerenkov counters. For both of electron and pion samples, we required that the

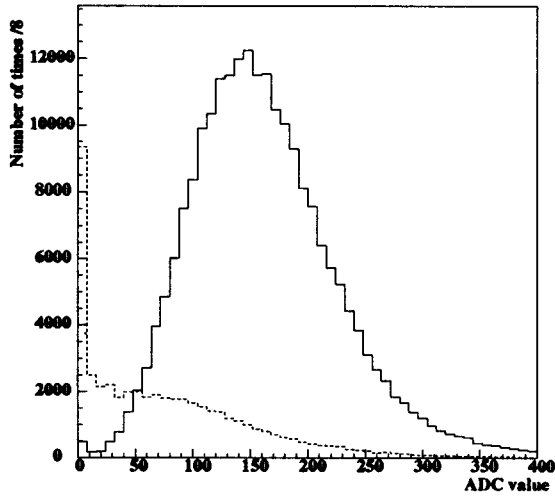


Figure 4.12: ADC spectra of Čerenkov counter 1 for the 4.5° spectrometer. The solid line shows the ADC spectrum of Čerenkov counter 1 for electrons identified by the neural network response of the shower counter and the E/P ratio. The dashed line shows the spectrum for pions defined by the requirements for the neural network and E/p ratio opposite to those for electrons.

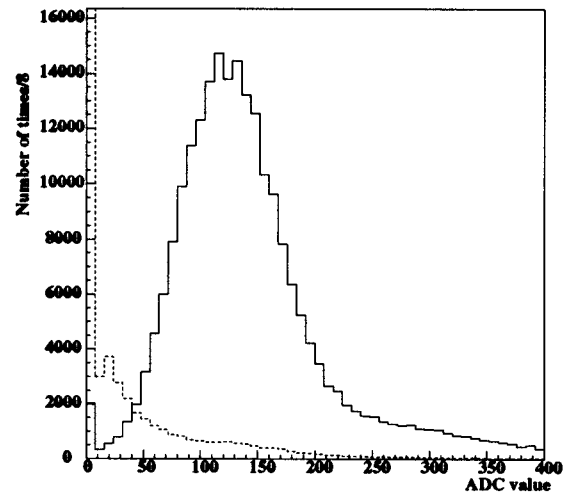


Figure 4.13: ADC spectra of Čerenkov counter 2 for the 4.5° spectrometer. The spectra are shown with the same convention as Figure 4.12.

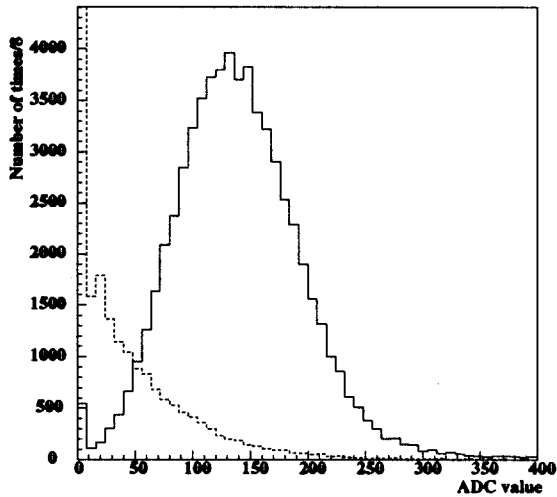


Figure 4.14: ADC spectra of Čerenkov counter 1 for the 7° spectrometer. The spectra are shown with the same convention as Figure 4.12.

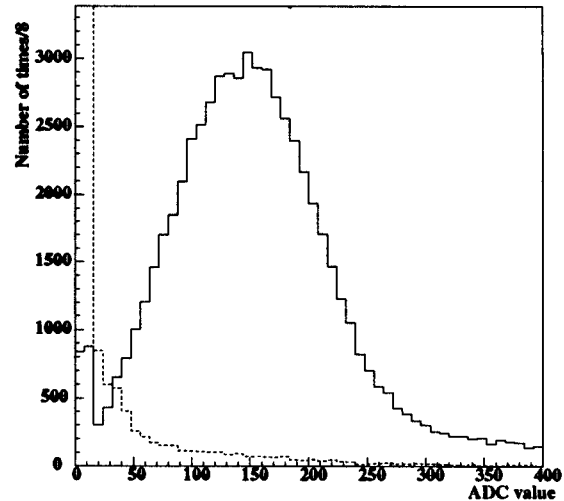


Figure 4.15: ADC spectrum of Čerenkov counter 2 for the 7° spectrometer. The spectra are shown with the same convention as Figure 4.12.

track is 'good track' which has a good association to the target and the shower cluster. We rejected tracks associated to the edge of the shower counter because the shower cluster on the edge was less reliable. From the sample of the good track, the electron and pion sample was defined by E/P ratio and the neural network response which will be mentioned in Section 4.1.4. The requirements for the electron and pion samples are summarized;

1. electron,
 - (a) E/P ratio between 0.8 and 1.2,
 - (b) The neural network response more than 0.9,
2. pion ,
 - (a) E/P ratio less than 0.8,
 - (b) The neural network response less than 0.0.

The Čerenkov spectra are shown for these two samples. The efficiency for electron ID were calculated from the fraction of electron tracks which had the Čerenkov ADC greater

than 40. The pion contamination was calculated from the ratio of the pion sample to the electron sample with ADC value of more than 40. Table 4.4 shows the efficiency for electron ID and the pion contamination for the four Čerenkov counters. The good efficiencies of more than 95% were obtained for all Čerenkov counters.

	4.5° C1	4.5° C2	7° C1	7° C2
Efficiency %	99.1 ± 0.0	97.7 ± 0.0	97.6 ± 0.1	95.2 ± 0.1
pion contamination %	14.6 ± 0.1	7.0 ± 0.1	12.9 ± 0.1	5.1 ± 0.2

Table 4.4: Efficiency for electron ID and pion contamination of the requirement for the Čerenkov counters.

E/P ratio

E/P is a ratio of the energy measured by the shower counter to that obtained from the tracking. Since the mass of the electron is negligible, it has become custom in this analysis to label the tracking energy as “momentum” and the shower counter energy as “energy”. The momentum was calculated from the tracking data using magnetic reverse matrix element, and the energy was extracted from the total energy deposited in the shower cluster.

Figure 4.16 and 4.17 shows the E/P ratios for the 4.5° and 7° spectrometers where we plotted only the “non-edge” sample given in Figure 3.34. The solid and dashed lines show the spectra for the electron and pion sample defined by using the hits from the Čerenkov counters and the neural network response of the shower counter. We accepted tracks with E/P of between 0.8 and 1.2 as electron tracks.

The efficiency for electron ID and the pion contamination were calculated using a electron sample and a pion sample which were defined by ADC value of the Čerenkov counters and the neural network response. We required for both of the electron and pion sample to be a ‘good track’ with a good association to the target and the shower cluster. The electron and pion samples were classified as follows:

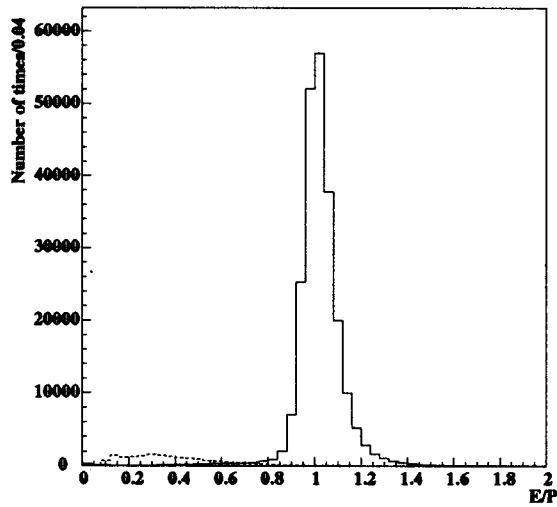


Figure 4.16: E/P on 4.5° spectrometer: The solid line shows the E/P spectrum for electron defined by the Čerenkov counters and the response of the neural network. The dashed line is the E/P spectrum for pions excluded by Čerenkov counters and neural network.

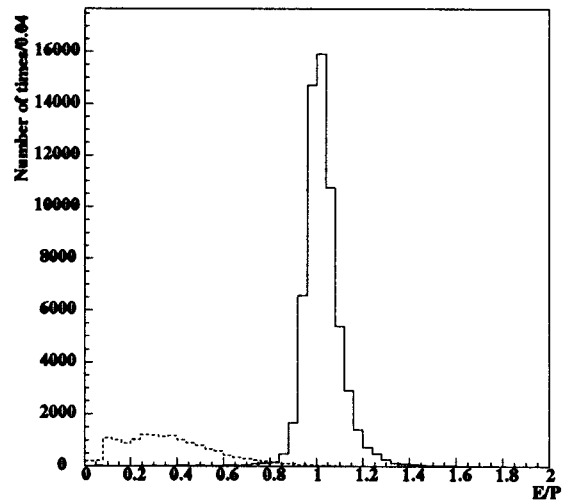


Figure 4.17: E/P on 7° spectrometer with the same convention as figure 4.16.

1. electron,
 - (a) Both Čerenkov ADC greater than 40,
 - (b) Neural network response more than 0.9,
2. pion,
 - (a) Both Čerenkov ADC less than 40,
 - (b) Neural network response less than 0.0.

The efficiency for electron ID and the pion contamination were calculated using the two samples. The efficiency for electron ID was the fraction of the electron sample in the region of E/P between 0.8 and 1.2. The pion contamination was the ratio of the pion sample to the electron sample in the region of E/P between 0.8 and 1.2. Table 4.5 shows the efficiency for electron ID and the pion contamination. This E/P cut did the effective pion rejection keeping the good efficiency for electron ID.

Spectrometer	4.5°	7°
Efficiency %	94.4 ± 0.1	95.5 ± 0.1
Pion contamination %	0.4 ± 0.0	1.1 ± 0.0

Table 4.5: The efficiency for electron ID and the pion contamination of the requirement for the E/P ratio.

neural network

We also used a neural network algorithm to identify the type of particle incident onto the shower counter. The main difference in shower response between electrons and pions is the total of the energy deposit. Generally, a pion has a lower momentum than an electron because the pion comes from the fragmentation of a nucleon. In addition, a hadron will lose only a part of its energy in the shower counter. Therefore, the energy deposited by a pion is distributed mostly below 5 GeV with a 29GeV electron beam.

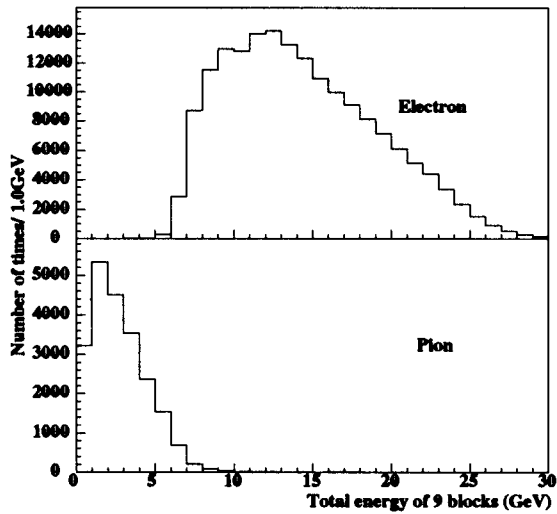


Figure 4.18: Total energy deposited in the nine blocks which are the central block of a cluster and eight blocks surrounding the central block. The upper and lower figures show the spectra for electron and pion samples. These electron and pion samples were defined by the ADC value of the Čerenkov counters and the E/P ratio.

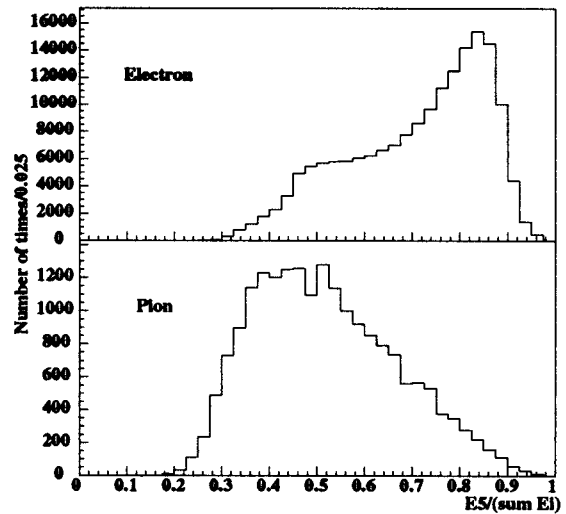


Figure 4.19: The ratio of the energy deposited in the central block of a cluster to the total energy deposited in the nine blocks defined in Figure 4.18 is plotted. The spectra are shown with the same conventions with Figure 4.18.

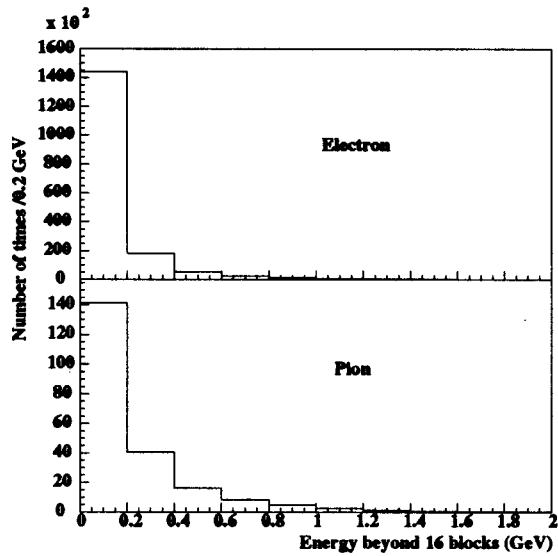


Figure 4.20: The spectrum of the energy deposited in 16 blocks surrounding the nine blocks is shown. The spectra are shown with the same conventions with Figure 4.18.

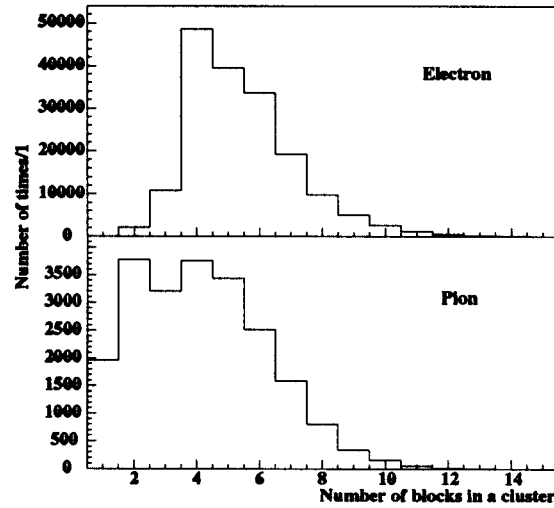


Figure 4.21: Number of blocks with the energy deposited more than 50 MeV in a cluster. The spectra are shown with the same conventions with Figure 4.18.

In order to demonstrate the difference of the characters of the electron and pion clusters, we investigated the several quantities of the shower counter for the electron and the pion sample which were defined by the Čerenkov counters and E/P ratio as:

1. electron,
 - (a) Both Čerenkov hits within 10 ns,
 - (b) E/P between 0.8 and 1.2,
2. pion,
 - (a) No hits on both Čerenkov counters within 10 ns,
 - (b) E/P less than 0.8,

Figure 4.18 shows the total energy deposited in nine blocks of a cluster. The nine blocks were defined by the central block and eight blocks surrounding the central block in a

cluster. While the spectrum for the electron sample is distributed in the region greater than 6 GeV, the energy deposited by the pion sample is found hardly beyond 7 GeV. Figure 4.19 shows the ratio of the energy deposited in the central block to the total energy deposited in the nine blocks. The spectrum for the electron sample peaks at ~ 0.8 and that for the pion sample, on the other hand, peaks at ~ 0.4 . Figure 4.20 shows the energy deposited in 16 blocks beyond the nine blocks. The spectrum for the pion sample has a tail longer than that for the electron sample. Figure 4.21 shows the number of blocks with the energy deposit more than 50 MeV in a cluster. The number of blocks involved by the pion cluster is less than that for the electron cluster.

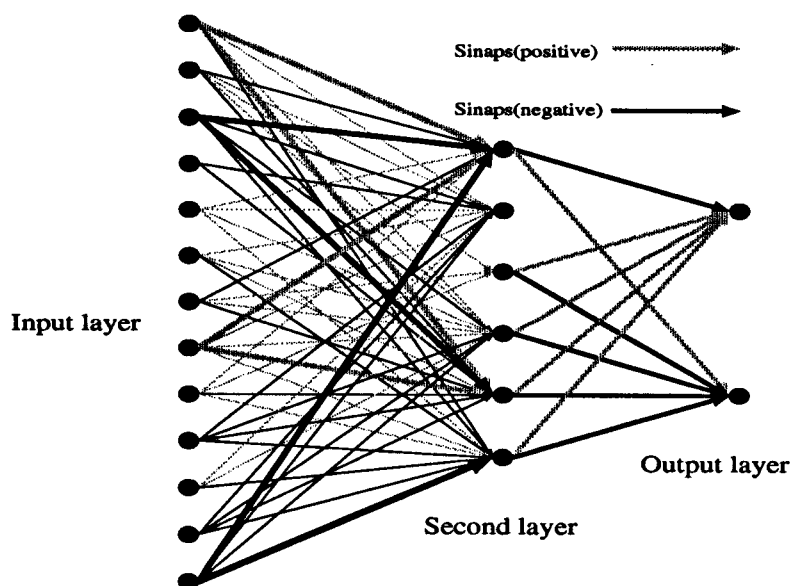


Figure 4.22: Multi layered perceptron for the particle identification on the shower counter has thirteen inputs. Gray and black arrows indicate positive and negative synapses. The thickness of these lines indicate approximately the amplitude of the synapses. For example, the first neuron in the input layer excites the first neuron of the second layer, but the third neuron of the input layer calms the first neuron of the second layer. The state of the neurons in the second layer was determined by the total of the signals from the input layer with a Sigmont function. The same was true between the second and output layer.

To identify the type of the particle using all of these information we used a neural

network algorithm. The network was a multi-layered perceptron as shown in Figure 4.22. There were 13 neurons in the input layer, and there were two outputs indicating electron and pion likelihoods. The network is a complex structure which works as a function which has 13 inputs. Each neuron has synapse joints with every adjacent neuron in the next layer. Each neuron, except those in the input layer, can be between 1 (=excited) and -1 (=calmed). The condition of a neuron in the second and output layers is determined by all of neurons in the previous layer. A signal from a neuron is mediated by a synapse. A synapse has an amplitude determined by training as mentioned later.

The condition of a neuron, y_i was determined by a Sigmont function as follows,

$$y_i = \frac{\exp^{ka} - 1}{\exp^{ka} + 1} \quad (4.6)$$

$$a = \sum_i \xi_{ij} x_i,$$

where x_i is the condition of a neuron in the input or second layer, ξ_{ij} is the amplitude of the signal mediation by a synapse from a neuron in the input or second layer to a neuron in the second or output layer respectively. The Sigmont function is similar with a step function varying from -1 to 1. We used the Sigmont function instead of a naive step function because the former can be differentiable.

The 13 inputs, $V_1 - V_{13}$, for the neural network were as follows,

1. V_1 : Total energy in the nine blocks of the cluster. The nine blocks are the center block of the cluster and eight blocks surrounding it.
2. V_2 : Ratio of the energy in the central block to total energy of the nine blocks.
3. V_3 : Energy in the sixteen blocks which are beyond the nine blocks.
4. $V_4 - V_{12}$: Energy deposited in each of the nine blocks.
5. V_{13} : Number of blocks in the cluster.

We developed the neural network using a Monte-Carlo simulation. A package for detector simulation, GEANT, simulated events in the shower counters. We studied the

response of the neural network for incident electrons and pions and we compared the responses of the neural network to the true answer which was the input to the simulation. If the response was not the same as the true answer (for example, the network said that the cluster was generated by electron, while the true answer was by pion), we adjusted every synapse's amplitude to give a more correct response. This correction was done using a back propagation method[43]. In the back-propagation method, the synapse between the output layer and the second layer is corrected at first. After that, the synapse between the second layer and the input layer is corrected. We iterated this process until we got the proper answer from the network.

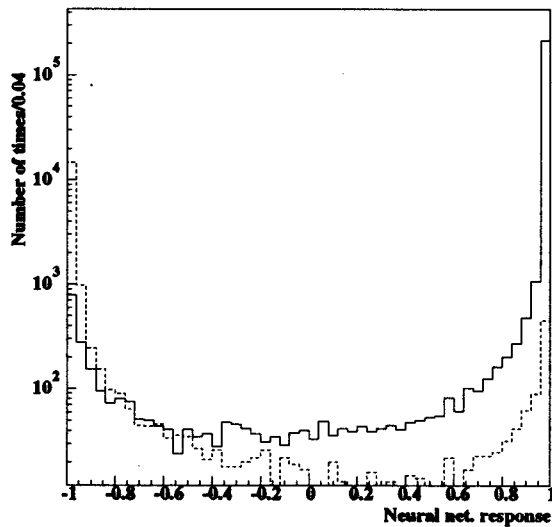


Figure 4.23: Spectrum of the neural network response for the 4.5° spectrometer is shown. Horizontal axis shows neural network response, +1 for electron like clusters and -1 for pion like clusters. Vertical axis shows number of times/0.04 in logarithm scale. The solid and dashed lines show the spectra for clusters matching with electron and pion tracks defined by the Čerenkov counters and E/P ratio respectively.

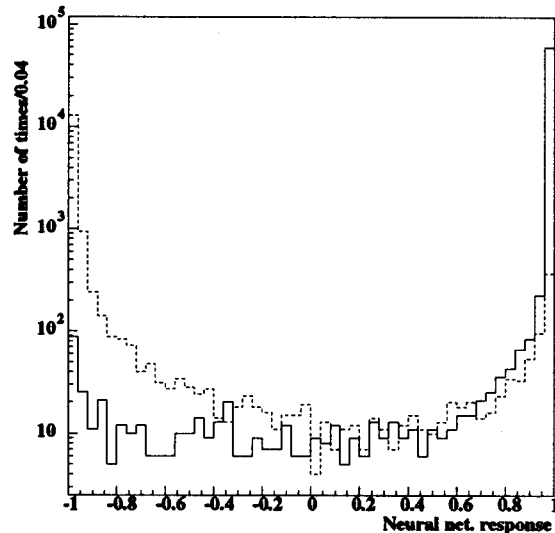


Figure 4.24: Spectrum of the neural network response for 7° spectrometer: The spectrum is shown with same conventions as the 4.5° results.

Figure 4.23 and 4.24 show the neural network response for run 1334. The horizontal axis shows the response which is 1 for electron clusters and -1 for pion clusters. The solid and dashed lines show the responses for the electron and pion samples respectively defined by the Čerenkov counters and the E/P ratio. We required that the neural network response had to be more than 0.9 to identify a particle as an electron.

The efficiency for electron ID and the pion contamination were extracted by a calculation similar to that for the ADC of the Čerenkov counters or the E/P ratio. The electron and pion samples were defined by

1. electron,
 - (a) Both Čerenkov ADC more the 40,
 - (b) E/P ratio between 0.8 and 1.2,
2. pion,
 - (a) Both Čerenkov ADC less than 40,
 - (b) E/P ratio less than 0.8.

Table 4.6 shows the efficiency for electron ID and the pion contamination calculated from these electron and pion samples. The results indicate the higher efficiency and the lower pion contamination comparing to a conventional method for the particle identification resulting $\sim 90\%$ of efficiency for electron ID and $\sim 10\%$ of pion contamination[43].

	4.5°	7°
Efficiency %	98.1 ± 0.0	98.8 ± 0.0
Pion contamination %	0.3 ± 0.0	0.8 ± 0.0

Table 4.6: Efficiency for electron ID and pion contamination for neural network response

The electron sample

Finally, the requirements for the electron sample are summarized to be

1. The main-trigger fired,
2. The ADC outputs from both Čerenkov counters were more than 40,
3. The track extrapolated back to the target within 10mm in x,
4. Track and Cluster agreed with each other by less than 40 mm in x and y and less than 10 ns in time,
5. $0.8 < E/P < 1.2$,
6. neural network response was more than 0.9,

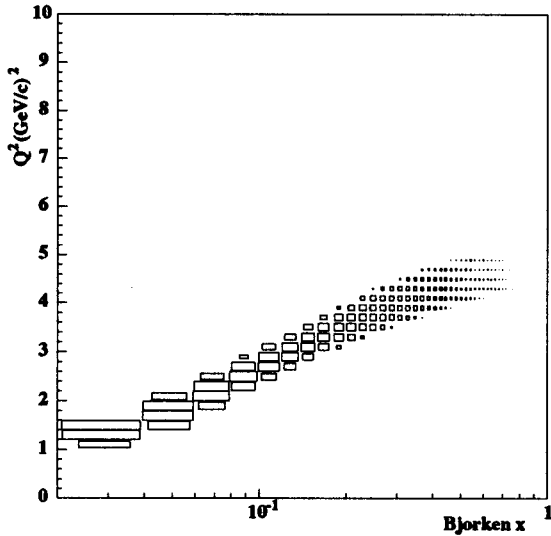


Figure 4.25: Data profile on $x-Q^2$ plane from run 1334 for the 4.5° spectrometer. The x and y axes show Bjorken x in logarithmic scale and Q^2 in linear scale respectively. The box area is proportional to the number of counts in each bin in logarithmic scale.

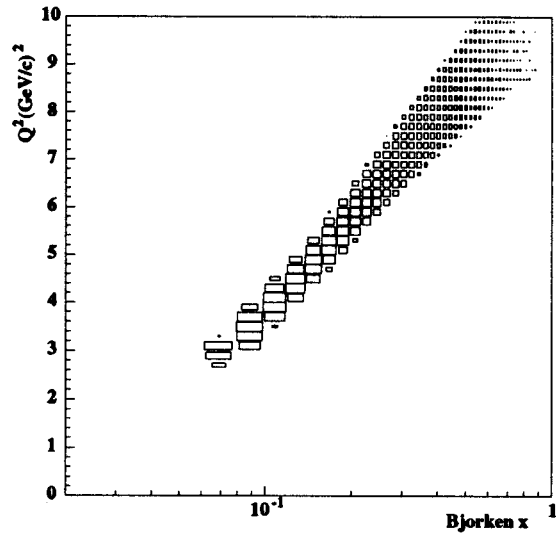


Figure 4.26: Data profile on $x-Q^2$ plane from run 1334 for the 7° spectrometer with the same convention as Figure 4.25.

We obtained electron data scattered inelastically from the deuteron target over a wide kinematical region as shown in Figure (4.25) and (4.26). The kinematics for the electron was calculated using the momentum evaluated from the tracking with the reverse matrix of the spectrometer magnets and the scattered angle from the beam axis. We excluded counts outside the deep-inelastic region where the momentum transfer was less than $1.0(\text{GeV}/c)^2$ where the scaling is not a good approximation for the structure function due to the large strong coupling constant. We also excluded data in the resonance region where the effective mass of the final hadron system was less than $2.0\text{GeV}/c^2$. The e-N scattering has Δ resonances in the region where the cross section does not indicate the proper information of the nucleon structure.

When satisfied, these two kinematical conditions retained enough statistics to give the cross section asymmetry in the region from 0.029 to 0.8 in Bjorken x and from $1.0(\text{GeV}/c)^2$ to $12.0(\text{GeV}/c)^2$ in Q^2 . The representative values of x and Q^2 for a bin was calculated from the averaged x and Q^2 over the data which were included in the bin.

4.2 The cross section asymmetry

As the results of the analysis in the previous section, we obtained a clean electron sample from the measurement. The purpose of this section is a derivation of the cross section asymmetries A_{\parallel} and A_{\perp} . These cross section asymmetries are calculated from the number of scattered electrons off the polarized deuteron target.

If we assume that the beam is polarized 100% and the pure deuteron target is also longitudinally or transversely polarized 100%, a number of electrons detected by the spectrometer, $N^{\uparrow(\leftarrow)\downarrow(\uparrow)}$ is expressed by,

$$N^{\uparrow(\leftarrow)\downarrow(\uparrow)} = \sigma^{\uparrow(\leftarrow)\downarrow(\uparrow)} Q^{\uparrow(\leftarrow)\downarrow(\uparrow)} \rho(t) N_A l \Omega(t) \quad (H = L, R), \quad (4.7)$$

where the superscripts of the arrows for N , σ , and Q indicate the directions of the target and beam helicities, σ is the cross section for the scattering, Q is a total beam flux, $\rho(t)$ is the target density, N_A is the Avogadro number, l is the length of the target, and $\Omega(t)$

is the acceptance and the detection efficiency of the spectrometer. In principle, the $\rho(t)$ and the $\Omega(t)$ may change during the experiment and then are functions of the time, t .

Using the number of electrons detected by the spectrometer and the total beam flux, the rate asymmetry is written by

$$\Delta_{\parallel(\perp)} = \frac{N^{\uparrow(\leftarrow)\downarrow}/Q^{\uparrow(\leftarrow)\downarrow} - N^{\uparrow(\leftarrow)\uparrow}/Q^{\uparrow(\leftarrow)\uparrow}}{N^{\uparrow(\leftarrow)\downarrow}/Q^{\uparrow(\leftarrow)\downarrow} + N^{\uparrow(\leftarrow)\uparrow}/Q^{\uparrow(\leftarrow)\uparrow}} \quad (4.8)$$

Although the target density and the acceptance and the detection efficiency of the spectrometer was varied during the experiment, influences due to the time fluctuation of these factors was negligible because the beam helicity was changed randomly spill by spill. Therefore, the factors of $\rho(t)N_A I \Omega(t)$ were same for left- and right-handed spills and were canceled in the rate asymmetry. The rate asymmetry is then supposed to be same as the cross section asymmetry in the ideal case.

In the actual experiment, the beam polarization and the target polarization were less than 100% and the target contained many nucleons other than the deuteron. The beam and target polarization and the dilution factor which is the ratio of electrons scattered from the deuteron to those from all of the target materials relate the rate asymmetry to the cross section asymmetry to be

$$A_{\parallel,\perp} = \frac{\Delta_{\parallel,\perp}}{p_b p_t f}, \quad (4.9)$$

where p_b is the beam polarization, p_t is the target polarization, and f is the dilution factor.

Equations (4.9) is the relation of the rate asymmetry and the cross section asymmetry accounting only the leading corrections. Actually, the other corrections smaller than these leading corrections are also important to the high precision measurement for the spin structure function. To do that, we measure the rate asymmetry not only for the electron, but also for the positron defined to be

$$\Delta_{\parallel(\perp)}^{e,p} = \frac{N_{e,p}^{\uparrow(\leftarrow)\downarrow}/Q_{e,p}^{\uparrow(\leftarrow)\downarrow} - N_{e,p}^{\uparrow(\leftarrow)\uparrow}/Q_{e,p}^{\uparrow(\leftarrow)\uparrow}}{N_{e,p}^{\uparrow(\leftarrow)\downarrow}/Q_{e,p}^{\uparrow(\leftarrow)\downarrow} + N_{e,p}^{\uparrow(\leftarrow)\uparrow}/Q_{e,p}^{\uparrow(\leftarrow)\uparrow}} \quad (4.10)$$

where $\Delta_{\parallel(\perp)}^{e,p}$ is the rate asymmetry for the electron and positron, $N_{e,p}^{\uparrow(\leftarrow)\downarrow}$ is the number of electrons or positrons detected by the spectrometer, $Q_{e,p}^{\uparrow(\leftarrow)\downarrow}$ is the total of the beam

current. The rate asymmetry for the positron was investigated reversing the polarity of the spectrometer magnet.

In the following subsections, we will discuss about the procedure to extract the cross section asymmetry from the rate asymmetry measured directly in the experiment.

4.2.1 The dead time correction

The dead time correction is defined by the ratio between the true trigger rate and the measured trigger rate. The dead time effect basically depends on the trigger rate. Consequently, it may affect the rate asymmetry if the trigger rates for left- and right-handed spills had a large difference.

The rate asymmetry corrected by the dead time effect is expressed as,

$$(\Delta_{\parallel(\perp)}^{e,p})' = \frac{\frac{N_{e,p}^{\uparrow(\leftarrow)\downarrow}}{Q_{e,p}^{\uparrow(\leftarrow)\downarrow}} C_L - \frac{N_{e,p}^{\uparrow(\leftarrow)\uparrow}}{Q_{e,p}^{\uparrow(\leftarrow)\uparrow}} C_R}{\frac{N_{e,p}^{\uparrow(\leftarrow)\downarrow}}{Q_{e,p}^{\uparrow(\leftarrow)\downarrow}} C_L + \frac{N_{e,p}^{\uparrow(\leftarrow)\uparrow}}{Q_{e,p}^{\uparrow(\leftarrow)\uparrow}} C_R} \quad (4.11)$$

where $C_{L,R}$ is the dead time coefficient for the electron (positron) rate obtained by the left- or right-handed spill.

We calculated the dead time coefficient for a given run;

$$C_{L,R} = \frac{\sum_m t_m \sum_n n \times P(n, m)}{\sum_m \min(m, 4) \times t_m}, \quad (4.12)$$

where t_m is the number of times there were m trigger(s) in a spill, n is the index to indicate the expected trigger rate, and $P(n, m)$ is the matrix element which is defined as the probability to detect m triggers if there are n real triggers. Because the number of triggers in a spill was limited by shower counter electronics to four or less, the measured trigger number could only go up four even if there were more triggers in a spill. The term of $\min(m, 4)$ was inserted instead of m due to this trigger logic.

The matrix element $P(n, m)$ was calculated by a Monte Carlo simulation[49]. In the simulation, we assumed;

1. Triggers distributed randomly in time,
2. Dead time between triggers was $32ns$,
3. n and m were limited to 10.

The 10×10 unitary matrix elements are shown in Table 4.7.

measured trigger	true trigger									
	1	2	3	4	5	6	7	8	9	10
1	1.000	0.028	0.002							
2		0.972	0.086	0.007						
3			0.913	0.155	0.019	0.003				
4				0.838	0.235	0.049	0.008	0.002		
5					0.745	0.321	0.088	0.022	0.006	0.002
6						0.627	0.371	0.147	0.049	0.013
7							0.532	0.407	0.206	0.083
8								0.422	0.415	0.249
9									0.323	0.405
10										0.249

Table 4.7: The probability matrix to the number of triggers detected by the spectrometer. The matrix elements are calculated under the assumptions dead time= 32 ns, Spill length= 2200 ns. A blank means the element is 0.

We did not assume symmetry between left- and right-handed spills for the dead time coefficient, i.e. the coefficients were calculated separately for each handedness.

The dead time correction for both spectrometers are shown in Figure 4.27 and 4.28. The dead time coefficient depends on the trigger rate, and that increased the trigger rates by several percents. The corrections for the left- and right-handed spills usually were similar, so the dead time correction was very small on the asymmetry. Figure 4.29 and 4.30 indicate the asymmetry of the dead time correction for left- and right-handed spills defined by,

$$A_{dc} = \frac{C_L - C_R}{C_L + C_R}. \quad (4.13)$$

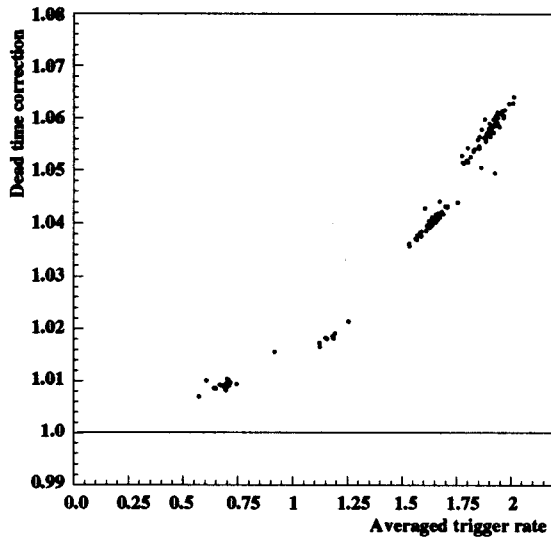


Figure 4.27: Dead time correction as a function of the averaged trigger rate for the 4.5° spectrometer: the horizontal axis shows the averaged rate for main-or trigger. The vertical axis shows the dead time correction. Only the results for left handed spill are plotted.

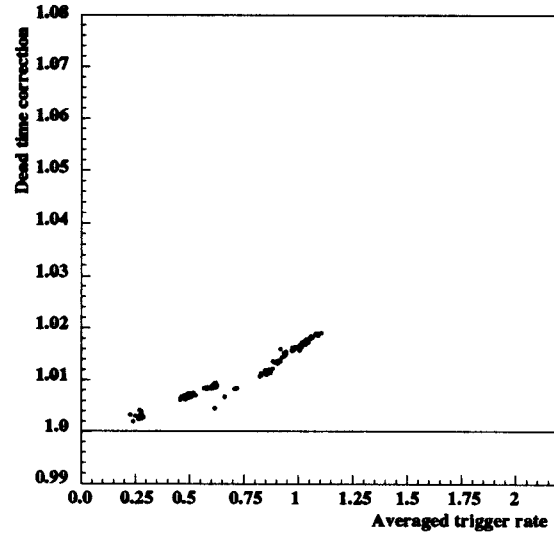


Figure 4.28: Dead time correction for the 7° spectrometer. The data for the left handed spill are shown with the conventions same as Figure 4.27.

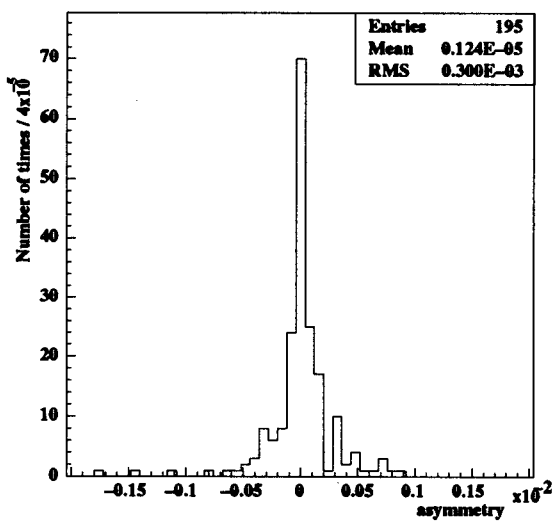


Figure 4.29: The left-right asymmetry on the dead time correction for the 4.5° spectrometer.

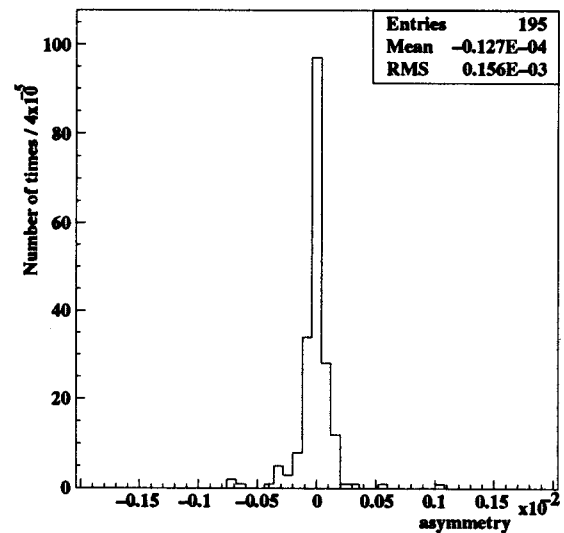


Figure 4.30: The left-right asymmetry on the dead time correction for the 7° spectrometer.

The uncertainty of the dead time correction was estimated to be less than 1.0% of $(1 - C_{L,R})$ from the detail study of the simulation. Therefore, the uncertainty on the asymmetry from the dead time correction was negligible.

4.2.2 beam polarization

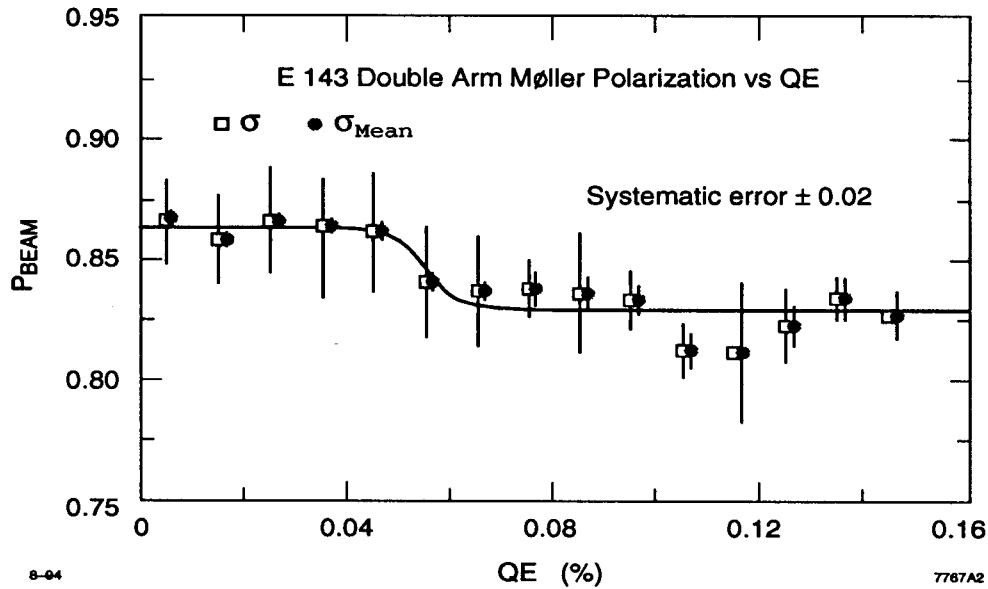


Figure 4.31: The electron polarization is plotted as a function of the quantum efficiency of the cathode of the polarized electron source. The electron polarization is measured by ESA Møller polarimeter. The σ shows the spread of the measurements and the σ_{Mean} shows the mean of these measurements. A step function plotted by a solid line was obtained from the fit with the σ_{Mean} and determined the beam polarization in the analysis.

The beam polarization was determined by ESA Møller polarimeter as mentioned in Section 3. The results from the single arm polarimeter and the double arm polarimeter, and also the Linac polarimeter which is located at the end of the Linac, were in good agreement with each other[34].

Figure 4.31 shows the relation between the quantum efficiency of the electron cathode and the beam polarization measured by the ESA Møller polarimeter. The σ shows the spread of the measurements and the σ_{Mean} is the mean of these measurements. From a

step function obtained from a fit to the σ_{Mean} , the beam polarization was determined for each run. The beam polarization was 84 - 86% during the experiment with the absolute uncertainty of 2%.

4.2.3 Target polarization

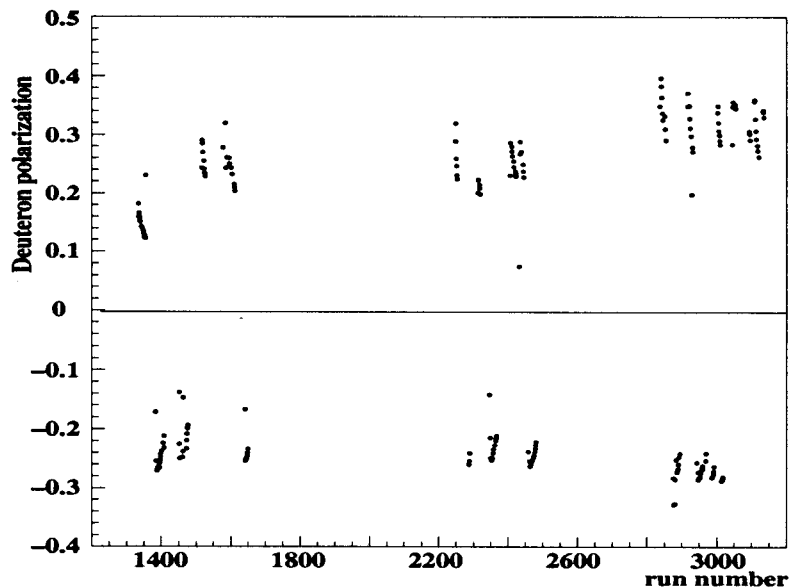


Figure 4.32: The horizontal axis shows run number, the vertical axis shows the ND_3 target polarization. The sign of the polarization is plus for forward, minus for backward to the beam direction.

Target polarization was measured by the NMR signal obtained by the Q-meter module of the Liverpool type calibrated by that for the thermal equilibrium shown in Figure 3.17. The uncertainty of the target polarization was dominated by the statistical error of the NMR measurement for thermal equilibrium to be 4.0% relative to the polarization [50].

Figure 4.32 shows the target polarization during the experiment as a function of the run number. The negative polarization mean that the direction of the polarization is opposite to the beam direction. The target polarization was obtained up to 40% and the average was about 25%.

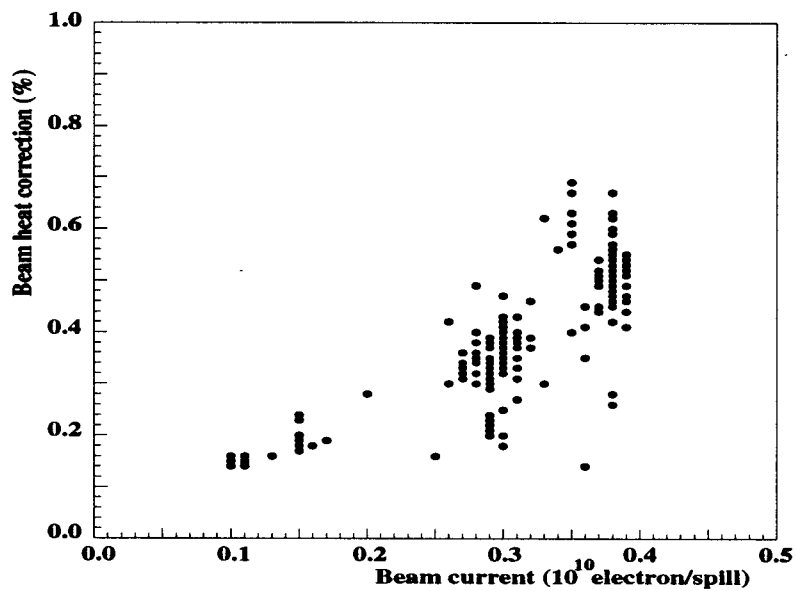


Figure 4.33: The correction for the target polarization due to the beam heat effect. The horizontal axis shows the beam current in a unit of 10^{10} electron/spill. The vertical axis shows the correction in % defined by the difference of the corrected polarization from the measured polarization.

The electron beam heated up the target center where the beam was rastered and the fringe part of the target was refrigerated by the circulated liquid helium directly. So, the target had a gradient of its temperature between the center and the fringe parts. Because the deuteron polarization depends on the temperature, the deuteron polarization is not uniform in the target cell due to the temperature gradient.

On the other hand, the NMR coil surrounded the larger volume of the target material than the volume which was actually on the beam line. So, the results from the NMR measurement averaged the gradient of the target polarization and gave a polarization higher than the polarization where the beam was rastered. The correction was estimated from the actual depolarization with varying the beam current [51]. The correction decreased the target polarization by 1.5% of that with a typical electron current. The correction factor for each run are plotted in Figure 4.33 as a function of the beam current. The correction factor is defined to be the difference between the uncorrected and corrected beam polarizations.

4.2.4 Dilution factor

The target contains not only polarized deuterons, but also unpolarized materials. The materials decrease the asymmetry in proportion to a factor called the dilution factor.

The dilution factor is the ratio between the number of electrons scattered from the deuterons in ND_3 and that from all materials. Neglecting common factors like Avogadro number and Beam flux etc., the number of electrons scattered by a material is generally to be

$$N = \frac{\rho \cdot l}{A} (N_p \sigma_p + N_n \sigma_n) g, \quad (4.14)$$

where ρ is the density of the material, l is the length of the material, A is the mass number of the nucleus, N_p and N_n are the numbers of proton and neutron in the nucleus, σ_p and σ_n are the cross sections for proton and neutron respectively, and g is the EMC effect coefficient for the nucleus. The EMC effect coefficient is the ratio of the cross section per nucleon between a heavier nucleus and a deuteron. The EMC effect coefficient was

determined by a fit done by S. Rock and L. Stuart using the data of deep-inelastic scattering experiments[52][53].

We introduced the packing fraction p_f which is the percentage of the target cell occupied by ND_3 beads. The number of electrons scattered from the ND_3 is expressed using the packing fraction by,

$$N_{\text{ND}_3} = \frac{\rho_{\text{ND}_3} \cdot l_{\text{cell}} \cdot p_f}{21} \{3(\sigma_p + \sigma_n) + (7\sigma_p + 8\sigma_n)g_N\}, \quad (4.15)$$

where ρ_{ND_3} is the density of ND_3 , 21 is the atomic mass number of ND_3 , l_{cell} is the length of the target cell, and g_N is the EMC effect for nitrogen nuclei. Similarly, the number of electrons scattered from the deuteron is

$$N_D = \frac{\rho_{\text{ND}_3} \cdot l_{\text{cell}} \cdot p_f}{21} 3(\sigma_p + \sigma_n). \quad (4.16)$$

We assumed that the other parts of the target cell were filled by liquid helium. The number of electrons scattered from the liquid helium is then expressed as,

$$N_{\text{He}} = \frac{\rho_{\text{He}} \cdot l_{\text{cell}} \cdot (1 - p_f)}{4} (2\sigma_p + 2\sigma_n), \quad (4.17)$$

where the ρ_{He} is the density of the liquid helium.

There were also other materials in or around the target, for example the wall of the cell, the NMR coil etc. Accounting for all of these materials, the dilution factor, f was calculated as follows,

$$f = \frac{N_D}{N_{\text{ND}_3} + N_{\text{He}} + \sum N_{\text{others}}}, \quad (4.18)$$

where the $\sum N_{\text{others}}$ represents the contributions from materials other than ammonia and helium.

We divide both of the numerator and the denominator by σ_p to simplify such that σ_p and σ_n are replaced by 1 and σ_n/σ_p respectively. In the actual calculation, we assumed the ratio of σ_n/σ_p is equal to F_{2n}/F_{2p} which is calculable from the well measured F_{2d}/F_{2p} . The Figures 4.34 and 4.35 show the dilution factor for the 4.5° and 7° spectrometers. The dilution factor was obtained to be $0.23 \sim 0.25$ depending on x because of the variation of the cross sections and the EMC effect. The error of the dilution factor was calculated from the errors of the cross section, EMC effect, the packing fraction, density of materials.

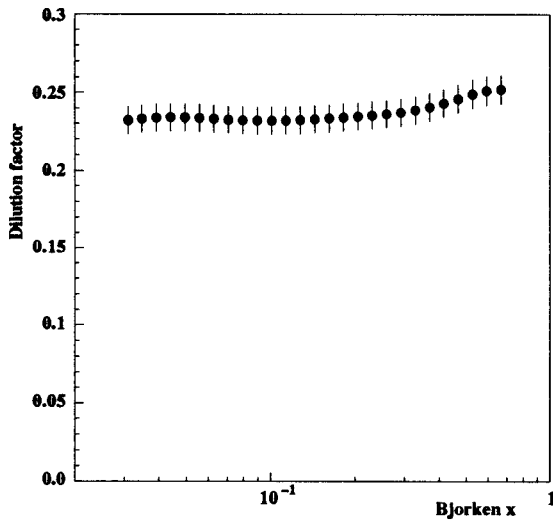


Figure 4.34: Dilution factor on 4.5° spectrometer. The dilution factors are calculated from averaged x and Q^2 for each data point.

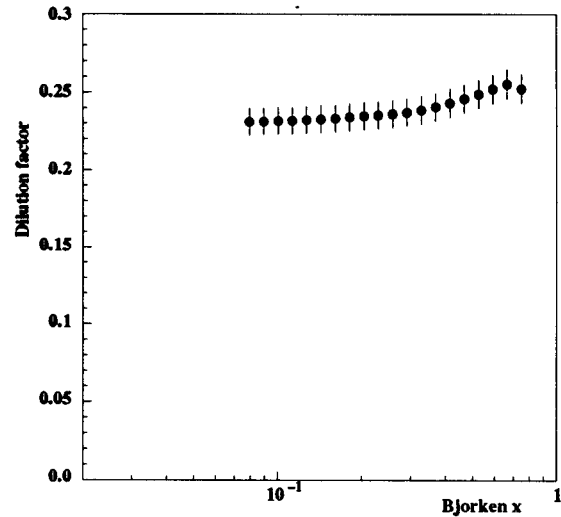


Figure 4.35: Dilution factor on 7° spectrometer. The dilution factors are calculated from averaged x and Q^2 for each data point.

4.2.5 Nitrogen correction

Nucleons (nuclei) other than deuteron could either dilute the asymmetry, or contribute to the asymmetry because a small fraction of these nucleons (nuclei) is polarized. In addition, a contamination of NH_3 gives an asymmetry of protons. We named the correction due to these polarized nucleons (nuclei) other than deuterons as nitrogen correction.

As mentioned in Section 3.4, we used $^{15}\text{ND}_3$ as the target material. The nominal ^{14}N nucleus contaminated the target material by 2.0%. The contamination of proton, i.e. NH_3 , was estimated to be 1.5%. These three kinds of nuclei and nucleon other than deuteron, ^{15}N , ^{14}N , and proton, were polarized in the target. These nitrogen and proton polarizations as a function of the deuteron polarization were measured as shown in Figure D.2 and D.1. We measured only the ^{15}N polarization and assumed that the ^{14}N polarization had the same magnitude and the sign opposite to that for the ^{15}N .

Assuming the contamination by these nuclei and nucleon, the cross section asym-

metry was corrected by the nitrogen correction as follows ¹,

$$(A_{\parallel,\perp}^{e,p})' = \frac{1}{\nu_1} \left[\frac{(\Delta_{\parallel,\perp}^{e,p})'}{p_d p_{df}} - \nu_2 A_h \right], \quad (4.19)$$

where the factor of ν_1 and ν_2 are the functions of the deuteron polarization and typically to be

$$\nu_1 \sim 0.98, \quad (4.20)$$

$$\nu_2 \sim 0.06, \quad (4.21)$$

and A_h is the asymmetry for the proton measurement which we used the results from the E143 measurement using NH_3 target for.

This correction depends on the deuteron polarization varied due to the experimental conditions and the correction was then applied for each run in the analysis.

4.2.6 Positron subtraction

The measured tracks are not only electrons which come from deep-inelastic scattering, but also from other processes, such as pair creation by gammas from neutral pion.

Taking an account of the processes other than deep-inelastic scattering, the cross section counting the electron, $\sigma_e^{\uparrow(\leftarrow)\downarrow(\uparrow)}$ is expressed by,

$$\sigma_e^{\uparrow(\leftarrow)\downarrow(\uparrow)} = \sigma_{dis}^{\uparrow(\leftarrow)\downarrow(\uparrow)} + \sigma_{pair}^{\uparrow(\leftarrow)\downarrow(\uparrow)}, \quad (4.22)$$

where $\sigma_{dis}^{\uparrow(\leftarrow)\downarrow(\uparrow)}$ is the cross section counting the electron from the deep inelastic scattering, and $\sigma_{pair}^{\uparrow(\leftarrow)\downarrow(\uparrow)}$ is the cross section counting the electron from the pair creation etc.

We assumed that the cross section counting electrons from the back-ground processes for deep-inelastic scattering was charge symmetric. Under the assumption, this cross section was estimated from the measurement counting positrons using the reverse magnetic field because the positrons came only from the charge symmetric process. Therefore, the cross section counting the positron $\sigma_p^{\uparrow(\leftarrow)\downarrow(\uparrow)}$ gives the cross section of the charge

¹refer Appendix D for the detail of the derivation of the formula.

symmetric process as,

$$\sigma_{pair}^{\uparrow(\leftarrow)\downarrow(\uparrow)} = \sigma_p^{\uparrow(\leftarrow)\downarrow(\uparrow)}. \quad (4.23)$$

The cross section for deep-inelastic scattering was extracted by subtracting the cross section counting positrons from that counting electrons. We define the total cross sections, σ^e and σ^p , and cross section asymmetries, A^e and A^p , counting electrons and positrons by,

$$\sigma^e = \sigma_e^{\uparrow(\leftarrow)\downarrow} + \sigma_e^{\uparrow(\leftarrow)\uparrow}, \quad (4.24)$$

$$\sigma^p = \sigma_p^{\uparrow(\leftarrow)\downarrow} + \sigma_p^{\uparrow(\leftarrow)\uparrow}, \quad (4.25)$$

$$A_{\parallel(\perp)}^e = \frac{\sigma_e^{\uparrow(\leftarrow)\downarrow} - \sigma_e^{\uparrow(\leftarrow)\uparrow}}{\sigma_e^{\uparrow(\leftarrow)\downarrow} + \sigma_e^{\uparrow(\leftarrow)\uparrow}} \quad (4.26)$$

$$A_{\parallel(\perp)}^p = \frac{\sigma_p^{\uparrow(\leftarrow)\downarrow} - \sigma_p^{\uparrow(\leftarrow)\uparrow}}{\sigma_p^{\uparrow(\leftarrow)\downarrow} + \sigma_p^{\uparrow(\leftarrow)\uparrow}} \quad (4.27)$$

The cross section asymmetry for deep-inelastic scattering, $A_{\parallel,\perp}^{dis}$, is described with these electron and positron cross sections by,

$$\begin{aligned} A_{\parallel(\perp)}^{dis} &= \frac{(\sigma_e^{\uparrow(\leftarrow)\downarrow} - \sigma_p^{\uparrow(\leftarrow)\downarrow}) - (\sigma_e^{\uparrow(\leftarrow)\uparrow} - \sigma_p^{\uparrow(\leftarrow)\uparrow})}{(\sigma_e^{\uparrow(\leftarrow)\downarrow} - \sigma_p^{\uparrow(\leftarrow)\downarrow}) + (\sigma_e^{\uparrow(\leftarrow)\uparrow} - \sigma_p^{\uparrow(\leftarrow)\uparrow})} \\ &= A_{\parallel(\perp)}^e \frac{\sigma^e}{\sigma^e - \sigma^p} - A_{\parallel(\perp)}^p \frac{\sigma^p}{\sigma^e - \sigma^p}. \end{aligned} \quad (4.28)$$

The factor $\frac{\sigma^e}{\sigma^e - \sigma^p}$ is the correction for the dilution for the cross section asymmetry due to the contamination of the charge symmetric process. The second term in Equation (4.28) is the correction due to the asymmetry which the charge symmetric process has.

Figures 4.36 to 4.43 show these factors.

In the actual calculation, we used the electron and positron asymmetry obtained from the Equation 4.19 for the ideal A^p and A^e in the Equations (4.26) and (4.27). We used also the ratio of the counting rates defined to be

$$\frac{\sigma^e}{\sigma^e - \sigma^p} = \frac{N_e^{\uparrow(\leftarrow)\downarrow}/Q_e^{\uparrow(\leftarrow)\downarrow} + N_e^{\uparrow(\leftarrow)\uparrow}/Q_e^{\uparrow(\leftarrow)\uparrow}}{N_e^{\uparrow(\leftarrow)\downarrow}/Q_e^{\uparrow(\leftarrow)\downarrow} + N_e^{\uparrow(\leftarrow)\uparrow}/Q_e^{\uparrow(\leftarrow)\uparrow} - N_p^{\uparrow(\leftarrow)\downarrow}/Q_p^{\uparrow(\leftarrow)\downarrow} - N_p^{\uparrow(\leftarrow)\uparrow}/Q_p^{\uparrow(\leftarrow)\uparrow}}, \quad (4.29)$$

for the ideal ratio of the $\sigma_e/(\sigma_e - \sigma_p)$. This is true for the ratio of the $\sigma_p/(\sigma_e - \sigma_p)$. It is allowed if the temporal fluctuation of the target density and the acceptance and efficiency

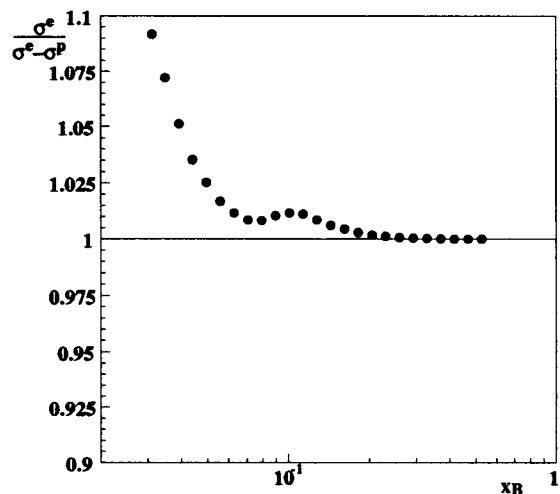


Figure 4.36: The correction for the dilution due to the contamination of electrons from processes other than deep-inelastic scattering on 4.5° spectrometer for A_{\parallel} .

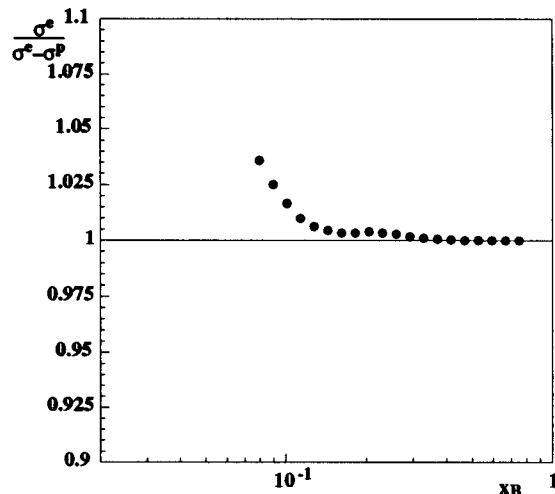


Figure 4.37: The correction for the dilution due to the contamination of electrons from processes other than deep inelastic scattering on 7° spectrometer for A_{\parallel} .

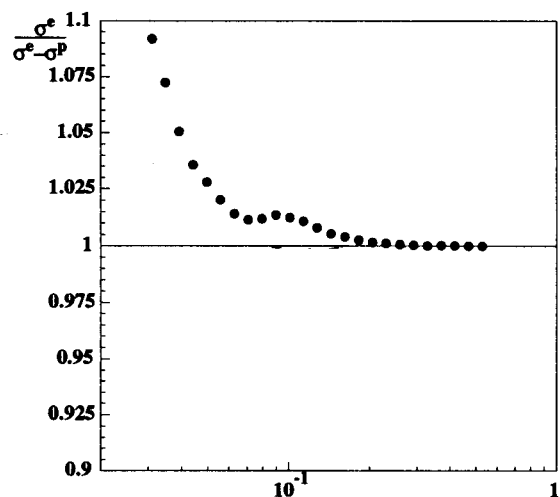


Figure 4.38: The correction for the dilution due to the contamination of electrons from processes other than deep-inelastic scattering on 4.5° spectrometer for A_{\perp} .

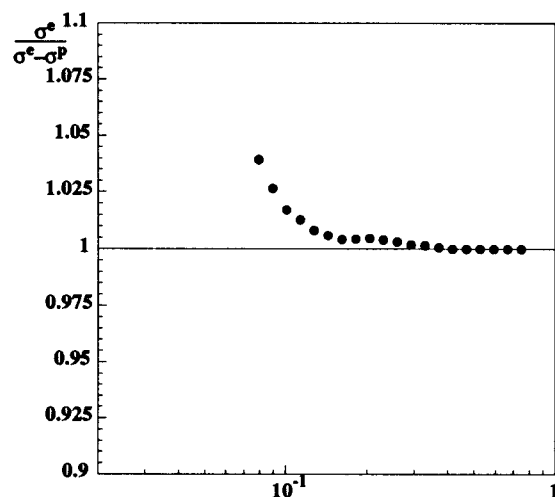


Figure 4.39: The correction for the dilution due to the contamination of electrons from processes other than deep-inelastic scattering on 7° spectrometer for A_{\perp} .

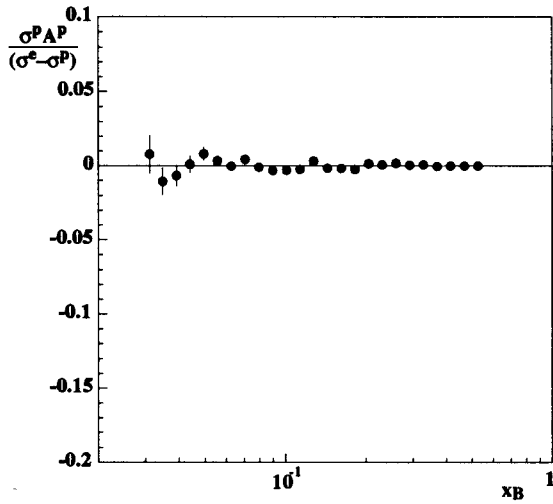


Figure 4.40: The correction due to the asymmetry of the charge symmetric process on 4.5° spectrometer for A_{\parallel} .

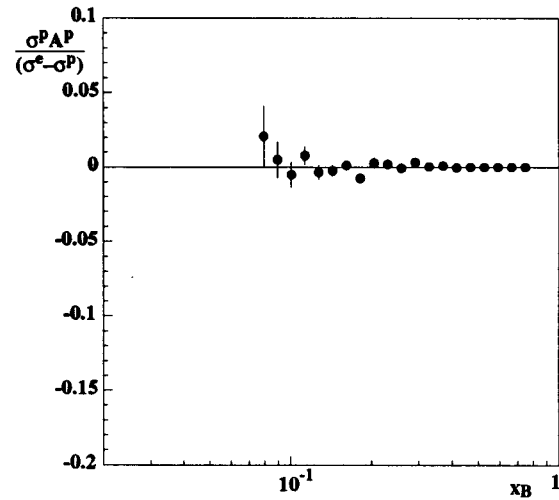


Figure 4.41: The correction due to the asymmetry of the charge symmetric process on 7° spectrometer for A_{\parallel} .

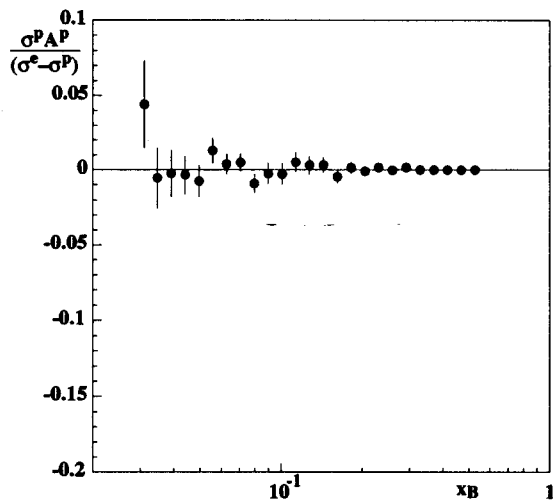


Figure 4.42: The correction due to the asymmetry of the charge symmetric process on 4.5° spectrometer for A_{\perp} .

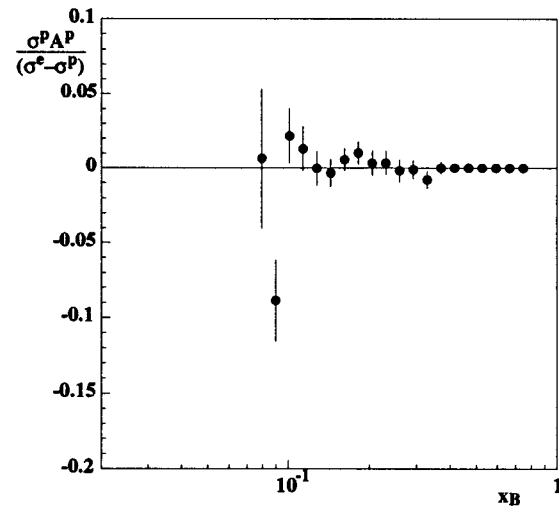


Figure 4.43: The correction due to the asymmetry of the charge symmetric process on 7° spectrometer for A_{\perp} .

of spectrometers were averaged and there was no bias for the electron and positron data and the assumption was guaranteed because we changed the magnet setting several times during the experiment.

4.2.7 Radiative correction

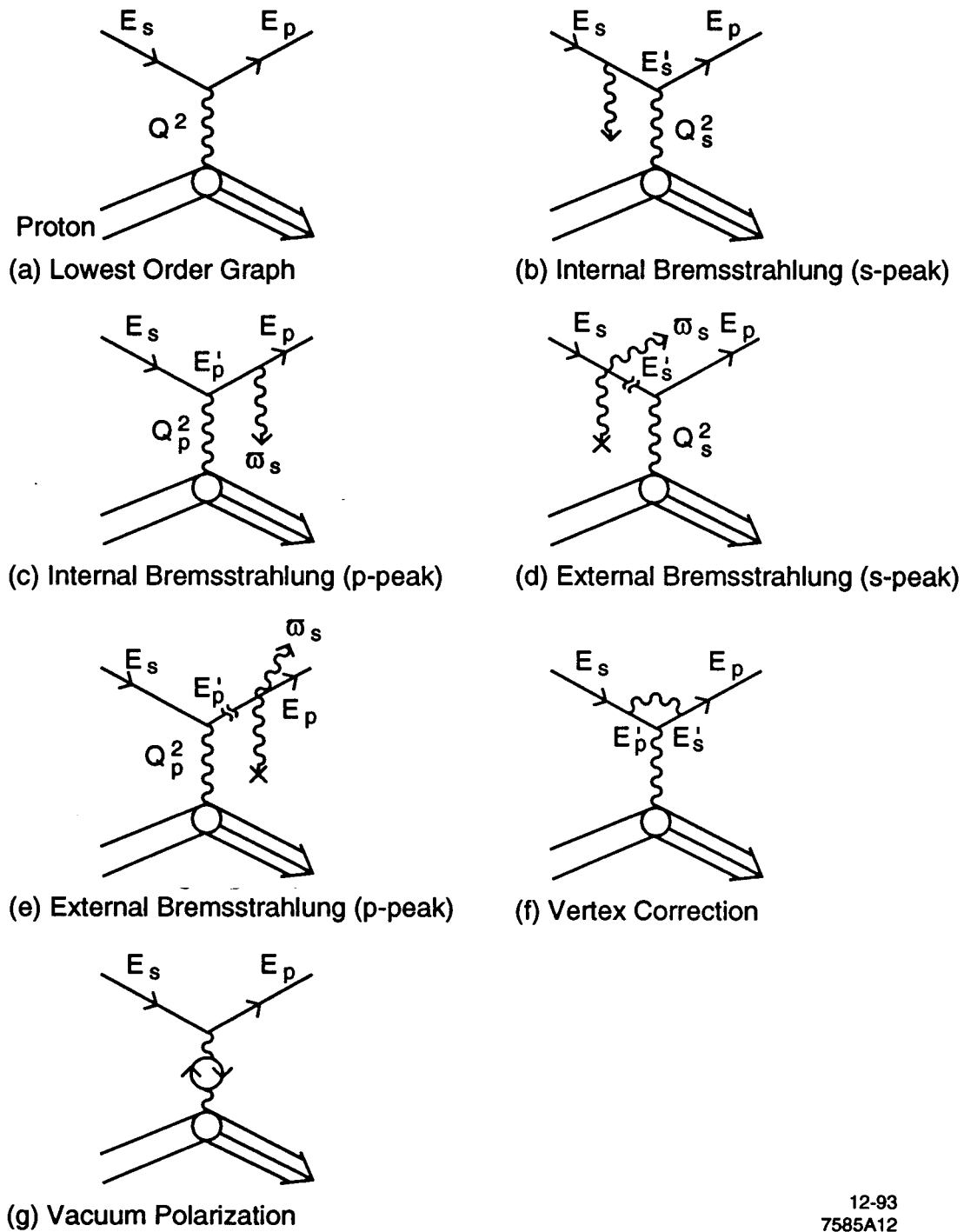
The cross section for deep-inelastic scattering is dominated by the one photon exchange process as shown in the Feynman diagram in Figure 2.1. However, the actual processes of the deep-inelastic scattering contain not only the naive one photon exchange process, but also other processes, for example two photon exchange processes, vacuum polarization, internal-bremsstrahlung etc. In addition, the energy of the scattered electron is varied by the interaction with the external field. To extract the cross section asymmetry for the one photon exchange process from the measured cross section asymmetry, we should estimate the radiative correction.

The radiative correction is categorized into internal and external radiative corrections. The internal radiative correction is due to processes involving self interaction like vertex correction or real photon emission. The external radiative correction is due to interactions with external fields. Leading diagrams accounting in the radiative correction, are shown in Figure 4.44.

The internal radiative correction was calculated based on the method by N.Kukhto and N.Shmeiko [54]. In the radiative correction, contributions from the various higher order diagrams and radiative processes were accounted as follows:

1. Electron vertex correction,
2. Vacuum polarization,
3. Two photon exchange,
4. Elastic radiative process,
5. Quasi-elastic radiative process,

RADIATIVE CORRECTIONS



12-93
7585A12

Figure 4.44: Leading diagrams accounting the in radiative correction

6. Inelastic radiative process.

The proton and neutron form factors for elastic- and quasi-elastic processes were taken from References [55] and [56]. The deuteron form factor for elastic- and quasi-elastic radiative processes was extracted from a fit done by L.M.Stuart [57]. The unpolarized nucleon structure function for inelastic radiative process was taken from References [59] and [60].

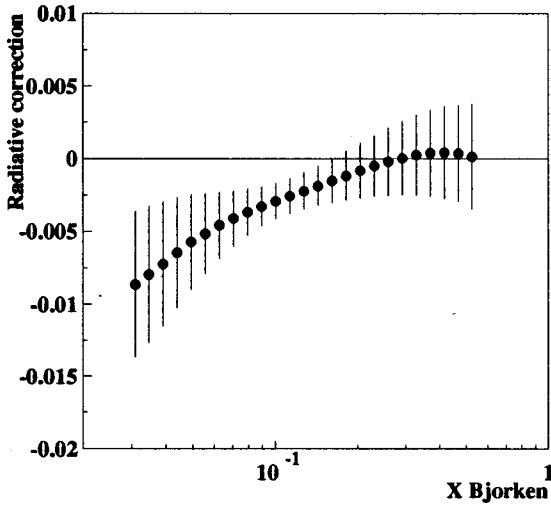


Figure 4.45: Radiative correction on 4.5° for A_{\parallel}

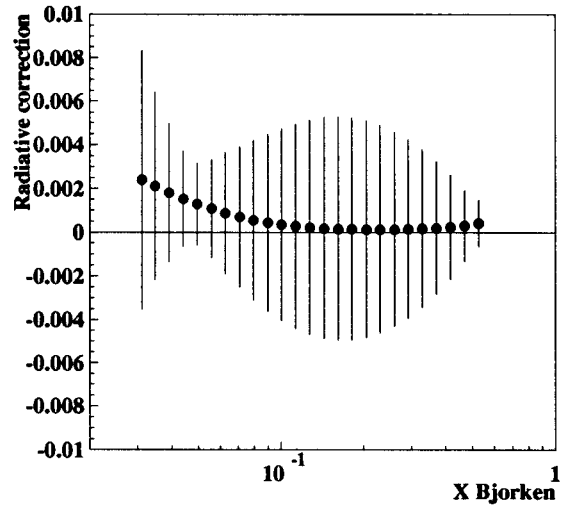


Figure 4.46: Radiative correction on 4.5° for A_{\perp}

The external radiative correction was calculated by Stuart [57] with the formula of

$$\sigma_{ext}(t_a, t_b) = \int I(E_0, E, t_b) \sigma_{int}(E, E') I(E', E'_F, t_a) dE dE', \quad (4.30)$$

where E_0 is the initial energy of electron, E'_F is the energy of the final state electron, and $I(E, E', t)$ is the probability that the energy E becomes to E' after passing through a material of depth t . Then, Equation (4.30) means a cross section that final scattered electron has energy E'_F for given materials.

The external radiative correction was calculated assuming a target model estimated by T. Liu [51] accounting only the external bremsstrahlung.

Figure 4.45, 4.46, 4.47, and 4.48. show the evaluated radiative correction for A_{\parallel} and A_{\perp} of the 4.5° and 7° spectrometers. The radiative correction, $RC_{\parallel, \perp}$, is the difference

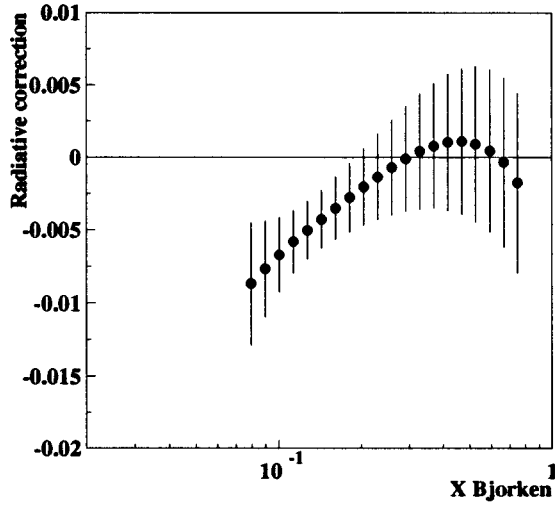


Figure 4.47: Radiative correction on 7° for $A_{||}$

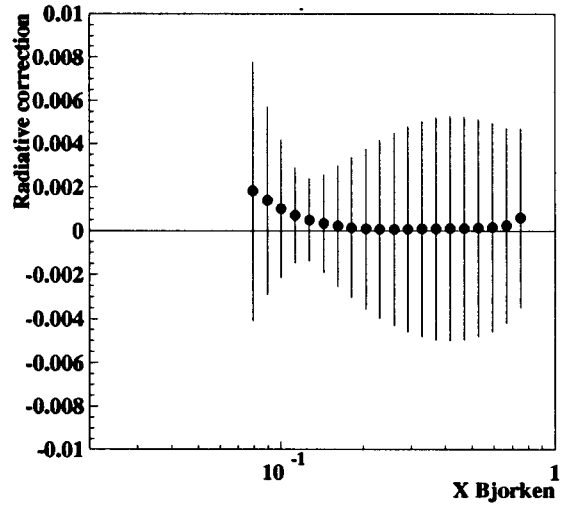


Figure 4.48: Radiative correction on 7° for A_{\perp}

of the cross section asymmetry defined by the one photon exchange process (Born cross section), $A_{||,\perp}$, and that defined by the measured cross section including any radiative and higher order interactions, $A_{||,\perp}^{dis}$.

$$A_{||,\perp} = A_{||,\perp}^{dis} + RC_{||,\perp}. \quad (4.31)$$

The radiative correction for $A_{||}$ decrease the asymmetry in low-x region by less than 0.01. On the other hand, the radiative correction for A_{\perp} is consistent with zero but the large uncertainty.

We defined the radiative correction for the cross section asymmetry in the additional form as shown in Equation (4.31). The reason why we did not introduce the multiplicative form was the definition is too sensitive to the statistical fluctuation on where the asymmetry, $A_{||,\perp}^{dis}$ was very small. In principle, the radiative correction due to the background from the elastic and quasi-elastic scattering etc. should be defined to be a multiplicative form and it corrects not only the central point of the data, but also the magnitude of the statistical error. Therefore, We prepared another correction factor for the statistical error. The statistical error was corrected by the factor to be

$$\delta_{||} = \delta_{||}^{dis} / RC_{||}^{st}, \quad (4.32)$$

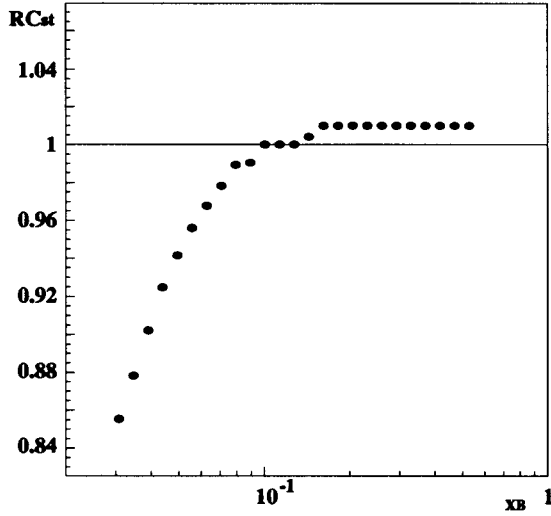


Figure 4.49: Radiative correction for statistical error of A_{\parallel} in the 4.5° spectrometer

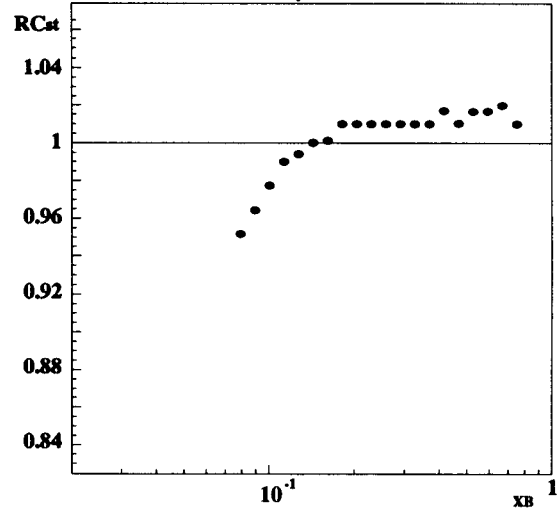


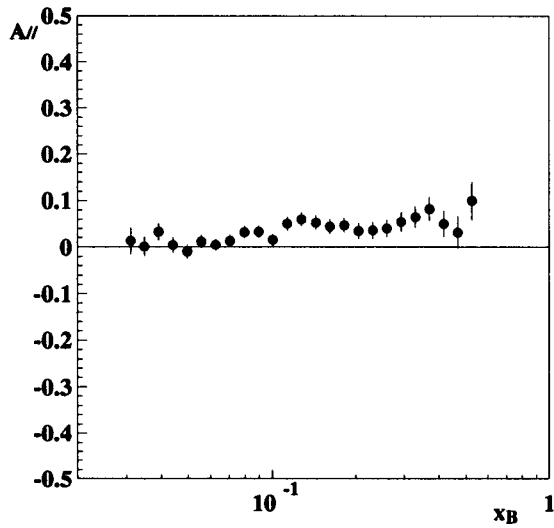
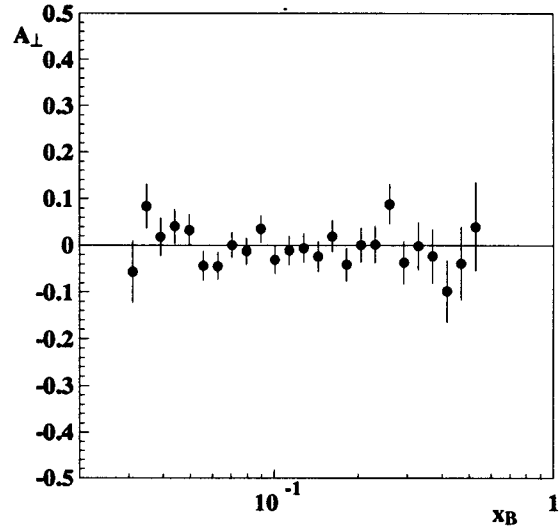
Figure 4.50: Radiative correction for statistical error of A_{\parallel} in the 7° spectrometer

where δ_{\parallel} is the statistical error radiatively corrected, δ_{\parallel}^{dis} is the statistical error for the asymmetry before the radiative correction, and RC_{\parallel}^{st} is the correction factor. The factor for A_{\parallel} on both spectrometers was calculated as shown in Figures 4.49 and 4.50.

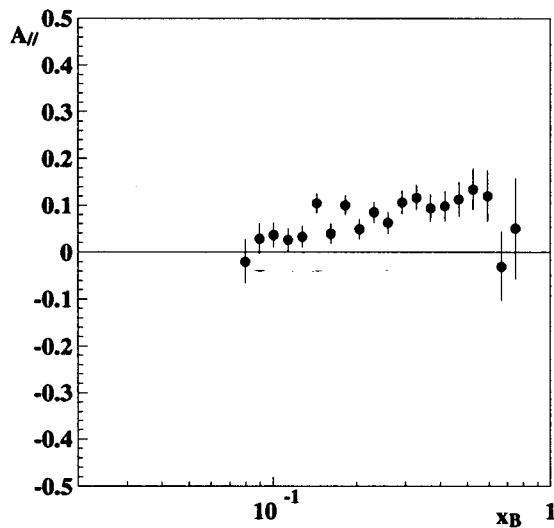
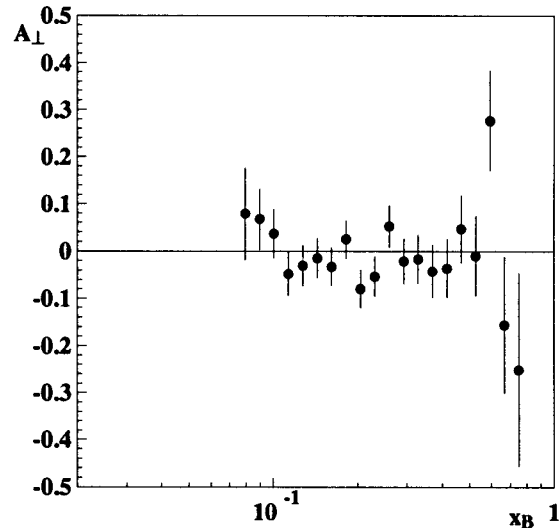
4.2.8 Results

The corrections from the dead time, the beam polarization, the target polarization, the dilution factor, and the nitrogen polarization are the factors which depend strongly on the experimental conditions. We then applied these corrections for each run data. Results from many runs were summarized on the corrected asymmetry separately for the target configuration (longitudinal or transverse), the spectrometer (4.5° or 7°), and the spectrometer magnet setting (electron or positron mode) as follows,

$$\langle A(x)_{\parallel,\perp}^{e,p} \rangle = \frac{\sum_i \left[\frac{1}{\nu_1(x)} \left(\frac{(\Delta_i(x)_{\parallel,\perp}^{e,p})'}{(P_b)_i (P_t)_i f(x)_i} - \nu_2(x) A_h(x) \right) \frac{1}{(\delta_i(x)_{\parallel,\perp}^{e,p})^2} \right]}{\sum_j \frac{1}{(\delta_j(x)_{\parallel,\perp}^{e,p})^2}}, \quad (4.33)$$

Figure 4.51: A_{\parallel} on 4.5° spectrometerFigure 4.52: A_{\perp} on 4.5° spectrometer

where $\langle A(x)_{\parallel,\perp}^{e,p} \rangle$ is the averaged asymmetry, $(\Delta_i(x)_{\parallel,\perp}^{e,p})'$ is the rate asymmetry corrected by the dead time effect, $\delta_i(x)_{\parallel,\perp}^{e,p}$ is the statistical error of the cross section asymmetry for each run.

Figure 4.53: A_{\parallel} on 7° spectrometerFigure 4.54: A_{\perp} on 7° spectrometer

The cross section asymmetry for the deep-inelastic process was calculated by using the Equation (4.28) with the averaged electron and positron asymmetry. Finally, we

applied the radiative correction for the asymmetry. Figure 4.51, 4.52, 4.53, and 4.54 show the results of the cross section asymmetry for both spectrometers and both target configurations.

4.2.9 Study for the systematic effects on the asymmetry

We studied the systematic effects on the cross section asymmetry caused by the direction of the target polarization and the magnetic field on the target.

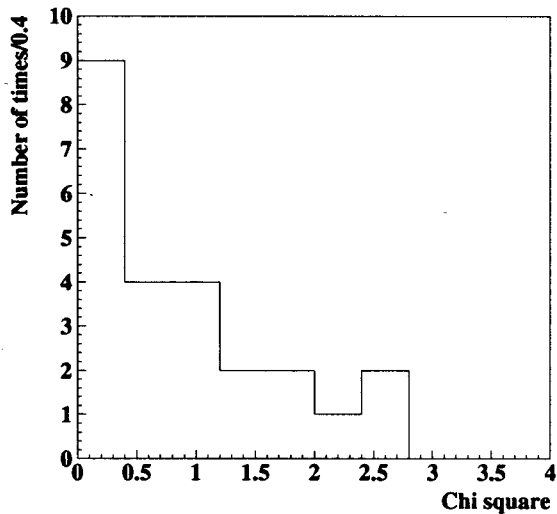


Figure 4.55: The χ^2 distribution of the difference of the A_{\parallel} taken with different target polarization direction in 4.5° spectrometer.

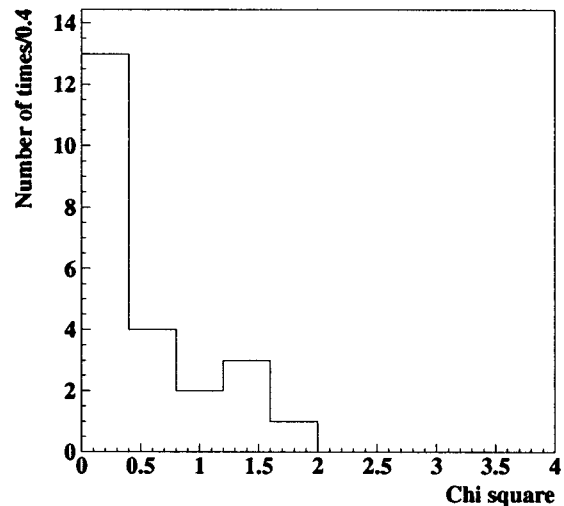


Figure 4.56: The χ^2 distribution of the difference of the A_{\perp} taken with different target polarization direction in 4.5° spectrometer.

The target is polarized by the DNP method with a strong magnetic field and a microwave relaxation technique as mentioned in Section 3. The combination of the direction of the magnetic field and the wave length of the microwave determines the direction of the target polarization. The backward and forward polarization is then possible with the same magnetic field.

We calculated the asymmetry separately for runs which were taken with the positive and negative polarization and magnetic field respectively. Then, we took the difference

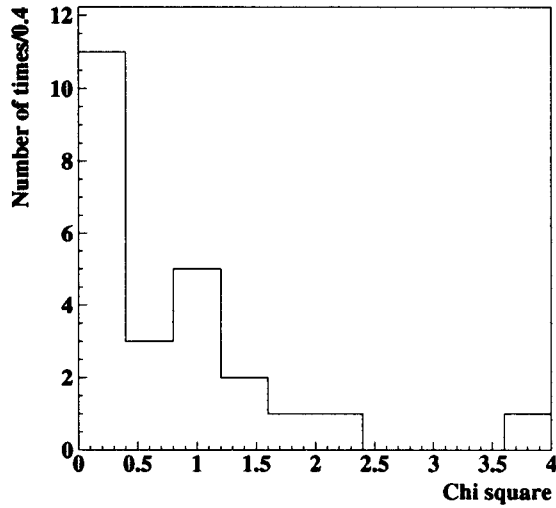


Figure 4.57: The χ^2 distribution of the difference of the A_{\parallel} taken with different target polarization direction in 7° spectrometer.

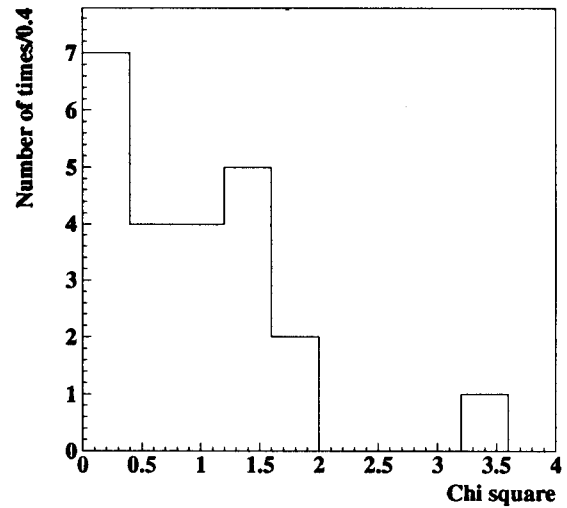


Figure 4.58: The χ^2 distribution of the difference of the A_{\perp} taken with different target polarization direction in 7° spectrometer.

of these two results and calculated the χ^2 of the data by,

$$\chi^2 = A_d(x)^2 / \sigma_d(x)^2, \quad (4.34)$$

where A_d is the difference of two asymmetries, σ_d is the statistical error of A_d calculated by,

$$\sigma_d(x) = \sqrt{\sigma_{pos}(x)^2 + \sigma_{neg}(x)^2}, \quad (4.35)$$

where σ_{pos} and σ_{neg} are the statistical errors of the asymmetries taken with the positive and negative polarization or magnetic field. Figures 4.55 to 4.58 show the χ^2 spectra of the difference of the asymmetries taken with the different target polarization direction. In these four spectra, much part of the data distributes in the region of χ^2 less than 2.0. Our results then seem to have no significant difference due to the polarization direction. We calculated also the mean of the difference for each data set. These mean values are within two standard deviations from zero as follows,

$$\begin{aligned} - A_{\parallel}(4.5) : \quad \overline{A_d} &= -0.006 \pm 0.007, \\ A_{\perp}(4.5) : \quad \overline{A_d} &= -0.011 \pm 0.014, \end{aligned}$$

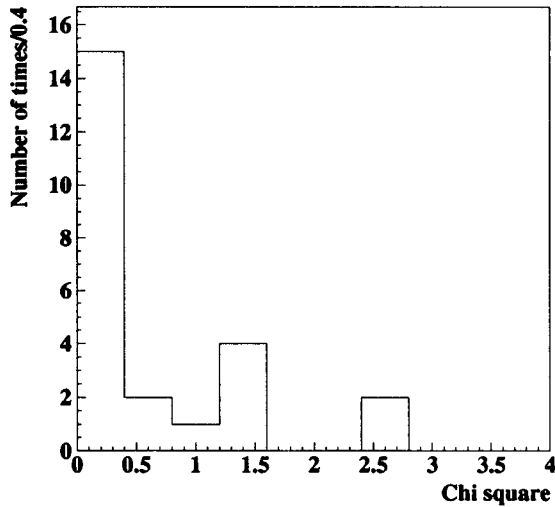


Figure 4.59: The χ^2 distribution of the difference of the A_{\parallel} taken with different magnetic field direction in 4.5° spectrometer.

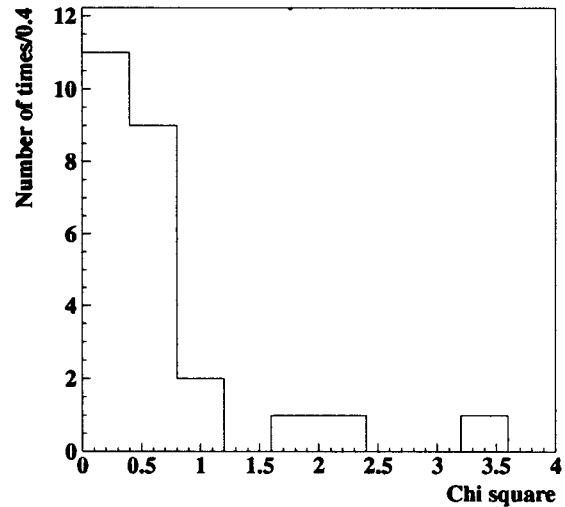


Figure 4.60: The χ^2 distribution of the difference of the A_{\perp} taken with different magnetic field direction in 4.5° spectrometer.

$$A_{\parallel}(7) : \quad \overline{A_d} = 0.010 \pm 0.012,$$

$$A_{\perp}(7) : \quad \overline{A_d} = -0.015 \pm 0.022.$$

Therefore, we observed no significant effect due to the direction of the target polarization.

Figures 4.59 to 4.62 show the χ^2 spectra of the difference of the asymmetries taken with the different direction of the magnetic field. Much part of the data distributes in the region of χ^2 less than 2.0 in these four spectra. Our results then seem to have no significant difference due to the polarization direction. We calculated also the means of the difference for each data set as,

$$A_{\parallel}(4.5) : \quad \overline{A_d} = 0.003 \pm 0.008,$$

$$A_{\perp}(4.5) : \quad \overline{A_d} = -0.014 \pm 0.017,$$

$$A_{\parallel}(7) : \quad \overline{A_d} = -0.023 \pm 0.012,$$

$$A_{\perp}(7) : \quad \overline{A_d} = -0.003 \pm 0.023,$$

which give no significant differences from zero beyond two standard deviations. We observed no systematic effect on the asymmetry due to the magnetic field on the target.

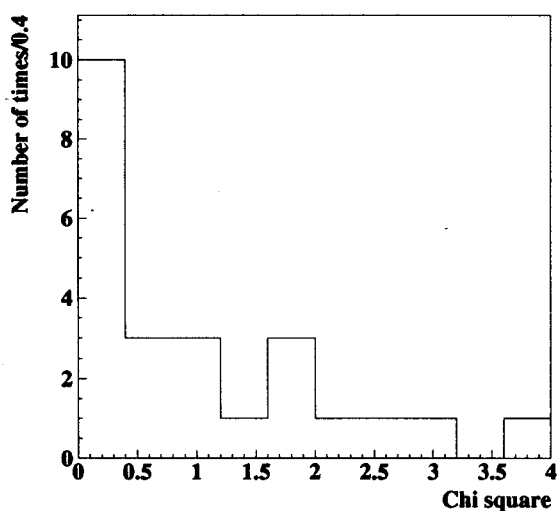


Figure 4.61: The χ^2 distribution of the difference of the A_{\parallel} taken with different direction of the magnetic field in 7° spectrometer.

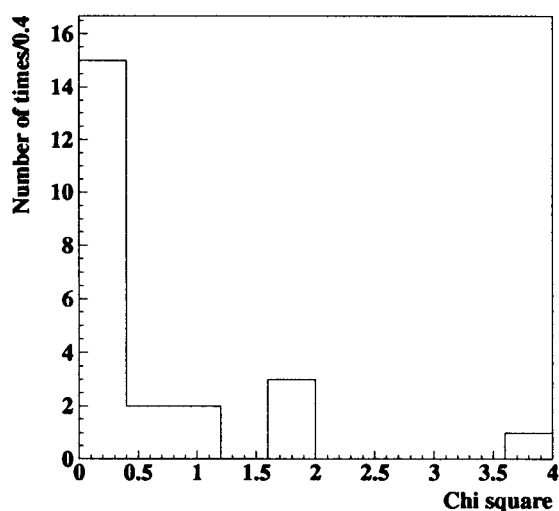


Figure 4.62: The χ^2 distribution of the difference of the A_{\perp} taken with different direction of the magnetic field in 7° spectrometer.

Chapter 5

Results

We will first show our calculation of the spin structure function g_1 for deuteron from the cross section asymmetries obtained in the previous chapter. We determine the integral of the $g_1^d(x)$ over x to examine the prediction from the Ellis-Jaffe sum rule. The quark polarization are also measured for each flavor using the integral of the $g_1^d(x)$.

Combining the $g_1^d(x)$ to the proton spin structure function from E143[18], we obtain the spin structure function for neutron, $g_1^n(x)$ and the difference of the spin structure functions for proton and neutron, $g_1^p(x) - g_1^n(x)$ and calculate these integrals to compare to the predictions from the Ellis-Jaffe sum rule and the Bjorken sum rule.

5.1 g_1 at a common Q^2

The cross section asymmetries, A_{\perp} and A_{\parallel} were measured at the fixed angles and the fixed beam energy which gives Q^2 correlated with x as shown in Figures 4.25 and 4.26. For comparison of the measured Γ_1 with the predictions from the Bjorken and Ellis-Jaffe sum rules, we have to obtain the spin structure function g_1 at a common Q^2 because the predictions depend on Q^2 due to the power corrections of the strong coupling constant $\alpha_s(Q^2)$ as shown in Equations 2.70 and 2.76.

We calculated the $g_1(x)$ at a common Q^2 using two empirical methods treating the Q^2 dependence of the spin structure function in order to obtain the $g_1(x)$ at a common

Q^2 ; one is to assume that $A_1(x, Q^2)$ and $A_2(x, Q^2)$, the virtual photon cross section asymmetries are independent of Q^2 , and other is to assume that $g_1(x, Q^2)/F_1(x, Q^2)$ is independent of Q^2 . In both assumptions, the spin structure function was calculated via the $A_1(x, Q^2)$ and $A_2(x, Q^2)$, or $g_1(x, Q^2)/F_1(x, Q^2)$ respectively. These quantities related the cross section asymmetries $A_{\parallel}(x, Q_m^2)$ and $A_{\perp}(x, Q_m^2)$ to the spin structure function $g_1(x, Q_0^2)$ whose Q_m^2 and Q_0^2 are the measured Q^2 and the common Q^2 , at which those asymmetries were measured or obtained respectively.

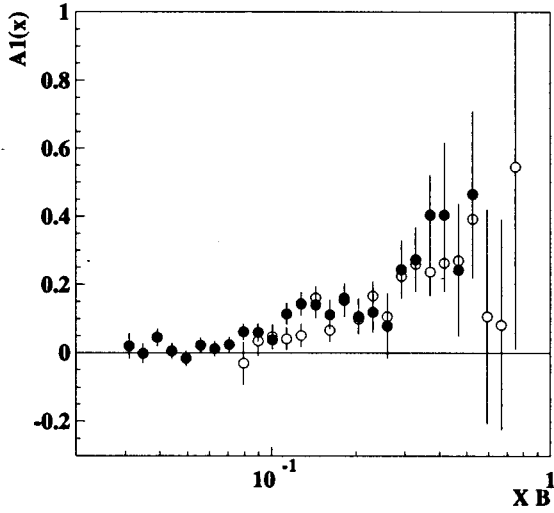


Figure 5.1: The closed and the open circles show $A_1(x)$ from 4.5° and 7° spectrometers respectively. The error bars are statistical only.

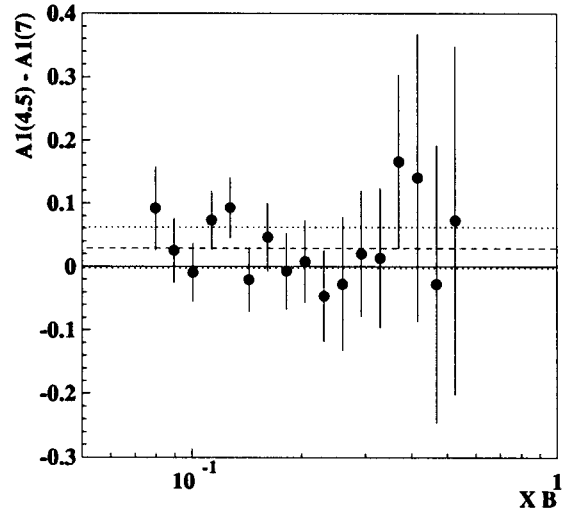


Figure 5.2: The difference between $A_1(x)$ from both spectrometers is plotted. We subtracted the results of the 7° spectrometer from those of the 4.5° spectrometer. The error bar is the quadratic sum of those statistical errors. The dashed and two dotted lines indicate the center value and the band within two standard deviations from the mean of these points.

In the first method, the virtual photon cross sections, $A_1(x, Q_m^2)$ and $A_2(x, Q_m^2)$ are first calculated from the cross section asymmetries, $A_{\parallel}(x, Q_m^2)$ and $A_{\perp}(x, Q_m^2)$ in Equations (2.41) and (2.42) as follows,

$$A_1(x, Q_m^2) = \frac{A_{\parallel}(x, Q_m^2)}{D(1 + \eta\zeta)} - \frac{\eta A_{\perp}(x, Q_m^2)}{d(1 + \eta\zeta)} \quad (5.1)$$

$$A_2(x, Q_m^2) = \frac{\zeta A_{\parallel}(x, Q_m^2)}{D(1 + \eta\zeta)} + \frac{A_{\perp}(x, Q_m^2)}{d(1 + \eta\zeta)}, \quad (5.2)$$

where A_{\parallel} and A_{\perp} were measured at various Q_m^2 from 1.27 to $9.17(\text{GeV}/c)^2$. The kinematical variables, D , d , η , and ζ were given by Equations 2.43, 2.44, 2.45, and 2.46 at the measured Q^2 , Q_m^2 . From the assumption, these $A_1(x, Q_m^2)$ and $A_2(x, Q_m^2)$ are considered to be same as $A_1(x, Q_0^2)$ and $A_2(x, Q_0^2)$ at the common Q^2 , Q_0^2 . Therefore, the following formula gives the spin structure function at the common Q_0^2 ,

$$g_1(x, Q_0^2) = \frac{F_1(x, Q_0^2)}{1 + \gamma^2} [A_1(x, Q_m^2) + \gamma^2 A_2(x, Q_m^2)], \quad (5.3)$$

where γ^2 and F_1 were given at the common Q_0^2 .

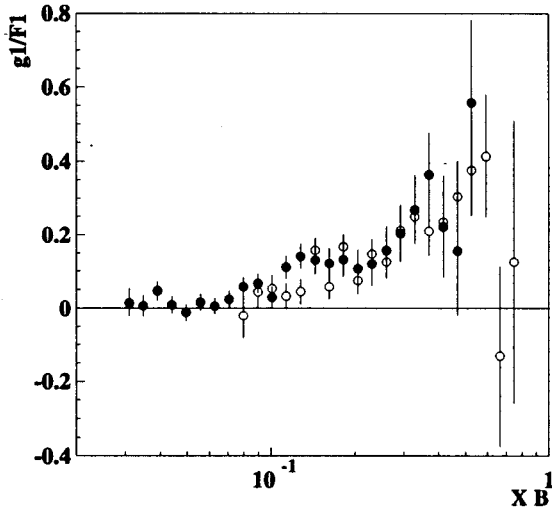


Figure 5.3: g_1/F_1 from both spectrometers are plotted together. The closed and open circle indicate the results from 4.5° spectrometer and 7° spectrometer respectively. The error bars show only the statistical error.

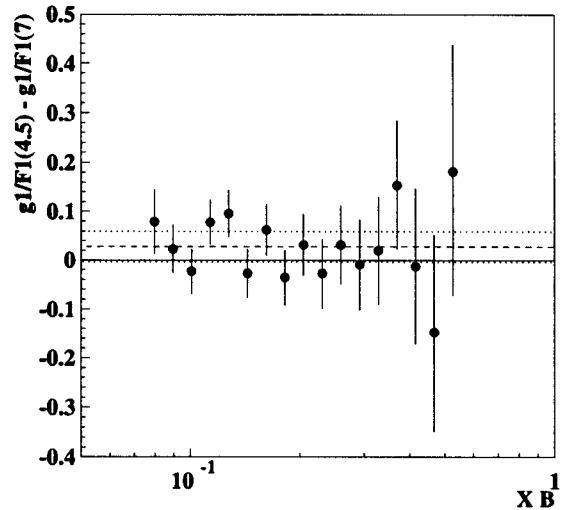


Figure 5.4: The difference of $g_1(x)/F_1(x)$ by 7° spectrometer from those by 4.5° spectrometer are plotted. The error bar indicates the quadratic sum of those statistical errors. The dashed and dotted lines show the central value and the band within two standard deviations from the mean value.

In the second method, the quantity, $g_1(x, Q_m^2)/F_1(x, Q_m^2)$ was calculated from the cross section asymmetries as follows,

$$\frac{g_1(x, Q_m^2)}{F_1(x, Q_m^2)} = \frac{1}{D'} (A_{\parallel}(x, Q_m^2) + \tan(\theta/2) A_{\perp}(x, Q_m^2)), \quad (5.4)$$

x_j	4.5° spectrometer		7° spectrometer	
	$\overline{Q_m^2}$	A_1	$\overline{Q_m^2}$	A_1
0.029 – 0.033	1.27	0.020 ± 0.038	-	-
0.033 – 0.037	1.39	-0.002 ± 0.028	-	-
0.037 – 0.041	1.52	0.045 ± 0.025	-	-
0.041 – 0.047	1.65	0.005 ± 0.025	-	-
0.047 – 0.052	1.78	-0.016 ± 0.023	-	-
0.052 – 0.059	1.92	0.022 ± 0.022	-	-
0.059 – 0.066	2.07	0.012 ± 0.022	-	-
0.066 – 0.075	2.22	0.024 ± 0.022	-	-
0.075 – 0.084	2.38	0.061 ± 0.024	3.17	-0.031 ± 0.062
0.084 – 0.095	2.53	0.060 ± 0.026	3.48	0.034 ± 0.043
0.095 – 0.107	2.69	0.038 ± 0.029	3.79	0.047 ± 0.036
0.107 – 0.120	2.84	0.114 ± 0.031	4.11	0.041 ± 0.034
0.120 – 0.135	3.00	0.144 ± 0.034	4.43	0.051 ± 0.033
0.135 – 0.152	3.15	0.141 ± 0.038	4.77	0.161 ± 0.033
0.152 – 0.171	3.30	0.113 ± 0.042	5.13	0.066 ± 0.033
0.171 – 0.193	3.45	0.154 ± 0.049	5.49	0.161 ± 0.034
0.193 – 0.217	3.59	0.107 ± 0.051	5.86	0.099 ± 0.039
0.217 – 0.245	3.73	0.120 ± 0.059	6.23	0.166 ± 0.042
0.245 – 0.275	3.85	0.079 ± 0.095	6.60	0.106 ± 0.047
0.275 – 0.310	3.98	0.244 ± 0.085	6.96	0.224 ± 0.051
0.310 – 0.349	4.10	0.273 ± 0.094	7.33	0.260 ± 0.058
0.349 – 0.393	4.20	0.404 ± 0.118	7.68	0.238 ± 0.070
0.393 – 0.442	4.30	0.404 ± 0.212	8.03	0.263 ± 0.082
0.442 – 0.498	4.40	0.243 ± 0.193	8.36	0.270 ± 0.103
0.498 – 0.561	4.47	0.464 ± 0.245	8.67	0.392 ± 0.125
0.561 – 0.631	-	-	8.92	0.106 ± 0.313
0.631 – 0.711	-	-	9.05	0.082 ± 0.308
0.711 – 0.800	-	-	9.17	0.546 ± 0.534

Table 5.1: A_1 for both spectrometer. The error is statistical only.

where D' is defined in Equation (2.17). This $g_1(x, Q_m^2)/F_1(x, Q_m^2)$ is equal to that at the common Q_0^2 under the assumption that the $g_1(x, Q^2)/F_1(x, Q^2)$ is independent of the Q^2 . The $g_1(x, Q_0^2)$ at the common Q_0^2 was given to be

$$g_1(x, Q_0^2) = \frac{g_1(x, Q_m^2)}{F_1(x, Q_m^2)} F_1(x, Q_0^2). \quad (5.5)$$

Figure 5.1 shows the $A_1(x)$ as a function of x for the 4.5° (closed circles) and 7° (open circles) spectrometers. Table 5.1 lists the measured values of the $A_1(x)$ for both spectrometers. In order to examine the Q^2 dependence of the $A_1(x)$, figure 5.2 shows the difference of $A_1(x)$ between the 4.5° and 7° spectrometers. The error bar is the quadratic sum of the statistical errors. The dashed and dotted lines indicate the mean and the band within two standard deviations from the mean. The mean of these data were 0.030 ± 0.016 which is within two standard deviations from zero indicating the validity of the assumption that the $A_1(x)$ is independent of Q^2 .

Figure 5.3 shows the $g_1(x)/F_1(x)$ as a function of x for the 4.5° (open circles) and 7° (open circles) spectrometers. Table 5.2 lists the measured values of the $g_1(x)/F_1(x)$ for both spectrometers. Figure 5.4 shows the difference of $g_1(x)/F_1(x)$ between the 4.5° and 7° spectrometers to examine the Q^2 dependence of the $g_1(x)/F_1(x)$. The dashed and dotted lines indicate the mean value of 0.028 ± 0.016 and the band within two standard deviations from the mean value. The mean value was within two standard deviations from zero indicating the validity of the assumption that the $g_1(x)/F_1(x)$ is independent of Q^2 .

From Figures 5.2 and 5.4, we concluded that $g_1(x)/F_1(x)$ and $A_1(x)$ are independent of Q^2 . Thus, for further calculation, we combined the 4.5° and 7° data weighted by the statistical error for g_1/F_1 and A_1 . The combined results are shown in Figure 5.5 and 5.6 together with the $A_1(x)$ data from SMC[16]. Our measurements of $A_1(x)$ are in good agreement to those from SMC in the overlapped region and shows similar behavior as predicted by Carlitz and Kauer model in Appendix C, ie. the $A_1(x)$ approaches to 1 at $x = 1$ and 0 at $x = 0$ respectively.

As will be mentioned later, these two assumptions did not cause any significant

x_j	4.5° spectrometer		7° spectrometer	
	$\overline{Q_m^2}$	g_1/F_1	$\overline{Q_m^2}$	g_1/F_1
0.029 – 0.033	1.27	0.015 ± 0.037	-	-
0.033 – 0.037	1.39	0.006 ± 0.028	-	-
0.037 – 0.041	1.52	0.047 ± 0.025	-	-
0.041 – 0.047	1.65	0.009 ± 0.024	-	-
0.047 – 0.052	1.78	-0.012 ± 0.023	-	-
0.052 – 0.059	1.92	0.016 ± 0.022	-	-
0.059 – 0.066	2.07	0.006 ± 0.022	-	-
0.066 – 0.075	2.22	0.024 ± 0.022	-	-
0.075 – 0.084	2.38	0.058 ± 0.024	3.17	-0.020 ± 0.062
0.084 – 0.095	2.53	0.067 ± 0.026	3.48	0.044 ± 0.043
0.095 – 0.107	2.69	0.030 ± 0.028	3.79	0.053 ± 0.036
0.107 – 0.120	2.84	0.111 ± 0.031	4.11	0.033 ± 0.034
0.120 – 0.135	3.00	0.141 ± 0.034	4.43	0.045 ± 0.033
0.135 – 0.152	3.15	0.131 ± 0.037	4.77	0.158 ± 0.033
0.152 – 0.171	3.30	0.121 ± 0.041	5.13	0.058 ± 0.033
0.171 – 0.193	3.45	0.131 ± 0.046	5.49	0.167 ± 0.034
0.193 – 0.217	3.59	0.107 ± 0.051	5.86	0.075 ± 0.037
0.217 – 0.245	3.73	0.120 ± 0.059	6.23	0.147 ± 0.040
0.245 – 0.275	3.85	0.157 ± 0.067	6.60	0.125 ± 0.044
0.275 – 0.310	3.98	0.203 ± 0.078	6.96	0.213 ± 0.050
0.310 – 0.349	4.10	0.268 ± 0.093	7.33	0.249 ± 0.058
0.349 – 0.393	4.20	0.364 ± 0.112	7.68	0.210 ± 0.067
0.393 – 0.442	4.30	0.222 ± 0.138	8.03	0.235 ± 0.079
0.442 – 0.498	4.40	0.156 ± 0.175	8.36	0.304 ± 0.098
0.498 – 0.561	4.47	0.558 ± 0.223	8.67	0.376 ± 0.123
0.561 – 0.631	-	-	8.92	0.414 ± 0.166
0.631 – 0.711	-	-	9.05	-0.131 ± 0.243
0.711 – 0.800	-	-	9.17	0.125 ± 0.384

Table 5.2: g_1/F_1 for both spectrometer. The error is only statistical

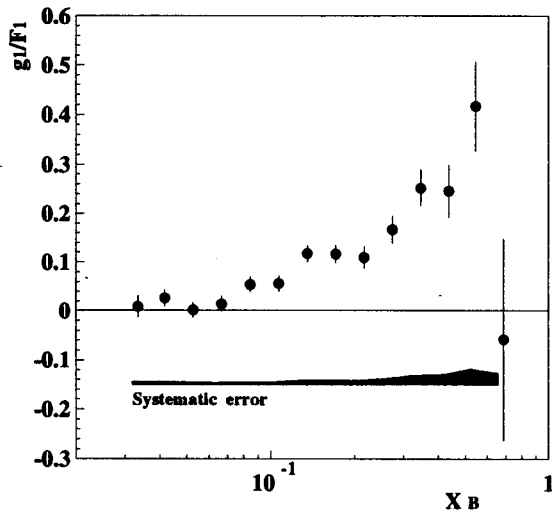


Figure 5.5: g_1/F_1 for deuteron: The results from both spectrometers were combined. The error bars are statistical only. The black area indicates the size of the systematic errors.

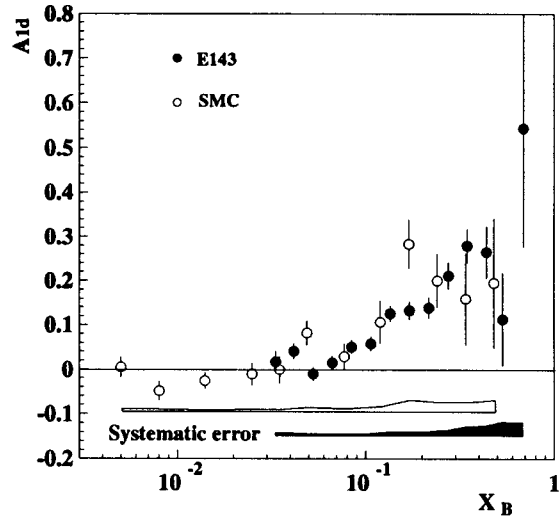


Figure 5.6: A_1 for deuteron: The closed and open circle show the $A_1(x)$ results from E143 and SMC respectively. The error bars are statistical only. The open and closed areas indicate the sizes of the systematic errors for E143 data and SMC data respectively.

difference for $g_1(x)$. Furthermore, the E143 analysis including the data taken at beam energies of 16 GeV and 10 GeV demonstrated that $g_1(x)/F_1(x)$ was independent of Q^2 over the range of $0.3 < Q^2 < 10.0(\text{GeV}/c)^2$ [58]. Therefore, I used the $g_1(x)$ obtained by the second method under the assumption that $g_1(x, Q^2)/F_1(x, Q^2)$ is independent of Q^2 in the further calculation.

5.2 Deuteron spin structure function

The spin structure function for the deuteron was calculated from $A_{\parallel}(x, Q_m^2)$ and $A_{\perp}(x, Q_m^2)$ using the Equations (5.4) and (5.5). The structure function $F_1(x, Q^2)$ was evaluated by using $F_2(x, Q^2)$ and $R(x, Q^2)$ in the Equation (2.14). The $F_2(x, Q^2)$ was calculated by using the parameterization obtained from the results of muon-nucleon scattering at CERN by New Muon Collaboration (NMC)[59]. The $R(x, Q^2)$ was calculated from a global analysis for the past SLAC electron-nucleon deep-inelastic experiments[60]. We set the

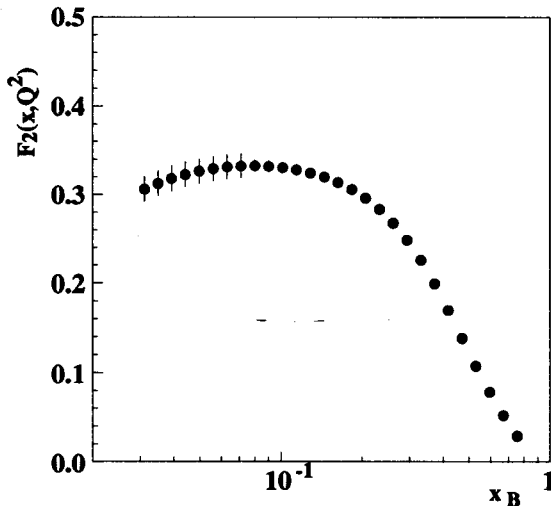


Figure 5.7: $F_2(x, Q^2)$ by the NMC parameterization at $Q_0^2 = 3.0(\text{GeV}/c)^2$

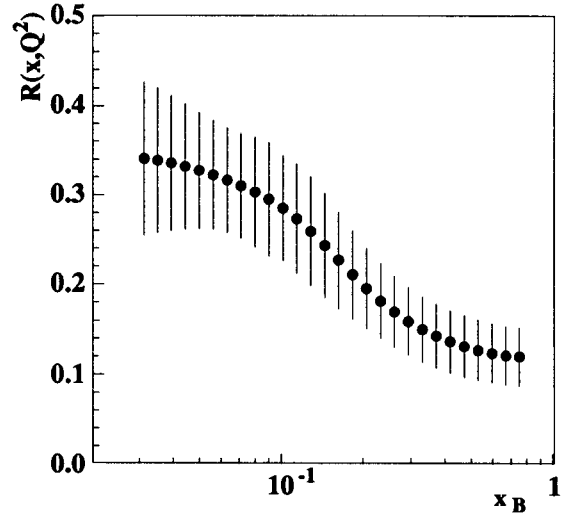


Figure 5.8: $R(x, Q^2)$ by the SLAC global analysis at $Q_0^2 = 3(\text{GeV}/c)^2$

common Q_0^2 at $3.0(\text{GeV}/c)^2$ which was nearly equal to the average of the measured Q^2 . Figures 5.7 and 5.8 show $F_2(x, Q_0^2)$ and $R(x, Q_0^2)$ at the common $Q_0^2 = 3.0(\text{GeV}/c)^2$.

Figure 5.9 shows the g_1 for the deuteron at $Q^2 = 3.0(\text{GeV}/c)^2$ obtained from

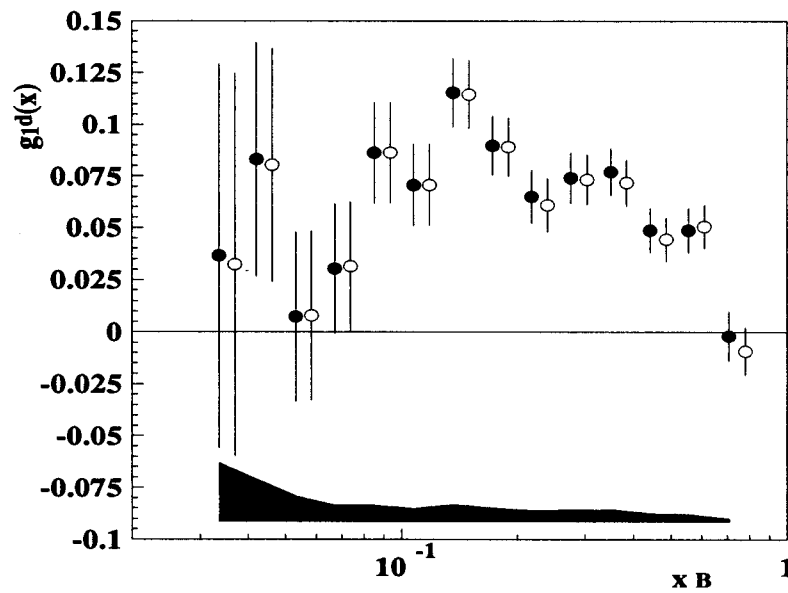


Figure 5.9: The closed circles show the $g_1(x)$ for deuteron at $Q^2 = 3.0(GeV/c)^2$. The error bars are statistical only. The results under the assumptions that A_1 is independent of Q^2 are shown by the open circles for comparison. The dark area indicates the size of the systematic error of $g_1^d(x)$.

the E143 measurement. The closed circles show the $g_1(x)$ under the assumption that $g_1(x, Q^2)/F_1(x, Q^2)$ is independent of Q^2 . The error bars are only statistical. The dark area shows the size of the systematic error. For comparison, the results obtained under the assumption that $A_1(x, Q^2)$ and $A_2(x, Q^2)$ are independent of Q^2 are also plotted by the open circles just aside of the closed circles indicating that the two assumptions caused no significant difference for g_1 .

5.3 Proton spin structure function

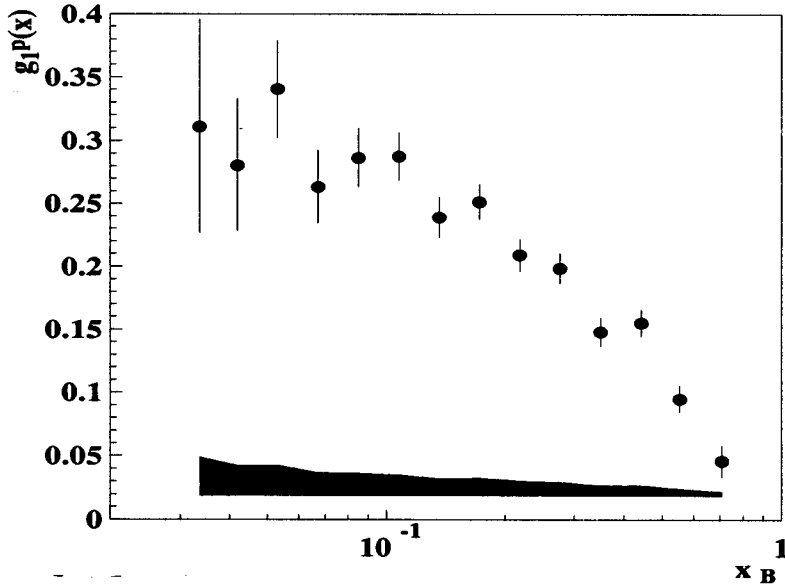


Figure 5.10: The spin structure function $g_1(x)$ for proton at $Q^2 = 3.0(\text{GeV}/c)^2$; The $g_1(x)$ for proton was recalculated using the results of the polarized e-p scattering from E143 [18]. The error bars are statistical only. The dark area shows the size of the systematic error.

The results for the proton spin structure function, $g_1^p(x)$ from E143 were published elsewhere [18]. We recalculated the $g_1^p(x)$ for this analysis with the updated programs using the new data set. The updated programs used for this analysis were basically same as those used for analysis in Ref. [18], but we applied newly the beam heating correction

x_j	$\overline{Q^2}$	$g_1^d(g_1/F_1)$	$g_1^d(A_1A_2)$
0.029 – 0.033	1.27	.065 ± .166	.073 ± .166
0.033 – 0.037	1.39	.024 ± .111	.014 ± .111
0.037 – 0.041	1.52	.164 ± .089	.162 ± .089
0.041 – 0.047	1.65	.028 ± .073	.025 ± .073
0.047 – 0.052	1.78	-.033 ± .062	-.036 ± .062
0.052 – 0.059	1.92	.038 ± .054	.041 ± .054
0.059 – 0.066	2.07	.012 ± .047	.014 ± .046
0.066 – 0.075	2.22	.045 ± .042	.045 ± .042
0.075 – 0.084	2.48	.081 ± .037	.082 ± .037
0.084 – 0.095	2.78	.090 ± .033	.090 ± .033
0.095 – 0.107	3.11	.051 ± .029	.052 ± .029
0.107 – 0.120	3.43	.087 ± .027	.086 ± .027
0.120 – 0.135	3.74	.094 ± .024	.094 ± .024
0.135 – 0.152	4.07	.133 ± .023	.132 ± .023
0.152 – 0.171	4.41	.067 ± .021	.066 ± .021
0.171 – 0.193	4.75	.110 ± .020	.109 ± .020
0.193 – 0.217	5.10	.054 ± .019	.049 ± .019
0.217 – 0.245	5.44	.076 ± .018	.072 ± .018
0.245 – 0.275	5.76	.063 ± .017	.066 ± .017
0.275 – 0.310	6.08	.084 ± .017	.080 ± .017
0.310 – 0.349	6.43	.085 ± .016	.081 ± .016
0.349 – 0.393	6.77	.069 ± .016	.063 ± .016
0.393 – 0.442	7.11	.051 ± .015	.044 ± .015
0.442 – 0.498	7.41	.046 ± .015	.045 ± .015
0.498 – 0.561	7.67	.055 ± .014	.050 ± .014
0.561 – 0.631	8.92	.040 ± .016	.051 ± .016
0.631 – 0.711	9.05	-.009 ± .017	-.015 ± .016
0.711 – 0.800	9.17	.006 ± .017	-.004 ± .016

Table 5.3: g_1^d under the two assumptions; $g_1^d(g_1/F_1)$ was taken assuming that $g_1(x, Q^2)/F_1(x, Q^2)$ was independent of Q^2 . $g_1^d(A_1A_2)$ was calculated assuming that $A_1(x, Q^2)$ and $A_2(x, Q^2)$ are independent of Q^2 .

for the present analysis. For the old date set, we added a series of runs which were lost in the previous due to the wrong headers of the data files. We removed data from several runs due to the bad beam conditions, the bad target conditions etc. From these improvements, the $g_1^p(x)$ integral for the data region was obtained to be

$$\text{recalculated : } \int_{0.029}^{0.8} g_1(x)^p dx = 0.117 \pm 0.004(\text{stat}) \pm 0.007(\text{syst}), \quad (5.6)$$

to be compared with the previous value of

$$\text{published : } \int_{0.029}^{0.8} g_1(x)^p dx = 0.120 \pm 0.004(\text{stat}) \pm 0.008(\text{syst}), \quad (5.7)$$

where the systematic error decreased slightly because the error of the beam polarization was estimated to be 2% which was taken to be 4% in the previous calculation. Figure 5.10 shows the $g_1^p(x)$ obtained from the reanalysis at $Q^2 = 3.0(\text{GeV}/c)^2$. The error bars are statistical only. The dark area shows the size of the systematic error. In the followings, we use the updated $g_1^p(x)$.

5.4 Neutron spin structure function and $g_1^p(x) - g_1^n(x)$

From the deuteron and proton spin structure functions, we can derive the neutron structure function. The Equation (2.58) gives the relation between the $g_1(x)$ of deuteron, neutron, and proton to be

$$g_1^n(x) = \frac{2}{1 - 3/2w_D} g_1^d(x) - g_1^p(x), \quad (5.8)$$

where w_D is the D-state probability of the deuteron fixed at 0.06 ± 0.01 [28] in the whole x region. Figure 5.11 shows the results of the neutron $g_1^n(x)$ at $Q^2 = 3.0(\text{GeV}/c)^2$. The error bars are statistical only. The dark area shows the size of the systematic error.

The difference $g_1^p(x) - g_1^n(x)$ which can be compared to the prediction from the Bjorken sum rule was calculated by combining of our deuteron and proton results. This difference is expressed in terms of $g_1^d(x)$ and $g_1^p(x)$ by,

$$g_1^p(x) - g_1^n(x) = 2g_1^p(x) - \frac{2}{1 - 3/2w_D} g_1^d(x). \quad (5.9)$$

Figure 5.12 shows the difference, $g_1^p(x) - g_1^n(x)$ at $Q^2 = 3.0(\text{GeV}/c)^2$.

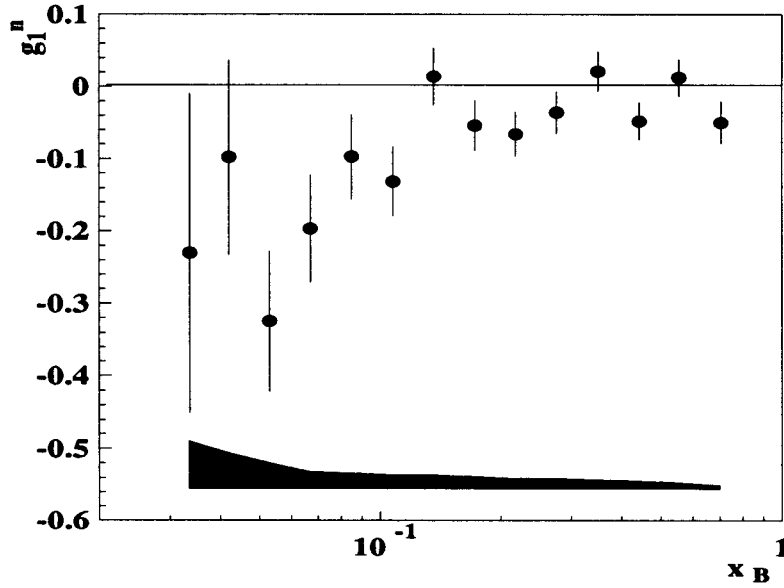


Figure 5.11: The neutron $g_1(x)$: the closed circle shows the results from the E143 at $Q^2 = 3.0(\text{GeV}/c)^2$. The error bars are statistical only. The dark area shows the size of the systematic error.

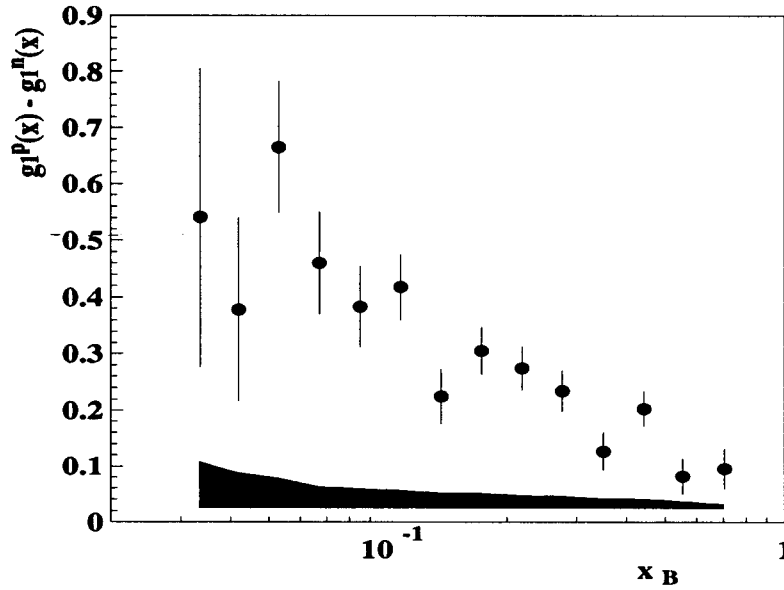


Figure 5.12: $g_1^p(x) - g_1^n(x)$ at $Q^2 = 3.0$. The error bars are statistical only. The dark area shows the size of the systematic error.

5.5 systematic error

We estimated the systematic errors for g_1 possibly arose from the following sources,

1. Beam polarization,
2. Target polarization,
3. Target dilution factor,
4. Radiative correction,
5. F_2 and R ,
6. D-state probability of deuteron,
7. Nitrogen correction,

which will be explained in the following sections.

5.5.1 Beam polarization

Beam polarization was evaluated from the quantum efficiency of the cathode of the polarized electron source. The correlation between the quantum efficiency and the beam polarization was calibrated by the measurement of Møller polarimeter as shown in Figure 4.31. The E143 collaboration studied the following uncertainties and estimated to be [61];

1. Quantum efficiency parameterization 0.25%,
2. Analyzing power 0.25%,
3. Agreement between foils 0.5 %,
4. Foil measurement uncertainty 1.0 %,
5. Environmental influences 1.0 %,
6. Anomalous data spread 1.2 %,

where the 'Agreement between foils' is the systematic error due to the deviation of the data obtained from the foils with various thicknesses, the 'Environmental influences' is the error due to the geometrical location of the foil and other equipments near the

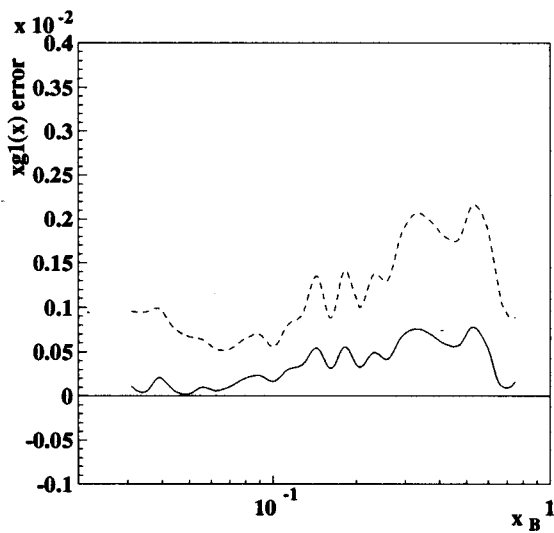


Figure 5.13: Systematic error of xg_1 for deuteron due to the beam polarization. Horizontal axis indicates Bjorken x in logarithm scale. Vertical axis shows x times error of $g_1(x)$: The solid and dashed curves are the systematic error of $xg_1(x)$ due to the beam polarization and the total systematic error.

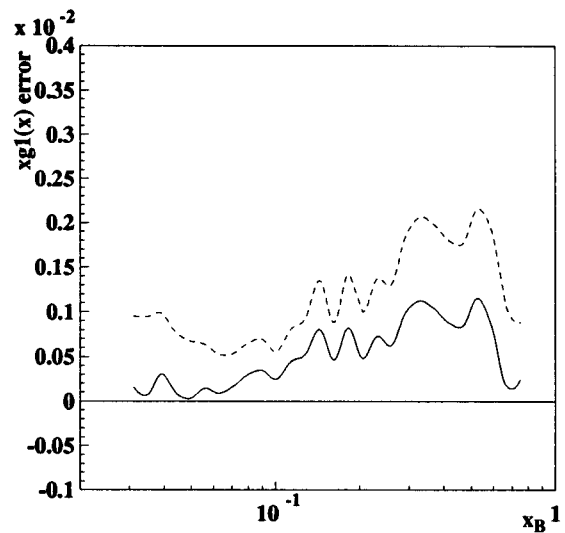


Figure 5.14: Systematic error of xg_1 deuteron due to the target polarization: the results are shown with the same conventions as Figure 5.13

foil target. The total uncertainty of the beam polarization was estimated to be 2.0% in absolute. Because the beam polarization was 84 ~ 86% typically, the fractional error, $\delta P_b/P_b$ was to be 2.4%. The error of g_1 due to the uncertainty of the beam polarization was estimated by using,

$$\delta g_1(x) = \frac{F_1(x, Q_0^2)}{D'} (A_{\parallel} - RC) \frac{\delta P_b}{P_b}, \quad (5.10)$$

where we neglect of the error of A_{\perp} because this error is suppressed by the factor of $\tan(\theta/2)$ which is 0.04 for 4.5° spectrometer and 0.06 for 7° spectrometer. The $A_{\parallel} - RC$ is the cross section asymmetry including any higher order and radiative process, ie. the cross section asymmetry measured actually. Because the radiative correction is independent of the beam polarization, we subtracted the radiative correction from the A_{\parallel} .

Figure 5.13 shows the beam polarization uncertainty of $x\delta g_1(x)$ for deuteron. The solid curve shows the error of $xg_1(x)$ due to the beam polarization and the dashed line is the total systematic error of $xg_1(x)$. Because the x axis is in logarithm scale, the $g_1(x)$ integral over x is proportional to the area of $xg_1(x)$ in this figure, that is

$$g_1(x)dx = xg_1(x)d(\log x). \quad (5.11)$$

Therefore, the plot of the error of $xg_1(x)$ in logarithm scale is good to see the contribution of the error to the integral of $g_1(x)$.

5.5.2 Target polarization

The target polarization was extracted from the measurement of the NMR signal calibrated by thermal equilibrium signal which corresponds to polarization by the Boltzmann distribution. The statistical error of the thermal equilibrium measurement dominated the uncertainty of the target polarization which was estimated to be 4.0% for the deuteron target [50],

$$\frac{\delta P_t}{P_t} = 0.040 \quad (5.12)$$

The error of g_1 was calculated with Equation (5.10) substituting P_t for P_b . Figure 5.14 shows the systematic error of $xg_1(x)$ for deuteron due to the uncertainty of the target polarization with the conventions same as those in Figure 5.13.

5.5.3 Dilution factor

The dilution factor is defined to be the fraction of events from the polarized deuteron in the target to the total events. The error of the dilution factor was calculated from the following sources;

1. The coefficient of the EMC effect — the ratio of the cross section of a nuclear per nucleon with respect to that of the deuteron. The uncertainty of the EMC coefficient was estimated from 0.3 to 1.3% relative depending on x [53]. We assigned the EMC effect uncertainty conservatively to be 1.5% over all x .
2. Cross section ratio — The ratio σ_d/σ_p has 2.0% uncertainty relative to itself [62].
3. NMR coil uncertainty — The NMR coil uncertainty is due to the lack of knowledge of how much wire exist in the target effectively. We assumed it had 20% relative error [63].
4. Packing fraction — The packing fraction is a percentage filled by the ammonia beads in the target cell. The packing fraction error depends on the target cell. We used the error of the most frequently used one, which is 2.0% [64].
5. Material weight — We included also the absolute uncertainties in the weight of the ammonia and helium in the target which we assumed to be 4% relative. [65].

Figure 5.15 shows the systematic error of $xg_1^d(x)$ due to the dilution factor.

5.5.4 Radiative correction

The radiative correction gives the uncertainty of $g_1^d(x)$. Only the uncertainty of the radiative correction for the $A_{\parallel}(x)$ was included because that for $A_{\perp}(x)$ was suppressed

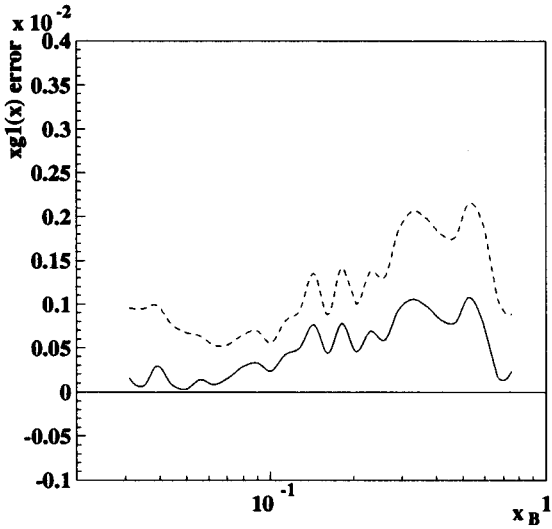


Figure 5.15: The systematic error of xg_1 of deuteron due to the dilution factor: the results are shown by the solid curve. The dashed curve is the total of the systematic error.

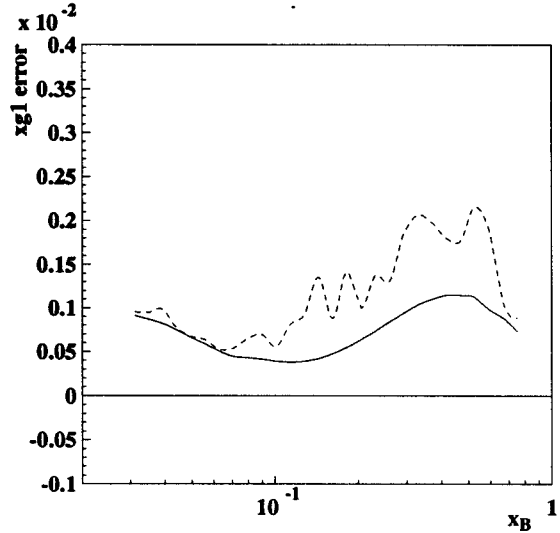


Figure 5.16: The systematic error of $xg_1^d(x)$ due to the radiative correction: only the uncertainty on the correction for A_{\parallel} was accounted. The results are shown with the same conventions as Figure 5.15

by the small factor $\tan \theta/2$ as shown in Equation (5.5). The uncertainty of the radiative correction was evaluated with a varying of input models and the error of the data points. The error of $g_1^d(x)$ due to the radiative correction was calculated by,

$$\delta g_1 = \frac{F_1}{D'} \delta RC, \quad (5.13)$$

where δRC is the uncertainty of the radiative correction for the A_{\parallel} . Figure 5.16 shows the error of $xg_1^d(x)$.

5.5.5 Total cross section

F_1/D' in Equation (5.5) has an uncertainty due to the error of the spin-averaged structure functions. This uncertainty contributes to the systematic error of $g_1^d(x)$.

F_1/D' in Equation (5.5) is expressed in terms of F_2 and R by,

$$\frac{F_1}{D'} = F_2 \frac{(1 + \gamma^2)y(1 + \epsilon R)}{2x(1 + R)(1 - \epsilon)(2 - y)}, \quad (5.14)$$

and in terms of the total cross section by [22],

$$\frac{F_1}{D'} = \frac{\sigma}{\sigma_{Mott}} \frac{My}{2(2-y)\tan^2(\theta/2)}, \quad (5.15)$$

where σ is the total cross section, σ_{Mott} is the Mott cross section given by,

$$\sigma_{Mott} = \frac{4\alpha^2(E')^2 \cos^2(\theta/2)}{Q^4}. \quad (5.16)$$

In principle, the uncertainty of F_1/D' calculated by using Equation (5.15) or (5.14) should be identical. On the other hand, the uncertainty calculated by using the Equation (5.14) without any account for a correlation between the errors of F_2 and R is larger than that calculated by using the Equation (5.15) because the accuracy of the total cross section is nearly equal to that for F_2 . Therefore, the proper way to calculate the uncertainty of F_1/D' is either using Equation (5.14) accounting the correlation between the errors of F_2 and R or using the Equation (5.15). We calculated the error of F_1/D' by using Equation (5.15).

We assumed that the fractional uncertainty of the total cross section is same as that of F_2 . We estimated the uncertainty of the F_2 using two FORTRAN codes, F2GLOB.F and F2NMC.F. F2GLOB.F provides the F_2 for various kinematic region from a fit using results of past SLAC experiments [62]. It also gives the statistical, systematic, and normalization errors evaluated from the experimental results. F2NMC.F provides F_2 with NMC parameterization [59] which was obtained from the NMC muon-nucleon scattering. F2NMC.F is more reliable than F2GLOB.F in low x region due to the availability of the data used to determine the parameters.

The error of F_2 was calculated by,

$$\frac{\delta F_2}{F_2} = \sqrt{\left(\frac{\delta F_2^{stat}}{F_2}\right)^2 + norm^2 + \left(1 - \frac{F_2^{glob}}{F_2^{NMC}}\right)^2}, \quad (5.17)$$

where F_2^{stat} is the statistical error which was provided by F2GLOB.F, $norm$ is a normalization uncertainty 1.7% which was derived from Ref.[62], and the last term comes from the model dependence. Using the fractional error of F_2 , the systematic error of g_1 due to

the total cross section is given by,

$$\delta g_1(x) = g_1(x) \frac{\delta \sigma(x)}{\sigma(x)} = g_1(x) \frac{\delta F_2(x)}{F_2(x)}. \quad (5.18)$$

The last term in Equation (5.17) gives a huge uncertainty in the low x region of $x < 0.08$ because of large discrepancy between $F_2(x)$ obtained from F2GLOB.F and F2NMC.F. It is an obvious over-estimation for the error because the NMC parameterization is more reliable at low x than F2GLOB. F2GLOB states that the routine is not useful in the region of $x < 0.08$ due to the poor statistics in the fit.

Figure 5.17 shows $F_2(x)$ data from the NMC experiment and the parameterization curve at $Q^2 = 3.0(\text{GeV}/c)^2$ [59]. Only the data obtained at Q^2 between 2.5 and 3.5 $(\text{GeV}/c)^2$ are plotted. The two dotted lines indicate the band within 4% relative uncertainty from the parameterization curve. This relative uncertainty of 4% is acceptable for the F_2 error in the low x region from the figure. Therefore, we took that F_2 has the relative uncertainty of 4% in the region of $x < 0.08$.

Figure 5.18 shows the error of $xg_1^d(x)$ due to the uncertainty of F_1/D' .

5.5.6 D-state probability

The D-state probability, w_D is a fraction of the deuteron in D-state ($L=2$) as mentioned in Section 2.5. It was estimated from the calculation using various models to be 5.5 ~ 6.5%[28] and we assigned to be $w_D = 6 \pm 1\%$ which covers all of the results. This uncertainty causes an ambiguity of the g_1 not for deuteron but for neutron and proton - neutron showing Equations (5.8) and (5.9). The uncertainties of Γ^n and $\Gamma^p - \Gamma^n$ due to the D-state probability are 3% of Γ^d .

5.5.7 Nitrogen correction

Nitrogen correction is a correction due to the polarized nucleon other than deuteron in the target. This is a small correction and the uncertainty of the correction factors are negligible for the cross section asymmetry or $g_1(x)$ as stated in Section 4.2.5. The nitrogen

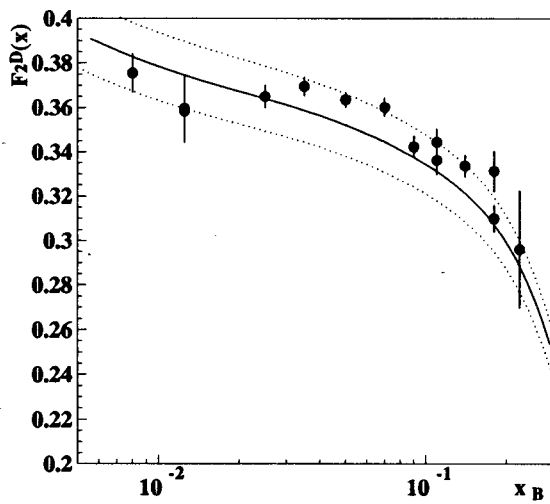


Figure 5.17: F_2 data from NMC experiment and the parameterization curve. Only the data between $Q^2 = 2.5(\text{GeV}/c)^2$ and $Q^2 = 3.5(\text{GeV}/c)^2$ are plotted. The dotted lines show the band within the relative uncertainty of 4% from the parameterization curve.

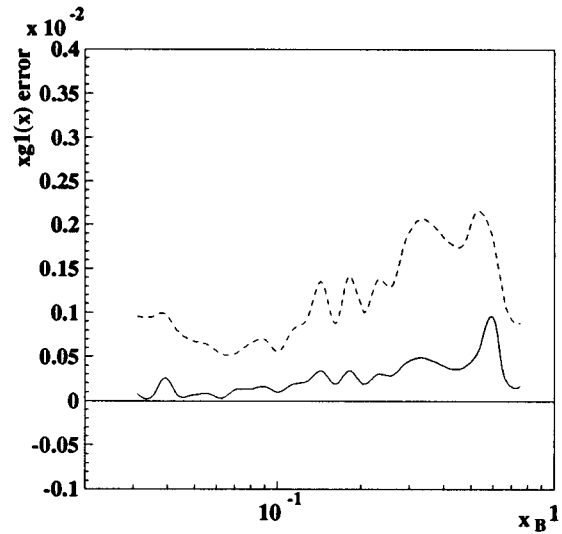


Figure 5.18: Systematic error of $xg_1^d(x)$ due to the F_1/D' : the solid curve shows the result. The dashed curve is the total of the systematic errors of $xg_1(x)$.

correction for the cross section asymmetry is expressed to be,

$$A_d = \frac{1}{\nu_1} \left[\frac{\Delta}{p_d p_{df}} - \nu_2 A_p \right], \quad (5.19)$$

where ν_1 and ν_2 are the correction factors which are approximately 0.98 and 0.06 respectively and A_p is the cross section asymmetry for proton. Although the uncertainties for the ν_1 and ν_2 are negligible, the error of the cross section asymmetry of the proton in the correction may affect due to the large magnitude of the asymmetry for proton in contrast to that for deuteron. Therefore, we estimated the uncertainty due to the proton asymmetry by

$$\delta g_1 = \frac{F_1}{D'} \frac{\nu_2}{\nu_1} \delta A_p, \quad (5.20)$$

where δA_p is the statistical error of the proton asymmetry. We calculated only the uncertainty from the $A_{||}$ due to the proton asymmetry.

The uncertainty of Γ^d due to the error of A_p was estimated to be 0.0001 which was smaller than ten times of the other error, for example 0.0016 for the dilution factor and then it was negligible to the Γ^d .

5.6 Integrals of $g_1(x)$

We first calculated the integral of $g_1(x)$ over the data region of $0.029 < x < 0.8$. To estimate the shape of $g_1(x)$ in the outside of the data region where ($0.8 < x < 1$) and ($0 < x < 0.029$), we used the extrapolation for $g_1(x)$ towards $x = 1$ and $x = 0$ respectively.

5.6.1 integral in data region

We calculated the integral of g_1 , Γ_{data} over the data region of $0.029 < x < 0.8$ using the rectangle approximation of,

$$\Gamma_{data} = \sum_i g_1(x_i) \times \Delta x_i, \quad (5.21)$$

where i is the index for the bin, Δx_i is the size of the bin. The statistical error, $\delta\Gamma_{data}^{stat}$ was calculated by,

$$(\delta\Gamma_{data}^{stat})^2 = \sum_i \left\{ \delta g_1(x_i)^{stat} \times \Delta x_i \right\}^2, \quad (5.22)$$

where $\delta g_1(x_i)^{stat}$ is the statistical error of $g_1(x_i)$. The total systematic error, $\delta\Gamma_{data}^{sys}$ was calculated by,

$$(\delta\Gamma_{data}^{sys})^2 = \sum_j \left[\sum_i \delta g_1(x_i)_j^{sys} \Delta x_i \right]^2 \quad (5.23)$$

where j is the index for the source of the systematic error, $\delta g_1(x_i)_j^{sys}$ is the uncertainty of g_1 due to the systematic error. The systematic errors of $g_1(x)$ for different bins from the same source are correlated to each other. We therefore summed the error on all bins linearly as shown in Equation (5.23). The results of Γ_{data} , $\delta\Gamma_{data}^{stat}$, and $\delta\Gamma_{data}^{sys}$ are shown in Table 5.4.

	g_1^d	g_1^n	$g_1^p - g_1^n$
Γ_{data}	0.0384	-0.0326	0.1495
$\delta\Gamma_{data}^{stat}$	0.0035	0.0083	0.0103
$\delta\Gamma_{data}^{sys}$	0.0036	0.0095	0.0142

Table 5.4: Integral of $g_1(x)$ on the data region: The integral of $g_1(x)$ for deuteron, neutron, and proton - neutron in the region of $0.029 < x < 0.8$ are shown.

5.6.2 Low x extrapolation

Because our measurement reached down to $x=0.029$, we had to estimate the g_1 for $x < 0.029$. In such a low x region, sea quarks dominate the scattering and the information of the initial parton spin is then lost by the gluon emission. According to Regge theory[66] g_1 approaches to 0 at the low x region and is proportional to x^α with $0 \leq \alpha \leq 0.5$, where the α is the Regge intercept at $t = 0$.

In the past experiments, the spin-averaged structure function $F_2(x)$ has been measured down to a lower x region with higher accuracy than the spin structure function, $g_1(x)$.

These experiments showed that the spin-averaged structure function is described by the Regge theory in such a low x region. The Figure 5.19 shows the $F_2(x)$ for deuteron from NMC, where only the data taken between $Q^2 = 2.5(\text{GeV}/c)^2$ and $Q^2 = 3.5(\text{GeV}/c)^2$ are plotted. The solid line shows the NMC parameterization for $F_2(x)$ at $Q^2 = 3.0(\text{GeV}/c)^2$. The dash-dotted line show the reduced χ^2 if we involve the data into the Regge form fitting up to there. The evolution of the reduced χ^2 demonstrated that the fit by the Regge form is acceptable up to around $x = 0.1$.

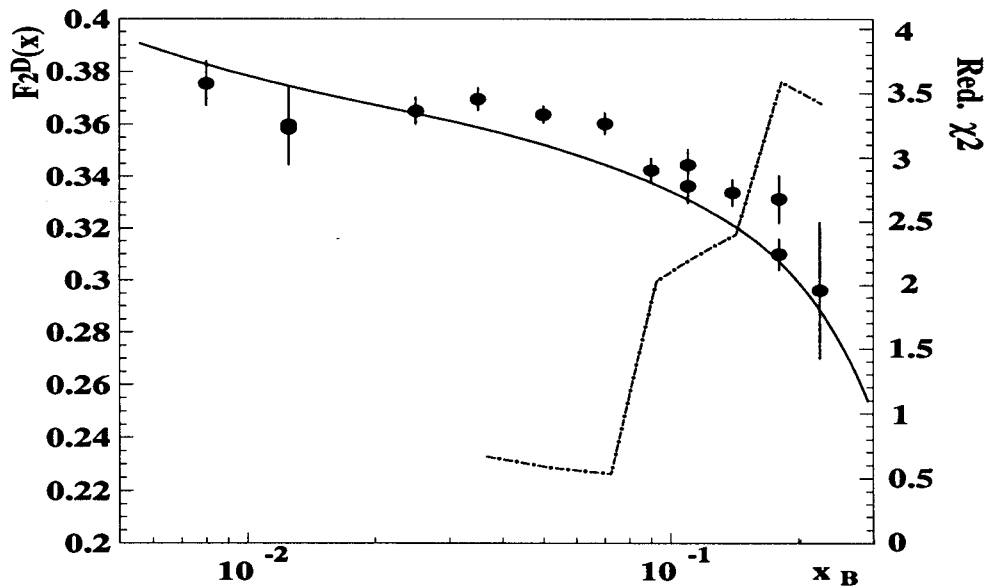


Figure 5.19: F_2 from NMC in the region between $2.5 < Q^2 < 3.5(\text{GeV}/c)^2$. The left y-axis shows the F_2 and the right-hand y-axis shows the reduced χ^2 . The solid line shows NMC parameterization at $Q^2 = 3.0(\text{GeV}/c)^2$. The dashed line shows the reduced χ^2 for the fit with the data up to there. The fit was done with two parameters $p_1 x^{p_2}$ suggested by Regge theory.

Therefore, assuming that g_1 was proportional to x^α in the low x region of $x < 0.1$, we fitted the Regge forms with three fixed α of 0, 0.25 and 0.5 to the data up to $x=0.1$. Figures 5.20, 5.21, and 5.22 show the low x fits for g_1^d , g_1^n , and $g_1^p - g_1^n$ respectively. All of these fitting curves do not describe the data well. However since the contribution to the integral from the low- x region is small, we took the shape of $g_1(x)$ determined by the

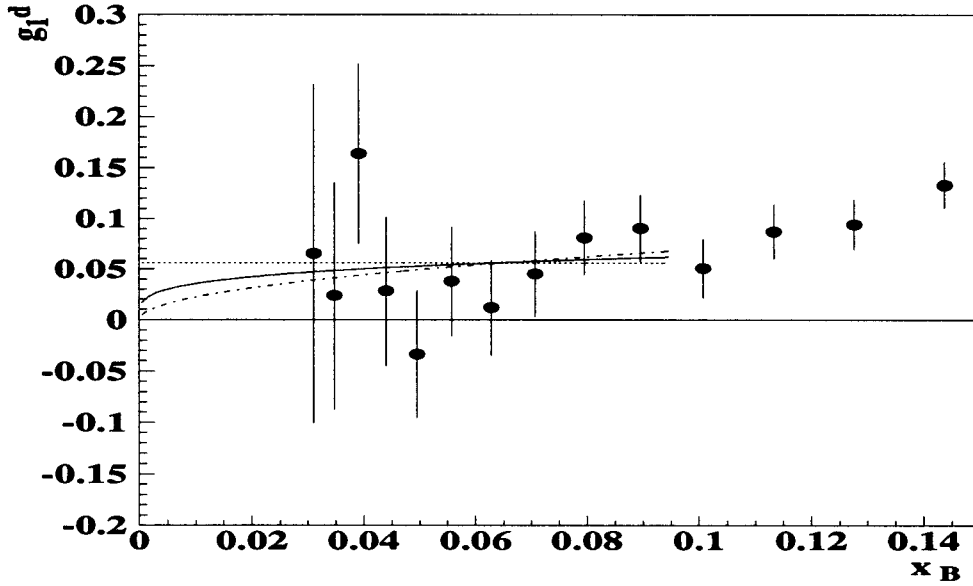


Figure 5.20: Extrapolation toward $x = 0$ for g_1 of deuteron with Regge form. The dotted, solid, and dashed lines show the fits with the forms of Cx^0 , $Cx^{0.25}$, and $Cx^{0.5}$ where C is a fitting parameter. These fits were done using the data up to $x=0.1$.

fit with $\alpha = 0.25$ and calculated the integral,

$$\Gamma_{low} = \int_0^{0.029} Cx^{0.25} dx, \quad (5.24)$$

where C is the parameter determined from the fit.

To estimate the uncertainties in the low- x region, we considered the statistical and systematic errors of the data points, uncertainty of the parameter α and the data region used in the fit.

The statistical error of the extrapolation, $\delta\Gamma_{low}^{stat}$ was calculated by,

$$\delta\Gamma_{low}^{stat} = \int_0^{0.029} \delta C x^{0.25} dx, \quad (5.25)$$

where δC is the error of the fitting parameter.

For the systematic error, we assume that the fitted curve has the fractional uncertainty same as the average of the fractional systematic error of the data points, $\overline{\delta g_1^{sys}}$ and

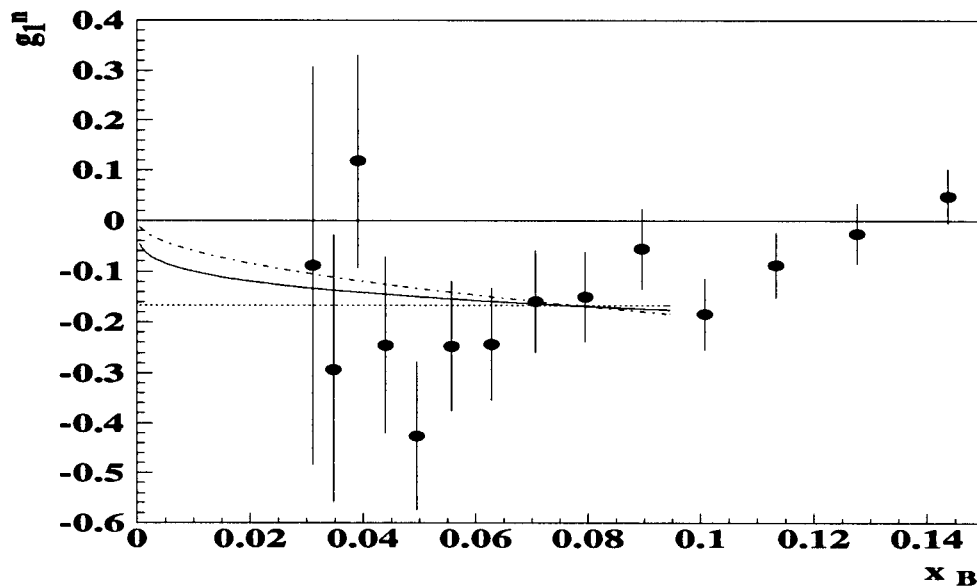


Figure 5.21: Extrapolation toward $x=0$ of g_1 of neutron. The fitted curves are indicated with the same conventions as Figure 5.20.

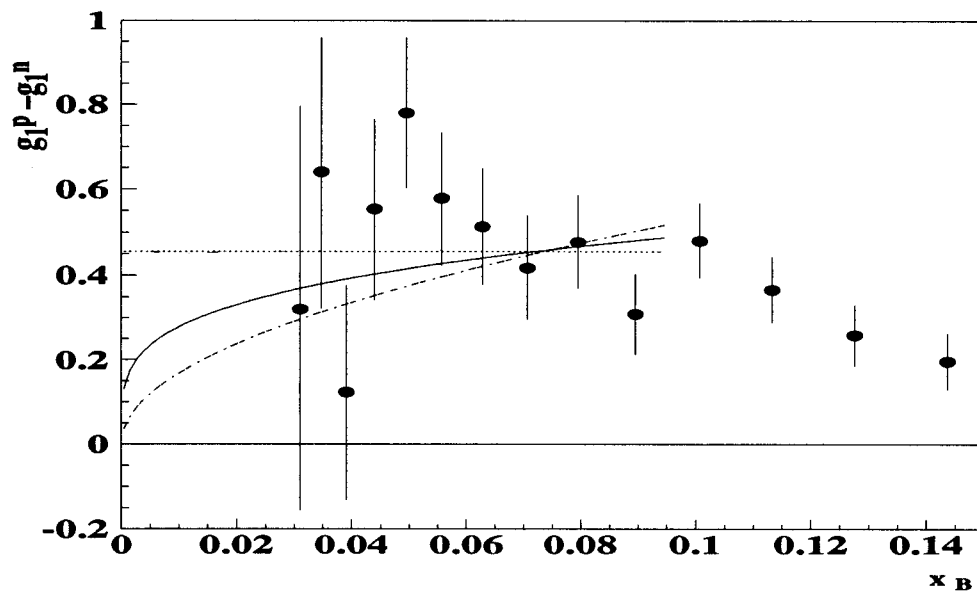


Figure 5.22: Extrapolation toward $x=0$ of $g_1^p - g_1^n$. The fitted curves are indicated with the same conventions as Figure 5.20.

calculated the systematic error of the extrapolation, $\delta\Gamma_{low}^{sys}$

$$\delta\Gamma_{low}^{sys} = \overline{\delta g_1^{sys}} \int_0^{0.029} Cx^{0.25} dx, \quad (5.26)$$

where C is the fitted parameter with $\alpha = 0.25$.

The uncertainty of the extrapolation due to the parameter α was estimated to be the largest difference in Γ_{low} with $\alpha = 0$, or $\alpha = 0.5$ from that with $\alpha + 0.25$.

The uncertainty due to the fitted region was evaluated by varying the upper limit from $x = 0.05$ to 0.13 corresponding to the first 5 to 13 data points. The largest difference in Γ_{low} from that obtained at the upper limit of $x=0.1$ was taken as the uncertainty due to the fitting region.

Table 5.5 shows the summary of the integral and the errors of the low x integral. The $\delta\Gamma_{low}^{fit}$ is the quadratic sum of the uncertainties due to the parameter α and the fitted region.

	g_1^d	g_1^n	$g_1^p - g_1^n$
Γ_{low}	0.0011	-0.0030	0.0084
$\delta\Gamma_{low}^{stat}$	0.0003	0.0007	0.0009
$\delta\Gamma_{low}^{sys}$	0.0002	0.0005	0.0008
$\delta\Gamma_{low}^{fit}$	0.0008	0.0028	0.0059
fitting parameter	0.11	-0.32	0.88
error of parameter	0.03	0.08	0.09
Reduced χ^2	0.66	1.01	1.23

Table 5.5: Integral of g_1 in the low x region, $0 < x < 0.029$: The extrapolations were determined from the fits using the Regge form with $\alpha = 0.25$ with the data up to $x = 0.1$. The $\delta\Gamma_{low}^{stat}$ is the uncertainty due to the error of the fitted parameter. The $\delta\Gamma_{low}^{sys}$ is the uncertainty due to the systematic error of the data which were used by the fit. The $\delta\Gamma_{low}^{fit}$ was the quadratic sum of the uncertainties due to the Regge parameter α and the variation of the fitting region.

5.6.3 High x extrapolation

For the region of $x > 0.8$, we determined the shape of $g_1(x)$ using a formula, $C(1-x)^3$. This formula is based on the assumption that a struck parton with a large momentum fraction is also carrying the spin of the nucleon [67].

	g_1^d	g_1^n	$g_1^p - g_1^n$
fitting parameter	0.41	-0.50	1.90
error of parameter	0.21	0.50	0.62
Reduced χ^2	1.35	1.06	1.03

Table 5.6: The fitting parameter evaluated from the fits with the last three data using the formula of $C(1-x)^3$ where C is the fitting parameter.

The fit was performed using the last three data points in the region of $0.55 < x < 0.8$. The integral for the high x region of $0.8 < x < 1.0$, Γ_{high} is calculated by $\int_{0.8}^{1.0} C(1-x)^3 dx$ with the parameter C determined by the fit. The statistical and systematic errors of the integral, $\delta\Gamma_{high}^{stat}$ and $\delta\Gamma_{high}^{sys}$ were evaluated from the errors of the data points using the similar method as used for the low x extrapolation. Table 5.6 shows the fitting parameter obtained from the fits. Figures 5.23, 5.24, and 5.25 show the fits for g_1 of deuteron, proton, and the difference of proton - neutron respectively.

The uncertainty due to the variation of the lower limit of the fitting region was estimated in a similar manner as used for the low-x fitting. The lower x limit was varied from 0.4 to 0.6 corresponding to the last six to two data points. The largest difference in Γ_{high} at $x = 0.55$ was taken as the uncertainty.

As mentioned in Section 3.5, the expected momentum resolution is worse than that corresponding to the bin size of the x in the high x region of $0.53 < x$. It may be critical for the high x extrapolation because the extrapolation using the data binned on x with the narrower size than the resolution of the spectrometer affects the result. We examined the variation of the high x extrapolation with the data which were combined by each two data points. The fitting was done with the last two points which correspond to the last

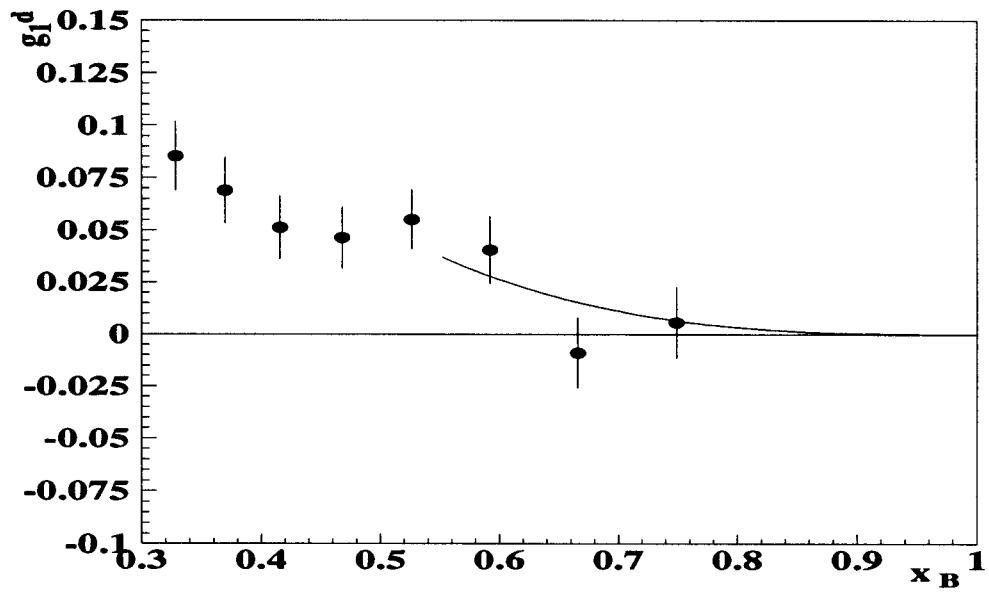


Figure 5.23: Extrapolation toward $x=1$ of g_1 of deuteron. The last three points determined the fit.

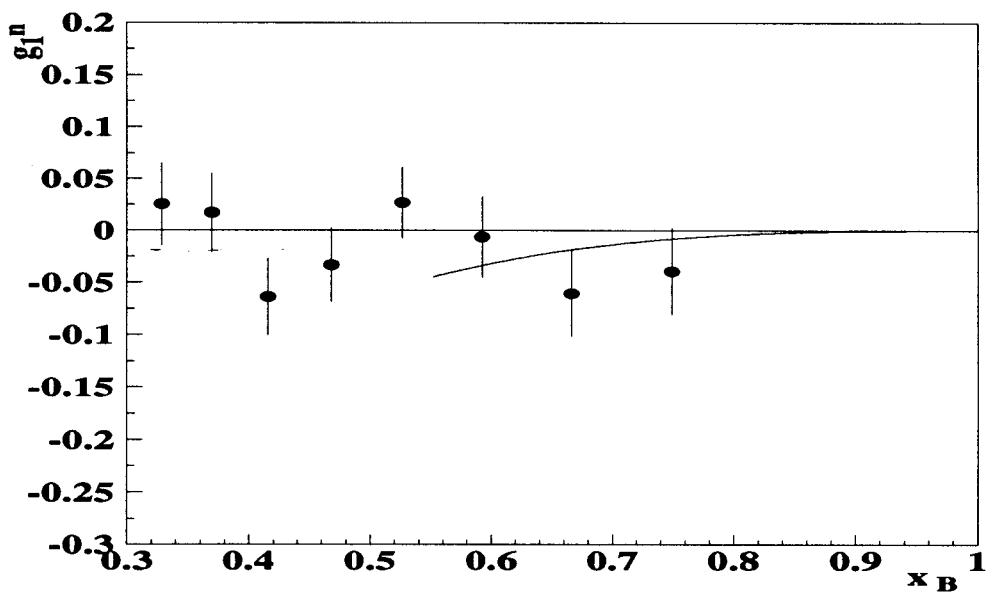


Figure 5.24: Extrapolation toward $x=1$ of g_1 for neutron. The last three points determined the fit.

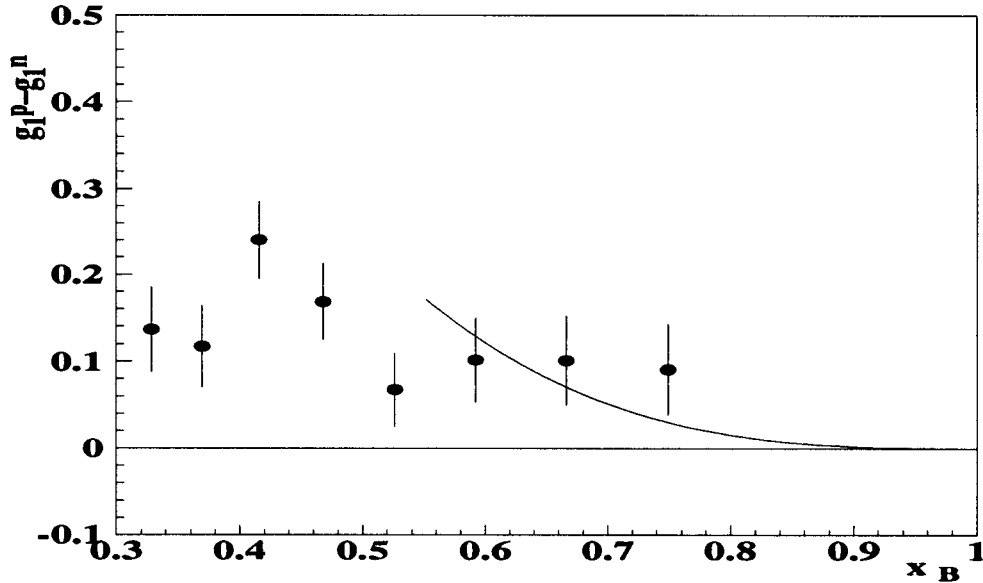


Figure 5.25: Extrapolation toward $x=1$ on $g_1^p(x) - g_1^n(x)$. The last three data points determined the fit.

four data in the original data array. The deviation of the integral from that obtained using the original data was accounted as one of the systematic error.

The Table 5.7 shows the summary of the integrals of g_1 for deuteron, neutron, and proton - neutron in the region of $0.8 < x < 1.0$ obtained from the extrapolations. The $\delta\Gamma_{high}^{fit}$ is the quadratic sum of the uncertainties due to the variation of the fitting region and the bin size of the data used to determine the fit.

5.7 Test of the sum rules

The complete integral of $g_1(x)$ in the region of $0 < x < 1$, Γ was obtained by combining the results of the three regions as,

$$\Gamma = \Gamma_{low} + \Gamma_{data} + \Gamma_{high}. \quad (5.27)$$

The statistical errors in the three regions were combined quadratically by,

$$\delta\Gamma^{stat} = \sqrt{(\delta\Gamma_{low}^{stat})^2 + (\delta\Gamma_{data}^{stat})^2 + (\delta\Gamma_{high}^{stat})^2} \quad (5.28)$$

	g_1^d	g_1^n	$g_1^p - g_1^n$
$\Gamma_{for}(0.8 < x < 1)$	0.0002	-0.0002	0.0008
$\delta\Gamma_{high}^{stat}$	0.0001	0.0002	0.0003
$\delta\Gamma_{high}^{sys}$	0.0000	0.0000	0.0001
$\delta\Gamma_{high}^{fit}$	0.0002	0.0005	0.0006

Table 5.7: Integral of $g_1(x)$ in the high x region of $0.8 < x < 1.0$ were evaluated from the extrapolation toward $x = 1$. The statistical error of the integral, $\delta\Gamma_{high}^{stat}$ is the uncertainty due to the statistical error of the data points. The systematic error, $\delta\Gamma_{high}^{sys}$ is the uncertainty due to the systematic error of the data points. $\delta\Gamma_{high}^{fit}$ is the quadratic sum of the the uncertainties due to the variation of the fitting region and the bin size of the data used to determine the fit.

where the $\delta\Gamma^{stat}$ is the statistical error of the complete integral. The systematic errors in the three regions were combined linearly. The uncertainty of the fit in the low and high x regions, $\delta\Gamma_{low}^{fit}$ and $\delta\Gamma_{high}^{fit}$ were included into the total systematic error, $\delta\Gamma^{sys}$ as,

$$\delta\Gamma^{sys} = \sqrt{\left(\delta\Gamma_{low}^{sys} + \delta\Gamma_{data}^{sys} + \delta\Gamma_{high}^{sys}\right)^2 + \left(\delta\Gamma_{low}^{fit}\right)^2 + \left(\delta\Gamma_{high}^{fit}\right)^2}. \quad (5.29)$$

Table 5.8 shows the integrals of g_1 at $Q^2 = 3.0(GeV/c)^2$ with the statistical and systematic errors. The lower part of the rows shows the contributions from the various uncertainties to the total systematic error.

We also calculated the integrals of $g_1(x)$ at $Q^2 = 10.0(GeV/c)^2$ to compare to the results from Spin Muon Collaboration (SMC) under the assumption that g_1/F_1 was independent of Q^2 . Table 5.9 shows the Γ at $Q^2 = 10.0(GeV/c)^2$. The statistical and the systematic errors were calculated in the same procedure as used for the calculation at $Q^2 = 3.0(GeV/c)^2$.

5.7.1 Ellis-Jaffe sum rule for deuteron

As shown in the Table 5.8, the $g_1(x)$ integral for deuteron at $Q^2 = 3.0(GeV/c)^2$ was evaluated as,

$$\Gamma^d = 0.0396 \pm 0.0035(stat.) \pm 0.0039(syst.), \quad (5.30)$$

		g_1^d	g_1^n	$g_1^p - g_1^n$
Γ		0.0396	-0.0358	0.1586
$\delta\Gamma^{stat}$		0.0035	0.0084	0.0103
Γ^{sys}	Beam polarization	0.0011	0.0008	0.0039
	Target polarization	0.0016	0.0049	0.0071
	Dilution factor	0.0016	0.0054	0.0079
	Radiative correction	0.0024	0.0057	0.0068
	F_1/D'	0.0009	0.0022	0.0053
	D-state probability	-	0.0012	0.0012
	Low x extrapolation	0.0009	0.0030	0.0060
	High x extrapolation	0.0002	0.0005	0.0007
	Total	0.0039	0.0105	0.0162

Table 5.8: Integral of g_1 in the region of $0 < x < 1$ at $Q^2 = 3.0(\text{GeV}/c)^2$: contributions to the systematic error from each source are shown in the lower part of the table.

	g_1^d	g_1^n	$g_1^p - g_1^n$
$\Gamma_{for}(0 < x < 1)$	0.0400	-0.0380	0.1641
Statistical error	0.0030	0.0073	0.0089
Systematic error	0.0041	0.0115	0.0183

Table 5.9: Integral of g_1 in the region of $0 < x < 1$ at $Q^2 = 10.0(\text{GeV}/c)^2$. The results were evaluated under the assumption that $g_1(x)/F_1(x)$ is independent of Q^2 .

where the first error is the statistical error and the second error is the systematic error. The theoretical prediction including the QCD correction up to third order of the $\alpha_s = 0.36 \pm 0.05$ [27] at $Q^2 = 3.0(\text{GeV}/c)^2$ is,

$$\Gamma^d = 0.068 \pm 0.005, \quad (5.31)$$

with the D-state probability of deuteron $w_D = 0.06$. Γ^d from the E143 experiment differs from that of the Ellis-Jaffe sum rule for deuteron by about four standard deviations, where the standard deviation was taken as a quadratic sum of the statistical and systematic errors of the integral and the uncertainty in the Ellis-Jaffe sum rule.

In order to verify the consistency of our results to those from SMC, we calculated the $g_1(x)$ for deuteron at $Q^2 = 10.0(\text{GeV}/c)^2$. The results of $xg_1^d(x)$ from E143 and SMC are plotted in Figure 5.26 together. The closed and open circles show the $xg_1(x)$ for deuteron from E143 and SMC respectively. The error bars are only statistical. The dark and open areas indicate the size of the systematic errors for E143 and SMC respectively. These results are in a good agreement to each other in the overlapped region.

These results are summarized together with the theoretical prediction from the Ellis-Jaffe sum rule at $Q^2 = 10.0(\text{GeV}/c)^2$,

$$\begin{aligned} \Gamma^d &= 0.0400 \pm 0.0030(\text{stat.}) \pm 0.0041(\text{syst.}) & : E143, \\ \Gamma^d &= 0.034 \pm 0.009(\text{stat.}) \pm 0.006(\text{syst.}) & : SMC, \\ \Gamma^d &= 0.070 \pm 0.004 & : \text{theory}, \end{aligned} \quad (5.32)$$

showing that Γ^d from E143 at $Q^2 = 10.0(\text{GeV}/c)^2$ is consistent to that from SMC. However, the Γ^d predicted by the Ellis-Jaffe sum rule is different from both of the experimental results by more than three standard deviations.

The Figure 5.27 illustrates the comparison of the Γ^d measurements and the theoretical prediction as a function of Q^2 . The closed and open circles show the results from E143 and SMC at $Q^2 = 3.0$ and $10.0(\text{GeV}/c)^2$ respectively. The error bars are the quadratic sum of the statistical and systematic errors. The solid line shows the theoretical prediction including the QCD correction up to third order of $\alpha_s(Q^2)$. The Q^2

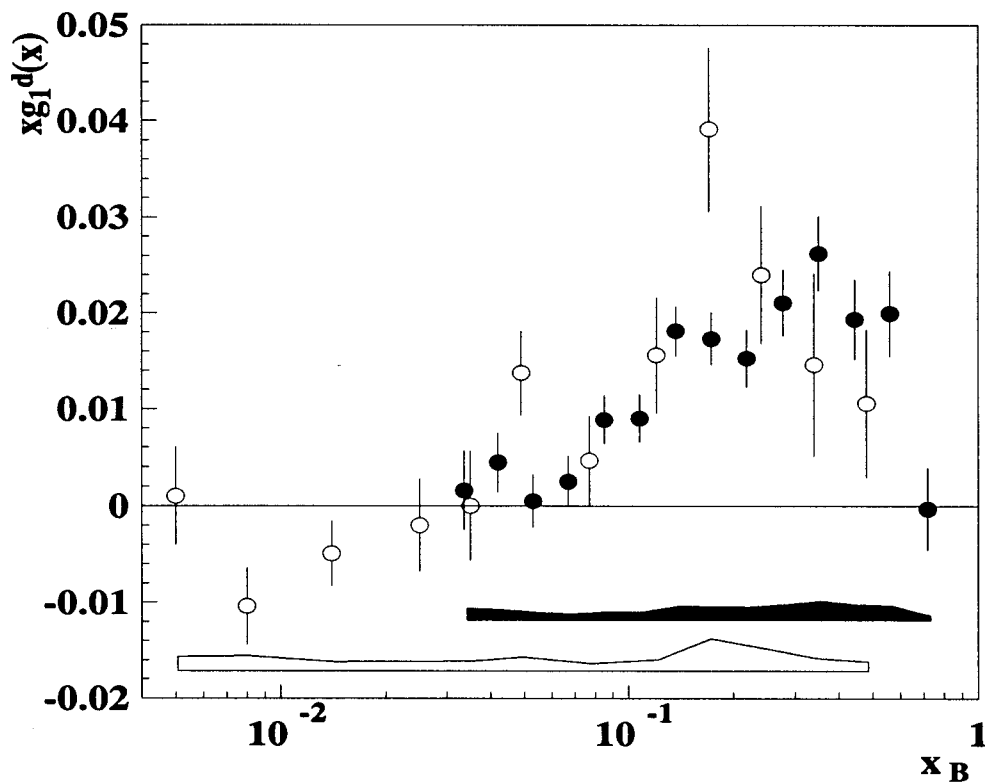


Figure 5.26: xg_1 of deuteron: the results from E143 and SMC are plotted together by the open and closed circles respectively. Both results were evaluated at the common $Q^2 = 10.0(\text{GeV}/c)^2$. The error bars are statistical only. The dark and open areas indicate the size of the systematic errors for E143 and SMC respectively.

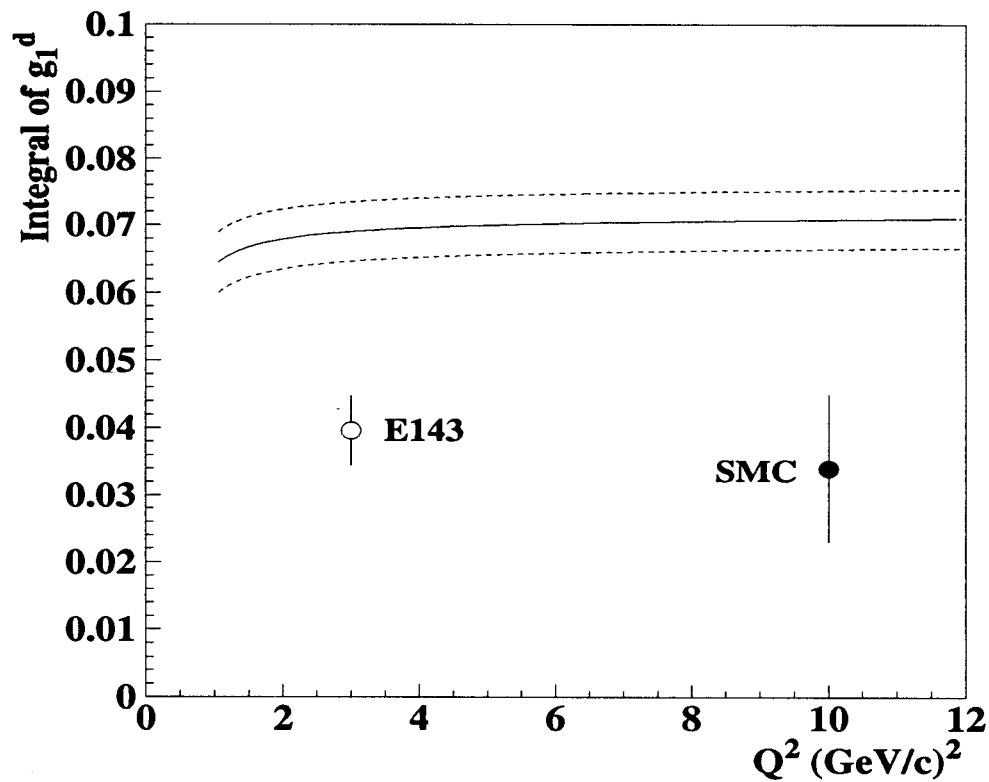


Figure 5.27: Γ^d with the prediction of the Ellis-Jaffe sum rule: The horizontal axis shows Q^2 and the vertical axis shows Γ^d . The open and closed circles indicate the results from E143 and SMC respectively. The error bars are the quadratic sum of the statistical and systematic errors. The solid line shows the prediction of the Ellis-Jaffe sum rule up to third order of α_s . The dotted lines show the band within one standard deviation from the prediction.

evolution of the prediction was calculated using the running strong coupling constant, $\alpha_s(Q^2)$ with $\Lambda^{(n_f=4)} = 0.364 \pm 0.052$ GeV which was evaluated in Section 5.7.3, where n_f is the number of quark flavors. The dotted lines show the band within one standard deviation from the prediction. The uncertainty of the prediction was calculated from the errors of the $\Lambda^{(n_f=4)}$, hyperon decay constants, F and D, and the D-state probability of the deuteron. The results from both experiments indicate a large discrepancy of more than three standard deviation from the prediction.

5.7.2 Ellis-Jaffe sum rule for neutron

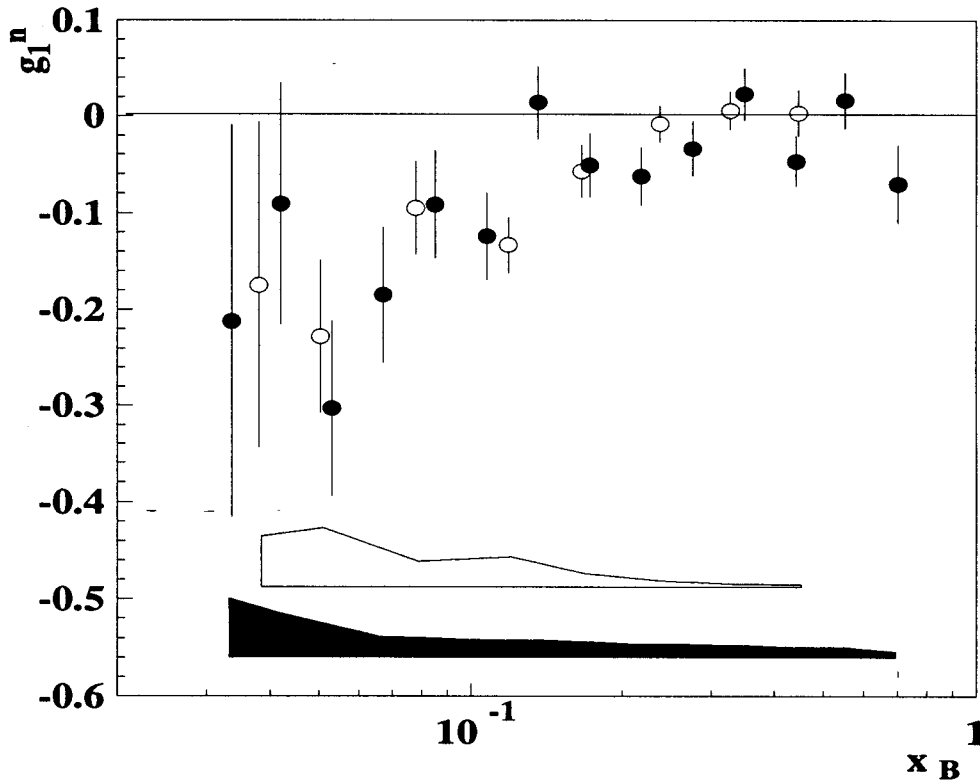


Figure 5.28: The g_1 of neutron from E143 and E142 are plotted together by the open and closed circles respectively. Both results were evaluated at the common $Q^2 = 2.0(\text{GeV}/c)^2$. The error bars are statistical only. The dark and open areas indicate the size of the systematic errors for E143 and E142 respectively.

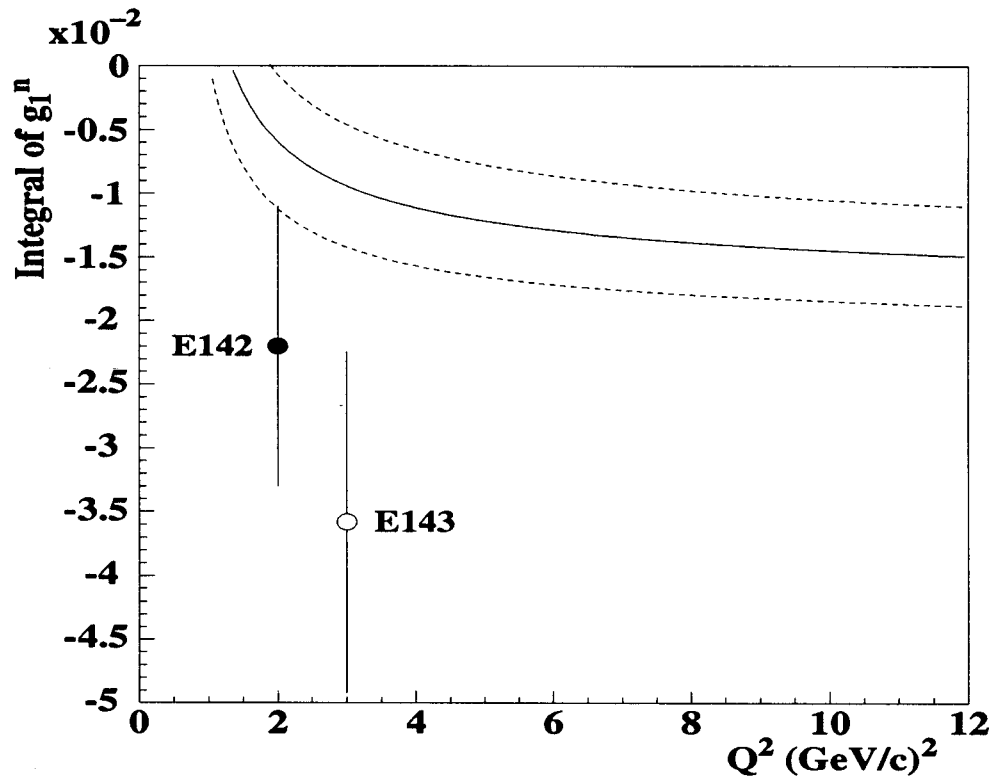


Figure 5.29: Γ^n results with the prediction of the Ellis-Jaffe sum rule: The horizontal axis shows Q^2 and the vertical axis shows Γ^n . The open and closed circles indicate the results from E143 and E142 respectively. The error bars are the quadratic sum of the statistical and the systematic errors. The solid line shows the prediction of the Ellis-Jaffe sum rule up to third order of α_s . The dotted lines show the band within one standard deviation from the prediction.

The Γ for the neutron at $Q^2 = 3.0(\text{GeV}/c)^2$ using our deuteron and proton results was obtained to be,

$$\Gamma^n(Q^2 = 3.0) = -0.0358 \pm 0.0084(\text{stat.}) \pm 0.0105(\text{sys.}). \quad (5.33)$$

This result indicates a discrepancy from the prediction of the Ellis-Jaffe sum rule for neutron,

$$\Gamma^n(Q^2 = 3.0) = -0.009 \pm 0.006 \quad : \text{theory}, \quad (5.34)$$

by 1.8 times of the standard deviation.

Figure 5.28 shows the $g_1(x)$ for neutron at $Q^2 = 2.0(\text{GeV}/c)^2$. The closed and open circles show the $g_1^n(x)$ obtained from E143 and E142 [12] respectively. These results are in a good agreement to each other.

Figure 5.29 shows Γ^n from E143 and E142 with the predicted curve by Ellis-Jaffe sum rule including the QCD correction up to third order of α_s as a function of Q^2 . The Q^2 evolution of the prediction was calculated using the running strong coupling constant, $\alpha_s(Q^2)$ with $\Lambda^{(n_f=4)} = 0.364 \pm 0.052\text{GeV}$ which was evaluated in the next section. The error bars are the quadratic sum of the statistical and systematic errors. The results from E143 and E142 which are shown by the open and solid circles are in a good agreement and lower than the prediction. However, the accuracies of the results are not enough to exclude the Ellis-Jaffe sum rule for neutron.

5.7.3 Bjorken sum rule

The difference of the integrals of $g_1^p(x)$ and $g_1^n(x)$, $\Gamma^p - \Gamma^n$ are obtained from Table 5.8 to be,

$$\Gamma^p - \Gamma^n(Q^2 = 3.0) = 0.1586 \pm 0.0103(\text{stat.}) \pm 0.0162(\text{sys.}), \quad (5.35)$$

which is consistent with the prediction from the Bjorken sum rule at $Q^2 = 3.0(\text{GeV}/c)^2$ given by,

$$\Gamma^p - \Gamma^n(Q^2 = 3.0) = 0.169 \pm 0.008 \quad : \text{theory}. \quad (5.36)$$

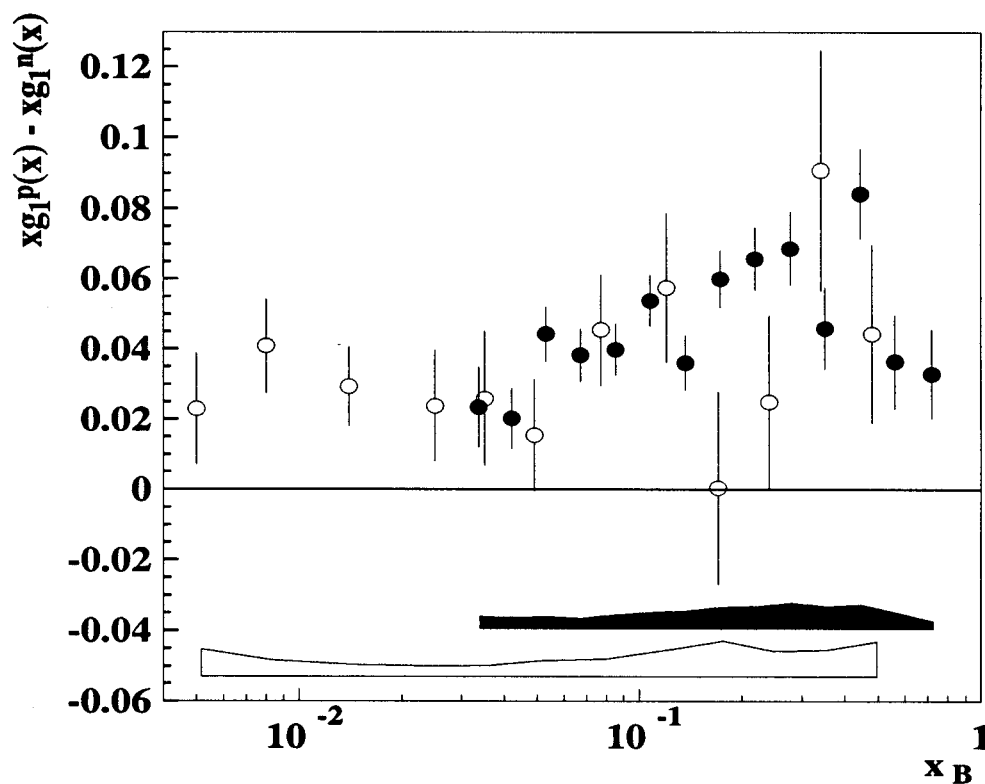


Figure 5.30: $xg_1^p - xg_1^n$: the closed and open circle show the results at $Q^2 = 10.0(\text{GeV}/c)^2$ from E143 and SMC [16] respectively. The error bars are only statistical. The closed and open areas show the size of the systematic errors for E143 and SMC results.

We evaluated the $g_1^p(x) - g_1^n(x)$ at $Q^2 = 10.0(\text{GeV}/c)^2$ for comparison to the SMC results. These two data are consistent with each other as shown in Figure 5.30. The integrals from these measurements are,

$$\Gamma^p - \Gamma^n(Q^2 = 10.0) = 0.1641 \pm 0.0089(\text{stat.}) \pm 0.0183(\text{sys.}) : E143 \quad (5.37)$$

$$\Gamma^p - \Gamma^n(Q^2 = 10.0) = 0.199 \pm 0.038 : SMC \quad (5.38)$$

where the error of the SMC result contains both of the statistical and systematic errors [16]. The two results are in good agreement with the prediction of the Bjorken sum rule at $Q^2 = 10.0(\text{GeV}/c)^2$ given by,

$$\Gamma^p - \Gamma^n(Q^2 = 10.0) = 0.187 \pm 0.003 : \text{theory.} \quad (5.39)$$

The Figure 5.31 shows the comparison of the $\Gamma^p - \Gamma^n$ measurements and the theoretical prediction as a function of Q^2 . The solid and open circles show the results from E143 and SMC at the averaged Q^2 respectively. The solid line shows the theoretical prediction including the QCD correction up to third order of $\alpha_s(Q^2)$. The dotted lines show the band within one standard deviation from the prediction. The uncertainty of the prediction was calculated from the errors of the $\Lambda^{(n_f=4)}$ and the hyperon decay constants, F and D. The results from both experiments are in good agreement with the prediction.

Figure 5.32 shows the strong coupling constants obtained from the various experiments. Using the measurement of $\Gamma^p - \Gamma^n$, we calculated the strong coupling constant $\alpha_s(Q^2 = 3.0)$ to be $0.417_{-0.110}^{+0.086}$ with the Equation (2.72) and plotted as the open circle. The closed triangle is the average of the results of τ decay measurements by Particle Data Group (PDG) [26]. The closed square is the NMC result obtained from the measurements for the scaling violation of the spin-averaged nucleon structure function [68]. The closed circle is the result of CCFR obtained from the measurement for the Gross-Llewellyn Smith sum rule [69]. The solid curve is the running coupling constant, $\alpha_s(Q^2)$ obtained from the fitting using these data plotted in the figure. We used the renormalization scheme with the number of flavor, $n_f = 4$ to obtain the running strong coupling

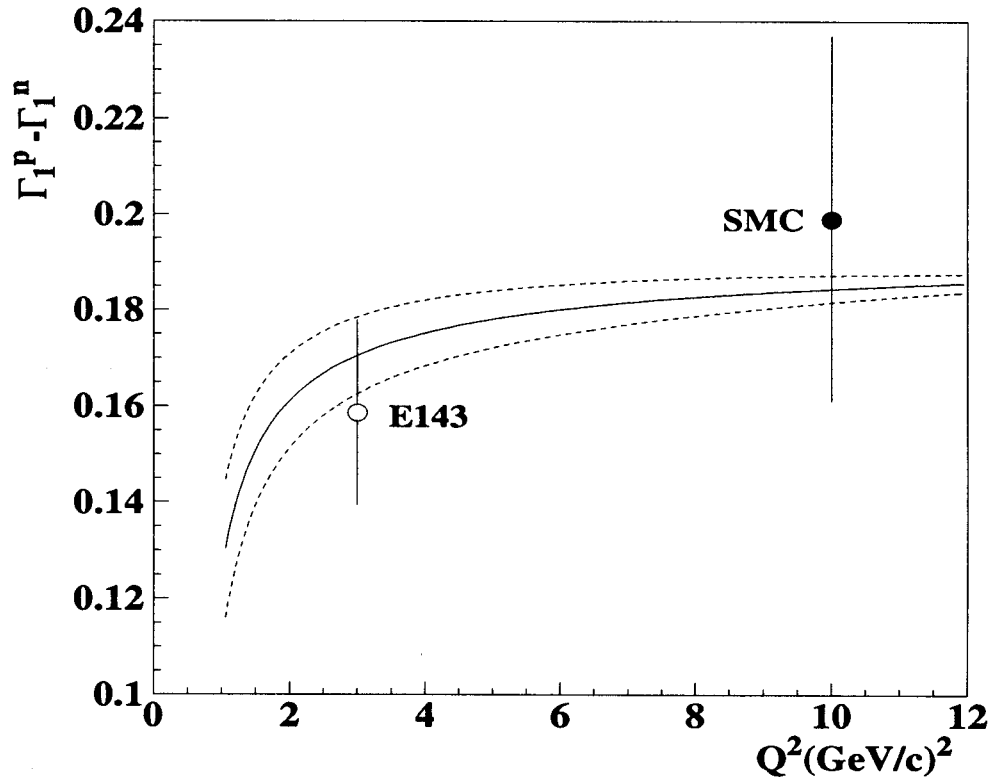


Figure 5.31: $\Gamma^p - \Gamma^n$ with the prediction of the Bjorken sum rule: The horizontal axis shows Q^2 and the vertical axis shows $\Gamma^p - \Gamma^n$. The open and closed circles show the results from E143 and SMC respectively. The error bars are the quadratic sum of the statistical and systematic errors. The solid line shows the prediction of the Bjorken sum rule up to third order of α_s . The dotted lines show the band within one standard deviation from the prediction.

constant. The data were fitted to the formula of [26]

$$\alpha_s(Q^2) = \frac{12\pi}{(33 - 2n_f) \log(Q^2/\Lambda^2)} \left[1 - \frac{6(153 - 19n_f) \log[\log(Q^2/\Lambda^2)]}{(33 - 2n_f)^2 \log(Q^2/\Lambda^2)} \right], \quad (5.40)$$

where Λ is the parameter determined to be 0.364 ± 0.052 GeV by the fitting. The reduced χ^2 of the fit was 0.33. This running coupling constant was used to obtain the Q^2 evolution of the sum rules shown in Figures 5.27, 5.29, and 5.31.

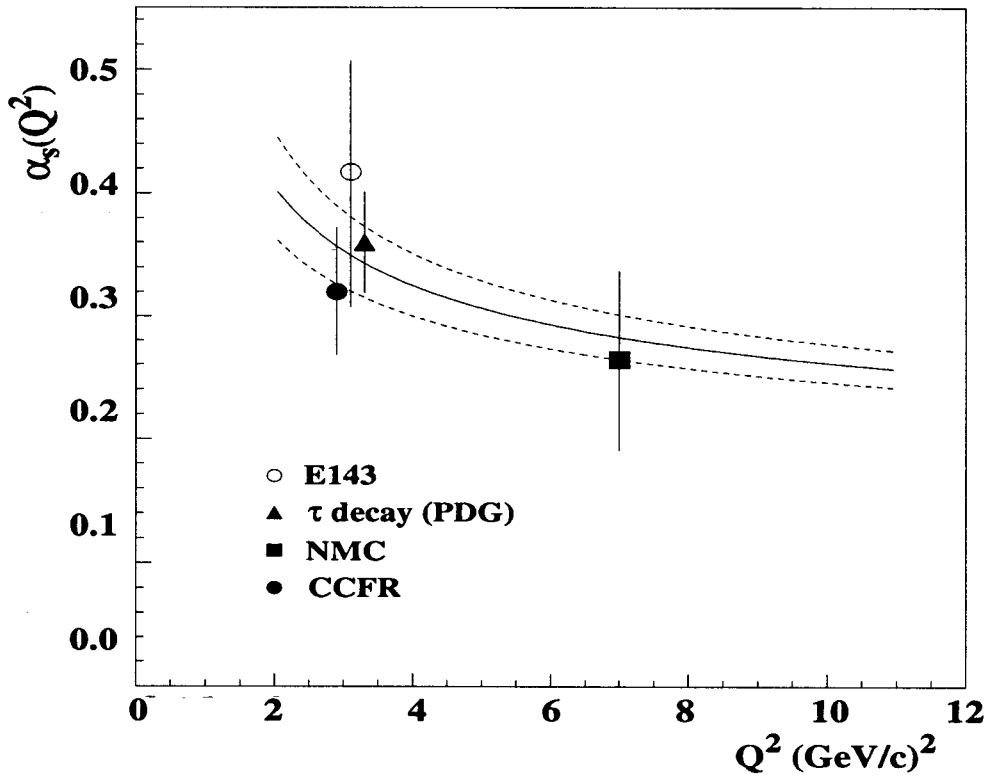


Figure 5.32: The strong coupling constant α_s as a function of Q^2 . The open circle is the result from E143. The closed triangle is the result obtained from the decay width of the τ lepton [26]. The closed circle is the result from NMC [68] obtained by the measurement for the scaling violation of the spin-averaged nucleon structure function. The closed circle is the result from CCFR [69] obtained by the measurement for the Gross-Llewellyn Smith sum rule. The solid line and the dotted lines show the running coupling constant and the band within one standard deviation obtained by the fit using these data.

5.8 Quark polarization

We calculated the quark polarization with Γ^d by using the Equation (2.87). We found the quark polarization to be,

$$\begin{aligned}\Delta u &= 0.822 \pm 0.019, \\ \Delta d &= -0.435 \pm 0.019, \\ \Delta s &= -0.101 \pm 0.023, \\ \Delta\Sigma \equiv \Delta u + \Delta d + \Delta s &= 0.286 \pm 0.055,\end{aligned}\tag{5.41}$$

where the errors include both of statistical and systematic uncertainties of Γ^d , the error of D-state probability on the deuteron, uncertainties of axial vector couplings, and the error of the strong coupling constant in the QCD correction. These results demonstrate that the strange quark is polarized significantly opposite to the nucleon spin and the total quark polarization is about 30% of that for the nucleon; indicating that a large portion of the nucleon spin is still missing.

Figure 5.33 shows the strange quark polarizations as a function of the total quark polarization from various experiments. We recalculated the quark polarizations from EMC[11] and E142[12] with the QCD correction up to third order of α_s [27]. The values from the E143 deuteron measurement is in good agreement with the other results with the highest accuracy among these measurements. The averages of the quark polarizations were calculated to be

$$\Delta s = -0.103 \pm 0.015,\tag{5.42}$$

$$\Delta u + \Delta d + \Delta s = 0.279 \pm 0.039,\tag{5.43}$$

indicating again that the strange quark is polarized significantly opposite with respect to the nucleon spin and the quark carries only about 30% of the nucleon spin. These results denote that the assumption of the unpolarized strange quark to derive the Ellis-Jaffe sum rule is invalid and reconfirmed the 'spin crisis' with the higher accuracy than those obtained before.

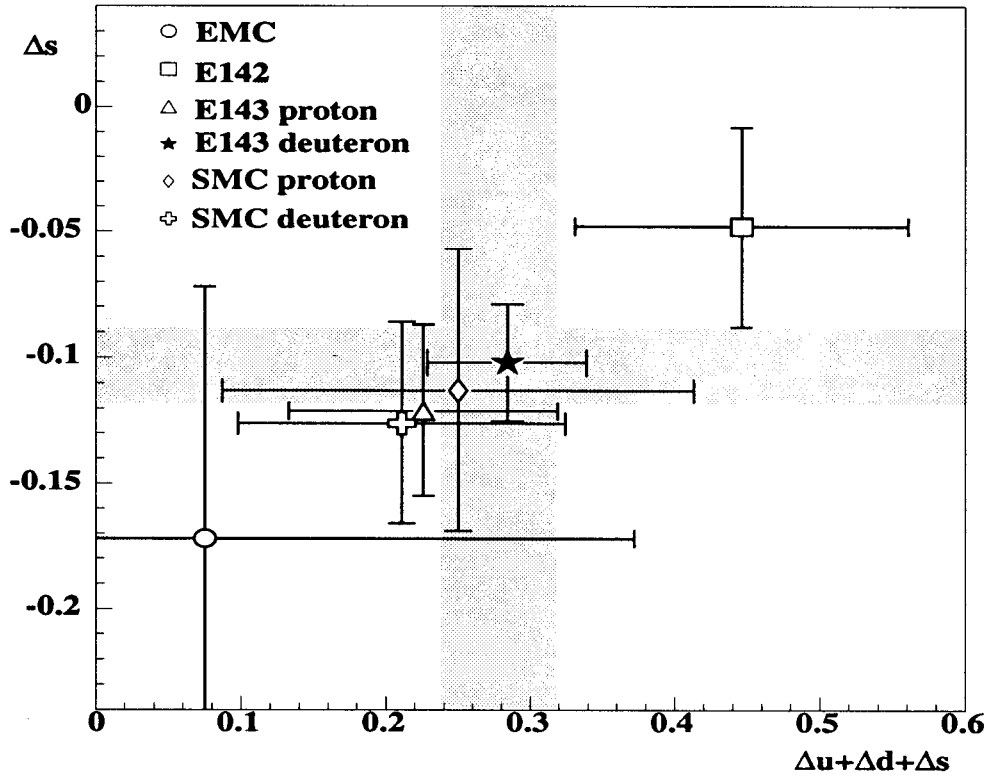


Figure 5.33: The quark polarization evaluated from various experiments are plotted. The horizontal and vertical axes show the total quark polarization and the strange quark polarization. The shaded areas indicate the band within one standard deviation from the average of the polarizations, $\Delta s = -0.103 \pm 0.015$ and $\Delta u + \Delta d + \Delta s = 0.279 \pm 0.039$.

Chapter 6

Conclusion and a look into the future

We have measured the deuteron spin structure function $g_1(x)$ in the E143 experiment at SLAC using the highly polarized electron beam and the highly polarized frozen ND_3 target. The experiment provided the high precision data for the structure function from $x = 0.029$ to 0.8 . The integral of the spin structure function g_1 for deuteron over x at the averaged $Q^2 = 3.0(\text{GeV}/c)^2$ and the prediction from the Ellis-Jaffe sum rule were found to be,

$$\text{Experiment } \Gamma^d = 0.0396 \pm 0.0035(\text{stat.}) \pm 0.0039(\text{sys.}), \quad (6.1)$$

$$\text{Theory } \Gamma^d = 0.068 \pm 0.005. \quad (6.2)$$

The result indicate that the Ellis-Jaffe sum rule describes the data improperly. It denotes that the assumption to derive the Ellis-Jaffe sum rule which is the unpolarized strange sea quark, is not valid.

Combining the E143 deuteron and proton data [18], we obtained the difference of the integrals, $\Gamma^p - \Gamma^n$. The $\Gamma^p - \Gamma^n$ from this experiment and the prediction by the Bjorken sum rule are to be,

$$\text{Experiment } \Gamma^p - \Gamma^n = 0.1586 \pm 0.0103(\text{stat.}) \pm 0.0162(\text{sys.}), \quad (6.3)$$

$$\text{Theory } \Gamma^p - \Gamma^n = 0.169 \pm 0.008. \quad (6.4)$$

From these results, we confirmed that the Bjorken sum rule gives a consistency to the

experimental results at $Q^2 = 3.0(\text{GeV}/c)^2$ with the high accuracy. It means that Iso Spin symmetry is valid for the spin structure function g_1 for nucleon and the Perturbative QCD well describes the scaling violation of the spin structure function.

Strong coupling constant α_s at $Q^2 = 3.0(\text{GeV}/c)^2$ was evaluated by using up to the third order of QCD correction for the Bjorken sum rule to be,

$$\alpha_s(Q^2 = 3.0(\text{GeV}/c)^2) = 0.417_{-0.110}^{+0.086}, \quad (6.5)$$

giving the consistency with the other measurements.

Quark polarization for each flavor was calculated using our deuteron data and hyperon decay constants under the assumption of flavor SU(3). The polarization of strange quark was found to be significantly negative, $\Delta s = -0.101 \pm 0.023$, suggesting that the assumption of the Ellis-Jaffe sum rule that the strange quark in nucleon is unpolarized, is incorrect. The total quark polarization was found to be 0.286 ± 0.055 which is much less than the prediction of 1.0 from the non-relativistic quark model and of 0.65 from the relativistic treat of bag model[70]. Now, 'spin crisis' is not 'crisis' anymore. Our understanding of the nucleon spin had been wrong and we have to establish a new model to describe the spin of the nucleon properly.

Many theoretical works have been carried out to explain the small total quark polarization.

The quark content of the nucleon spin was calculated employing the lattice QCD. M. Fukugita et al.[71] obtained $\Delta\Sigma = 0.18 \pm .10$ and $\Delta s = -.109 \pm .030$ which is reasonably consistent with our results. S. J. Dong et al. [72] calculated to be $\Delta\Sigma = 0.25 \pm .12$ and $\Delta s = -.12 \pm .01$ which is also consistent with our results.

A way to salvage the naive quark model of the nucleon, is to introduce a large gluon polarization. The diagram shown in Figure 6.1 causes a gluon contribution to the total quark polarization evaluated from the polarized e-N scattering. Accounting this effect called axial anomaly, the quark polarization evaluated from the polarized e-N scattering, $\Delta\tilde{q}$ is expressed to be [73]

$$\Delta\tilde{q} = \Delta q - \frac{\alpha_s}{2\pi} \Delta G, \quad (6.6)$$

where ΔG is the gluon polarization. The strong coupling constant α_s decreases with the increasing Q^2 and ΔG has Q^2 dependence like $\ln Q^2$ thus the second term of the RHS. of Equation (6.6) does not vanish in the scaling limit of $Q^2 \rightarrow \infty$. Therefore, the QCD correction by the power of α_s is not valid to correct this anomalous gluon contribution and we measure not the Δq , but the $\Delta \tilde{q}$ in the e-N scattering. If $\Delta G \sim 2$, the total quark polarization are corrected to be $\delta \Sigma \sim 0.6$ and $\Delta s \sim 0$ which are consistent to the results of the relativistic treat of the bag model. Of course, this large gluon polarization have to be canceled by the orbital angular momentum to conserve the angular momentum of the nucleon. An advantage of this model is conserving a non-singlet term like $\Delta u - \Delta d$ in the e-N scattering if the anomalous contribution is identical for three flavors. The Bjorken sum rule is then still valid in this model.

Skyrme model is being discussed recently because this model gives 0 quark polarization. In this model, the quark is interpreted to be a soliton solution of the $SU(N_c) \times SU(N_f)$ chiral Lagrangian where N_c and N_f are the numbers of the color and flavor of quarks in the nucleon. Notice that the quark in this model is mass-less. Although the whole of the nucleon spin is carried by the orbital motion of the quarks in this model, an possibility is denoted by Ref.[74] that the $1/N_c$ expansion and the quark mass correction make the quark carrying $\leq 30\%$ of the nucleon spin which is consistent to the experimental result.

More experiments are needed to make a further understanding of the spin structure of the nucleon. The Q^2 dependence and the low-x behavior of the spin structure function are curious to examine the perturbative QCD and to study the higher twist effect.

SLAC-E154 directly measured the spin structure function of neutron using gaseous ^3He target which was previously measured in SLAC-E142, but with higher beam polarization and higher energy electron beam than SLAC-E142. This measurement will improves the results of E142 and give the precise data for the neutron spin structure function. E154 ended its measurement in Fall of 1995 and the analysis is in progress.

SLAC-E155 will start in 1996 to measure the spin structure function of proton and deuteron with the 50 GeV polarized electron beam. This 50 GeV electron beam allows us to provide precise data down to lower x than the current SLAC data and to clarify

the low- x behavior of the spin structure function with high accuracy.

SMC experiment will keep their measurement for the spin structure function until 1996 and the measurement will decrease the ambiguity of their current results [16] [15] and provide the more precise data of the g_1 at low x region due to the high energy beam.

The gluon polarization may be a key to solve the nucleon spin. An exclusive meas-

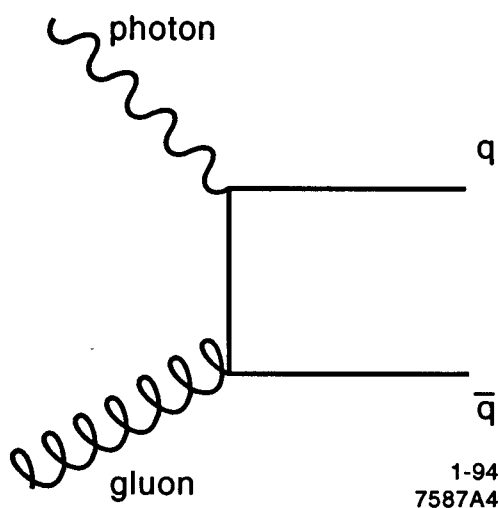


Figure 6.1: The Feynman diagram of photon-gluon fusion. The virtual photon and gluon make the quarkonium, $q\bar{q}$. The cross section of the interaction is supposed to depend on the gluon and photon helicities. charmonium, J/Ψ is the best candidate to tag the interaction because the charm quark is found hardly in the nucleon.

urement is suggested in positron-nucleon or proton-proton scattering to investigate gluon polarization[75]. The production rate for J/Ψ should depend on the gluon polarization in both cases, because the dominant process of the J/Ψ production is photon-gluon fusion as shown in Figure 6.1 or gluon-gluon scattering in e-N or NN scattering respectively. The following two projects, HERMES at DESY and Relativistic Hadron and Ion Collider, RHIC at BNL can possibly provide this most interesting measurement for the gluon polarization.

HERMES project[17] at DESY is measuring the polarized positron scattering with many kinds of polarized gaseous target. It has a large detector surrounding the interaction

point and the detector allows to study not only the inclusive cross section on a wide kinematical region, but also the exclusive measurement like quark-gluon fusion.

An polarized proton-proton scattering experiment is planed in RHIC at BNL. This experiment will measure the gluon polarization in the nucleon which is not found yet. Fermi National Accelerator Laboratory (FNAL) E-704 studied the gluon polarization in the nucleon using scattering of polarized protons or anti-protons off polarized proton target [76]and no gluon polarization was found but with the large experimental error.

Bibliography

- [1] R. W. McAllister and R. W. Hoftstadter, "Elastic Scattering of 188-MeV Electrons from the Proton and the Alpha." *Physical Review*, vol. 102, pp. 851, 1956.
- [2] R. Hoftstadter, *Electron scattering and Nuclear and Nucleon scattering*, Benjamin, New York, 1963.
- [3] A. Bodek et al., *Physics Letters B*, vol. 51, pp. 417, 1974.
- [4] T. Eichten et al., "Measurement of the Neutrino-Nucleon and Antineutrino-Nucleon Total Cross Sections", *Physics Letters B*, vol. 46, pp. 274, 1973.
- [5] F. Halzen and A. D. Martin, *Quark & Lepton*, John Wiley & Sons, Inc., 1986.
- [6] J. D. Bjorken, "Application of the Chiral $U(6) \otimes U(6)$ Algebra of Current Densities." *Physical Review*, vol. 148, pp. 26, 1966.
- [7] R. P. Feynman, *Photon Hadron Interactions*, Benjamin, New York, 1972.
- [8] J. Ellis and R. Jaffe, "Sum Rule for Deep-Inelastic Electro-production from Polarized Protons", *Physical Review D*, vol. 9, pp. 1444, 1974.
- [9] M. J. Alguard et al., "Deep Inelastic Scattering of Polarized Electrons by Polarized Protons", *Physical Review Letters*, vol. 37, pp. 1261, 1976.
- [10] G. Baum et al., "New Measurement of Deep-Inelastic E-P Asymmetry", *Physical Review Letters*, vol. 51, pp. 1135, 1983.

-
- [11] J. Ashman et al. (European Muon Collaboration), "A Measurement of the Spin Asymmetry and Determination of the Structure Function g_1 in Deep Inelastic Muon-Proton Scattering.", *Physics Letters B*, vol. 206, pp. 364, 1988.
- [12] E. Hughes et al. (E142 Collaboration), "Determination of the Neutron Spin Structure Function.", *Physical Review Letters*, vol. 71, pp. 959, 1993.
- [13] J. A. Dunne "Measurement of the Spin Structure Function of the Neutron g_1^n from Deep Inelastic Scattering of Polarized Electron from Polarized Neutrons in ^3He " *Ph. D. thesis*, American University, 1995
- [14] D. M. Kawall "A Determination of the Neutron Spin Structure Function" *Ph. D. thesis*, Stanford University, 1995
- [15] D. Adams et al. (Spin Muon Collaboration), "Measurement of the Spin-Dependent Structure Function $g_1(x)$ of the Proton" *Physics Letters B*, vol. 329, pp. 339, 1994.
- [16] D. Adams et al. (Spin Muon Collaboration), "A New Measurement of the Spin-Dependent Structure Function $g_1(x)$ of the Deuteron", *CERN-PPE 97, Submitted to Physics Letters B*, 1995,
- [17] HERMES collaboration, "A Proposal to Measure the Spin-Dependent Structure Functions Neutron and Proton at HERA" *DESY*, 1990.
- [18] K. Abe et al. (E143 collaboration), "Precision Measurement of the Proton Spin Structure Function g_1^p " *Physical Review Letters*, vol. 74, pp. 346, 1995.
- [19] K. Abe et al. (E143 collaboration), "Precision Measurement of the Deuteron Spin Structure Function g_1^d ." *Physical Review Letters*, vol. 75, pp 25, 1995
- [20] T. Averett "Measurement of the Spin Structure Function $g_2(x, Q^2)$ for the Proton and Deuteron" *Ph. D. thesis, University of Virginia*, 1995
- [21] T. Pussierx and R. Windmolders, "A Collection of Formulas for Spin Dependent Deep Inelastic Scattering.", *SMC-NOTE*, vol. 93, 1993.

-
- [22] P. Bosted "Polarized Asymmetry Formulas", *E143 Technical Note*, 1993.
- [23] J. Xu, Ph. D. thesis, Syracuse University, 1995
- [24] E. Hughes "Polarized Lepton-Nucleon Scattering" *Proceedings of SLAC Summer Institute*, 1994.
- [25] S. A. Larin and J. A. M. Vermaseren, "The α_s^3 Corrections to the Bjorken Sum Rule for Polarized Electro-production and the Gross-Llewellyn-Smith Sum Rule.", *Physics Letters B*, vol. 259, pp. 345, 1991.
- [26] Particle Data Group, "Review of Particle Property.", *Physical Review D*, vol. 50, 1994.
- [27] S. A. Larin, "The Next-to-Leading QCD Approximation to the Ellis-Jaffe Sum Rule", *Physics Letters B*, vol. 334, pp. 192, 1994.
- [28] B. Desplanques, "Deuteron D-state probability and energy-dependent NN interactions" *Physics Letters B*, vol. 203, pp. 200, 1988.
- [29] D. Schultz, R. Alley, J. Clendenin, G. Mulhollan, P. Saez, H. Tang, and K. Witte "The Polarized Electron Source of the Stanford Linear Accelerator Center" *SLAC-PUB*, 6606, 1994
- [30] T. Maruyama, E. L. Garwin, R. Prepost, and G. H. Zapalac "Electron-spin polarization in photo-emission from strained GaAs grown on GaAs_{1-x}P_x" *Physical Review B*, vol. 46, pp. 4261, 1992.
- [31] T. Maruyama, *Private Communication*
- [32] M. Woods, "Polarization at SLAC.", *SLAC-PUB*, 6694, 1995.
- [33] S. Kuhn and M. Hing, "Toroid Calibration for E143.", *E143 Technical Note*, 88, 1995.

- [34] H. Band, "Møller Polarimeter at SLAC.", *E143 Technical Note*, 84, 1994
- [35] R. Prepost "The Evaluation of g'_{eff} for the Møller Target Foils" *E143 Technical note*, 65, 1994
- [36] M. Swartz et al., *SLAC-PUB*, 6467, 1994.
- [37] G. D. Cates, Jr., "Polarization Targets in High Energy Physics.", *In Proceeding of SLAC Summer Institute*, 1993
- [38] Spin Muon Collaboration, "Enhancement of Nuclear Polarization with Frequency Modulated Microwaves" *CERN-PPE*, 95-31, 1995
- [39] G. R. Court, D. W. Gifford, P. Harrison, W. G. Heys, and M. A. Houlden, "A High Precision Q-Meter for the Measurement of Proton Polarization in Polarized Targets.", *Nuclear Instruments & Methods in Physics Research A*, vol. 324, pp. 433, 1993.
- [40] G. G. Petratos, R. L. Eisele, R. A. Gearhart, E. W. Hughes, and C. C. Young, "Large Acceptance Magnetic Spectrometers for Polarized Deep Inelastic Electron Scattering.", *SLAC-PUB*, 5678, 1991.
- [41] R. Erbacher, "SLAC E143 Čerenkov Technical Report.", *E143 Technical Note*, 1994
- [42] K. Kleinknecht, translated by K. Takahashi and H. Yoshiki, *Detektoren fuer Teilchenstrahlung*, Baifukan Co. Lmtd., Tokyo, Japan, 1987
- [43] V. Breton, H. Fronvieuille, P. Grenier, C. Guicheney, J.Jousset, Y. Roblin, and F. Tamin, "Application of Neural Networks and Cellular Automata to Calorimetric Problems", *E143 Technical Note*, 70, 1994
- [44] H. Fonvieuille and P. Grenier, "Shower Counter Calibration." *E143 Technical Note*, 36, 1994
- [45] H. Yuta et al., Presented in E143 collaboration meeting, 1993

-
- [46] M. Kuriki et al. "Performance of Trigger Counters for E143" *Tohoku HEP-NOTE*, 1995.
- [47] F. Staley, "Systematic Errors on the Cluster Centroid", *E143 Technical note*, 68, 1994.
- [48] F. Staley, "TDC for the Shower Counter", *E143 Technical note*, 69, 1994.
- [49] T. J. Liu "Dead Time Correction", *E143 Technical note*, 1994.
- [50] D. Crabb, *E143 Collaboration Meeting at SLAC*, 1994
- [51] Tingjun Liu, "Measurements of Spin Structure Function g_1^p and g_1^d for Proton and Deuteron at SLAC E143" *Ph.D. Thesis for University of Virginia*, 1996.
- [52] *Zeitschrift fuer Physik C*, vol. 51, pp. 387, 1991.
- [53] J. Gomez et al., "Measurement of A-Dependence of Deep-Inelastic Electron Scattering.", *SLAC-PUB*, 5813, 1993.
- [54] T. Kukhto and N. Schmeiko, *Nuclear Physics B*, vol. 219, pp. 412, 1983.
- [55] P. Bosted et al., "Measurements of the Electric and Magnetic Form-Factors of the Proton from $Q^2 = 1.75$ to $4.00(\text{GeV}/C)^2$." *Physical Review Letters*, vol. 68, pp. 3841, 1992.
- [56] A. Lung et al., "Measurements of the Electric and Magnetic Form Factors of the Neutron from $Q^2 = 1.75$ to $4.00(\text{GeV}/C)^2$." *Physical Review Letters*, vol. 70, pp. 718, 1993.
- [57] L. M. Stuart, "Deuteron Elastic Form Factor" *E143 Collaboration Meeting at SLAC*, March 1994.
- [58] K. Abe et al. (SLAC-E143 collaboration) "Measurement of the Q^2 -Dependence of the Proton and Deuteron Spin Structure Functions g_1^p and g_1^d ." *SLAC-PUB-95-6997*, Submitted to *Physical Review Letters*, 1995

-
- [59] P. Amaudruz et al. (New Muon Collaboration), "Proton and Deuteron F_2 Structure Functions in Deep Inelastic Muon Scattering", *Physics Letters B*, vol. 295, pp. 159, 1992.
- [60] L. Whitelow, S. Rock, A. Bodek, S. Dasu, and E. M. Riordan, "A Precise Extraction of $R = \sigma_L/\sigma_T$ from a Global Analysis of the Deep Inelastic e-P and e-D Scattering Cross Sections", *Physics Letters B*, vol. 250, pp. 193, 1990.
- [61] A. Feltham and P. Steiner, "Beam Polarization Update" *E143 Collaboration Meeting at SLAC*, September, 1994.
- [62] L. W. Whitelow et al., *Physics Letters B*, vol. 282, pp. 475, 1992.
- [63] O. A. Rondon, *Private Communication*, 1994
- [64] T. Averett, "Packing Fraction" *E143 Collaboration Meeting*, 1994.
- [65] P. Bosted, *Private Communication*, 1994.
- [66] R. Heimann, "Spin Dependent High Frequency Inelastic Electron Scattering and Helicity Flip Couplings", *Nuclear Physics B*, vol. 64, pp. 429, 1973.
- [67] S. J. Brodsky, M. Burkardt, and I. Schmidt "Perturbative QCD Constraints on the Shape of Polarized Quark and Gluon Distributions." *SLAC-PUB*, 6087, 1994.
- [68] M. Arneodo et al. (New Muon Collaboration) "Quark and gluon distributions and α_s from nucleon structure functions at low x " *Physics Letters B*, vol. 309, pp. 222, 1993.
- [69] W. C. Leung et al. *Physics Letters B*, vol. 317, pp. 655, 1993.
- [70] S. M. Troshin and N. E. Tyurin "Spin phenomena in particle interaction"
- [71] M. Fukugita, Y. Kurashima, M. Okawa, and A. Ukawa "Proton Spin Structure from Lattice QCD" *Physical Review Letters*, vol. 75, pp. 2092, 1995

-
- [72] S. J. Dong, J. -F. Lagaë, and K. F. Liu "Flavor-Singlet g_A from Lattice QCD" *Physical Review Letters*, vol. 75, pp.2096, 1995
- [73] M. Anselmino, A. Efremov, and E. Leader "The Theory and Phenomenology of Polarized Deep Inelastic Scattering" *CERN-TH. 7216/94*, 1994
- [74] J. Schechter et al. "Two-Component Approach to the "Proton Spin" Puzzle in Generalized Skyrme Models" *Physical Review Letters*, vol. 24, pp. 2955, 1990
- [75] T. Morii, S. Tanaka, and T. Yamanishi "Effects of the large gluon polarization on $xg_1^d(x)$ and J/Ψ productions at polarized ep and pp collisions" *KOBE-FHD-93-08*, 1993
- [76] D. L. Adams et al. (FNAL E581/E704 Collaboration) "Measurement of the double-spin asymmetry A_{LL} for inclusive multi- γ pair production with 200GeV/c polarized proton beam and polarized proton target" *Physics Letters B*, vol. 336, pp. 269, 1994.
- [77] I. J. R. Aithison and A. J. G. Hey, *GAUGE THEORIES IN PARTICLE PHYSICS*, Adam Hilger LTD., 1982
- [78] J. D. Bjorken and S. D. Drell, *Relativistic Quantum Mechanics*, McGraw-Hill Book Company, 1964.
- [79] R. Carlitz and J. Kauer "Chiral Structure of the Nucleon" *Physical Review Letters*, vol. 38, pp. 673, 1977.
- [80] D. G. Crabb and D. B. Day "The Virginia/Basel/SLAC Polarized Target: Operation and Performance during Experiment E143 at SLAC", *E143 Technical note*, 77, 1994.

Appendix A

The E143 Collaboration

K. Abe,¹⁵ T. Akagi,^{12,15} P. L. Anthony,¹² R. Antonov,¹¹ R. G. Arnold,¹ T. Averett,¹⁶ H. R. Band,¹⁷
J. M. Bauer,⁷ H. Borel,⁵ P. E. Bosted,¹ V. Breton,³ J. Button-Shafer,⁷ J. P. Chen,¹⁶ T. E. Chupp,⁸
J. Clendenin,¹² C. Comptour,³ K. P. Coulter,⁸ G. Court,¹² D. Crabb,¹⁶ M. Daoudi,¹² D. Day,¹⁶
F. S. Dietrich,⁶ J. Dunne,¹ H. Dutz,¹² R. Erbacher,^{12,13} J. Fellbaum,¹ A. Feltham,² H. Fonvieille,³
E. Frliez,¹⁶ D. Garvey,⁹ R. Gearhart,¹² J. Gomez,⁴ P. Grenier,⁵ K. Griffioen,¹¹ S. Hoibraten,¹⁶
E. W. Hughes,¹² C. Hyde-Wright,¹⁰ J. R. Johnson,¹⁷ D. Kawall,¹³ A. Klein,¹⁰ S. E. Kuhn,¹⁰
M. Kuriki,¹⁵ R. Lindgren,¹⁶ T. J. Liu,¹⁶ R. M. Lombard-Nelsen,⁵ J. Marroncle,⁵ T. Maruyama,¹²
X. K. Maruyama,⁹ J. McCarthy,¹⁶ W. Meyer,¹² Z. -E. Meziani,^{13,14} R. Minehart,¹⁶ J. Mitchell,⁴
J. Morgenstern,⁵ G. G. Petratos,¹² R. Pitthan,¹² D. Pocanic,¹⁶ C. Prescott,¹² R. Prepost,¹⁷
P. Raines,¹¹ B. Raue,¹⁰ D. Reyna,¹ A. Rijllart,¹² Y. Roblin,³ L. S. Rochester,¹² S. E. Rock,¹
O. Rondon-Aramayo,¹⁶ I. Sick,² L. C. Smith,¹⁶ T. B. Smith,⁸ M. Spengos,¹ F. Staley,⁵ P. Steiner,²
S. St. Lorant,¹² L. M. Stuart,¹² F. Suekane,¹⁵ Z. M. Szalata,¹ H. Tang,¹² Y. Terrien,⁵ T. Usher,¹²
D. Walz,¹² J. L. White,¹ K. Witte,¹² C. C. Young,¹² B. Youngman,¹² H. Yuta,¹⁵ G. Zapalac,¹⁷
B. Zihlmann,² D. Zimmermann¹⁶

1. The American University
2. Institute für Physik der Universität Basel
3. Laboratoire de Physique Corpusculaire, IN2P3/CNRS, University Blaise Pascal
4. Continuous Electron Beam Accelerator Facility
5. DAPNIA-Service de Physique Nucleaire Centre d'Etudes de Saclay
6. Lawrence Livermore National Laboratory
7. University of Massachusetts
8. University of Michigan
9. Naval Postgraduate School
10. Old Dominion University
11. University of Pennsylvania
12. Stanford Linear Accelerator Center
13. Stanford University
14. Temple University

15. Tohoku University
16. University of Virginia
17. University of Wisconsin

Appendix B

Spin-dependent cross section

The cross section in the laboratory frame are expressed in terms of the lepton tensor, $L^{\mu\nu}$ and the hadron tensor, $W_{\mu\nu}$ by [21]

$$\frac{d^2\sigma}{dE'd\Omega} = \frac{e^4}{16\pi^2Q^4} \frac{E'}{E} L^{\mu\nu} W_{\mu\nu}, \quad (\text{B.1})$$

where E and E' are the energy of the initial and final state electron respectively, Q^2 is defined in Equation (2.4). In the following sections, we derive these tensors and the cross section for the polarized electron and nucleon scattering. We will use the kinematics defined in Section 2.

B.1 Lepton tensor

The lepton tensor is calculated from Dirac spinor and electro-magnetic current[5],

$$\begin{aligned} L^{\mu\nu} &= \sum_{s'} \bar{u}(k', s') \gamma^\mu u(k, s) \bar{u}(k, s) \gamma^\nu u(k', s') \\ &= \text{Tr} \left[\sum_{s'} u(k', s') \bar{u}(k', s') \gamma^\mu u(k, s) \bar{u}(k, s) \gamma^\nu \right], \end{aligned} \quad (\text{B.2})$$

where u and \bar{u} are Dirac spinor and hermit conjugation of that, and γ^μ is gamma matrix. Because we investigate the inclusive scattering, the tensor is summed over the final spin states. A product of spinor summed over the spin states, is described by four momentum

and mass of the particle [77]. Then the term of the final lepton is expressed to be

$$\sum_{s'} u' \bar{u}' = (\not{k}' + m), \quad (\text{B.3})$$

where \not{k}' is the Feynman dagger defined in reference. [78]

Because the initial lepton is polarized, the products of the Dirac spinor are not summed over the initial spin states. Even though, we sum the product over the spin states and apply the spin projector[21] for our convenience. The spin projector extracts one of helicity states from the product,

$$u \bar{u} = (\not{k} + m) \frac{1}{2} (1 + \gamma_5 \not{s}), \quad (\text{B.4})$$

where γ_5 is defined by $\gamma_5 = i\gamma^0\gamma^1\gamma^2\gamma^3$ and s is a spin vector. Substituting these equations into equation(B.2), the lepton tensor is expressed by

$$L^{\mu\nu} = \frac{1}{2} \text{Tr} [(\not{k}' + m) \gamma^\mu (\not{k} + m) (1 + \gamma_5 \not{s}) \gamma^\nu]. \quad (\text{B.5})$$

The trace is expanded by using $g^{\mu\nu}$ and $\varepsilon^{\gamma\mu\delta\nu}$ as follows,

$$L^{\mu\nu} = 2 (k'^\mu k^\nu + k'^\nu k^\mu - (k \cdot k') g^{\mu\nu}) + 2m^2 g^{\mu\nu} + i2m \varepsilon^{\gamma\mu\delta\nu} q_\gamma s_\delta. \quad (\text{B.6})$$

The last term in this equation is an antisymmetric term with respect to a change of the initial lepton helicity. As shown later, the hadron tensor has also such symmetric and antisymmetric parts. To be convenient, we define the symmetric and antisymmetric parts of the lepton tensor to be,

$$L_S^{\mu\nu} = 2 (k'^\mu k^\nu + k'^\nu k^\mu - (k \cdot k') g^{\mu\nu}) + 4m^2 g^{\mu\nu} \quad (\text{B.7})$$

$$L_A^{\mu\nu} = i2m \varepsilon^{\gamma\mu\delta\nu} q_\gamma s_\delta \quad (\text{B.8})$$

B.2 Hadron tensor

The hadron has the complex substructure and thus we can not determine the hadron tensor in explicit terms. Although, the following assumptions limit which vector product can be involved into the tensor;

1. Parity conservation,
2. Time reversal conservation,
3. Hermiticity,
4. Translation invariance,
5. Current conservation.

Under these assumptions, the hadron tensor is expressed by using four structure functions to be [21],

$$\begin{aligned}
W_{\mu\nu} = & W_1 \left(-g_{\mu\nu} + \frac{q_\mu q_\nu}{q^2} \right) + \frac{\nu}{M} \frac{W_2}{p \cdot q} \left(p_\mu - \frac{p \cdot q}{q^2} q_\mu \right) \left(p_\nu - \frac{p \cdot q}{q^2} q_\nu \right) \\
& + \frac{iM^2 \nu G_1}{p \cdot q} \varepsilon_{\mu\nu\rho\tau} q^\rho \lambda^\tau + \frac{iM\nu^2 G_2}{(p \cdot q)^2} \varepsilon_{\mu\nu\rho\tau} q^\rho (p \cdot q \lambda^\tau - \lambda \cdot q p^\tau), \quad (\text{B.9})
\end{aligned}$$

where W_1 , W_2 , G_1 , and G_2 are four structure functions of the hadron. These structure functions are the function of ν and Q^2 .

The requirement of the current conservation for the lepton tensor is giving a relation of

$$\partial_\mu L^{\mu\nu} = q_\mu L^{\mu\nu} = 0 (\text{same for } \nu). \quad (\text{B.10})$$

This formula means that a term which has q_μ or q_ν is erased in the contracting with the lepton tensor. Effectively, we can erase terms which have q_μ or q_ν in the equation(B.10). If we divide the hadron tensor into symmetric and antisymmetric parts, the equation(B.10) is rewritten to be

$$W_{S\mu\nu} = -W_1 g_{\mu\nu} + \frac{\nu}{M} \frac{W_2}{p \cdot q} p_\mu p_\nu \quad (\text{B.11})$$

$$W_{A\mu\nu} = \frac{iM^2 \nu G_1}{p \cdot q} \varepsilon_{\mu\nu\rho\tau} q^\rho \lambda^\tau + \frac{iM\nu^2 G_2}{(p \cdot q)^2} \varepsilon_{\mu\nu\rho\tau} q^\rho (p \cdot q \lambda^\tau - \lambda \cdot q p^\tau) \quad (\text{B.12})$$

B.3 Tensor contraction and the cross section

The contraction of the lepton tensor and the hadron tensor is expressed in the symmetric and antisymmetric terms to be

$$L^{\mu\nu}W_{\mu\nu} = L_S^{\mu\nu}W_{S\mu\nu} + L_A^{\mu\nu}W_{A\mu\nu}, \quad (\text{B.13})$$

where the contraction between the symmetric and antisymmetric terms is to be 0 under the parity invariance.

Using Equations (B.7) and (B.11), the tensor contraction for the symmetric terms are expressed to be

$$\begin{aligned} L_S^{\mu\nu}W_{S\mu\nu} &= 2[k'^{\mu}k^{\nu} + k^{\nu}k'^{\mu} - (k \cdot k')g^{\mu\nu}] \left[-W_1g_{\mu\nu} + \frac{\nu W_2}{M(p \cdot q)}p_{\mu}p_{\nu} \right] \\ &= 4(k \cdot k')W_1 + \frac{2\nu W_2}{M(p \cdot q)}[2(p \cdot k')(p \cdot k) - (k \cdot k')p^2] \\ &= 4EE' [W_2 \cos^2(\theta/2) + 2W_1 \sin^2(\theta/2)]. \end{aligned} \quad (\text{B.14})$$

Using Equations (B.8) and (B.12), the tensor contraction for the antisymmetric terms are expressed to be

$$L_A^{\mu\nu}W_{A\mu\nu} = mMG_1 [(q \cdot \lambda)(q \cdot s) - q^2(s \cdot \lambda)] - 4m\nu G_2 q^2(s \cdot \lambda) + 4m\nu^2 G_2 [q^2(\lambda \cdot q)(s \cdot p)]. \quad (\text{B.15})$$

Let the electron polarize parallel or anti-parallel to its momentum, the electron polarization vector, s is expressed using its helicity, H_l , to be

$$s = H_l \left(\frac{E}{m}; 0, 0, \frac{E}{m} \right). \quad (\text{B.16})$$

We assume two nucleon polarizations parallel or perpendicular to the electron momentum. The polarization vector for these states are expressed to be

$$\textit{parallel} \quad \lambda = (0; 0, 0, 1), \quad (\text{B.17})$$

$$\textit{perpendicular} \quad \lambda = (0; \cos \phi, \sin \phi, 0), \quad (\text{B.18})$$

where the event plane is defined to be z-x plane and the sign of the momentum of the scattered electron in x to be positive. The nucleon in the perpendicular configuration is polarized in the angle of ϕ from the x-axis.

Using these polarization vectors, the tensor contractions for the anti-symmetric terms are expressed by

$$\text{parallel} \quad L_A^{\mu\nu} W_{A\mu\nu} = -2H_l Q^2 [MG_1(E' \cos \theta + E) - G_2 Q^2], \quad (\text{B.19})$$

$$\text{perpendicular} \quad L_A^{\mu\nu} W_{A\mu\nu} = -2H_l Q^2 E' \sin \theta \cos \phi [MG_1 + 2G_2 E]. \quad (\text{B.20})$$

Thus the cross section between the polarized electron and the polarized nucleon are expressed to be

$$\text{parallel} \quad \frac{d^2 \sigma^{\uparrow\downarrow(\uparrow)}}{dE' d\Omega} = \frac{e^4}{16\pi^2 Q^2} \frac{E'}{E} \left[[W_2 \cot^2(\theta/2) + 2W_1] - 2H_l [MG_1(E' \cos \theta + E) - G_2 Q^2] \right], \quad (\text{B.21})$$

$$\text{perpendicular} \quad \frac{d^2 \sigma^{\leftarrow\downarrow(\uparrow)}}{dE' d\Omega} = \frac{e^4}{16\pi^2 Q^2} \frac{E'}{E} \left[[W_2 \cot^2(\theta/2) + 2W_1] - 2H_l E' \sin \theta \cos \phi [MG_1 + 2G_2 E] \right], \quad (\text{B.22})$$

where the superscripts of the σ show the directions of the spin of the nucleon and electron respectively. The cross section for the unpolarized reaction is obtained averaging these cross sections for the polarized reaction over the electron helicity to be

$$\frac{1}{2} \left[\frac{d^2 \sigma^{\uparrow(\leftarrow)\downarrow}}{dE' d\Omega} + \frac{d^2 \sigma^{\uparrow(\leftarrow)\uparrow}}{dE' d\Omega} \right] = \frac{e^4}{16\pi^2 Q^2 \tan^2(\theta/2)} \frac{E'}{E} [W_2 + 2 \tan^2(\theta/2) W_1]. \quad (\text{B.23})$$

The differences of the cross sections with the flip of the electron helicity, on the other hand, are expressed as follows,

$$\text{parallel} \quad \frac{d^2 \sigma^{\uparrow\downarrow}}{dE' d\Omega} - \frac{d^2 \sigma^{\uparrow\uparrow}}{dE' d\Omega} = \frac{e^4}{16\pi^2 Q^2} \frac{E'}{E} 4 [MG_1(E' \cos \theta + E) - G_2 Q^2], \quad (\text{B.24})$$

perpendicular

$$\frac{d^2\sigma^{\leftarrow\downarrow}}{dE'd\Omega} - \frac{d^2\sigma^{\leftarrow\uparrow}}{dE'd\Omega} = \frac{e^4}{16\pi^2Q^2} \frac{E'}{E} 4E' \sin\theta \cos\phi [MG_1 + 2G_2E]. \quad (\text{B.25})$$

If the nucleon is polarized along the x axis, ie. $\phi = 0^\circ$ or 180° in the perpendicular configuration, the Equation (B.25) is rewritten to be

$$\frac{d^2\sigma^{\leftarrow\downarrow}}{dE'd\Omega} - \frac{d^2\sigma^{\leftarrow\uparrow}}{dE'd\Omega} = \frac{e^4}{16\pi^2Q^2} \frac{E'}{E} 4E' H \sin\theta [MG_1 + 2G_2E]. \quad (\text{B.26})$$

where H is $+1$ or -1 corresponding to $\phi = 0^\circ$ or 180° . Because ϕ is defined from the x-axis giving the positive sign of the scattered electron momentum in x, H is equal to the sign of the inner product of the electron momentum and the spin vector of the nucleon.

Appendix C

Kauer and Carlitz model

R. Carlitz and J. Kauer developed a phenomenological model for the spin structure of the nucleon[79]. They expressed the spin structure for three regions over x using three assumptions separately and combined them together.

They assumed the SU(6) model was useful at the middle region, $x \sim 0.3$ because the nucleon is composed by three quarks in the SU(6) model. In this model, the wave function of proton is expressed in terms of u and d quarks to be,

$$|p_{\uparrow}\rangle = \frac{1}{\sqrt{18}} [2u_{\uparrow}u_{\uparrow}d_{\downarrow} - u_{\uparrow}u_{\downarrow}d_{\uparrow} - u_{\downarrow}u_{\uparrow}d_{\uparrow} + \dots], \quad (\text{C.1})$$

where the arrow show the direction of the quark spin with respect to that of the nucleon spin. From the wave function, the expectation value for the quark polarization is given to be

$$\begin{aligned} \Delta u &= u_{\uparrow} - u_{\downarrow} = \frac{5}{3} - \frac{1}{3} = \frac{4}{3}, \\ \Delta d &= d_{\uparrow} - d_{\downarrow} = \frac{1}{3} - \frac{2}{3} = -\frac{1}{3}, \end{aligned} \quad (\text{C.2})$$

which give the total quark polarization to be

$$\frac{\hbar}{2} = \frac{\hbar}{2} \sum \Delta q (= 1). \quad (\text{C.3})$$

The virtual photon cross section asymmetry A_1 defined by Equation (2.36) is expected

by the SU(6) model for nucleons to be,

$$A_1^p = \frac{4/9\Delta u + 1/9\Delta d}{4/92 + 1/91} = \frac{5}{9} \quad (\text{C.4})$$

$$A_1^n = \frac{4/9\Delta d + 1/9\Delta u}{4/91 + 1/92} = 0 \quad (\text{C.5})$$

In the high x region, they assumed the struck parton with the large momentum fraction carrying also the nucleon spin. The asymmetry $A_1(x)$, then, approaches to 1 at $x = 1$.

In low x region, they assumed the Regge theory. Because the gluon take away the initial spin of the struck quark, the asymmetry approaches to 0 at $x = 0$ with Regge form.

Figure C.1 shows the expected shape for the virtual photon asymmetries $A_1(x)$ for proton and neutron from these three assumptions.

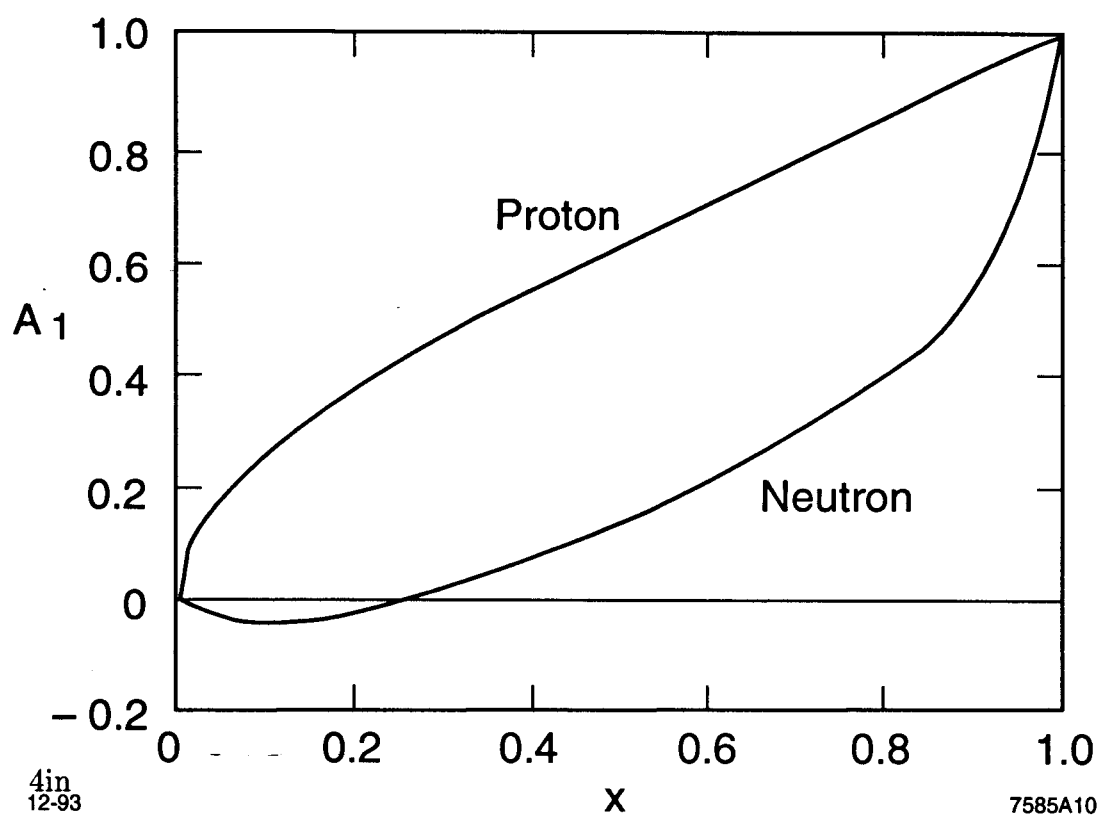


Figure C.1: The Carlitz and Kauer model for $A_1(x)$

Appendix D

Derivation of nitrogen correction

In the frozen $^{15}\text{ND}_3$ target, a small polarization of nucleons (nuclei) other than deuterons were recognized. Then the cross section asymmetry for the target included the contributions from those nucleons (nuclei). We derive the relation between the cross section asymmetry for the deuteron and that for the actual target.

We defined the contaminations of $^{14}\text{N}(\eta_{14})$ and proton(η_p) to be

$$\eta_p = \frac{\#of\text{NH}_3}{\#of\text{ND}_3 + \#of\text{NH}_3} \quad (\text{D.1})$$

$$\eta_{14} = \frac{\#of^{14}\text{N}}{\#of^{14}\text{N} + \#of^{15}\text{N}}, \quad (\text{D.2})$$

and the polarization, the cross section, and the cross section asymmetry of these nucleon and nuclei as p , σ , and A with subscription d , p , 14, and 15 respectively. The measured cross section asymmetry is expressed in terms of these quantities,

$$A = p_b \frac{3(1 - \eta_p)\sigma_d p_d A_d + 3\eta_p \sigma_p p_p A_p + (1 - \eta_{14})\sigma_{15} p_{15} A_{15} + \eta_{14} \sigma_{14} p_{14} A_{14}}{3\sigma_d + \sigma_{15} + \text{other}}, \quad (\text{D.3})$$

where we neglected η_p and η_{14} in the denominator. We introduce the dilution factor which was defined in Section 4.2.4, so the equation can be rewritten to be

$$A = p_b p_d f \left[(1 - \eta_p) A_d + \eta_p \frac{\sigma_p p_p}{\sigma_d p_d} A_p + (1 - \eta_{14}) \frac{\sigma_{15} p_{15}}{3\sigma_d p_d} A_{15} + \eta_{14} \frac{\sigma_{14} p_{14}}{3\sigma_d p_d} A_{14} \right]. \quad (\text{D.4})$$

The asymmetry of the nitrogen nucleus and deuteron is expressed in terms of the

unpaired nucleons to be

$$\sigma_{15}A_{15} = \frac{\sigma_p A_p}{3} g_N \quad (\text{D.5})$$

$$\sigma_{14}A_{14} = \frac{\sigma_p A_p + \sigma_n A_n}{3} g_N \quad (\text{D.6})$$

$$\sigma_d A_d = (1 - 1.5w_D)(\sigma_p A_p + \sigma_n A_n), \quad (\text{D.7})$$

where g_N is the EMC effect for nitrogen nucleus, and w_D is the D-state probability of the deuteron. We use the EMC effect of ^{14}N for both nitrogen nuclei. We assume the polarizations for both nitrogen nuclei to be $p_{14} = -p_{15} = p_N$ because the magnetic moments for those nuclei have opposite sign. We substitute these equations into Equation (D.4),

$$A = p_b p_d f \left[\left\{ (1 - \eta_p) + \frac{\eta_{14}}{9(1 - 1.5w_D)} \frac{p_N}{p_d} \right\} A_d + \left(\eta_p \frac{p_p}{p_d} + \frac{1 - \eta_{14}}{9} \frac{p_N}{p_d} g_N \right) \frac{\sigma_p}{\sigma_d} A_p \right]. \quad (\text{D.8})$$

We solved the equation for the cross section asymmetry of the deuteron and obtained

$$A_d = \frac{1}{\nu_1} \left[\frac{A}{p_d p_d f} - \nu_2 A_p \right], \quad (\text{D.9})$$

where ν_1 and ν_2 are given to be

$$\nu_1 = (1 - \eta_p) + \frac{\eta_{14}}{9(1 - 1.5w_D)} \frac{p_N}{p_d}, \quad (\text{D.10})$$

$$\nu_2 = \left(\eta_p \frac{p_p}{p_d} + \frac{1 - \eta_{14}}{9} \frac{p_N}{p_d} g_N \right) \frac{\sigma_p}{\sigma_d}. \quad (\text{D.11})$$

The contaminations of the η_{14} and η_p were estimated to be 2.0% and 1.5% respectively. The D-state probability is fixed to be $6.0 \pm 1.0\%$ [28]. We used the results from the proton measurement of E143 [18] for the proton asymmetry. We assumed that the ratio of the total cross sections, σ_p/σ_d , was the same as the ratio of the structure functions, F_{2p}/F_{2d} . The structure functions were obtained from the NMC parameterization[59]. The EMC effect is obtained from a fit using data from References [52] and [53]. The polarization of the proton and the nitrogen nucleus as a function of the deuteron polarization were measured by using the NMR technique as shown in Figures D.1 and D.2[80].

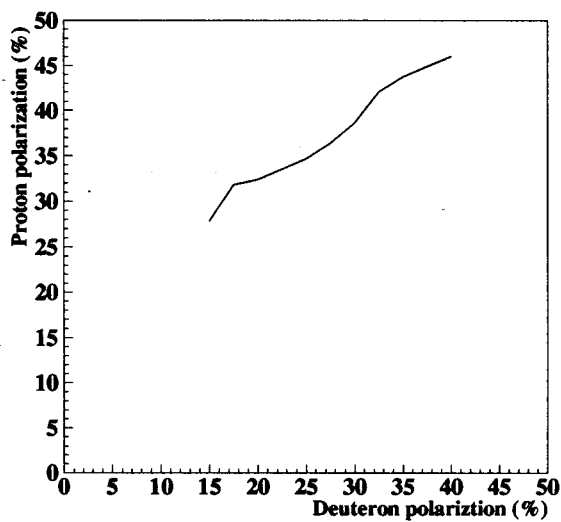


Figure D.1: Residual proton polarization as a function of the deuteron polarization.

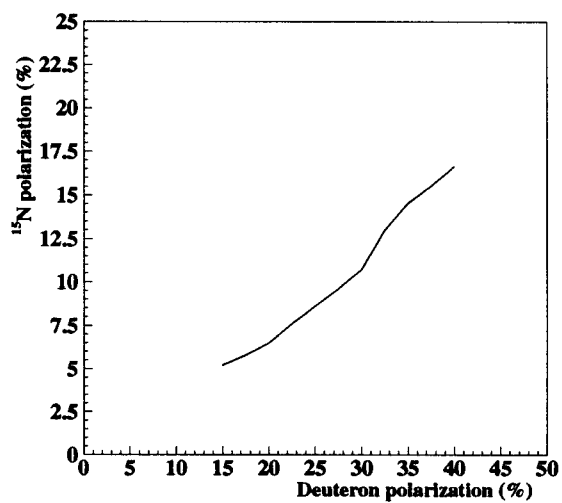


Figure D.2: ^{15}N polarization as a function of the deuteron polarization.